ScuDo

Scuola di Dottorato ~ Doctoral School

WHAT YOU ARE, TAKES YOU FAR

Doctoral Dissertation

Doctoral Program in Mechanical Engineering (32^{th}cycle)

High Fidelity Model of Ball Screws to Support Model-based Health Monitoring

By

Antonio Carlo Bertolino

******

Supervisor(s):

Prof. Massimo Sorli

Doctoral Examination Committee:

Prof. B. Allotta, Università degli Studi di Firenze, Italy

Prof. F. Braghin, Politecnico di Milano, Italy

Prof. G. Figliolini, Università di Cassino e del Lazio Meridionale, Italy

Prof. L. Garibaldi, Politecnico di Torino, Italy

Prof. S. Mauro, Politecnico di Torino, Italy

Politecnico di Torino

2020

Declaration

I hereby declare that, the contents and organization of this dissertation constitute my own original work and does not compromise in any way the rights of third parties, including those relating to the security of personal data.

Antonio Carlo Bertolino
2020

* This dissertation is presented in partial fulfillment of the requirements for **Ph.D. degree** in the Graduate School of Politecnico di Torino (ScuDo).

Reality leaves a lot to the imagination.

– John Lennon

Acknowledgements

First of all I wish to sincerely thank Prof. Massimo Sorli, who has been not only my supervisor but also a friend during this period, supporting me with his advice and encouragements. I am grateful to him to have made me live my Ph.D. with a positive perspective. I would like to thank also Profs. Giovanni Jacazio and Stefano Mauro for their kindness and support in the research activities.

A special thank goes to all my colleagues with which I spent almost entirely every day and who became an important part of my life. In particular I am thankful to Dr. Andrea De Martin for his huge support in every topic and his willingness to help me regardless his work, and to Andrea Raviola for being a good friend and have always supported me in the emotional sphere.

There are not enough words to thank Irene, the person with which I shared every single aspect of everything in the last eight years and who significantly helped me in the achievement of this objective, even if with some troubles.

Last but not least I would like to thank my family for their constant support and for being a constant source of inspiration.

Abstract

Born from environmental and cost saving concerns, the recent trend toward "more electric" aircraft has touched most of the more important on-board systems and equipment. For flight control devices, this tendency translated into several and still concurring efforts to replace the traditional electro–hydraulic configuration (EHSAs) with electro–mechanical actuators (EMAs) for primary and secondary aerodynamic surfaces, a technology already widely spread in several fields, such as the manufacturing industry.

EMAs theoretically provide several advantages over the hydraulic solution in terms of envelope, weight, environment pollution and so forth. Their widespread use is however hindered by a relatively higher jamming probability, which is beyond the imposed/required limit for manned and civil aircraft. To overcome this issue, several solutions have been proposed, mostly implying architectures with several redundancy levels of different actuator's components. These "jam-tolerant" solutions lead to the increase of the number of components and, consequently, to the increase of the overall weight and a significant reduction of the overall reliability, hence increasing the probability of fault occurrence during service.

An innovative solution is to employ a simple architecture with the minimum number of needed components, coupled with a prognostic and health monitoring system. This would allow to move from a preventive to a condition-based maintenance and potentially to predict the development of a jam-causing degradation, hence removing the need of encumbering mechanical redundancies. The awareness of fault modes is paramount to develop an effective PHM system: each fault occurrence has to be associated with one or multiple feature, indicative of the fault progression and actuator's health status. Monitoring these features in time it is possible to estimate the residual life of the components and to avoid the occurrence of a failure.

To do so, it is of primary importance to have a high–fidelity detailed dynamic model of the various EMA subcomponents, to be used as a virtual test bench on which to inject artificial defects, identify the appropriate feature and verify the PHM approach feasibility. Among all the components of an EMA, the ball screw is the most jam–critical.

Therefore, this thesis focuses on the development of a high–fidelity non–linear dynamic model of such component, with the ambition of accurately represent the physics of the system and the dynamics of the faults evolution in time as a direct consequence of the operative conditions. After an in-depth analysis of the current state of the art of ball screw modelling, the thesis describes the successive steps taken to prepare a multibody three–dimensional dynamic model of the system, complete with lubrication and degradation models. Several analysis are presented to prove the model capabilities and results are compared to the most advanced models available in literature. A number of selected degradations are hence simulated and the results discussed. To further test the model validity and support further analyses, a dedicated test bench has been designed and is currently under construction; both the model–based design and the final architecture of such test-bench are described in the thesis.

The proposed model puts the bases for the application of PHM strategies to ball screw mechanisms, allowing the effect of several kinds of defects to be investigated in a short time and a cost–effective way. This thesis is oriented mainly to aeronautical applications, since this is the field in which the introduction of the electromechanical technology is more challenging. Nevertheless, the content and applicability of this research is not only limited to this field, since ball screws are key components for actuation systems in several fields, in particular in machines for industrial applications.

Contents

List of Figures

List of Tables

Chapter 1

Introduction

1.1 Overview

In order to reduce pollution and increase the efficiency of aircraft, in the last decades a general trend towards the design of *more electric* aircraft has arisen [1–3]. The traditional civil aircraft architecture is based on various mutual interacting on–board systems, operated by different power sources, such as hydraulic, electrical, mechanical, pneumatic and so on [3–5]. The aim is to replace the currently wide–spread fly–by–wire electro-hydraulic servo–actuators (EHSA) with the electro-mechanical actuators (EMA) for flight controls [6–11], leading to the reduction of the complexity of the aircraft and, at the same time, of the environmental impact associated with the corrosive and dangerous fluid [12]. This is not an immediate process, though, since EMAs present a higher jamming probability with respect to the EHSAs, which makes this technology, in its base configuration, not suitable for safety critical applications, such as primary flight controls. Indeed, these actuators control the aircraft attitude and their correct functionality is of primary importance for the flight mission accomplishment.

Several mechanical layouts have been proposed in literature in order to mitigate the jamming issue and to reduce its occurrence probability [13–19]. Redundancies of several sub–components or of the entire actuator have been introduced in addition to the standard architecture, leading to the so called *jam–tolerant* actuators. These solutions can guarantee the controllability of the actuator even if a jamming occurs, although with decreased performances.

All these solutions, though, lead to an increase in terms of weight, volume and number of components: albeit reducing the jamming probability of the whole actuator and allowing it to operate even after a jam of an internal part, the larger number of components implies additional maintenance with the relative costs and a reduction in terms of reliability, making these solutions less attractive [20].

In order to overcome the afore–mentioned reliability and jam issues, a possible innovative and promising solution can be to adopt a minimal architecture of the EMA to minimize the failure rate, supported by an efficient prognostic and health management (PHM) system [20–22]. The latter should be able to rapidly detect the onset of faults and the insurgence of dangerous conditions (diagnosis), before they become critical turning faults into failures, to track their evolution and, eventually, to estimate the residual useful life of the component and, hence, of the entire actuator (prognosis) [23].

Currently, the maintenance process is *preventive* (or *time–based*), which means that each actuator is replaced with a new unit after a certain amount of flight hours, basing on historical failure data, or if its functionality is evidently degraded [24]. With this approach it can happen that a component is replaced even if it is healthy and it would be still able to work for more hours.

The PHM framework allows the maintenance process to become *predictive* (or *condition–based*), improving the aircraft operation reliability reducing ground immobilization time and delays. In fact, each component would not be replaced a priori, but based on its estimated health status, exploiting in such a way the maximum useful life possible, maintaining anyway a certain safety margin in order to avoid unexpected premature failures.

1.2 Problem statement

PHM is a promising and powerful technology, which has been adopted in different fields, such as on batteries [25], power–drives [26, 27], rotating machines [28], turbofan engines [29], bearings [29, 30], gears [27, 30] and so forth. Several studies have been carried out also in the aviation industry [31–33] and, in particular, on flight controls [22, 34–37]. In the latter field, the application of PHM techniques is more difficult, due to the following reasons:

- the introduction of any architectural variation or additional sensor must be thoroughly examined, approved and certified by the aviation authority, which barely allows modification unless after a large number of tests;
- the boundary and operative conditions of flight controls are extremely variable, hindering a straightforward application of standard prognostic techniques;
- in contrast to other fields, where large amounts of experimental data are available, on aircraft no extra sensors are allowed and therefore PHM must rely only on the information coming from the already installed ones [35];
- to be certified, the PHM framework should be able to operate in all the possible situations that can happen with a very low level of false positive and false negative situations. The effect of different progressing faults could shadow each other to the monitoring system, therefore the PHM system must be reliable and robust to be installed onboard;
- flight control actuators are complex systems, composed by different components which interact with each other: the PHM system should monitor all the components to guarantee a fully comprehensive indication of the overall health condition.

For these reasons EMAs are nowadays not employed as primary flight controls on civil aircraft (which have more stringent reliability requirements) but only on some unmanned aerial vehicle (UAV) or as backup actuators in secondary flight controls, on which jamming is not a strong issue. Indeed, in case of a failure of a secondary flight control, the preferred action is to maintain the aerodynamic surface stuck in the fail position to avoid uncontrolled movement under the external load actions [3].

PHM has thus to be still improved and developed to be applied as support for EMAs. In order to develop a reliable PHM system, it is mandatory to acquire a deep knowledge on the component under test and to analyse the effects of various fault entities on its performance under different operative conditions [23, 35]. In short, the PHM process can be subdivided in two main phases:

- The *offline* phase is the most time consuming part and it consists first in the definition of the possible failure modes of the system under analysis

(FMECA). A large number of experiments must be carried out inserting, in a healthy system, artificial defects reproducing the faults identified through the FMECA. From the analysis of the data acquired from the available sensors, different features must be identified and selected in such a way they are strictly correlated with the faults' extent. Finally, feature versus defects size maps are generated.

- The *online* phase is focused on the real component during its normal operations. From the experimental signals the same features identified in the offline phase are extracted. Basing on the previously obtained maps, the onset of one of the possible faults can be recognised and its size estimated. Eventually, the residual useful life before the ultimate failure is predicted, e.g. using the particle filter algorithm [37–39].

The detailed explanation of a PHM system is out of the scope of this thesis: the interested reader can found further details in [23].

During the offline phase, the link between faults and signal feature must be investigated, following either a data–driven or a model–based approach [35]. The first method can be applied either retrieving data from the real application or replicating the operative conditions in a test bench. This method is surely convenient in terms of truthfulness of the data since the extracted information would be a true representation of the real application. As already said, though, the aircraft operators and syndicates are reluctant to let the flight data to be examined and processed as well as the manufacturers to let new components and sensors to be added due to weight and reliability implications [40]. Experimental data can be then obtained by test benches, on which artificial faults seeding can be performed. Nevertheless, it is not easy to artificially reproduce the faults and the tests are expensive and time consuming.

With the evolution of the computer processors' performance in the last decades, a valid alternative has become to develop a mathematical model of the component under test to be used as a virtual bench, reducing the time and specially costs. It can be useful to understand the system behaviour under nominal and faulty conditions. Another advantage of this approach is that the measure uncertainties are eliminated and there is the certainty of which defect is active for each specific test/simulation. In such a way it becomes easier to understand the effect of each defect on the measured signals: the physics which causes its progression can be thoroughly analysed and an appropriate feature can be specifically designed to recognise each degradation

pattern and to track its evolution. Furthermore, several defects can be inserted at the same time to study the mutual interaction and, if the case, the mutual concealing. With experimental rigs, the defects have to be inserted physically: the component under test is degraded and tested but it is not possible to revert it to its initial healthy condition. Thus, only experiments with incremental defect extents can be performed and, in the end, the component is no more useful. With the simulation approach, obviously, this issue is easily avoided. In addition, to obtain statistically meaning results, several real components should be tested. During experimental tests, a lot of uncontrolled variables can influence the outcome of the analysis, including the uncertainty on the injected defect size, while with simulations these boundary conditions and uncertainties can be controlled and exploited.

Although all these advantages, in order to rely on the model results, it must be validated with experimental data. The mathematical model is a very powerful tool useful in a preliminary phase of the investigation to get an initial perspective of the system, but it must converge to the test field results. It has also to be highlighted that the model will never be able to give exactly the real representation of the system, but it approximates it more or less accurately, depending on the level of detail of the model. A compromise must be found between accuracy and simulation time, in relation to what the model is used for. Usually, a hybrid approach is followed, in which the modelling phase is followed by experimental campaigns of validation [35].

It is well known that, to support prognostic algorithms, it is paramount to develop a model with a high level of detail in which the defects representations are physic–based, specially if it is intended to model a particular component rather than the entire actuator.

1.3 Objectives of the research project

Several researches in literature have highlighted the need to accurately model the mechanical components of EMAs, since they are involved with friction, which is considered the major cause of jamming in EMAs [35, 41–43]. From the FMECA in [22, 43] it results that the ball screw is among the most critical components in EMAs, in terms of severity of faults, testability and repeatability of faulty conditions. The most critical degradations have been identified in scoring, wear and spalling

of the contact surfaces within the ball screw. Another critical failure of ball screws is the jam due to deformation of the return tube or seizure of damaged spheres inside it. Further fault modes of EMAs and their components will be extensively presented in Chapter 2. The closed system nature of this components makes it hard to investigate experimentally the behaviour of internal components, therefore several studies have been carried out in literature to investigate the motion of the spheres within the ball screw (see Chapter 4). Most of these models have been formulated in quasi–static conditions and cannot represent the system response to time variant position demands under the action of variable external loads.

The main aim of this research project was to develop a dynamic non–linear mathematical model with a high level of detail of the ball screw component, able to accurately describe the complete dynamics of this mechanism and that could be employed as virtual test bench to study the effect of several degradations on the actuator overall performance and on the measurable signals.

Specific aspects of the present research to address the above objective are:

- To represent the kinematic joint between the rotating and translating elements;
- To describe the motion of the spheres with all their degrees of freedom without imposing any kinematic constraint;
- To develop a new formula to calculate the curvature of the ball screw grooves, in order to improve the accuracy of the contact parameters;
- To construct and implement a three–dimensional multibody dynamic model of the mechanism that accept time variant inputs and disturbs and that can be easily integrated into a more complete EMA model;
- To develop a three–dimensional contact algorithm between spheres and grooves;
- To take into account the presence of lubrication in the contacts;
- To design an experimental test bench for ball screws from which to obtain the data to validate the model results;
- To build a detailed model of the test bench as a support for its robust design and to use it to perform a Monte Carlo analysis to verify the insensitivity of the measured signals on test rig from the sensors uncertainties, geometric tolerances and environmental disturbances.

1.4 Organization of the dissertation

The structure of the thesis is organised in ten chapters that are briefly introduced as following:

CHAPTER 1 gives an overview of the PhD dissertation.

CHAPTER 2 briefly describes the architecture of the electro–mechanical actuators and presents a number of anti–jamming possible solutions. A comprehensive FMECA on these kinds of actuator is presented.

CHAPTER 3 introduces the ball screw mechanism and its characteristics and describes the mathematical formulation to represent the mechanism's geometry, which will be recalled in the following chapters.

CHAPTER 4 summarises the state of art of investigations upon the ball screws from the first years of the second half of the 19^{th} century to 2020.

CHAPTER 5 describes the first version of the ball screw model and illustrates the results of a sensitivity analysis on the mechanical efficiency varying the external force, preload, friction coefficient and backlash.

CHAPTER 6 recalls the main achievements in the field of lubricated contacts and describes a simplified approach for explicitly modelling the presence of lubricant grease between the rolling elements and the grooves.

CHAPTER 7 presents an improved model of the ball screw mechanism considering three–dimensional dynamics by means of a multibody approach. The dynamic capabilities of the model are presented with several simulation results. Degradation models are introduced.

CHAPTER 8 presents a multibody dynamic model developed in a commercial software environment to investigate the effects of the recirculation channel, to perform vibrational analyses and to analyse the load distribution on the spheres in presence of geometric errors on the spheres or eccentricity in the external load application point.

CHAPTER 9 describes the designed test bench under construction that will be used to validate the model results. The robustness of the design with respect to uncertainty sources is validated by means of a Monte Carlo analyses on a mathematical model of the whole system.

CHAPTER 10 as final part of this thesis presents the conclusions arising from the current research along with the future developments that will be addressed and carried out.

Chapter 2

Electromechanical actuators

2.1 Background and applications

The recent advances in the electrical technology of the last decades led to very efficient and powerful electromechanical actuators (EMA) which have been employed in several very different fields [44]. The most common sector on which they are employed is the manufacturing, where CNC machines are the current standard for mechanical production. In robotics, electromechanical actuators are embedded into the manipulator joints and provide the torque needed to make the end–effector reaching the targeted position. In the railways field, EMAs are used for the active suspension system and to tilt the car body in high–speed trains, replacing the pneumatic actuation, such as on the Shinkansen E5 and E6 models of the East Japan Railway Company [45].

While in these fields EMAs are already a standard, in the aerospace sector they are still an emerging technology. In fact, where safety is important, the reliability of the actuators becomes crucial and must be taken into account. From mid-1980s researchers have been developing a new concept of *more/all electric aircraft*, which led to the trend of replacing the wide–spread hydraulic actuation technology with electromechanical solutions.

As usually happens, the first pushes towards this direction came from the space and military fields. EMAs have been installed to steer the nozzles in the thrust vector control (TVC) system of different launchers (Atlas V and VEGA)[46, 47] and missiles (M51) [48] and to perform advanced propellant control on Space Shuttles

[49, 50]. NASA conducted several studies to employ EMAs as flight controls on Space Shuttles [51]. The X-38 crew return vehicle wing flaps were actuated by EMAs in a redundant double–fail operative architecture [52]. The peculiarity of these kinds of application is that the actuators are single use and must withstand to quite short missions, therefore the reliability issue can be overcome with redundant architectures.

On the contrary, a different approach must be followed when EMAs should be installed as primary flight controls for large commercial manned aircraft. Indeed, for these applications, the expected life of an actuator is tens of thousands of hours and the safety requirements in terms of reliability and durability make EMAs still struggling to establish as main technology. The main drawback that hinders their diffusion is the possibility of jamming caused by a seizure of any of the internal component of the actuator, which would stick the control surface in the last position reached when the jamming occurred causing a very dangerous imbalance in the aircraft attitude. Although this situation probability is low, in the order of $2 \div 5 \times 10^{-8}$ per flight hour, it is still too large for safety critical applications, such as primary flight controls in manned aircraft, for which the required jamming probability must be lower than 1×10^{-9} per flight hour [20].

Several research programs have been conducted, aiming to the development of EMAs specifications to promote their integration in the aircraft architecture, such as EMAS, EPAD, ELAC, MOET, COVADIS, Actuation 2015 and ASTIB. In particular, the latter has as primary objective the development of a ground demonstrator (iron bird) of a new regional transport aircraft on which all the actuation systems are electrical. More details on the above mentioned research programs can be found in [3, 4, 53]. For the time being, a number of demonstrators have been built as results of the different researches, but EMAs found no practical application on real aircraft, except for some drones (UAV).

Instead, for secondary flight controls the safety requirements are less strict and EMAs have found successful applications on several aircraft. These kinds of flight actuators are not flight critical and their positioning is discrete. Furthermore, usually the preferred response to failure is to stick the surface in a position instead of leaving it fluttering under the aerodynamic actions (e.g. trimmable horizontal stabilizers or THS), thus the jamming occurrence does not represents an obstacle for these kinds of actuators [4]. Table 2.1 shows the applications of EMAs on different commercial

Table 2.1 In service secondary flight controls EMAs for commercial aircraft.

Aircraft	**Secondary flight controls**			**Brakes**	**Engines**	
	Slats	THS	Spoilers		Thrust reverser	Fuel valves
Boeing B787		✓	4 of 14	✓		
Airbus A350		✓		✓	✓	
Airbus A380	✓	✓			✓	✓
Bombardier C-Series				✓		
Embraer KC390		✓				

aircraft. As a result of the AFC (Advanced Flight Control) program, EMAs have been installed on the Boeing B787 for 4 of the 14 spoilers [54]. On the Airbus A380 and A350, EMAs are in service on the trimmable horizontal stabilizers and, only for the Airbus A380, on the slats as backup actuators [55]. Also the Embraer KC390 mounts EMAs to control the trimmable horizontal stabilizers. The ASTIB project is investigating the use of EMAs for the winglets and wingtips to perform functions of load alleviation.

The applications of EMAs on aircraft are not limited only to flight controls. The EABSYS project led to the implementation on the Boeing B787 and Bombardier C-Series of an electric braking system, in which they are used to press the brake disc on the rotating part on the tire set [4, 53]. The same solution is in service on the Airbus A350. On the Airbus A350 and A380 EMAs are the principal actuators of the electrical thrust reverse system on the aeronautic engines. On the A380 they are used to control flow valves as well.

Several research projects, such as ELGEAR, MELANY, CISACS and ARM-LIGHT have focused on the implementation of electromechanical solutions for landing gears, but, currently, they have not found real applications. The main issue is that the extraction/retraction system architecture must guarantee the damped free fall of the landing gears in case of failures of the actuators. A different response to failure is not accepted, therefore the jam risk of EMAs still hinders their use for this application.

A similar problem arises for the steering system. In case of failure, the failed actuator must act only as a damper, leaving the tires to self–align with the moving direction avoiding loss of control. Although different research programs have studied

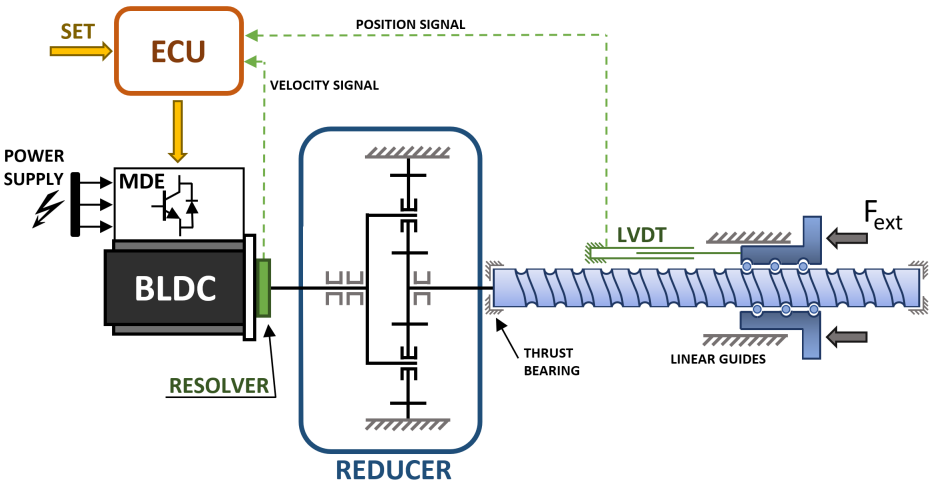

Fig. 2.1 Schematic EMA architecture [56].

solutions to avoid the jam issue of EMAs, such as the DRESS, ELGEAR and MELANY projects, the steering system remains still hydraulic for the time being.

EMAs can found applications also on helicopters but, due to the strict requirements in terms of high dynamics and reliability, they are not currently in service in any model. The HEMAS project aimed to introduce redundant EMAs to control the swashplate, while the Project Zero project studied their application for the Individual Blade Control, to improve the performance of the rotor, reducing the vibrations due to aerodynamic blade interaction.

2.2 Architecture

In this section the standard architecture of an EMA is presented. In general, an EMA is a device which converts the electrical in mechanical power. Depending on the typology of actuator, the output can be either rotative or linear. The latter is more common since it replicates the behaviour of the currently adopted electro–hydraulic actuators (EHSA): in such a way they can be easily replaced without the need of re–design the entire aircraft wing structure.

The linear output EMA divides in *geared* and *Direct Drive* solutions: in the first one, schematically depicted in Fig. 2.1, the linear to rotary converter is connected to the electric motor through a gearbox, while in the second one there is no reducer and, usually, the motor is directly integrated on the power screw component. The choice

of the architecture largely depends on the requirements and the available space for the installation: usually, a mass reduction is favourable and it can be adopted as one of the criteria for the design of the actuator [53, 57], together with the performance objectives fulfilment [58]. More details can be found in [4].

2.2.1 Servo motor

The servomotor is the converter from electrical to mechanical energy. Depending on the needs, it can be a brushless DC motor (BLDC), a permanent magnet synchronous motor (PMSM) or a switched reluctance motor [53]. In order to keep the motor in motion and to generate the requested torque, it is necessary to modulate the currents in an appropriate way depending on the angular position of the rotor. The commutation of the windings supply is handled by the drive electronics. The switching reluctance motors have the advantage that they can still operate even with the loss of one of the phases but they present a lower power to inertia ratio. The power density of the electric motor should be high in order to reduce the space required by the actuator and to minimize the overall mass and inertia. Further details can be found in [59].

2.2.2 Motor drive electronics

The motor drive electronics (MDE) is the electronics which controls the switching of the electrical supply between the different phases of the motor. The commutations take place switching on and off the MOSFETs synchronously with the rotor angle. Depending on the number of transistors, the typology can be *Y-connection* (with 6 transistors) or *full H-Bridge* (with 12 transistors): the last solution is more reliable but more expensive because of the larger number of MOSFETs required. The MDE is the responsible for the brake of the connection between the motor and the electrical system when the motor is acting as a brake: in fact, the return of energy on the supply line from the motor is not admitted. Further details can be found in [60].

2.2.3 Gearbox

In order to maintain contained inertia, mass and volume, high speed motor with moderate torque can be used. Therefore, it is necessary to interpose a gearbox

Table 2.2 Comparison between power screw characteristics.

	ACME	Ball screws	Roller screws
Speed	Low	Medium	Very high
Acceleration	Low	Medium	Very high
Load rating	High	High	Very high
Durability	Very low	Medium	Very high
Stiffness	Medium	Very high	Very high
Accuracy	Medium	High	High
Repeatability	Low	High	High
Backlash	Medium	Low	Low
Back drive	Hard	Easy	Medium
Misalignment	Low	High	Medium
Stroke length	Medium	Long	Long
Space required	Medium	Medium	Low
Maintenance	Frequent	Medium	Low
Efficiency	Low	Very high	High

between the motor output shaft and the power screw to reduce the speed and increase the transmitted torque. The typologies of gearboxes suitable for EMAs are those with compact structure, high efficiency and low backlash. Hence, the choice is usually between the harmonic, cycloidal or planetary gear reducers [53]. The higher the reduction ratio, the lower the reliability and the efficiency, since the number of components increases.

2.2.4 Rotary to linear converter

This component is needed in the linear EMAs to convert the rotational motion coming from the motor through the reducer into linear. Usually it can be either a ball screw (BS) or a roller screw (RS): both kinds of screw have high efficiency with regard to the traditional power ACME screw, which is not suitable for EMAs.

RSs have a larger number of contacts than BSs, hence the load rating is higher due to the larger total contact area. Therefore, smaller contact stresses result in longer life under normal operative conditions. Due to the more complex structure, RSs are more sensible to misalignments than BSs, but they are more compact and thus an appropriate solution for narrow space applications of EMAs. RSs can have smaller

leads than BSs, then realizing greater reduction ratios which allow the reducer to be more compact, with less stages and with a smaller reduction ratio, and, therefore, to reduce the motor inertia influence on the mechanical transmission. Smaller leads entail a better linear positioning resolution and repeatability of the entire EMAs.

Despite the various advantages of RSs with regard to BSs, summarised in Tab. 2.2, BSs are a valid alternative and are present in a large number of EMAs thanks to their higher efficiency, specially at low temperature, and their larger tolerance on misalignments. Furthermore, the simpler construction of BSs results in higher reliability and lower cost.

2.2.5 Sensors

In order to perform the speed and position control loops, different transducers are required. The final position of the translating part of the power screw is read by a linear sensor, which can be an LVDT. The speed loop exploits a rotative encoder or resolver, which is usually installed on the high speed shaft of the gearbox in order to increase the measurement accuracy. These two control loops are commonly performed by the electronic control unit (ECU) digitally, while the current control loop is most frequently analogue and it is realised within the MDE. The sensors needed to measure the motor shaft angle in order to correctly switch the MDE transistors are usually integrated inside the motor.

2.2.6 Electronic control unit

Nowadays, the flight controls actuators are *smart*, which means that the velocity and position loops are commissioned to the single actuators, which receive the position demand as input by the central flight control computer (FCC), which has only the task to perform the attitude control of the entire aircraft. The local control loops are performed by the electronic control unit (ECU) which receives as inputs the FCC position set and the speed and position feedbacks respectively from the resolver and the LVDT. As output, the ECU sends a low power command to the MDE, which acts as interface between the ECU and the high power supply line, controlling the electric motor.

2.2.7 Additional components

Besides the main components, presented above, other secondary parts contribute to the correct functioning of an EMA. For example, bearings are very important to reduce the friction between the actuator body and the rotating parts and to sustain the axial and radial loads. An anti–rotation device is required by the power screw to realise an only translating output of the EMA. A brake and/or a clutch can be included in the architecture to stop/disconnect the motor from the mechanical transmission in case of a fault.

2.3 Comparison between EMA and EHSA

In this section the hydraulic and electromechanical technologies are compared and the main advantages and drawbacks of EHSAs and EMAs are described and summarised in Tab. 2.3.

The hydraulic technology have been prevailing in the flight controls area since the birth of the very first fly–by–wire actuators thanks to its reliability and low jamming probability [3–5]. A point in favour of EHSAs, whose typical architecture scheme can be observed in Fig. 2.2, is that they can realise high force at low speed thanks to the hydraulic fluid in pressure, which, furthermore, serves to cool the actuator evacuating the heat to the fluid sink, away from the operative area. The EHSA has low inertia because of the lack of mechanical transmission and it can, thus, reach high frequencies. An EHSA is not susceptible to electromagnetic interferences and produces very low emissions. In case of a failure, it can easily be set in damping mode without the need of complex architectures: the two chambers are simply put in communication through a calibrated orifice, which performs the damping function.

On the other hand, using EHSAs involves to install different hydraulic circuits on the aircraft, with compressors, pipes, filters, reservoirs and so forth. These hydraulic supply lines usually are three and completely separate to ensure the operability of at least part of the aircraft actuators in case of loss of pressure in maximum two lines. The pipes routing makes the design of the aircraft structure quite hard, in particular for the integration in the wings, where the available space is low. All the hydraulic networks require a frequent maintenance and produce leakages of poisonous fluid. The exhaust filters and components replaced during maintenances

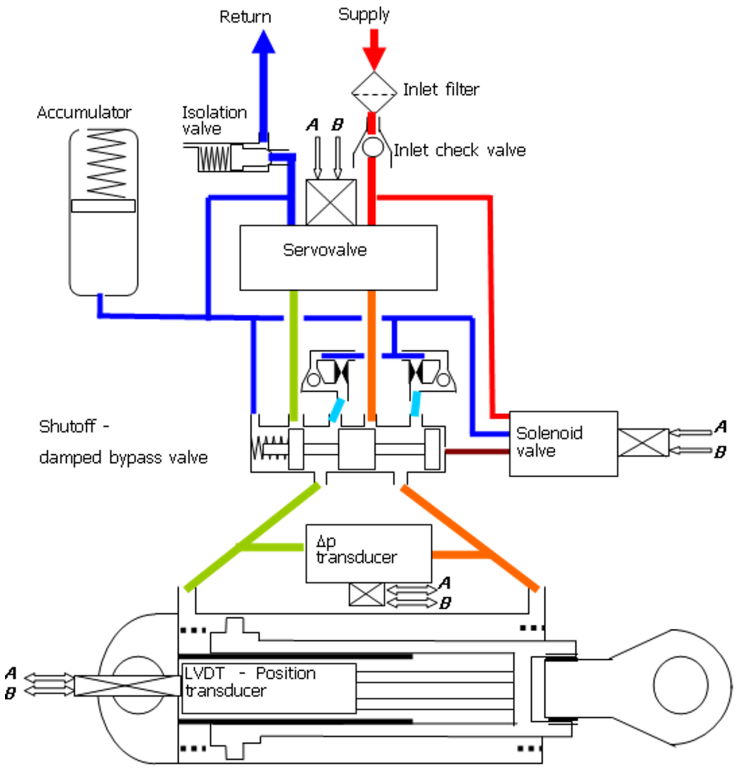

Fig. 2.2 Schematic EHSA architecture [24, 61].

need to be disposed with relative costs and environmental impact. The hydraulic fluid on the aircraft represents a not negligible fraction of the total weight, therefore its presence leads to a greater fuel consumption, making this solution not eco–friendly.

On the contrary, to install EMAs in an aircraft means to entirely eliminate the piping networks with large benefits from the points of view of weight, leakages, wing design, pollution and maintenance. In fact, the absence of the filters, leakages and the hydraulic fluid itself entails no need of disposal and stocking poisonous exhaust components and fluid. Substituting the pipes with electric cables leads to an overall reduction of the aircraft weight, volume and complexity of the system. Less maintenance is required and so the costs diminishes: indeed it is worth to be mentioned that the average time between two consecutive hydraulic oil refills is only approximatively 1000 flight hours. It is easier to perform on ground checks without the need of ground pressurised test stations. EMAs have greater energy efficiency than EHSAs and they can absorb only the required power from the supply network, contrary to EHSAs that uses the fluid at the maximum pressure wasting the not needed flow within the servovalve. Electric motors can also extend the

Table 2.3 Advantages and drawbacks of EHSAs and EMAs.

	Advantages	Drawbacks
EHSA	• Easy damping action without adding complex components	• Need of hydraulic network
	• Heat evacuation through the hydraulic fluid itself	• High environmental impact
	• High force at low actuator speed	• Increased weight due to piping and fluid and fuel consumption
	• Low piston inertia and high dynamics	• Difficult network integration in the aircraft design
	• Low susceptibility to electromagnetic interferences	• Difficult network integration in the aircraft design
	• High power density	• Frequent maintenance required
EMA	• Absence of hydraulic network, pipes, filters and leakages	• Suffering for electromagnetic interferences
	• Overall weight and pollution reduction and fuel saving	• Hard heat dispersal
	• Less maintenance and no need of pressurised test stations	• Power losses for constant load at low/null speed
	• High energy efficiency	• Backlash induced flutter of control surfaces
	• Speed range extension with flux weakening	• Stuck surface in case of jam, not anymore controllable by other parallel actuators
	• Ease of designing the aircraaft architecture	• Too high jamming probability, unacceptable for safety critical actuators

speed operative range through flux weakening and they are easily and efficiently controllable with transistors with a large number of control options [3].

However, EMAs suffer the electromagnetic interferences, due to the high frequency switches of MDE transistors and the strong magnetic field of the motor itself. In order to limit the current, aeronautic motors present high winding resistance values to operate with 270 V and, therefore, the heat thermal dispersion becomes an issue. Furthermore, even with a constant load, the electric motor needs to continuously generate torque and consequently heat: this problem is more present for primary flight controls, which needs to operate continuously without delays, and on which,

hence, it is not possible to install a stationary brake. The mechanical efficiency of the transmission varies extensively with the applied load, speed and temperature and it is affected by backlash. The latter originates from wear and increases with time: it can cause flutter of aerodynamic surfaces and has a negative effect on the actuator's dynamics. EMAs have a less fault rate than EHSAs but have also less reliability because of the larger number of component and, particularly, of mechanical contacts, which are the major factors determining the actuator's service life, depending on the operating conditions.

Among all, the most critical issue is the relative higher jamming probability: as already mentioned in Sec. 2.1, for EMAs it is in the order of $2 \div 5 \times 10^{-8}$ per flight hour, with respect to the 1×10^{-9} of EHSAs. This value is too large for manned aircraft and therefore it represents the main obstacle which hinders the diffusion of EMAs as primary flight controls. Even if the aerodynamic surface is controlled by multiple EMAs, if one of them jams the surface cannot be controlled by other actuators and remains stuck, jeopardizing the entire mission, the aircraft and the passengers' life.

2.4 Anti-jamming solutions

Several solutions have been proposed to overcome the jamming issue and they can be classified in four main categories [4, 62]:

- Fault–tolerant actuators
- Fault–free actuators
- Multiple actuators
- Multiple smaller surfaces

2.4.1 Fault-tolerant actuators

Fault–tolerant means an actuator on which the redundancy is present only for some components, on which multiple power paths are realised. If a fault occurs on one of them, the actuator can still operate and control the surface. As an example,

electric motor redundancy can ensure insensitivity to electric drive faults [13, 14, 62], while to overcome the mechanical jamming, telescopic ball screws can be adopted [16, 17, 63].

2.4.2 Fault-free actuators

Fault–free actuators present the redundancy of the complete actuator with a sum in velocity or force and with a single attachment to the control surface. In case of a fault in any component of one of the redundant actuator, the surface can still be controlled, even if with degraded performances. Various solutions have been proposed, such as a double back–to–back actuator [15], mechanical locking and damping devices which become engaged in case of some component's fault [18], two parallel actuators moving the control surface through a summing lever [19], and so forth.

2.4.3 Multiple actuators

The aerodynamic surface can be controlled by different separate actuators with multiple attachments [64]. With this architecture, if the electric part of one actuator fails, the other actuators can still move the surface dragging the failed one. A different situation comes if the mechanical transmission jams: in fact in such a case the other actuators cannot control anymore the surface, which is stuck. Pyrotechnic–operated detachment has been proposed [65] resulting, though, in no practical realization due to testability and reliability problems. Other disconnecting device options have also been studied [66]. This architecture has the disadvantage of *force fighting* [67], a phenomenon which happens when two nominally equal actuators control in active/active mode the surface: the manufacturing tolerances make their responses not exactly the same, leading to opposing forces generated by the two actuators to maintain the surface in a steady position. This situation leads to increased power consumption, premature failures and surface fatigue. To avoid it, it is possible to operate with an active actuator and the other deactivated, in back–up mode or in force controlled mode. With the first solution, the active actuator sees an increased surface inertia since it has to move the back–up actuator in stand–by. Therefore it has to be oversized, with consequent increased volume and power consumption. In case of a failure, a not negligible delay between the loss of controllability of the surface

and the activation of the back–up actuator is present. The oversizing issue can be overcome if the back–up actuator is kept in force–control mode: in such a way it compensates for its own inertia, but the delay in case of fault remain still present, because of the need of commutation of the force–control into a position–control strategy on the back–up actuator.

2.4.4 Multiple smaller surfaces

The last option would be to subdivide the control surfaces in multiple smaller surfaces, each one controlled by a single actuator. In such a way if one jams, the others can compensate for the generated imbalance and guarantee the aircraft controllability. However, this solution would imply a complete redesign of the aircraft wings.

2.4.5 An innovative approach: PHM supported actuators

The aforementioned solutions, although valid, did not allow anyway the diffusion of EMA as primary flight controls. Indeed, they introduce more components and complexity in the architecture and, then, increase the weight and the volume of the actuator, which are two stringent constraints for flight control actuators [68], making them unsuitable for implementation to safety critical aircraft applications [35]. Furthermore, the higher number of mechanical components increases the overall failure probability of one of them, and, therefore, such complex systems would require additional scheduled maintenance [35].

An innovative approach is to keep the actuator's architecture as simple as possible, with the minimum number of components and to compensate for the higher EMA failure rate supporting it with a *prognostic and health management* (PHM) system [41]. As already mentioned in Sec. 1.2, the PHM system monitors the actuator in real time and detects the insurgence of faults, analyses the health status of the various components and estimates the residual useful life before a catastrophic failure, which could be a jamming. Necessary conditions are that the degradation presents a progressive fault to failure evolution in time and not a suddenly unexpected failure and that this evolution occurs in a time span that allows at least to finish the mission in progress and to put in action adequate countermeasures. Several numerical and

experimental studies have been carried out in the last decade, simulating possible faults and analysing the actuator's response at the system level [33, 42, 43, 69, 70].

2.5 EMA faults

An important aspect of any PHM system is the ability of capture the onset of faults and their progression with time. A fundamental tool to determine how a fault develops into a failure is the knowledge of the different physics phenomena underneath it. The ability to capture the origins of a fault and its growth greatly facilitates the prediction of how the fault evolves and improves the accuracy of the estimation of the remaining useful life. In order to recognise a faults, information about its roots and effects are paramount: it is necessary to perform a preliminary analysis to classify all the possible faults.

In this section, an extensive description of several possible faults in an EMA is reported, basing on literature data [22, 43, 71, 72] and acquired knowledge from previous research projects. EMA faults can be classified in four general clusters:

- Faults to the electric/electronic parts;
- Faults to the motor;
- Faults to the mechanical components;
- Faults to the sensors.

Each row of Tab. 2.4 represents a possible fault for each of the four main categories. The final score associated to each fault is a combination of the *occurrence frequency* (F), *fault severity* (S), *testability* (T) and *replaceability* (R). For each of these evaluation criteria the score can vary between 1 and 4, correspondent respectively to the worst and best scenarios.

- The occurrence frequency is defined as the probability of a defect inception which, if sufficiently developed, can cause anomalies in the actuator performance. The value of 1 indicates a defect rate $> 1 \times 10^{-6}$, while the value of 4 means a defect rate $< 1 \times 10^{-8}$.

- The fault severity is related to the consequences of the fault development. The value of 1 means a critical situation in which the entire aircraft is in danger, while the value of 4 indicates not critical scenarios, in which just the performance are reduced.

- The testability classifies the faults in terms of fault observability: a score equal to 1 means that the onset of the fault is impossible to observe or it is hidden by other faults or measurement noise, while a score equal to 4 indicates that it can be easily observed online with no extra sensor to be mounted on the actuator. This parameter is susceptible to variations depending on the researches advances on this topic.

- The last criterion is the replaceability, which is an index that determines if, following a fault progression, the entire actuator must be replaced (1) or if only the component can be quickly substituted (4). Actually, this index assumes always the value of 1 since, to minimize the aircraft ground time during maintenance operations, usually it is more convenient to replace the entire actuator and thus to investigate the faulted components offline. Furthermore, the replaceability of a component heavily depends on the EMA design, which is usually very compact and in which all the component are integrated in a unique structure and work synergistically.

- The TOT index is finally simply the sum of the above mentioned criteria scores and gives an idea of the faults that requires more attention, correspondent to the rows with the smaller value.

As a results of this FMECA on EMAs, it can be seen that the most important faults to be addressed are those whose evolution would lead to the loss of the actuator controllability. The dielectric breakdown on the electronics in the ECU and MDE can cause the motor loss and therefore the inability to control the aerodynamic surface. Among the mechanical components, bearings and the power screw resulted to be the most critical: indeed, the different types of wear of contacting bodies generate debris that contaminates the lubricant and can lead to seizure or grip.

It has to be highlighted that Tab. 2.4 does not contain the possible faults of the lubricant since they are present in almost every mechanical subsystem. The lubricant faults will be addressed later in Chapter 6.

Table 2.4 EMA FMECA.

Category	Component	Main failure mode	Causes	Symptoms	Failure effect	Score				
						F	S	T	R	TOT
Electric / Electronics	EM - EPU	Parametric failures	Local overheating, electrical overstresses, vibration etc.	Asymmetric output voltages, performance degradation	Motor loss	3	2	4	1	10
	Capacitors and transistors	Dielectric breakdown	Insulant degradation	Abnormal currents, partial discharges	Short/open circuits and motor loss	3	2	2	1	8
	Power supply	Thermal runaway	Electrical overload	Dielectric breakdown	Short/open circuits and motor loss	2	2	2	1	7
	Solder joints	Intermittent contact	Local overheating, electrical overstresses, vibration etc.	Electrical noise	Disconnection and motor loss	3	2	2	1	8
Electric motor	Electric motor	Turn-to-turn	Insulant degradation	Non-symmetric/Lower/intermittent currents	Motor performance degradation/loss	1	2	4	1	8
		Uniform Magnets degradation	Overheating, advanced turn-to-turn short	Efficiency loss in power conversion	Motor performance degradation/loss	2	2	4	1	9
		Localized Magnets degradation	Local overheating, turn-to-turn short	Non-symmetric currents/efficiency loss	Motor performance degradation/loss	2	2	4	1	9
		Localized Magnets degradation	Local overheating, turn-to-turn short	Increased common node current	Bearing damage	2	2	4	1	9
		Connectors	Intermittent contact	Increased apparent resistance	Disconnection	2	1	3	1	7
		Eccentricity	Manufacturing assembly	Cyclic anomaly on phase currents	Support bearing failure	3	2	3	1	9
Mechanics	Bearings	Spalling	Insufficient lubrication, excessive load	Increased vibration, metal flakes separation	Increased risk of jamming	2	1	3	1	7
		Scoring	Natural degradation, overloads, fretting fatigue	Noise, increased friction	Motor loss/increased risk of jamming	2	1	3	1	7
		Indentation	Overloads	Increased friction, increased vibration	Increased risk of jamming	4	1	3	1	9
		Wear	natural degradation, insufficient/contaminated lubrication	Noise, increased friction	Performance loss, increased backlash	4	4	3	1	12
		Pitting	Fatigue degradation, excessive lubrication	Noise, increased friction	Performance loss, grip, noise	4	4	3	1	12

Continued on next page

Table 2.4 – continued from previous page

Category	Component	Main failure mode	Causes	Symptoms	Failure effect	Score				
						F	S	T	R	TOT
	Bearings	Corrosion	Insulants degradation, lubricant chemical contaminants	Increased vibration, metal flakes separation	Increased risk of jamming	3	3	2	1	9
		Seals degradation	Natural degradation, harsh environment, wear	Lubricant contamination/oxidation	Lubricant bleeding, performance degradation, risk of seizure	3	3	2	1	9
		Electric erosion	Insulants degradation, electric motor shorts	Noise, efficency loss, increased friction	Increased noise	3	2	3	1	9
		Tracks crack	Overloads, excessive vibration	Noise	Actuator loss (possible jamming)	3	1	3	1	8
	Gears	Crack	Fatigue degradation, overloads	Periodic stiffness variation, "localized" noise	Actuator loss (possible jamming)	3	1	3	1	8
		Wear	Natural degradation, insufficient/contaminated lubrication	Increased noise over wide frequency spectrum	Slow degradation in performance	4	4	4	1	13
		Pitting	Surface fatigue degradation, excessive lubrication may accelerate the process	Increased noise over wide frequency spectrum	Degraded performance	2	3	3	1	9
Mechanics	Power screw	Scoring	Natural degradation, overloads, fretting fatigue	Noise, increased friction, excessive heating	Performance loss, possible grip	2	1	3	1	7
		Spalling	Natural degradation, insufficient lubrication, excessive load	Increased vibration, metal flakes separation, excessive heating	Performance loss, possible grip	2	1	3	1	7
		Flaking	Overloads, excessive preload, mounting errors	Increased friction, increased vibration, metal flakes separation, excessive heating	Performance loss, possible grip	2	1	3	1	7
		Fretting	Metal flakes + high loads + small displacements	Increased friction, increased vibration, metal flakes separation	Performance loss, possible grip	2	1	3	1	7
		Wear	Natural degradation, insufficient/contaminated lubrication, lubricant ageing, too high temperature	Noise, increased friction, increased backlash, excessive heating	Degraded performance, loss of positioning accuracy, loss of preload, loss of rigidity, increased vibrations	3	4	4	1	12
		Return channel deformation	Overloads, localized impulsive loads	Vibration, significant efficiency loss, jamming risk	Severe efficiency loss, jamming	4	1	3	1	9
		Indentation	Overloads, metal flakes contamination	Increased friction, efficiency loss, increased vibrations	Jamming, performance loss	3	1	3	1	8
		Rolling element deformation	Overloads, too high speed	Increased vibrations	Performance loss, possible jamming	3	2	3	1	9

Continued on next page

Table 2.4 – continued from previous page

Category	Component	Main failure mode	Causes	Symptoms	Failure effect	Score				
						F	S	T	R	TOT
Mechanics	Power screw	Seals degradation	Natural degradation, harsh environment, wear	Lubricant contamination/oxidation	Lubricant bleeding, performance degradation, risk of seizure	3	3	2	1	9
	Rod end	Crack	Overloads, vibrations	Reduced connection stiffness	Detachment from aerodynamic surface	4	1	2	1	8
Sensors	Resolver	Coils turn-to-turn	Insulant degradation	Inaccurate reading	Performance loss	3	2	3	1	9
	Motor Hall sensors	Absent signal	Local overheating, electrical overstresses, vibration etc.	Incoherent signal	Motor control loss	4	2	3	1	10
	LVDT	Coils turn-to-turn	Insulant degradation	Inaccurate reading	Performance loss	3	2	3	1	9

While bearings have been extensively investigated by several researchers both in nominal and degraded conditions [30, 73–76], a complete awareness of the dynamics and fault–to–failure evolutions of power screws has not been reached yet. For this reason, this subsystem, and in particular the ball screw, has been chosen as the research topic of this thesis.

2.6 Summary

In this chapter, EMAs have been presented. A comparison between EHSAs and EMAs has been made and the advantages and disadvantages of both the technologies have been highlighted. It has been stated that the main drawback hindering the diffusion of EMAs as primary flight controls is their relative higher jamming probability with respect to EHSAs. The different solutions proposed in literature to overcome the jamming issue have been introduced. The innovative solution consisting in a simple architecture EMA supported by a PHM system has been presented. Finally, the results of an FMECA on EMAs have been reported.

Chapter 3

The ball screw mechanism

As seen in Chapter 2, the ball screw (BS) mechanism has been identified as the research topic for this thesis project. This chapter gives an overview of the principal features of such a component and presents its geometry from a mathematical point of view. New formulas to explicitly and more precisely calculate the grooves curvatures are introduced.

A BS is a mechanism that converts the motion from linear to rotational and/or vice versa. As can be seen in Fig. 3.1, it is usually composed by a screw shaft, one or two nuts, a set of spheres, seals and the recirculation inserts. It is characterised by low friction levels obtained by interposing rolling elements between the screw and nut grooves, as in bearings. However, in contrast to them, the rolling elements moves along a helical path. Therefore, to prevent them to come out from the nut, a recirculating channel is present, which picks up the spheres and lead back them to the beginning of the helical path contained inside the nut.

BSs are characterised by

- high efficiency;
- low drag torque;
- high stiffness;
- good positioning accuracy;
- the possibility to compensate the backlash applying a preload.

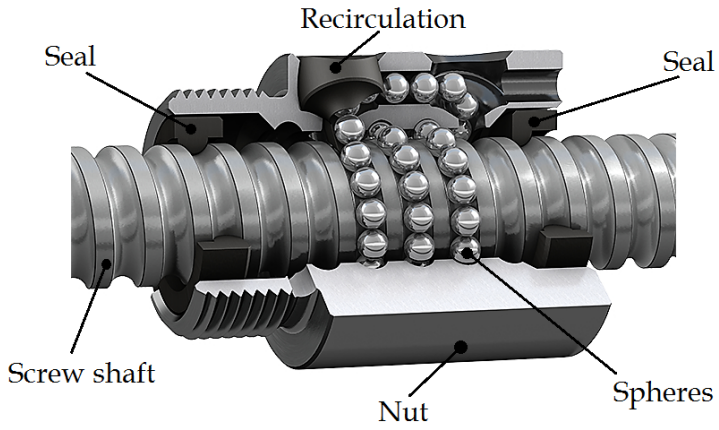

Fig. 3.1 An SKF ball screw [77]. In black the seals that prevent the grease to come out and the contaminants to enter. The spheres are brought back by the recirculating inserts and forced to remain within the nut.

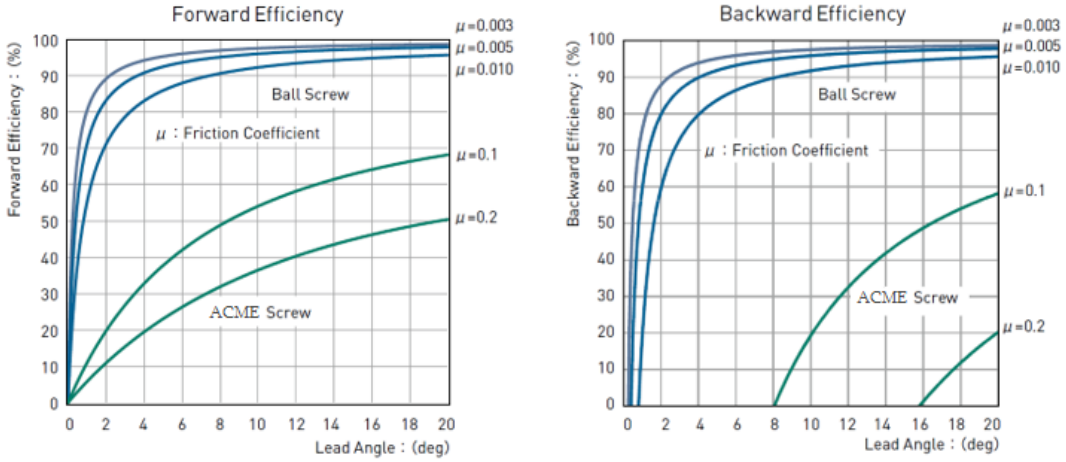

Fig. 3.2 Direct and reverse efficiency of ball and ACME screws depending on the overall friction coefficient μ and the lead angle [78].

BSs are employed in those applications in which the position control is the main focus. The high efficiency and low friction are key features for the positioning precision and accuracy [79]: indeed, in Fig. 3.2, it can be seen that BSs reach extremely high values of both direct and reverse efficiency, usually greater than 90%. In fact BSs replaced the classic trapezoidal ACME screws, which have much lower efficiency values, as can be seen in Fig. 3.2. It can be noted also that the BS is a reversible mechanism, i.e. a component on which the conversion of linear into rotational motion can be realised with high efficiency levels.

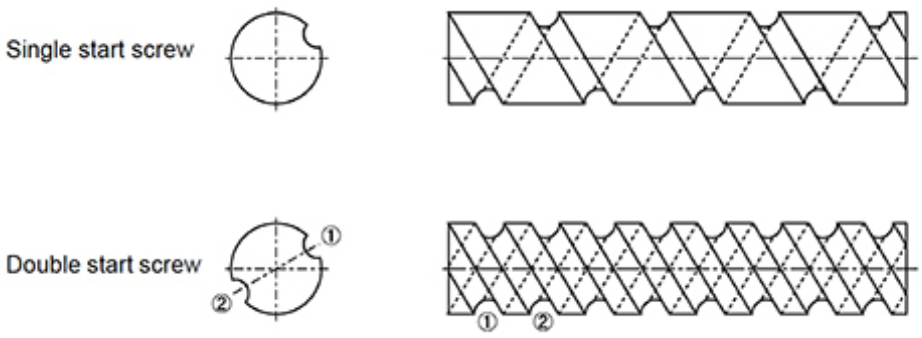

Fig. 3.3 Single and multi-starts ball screws [78].

BSs can be realised with single or multiple starts (Fig. 3.3): the latter is used when large leads and high load capacity are required. Indeed, using two or more parallel sphere circuits, a greater number of spheres can bear the external load, while keeping the axial length of the nut compact. It is worth to be mentioned that for single start BSs the terms *lead* and *pitch* are interchangeable while it is not the case for multi–starts BSs. In fact, the terms *lead* refers to the linear distance travelled by the nut for each complete rotation of the screw shaft, while the term *pitch* indicates the distance between adjacent screw threads. In this thesis, single–start BSs are considered and therefore these two terms are used indifferently.

3.1 Return system

During the BS operation, the spheres interposed between the grooves have different absolute tangential speeds in the contact points, thus they tend to lag behind the driving component, which can be either the screw or the nut. Hence, they would exit from the nut if there wasn't a recirculation system (called also recirculation channel, return system, return tube or return channel).

Various recirculation systems exist (Fig. 3.4), depending on the type of BS or on the operative speed:

- Internal return with single/multi liner;
- Internal return with end–deflector;
- Internal return with end–cap;

- External return with tubes and deflectors;
- External return with return plate.

In addition to these more common types, for very particular cases there is the possibility to create the return tube inside the screw shaft itself instead that in the nut body.

The internal return with liners allows to take up a minimum amount of space radially, keeping the mechanism compact. The spheres are brought back to their initial positions after one turn jumping a lead thanks to a slot realized inside the nut (liners), as shown in Fig. 3.4a. This system allows to separate the spheres in different ball circuits: in such a way if one circuit incurs in a failure the other can still operate and therefore the risk of a global seizure is reduced. The model in Fig. 3.4a presents all the liners aligned, but they can also be equally distributed circumferentially to share the load on the spheres more evenly and to not unbalance the mass distribution of the nut with regard to the screw shaft axis. This return system can be used in single–start BSs with short leads and for normal speed range.

Using the internal return with end deflector the spheres make more than one turn around the screw shaft before to enter in the recirculation channel, as shown in Fig. 3.4b. This system allows more smooth operations with respect to the previous one since there is only one recirculation system and the spheres are detached tangentially from the helical path in order to minimise the vibration produced by the impact of the spheres on the recirculation insert. The recirculation channel is usually realised axially within the nut body. This method is commonly adopted in BSs with long leads and for multi–starts BSs.

The internal return system with end–cap, depicted in Fig. 3.4d is similar to the previous one. The spheres are returned to their initial points through an axial channel. The small difference is only that, in this solution, the deflectors are located in two additional elements attached at the extremities of the nut, instead of being integrated within it. Also this solution is mainly used for BSs with long leads and for multi–starts BSs.

The external return with tubes and deflectors imply several turns of the spheres around the screw shaft before to enter into the recirculating path, as can be seen in Fig. 3.4c. The spheres are removed from the helical path by the tongue of the deflectors and returned back by external tubes added to the nut body. This

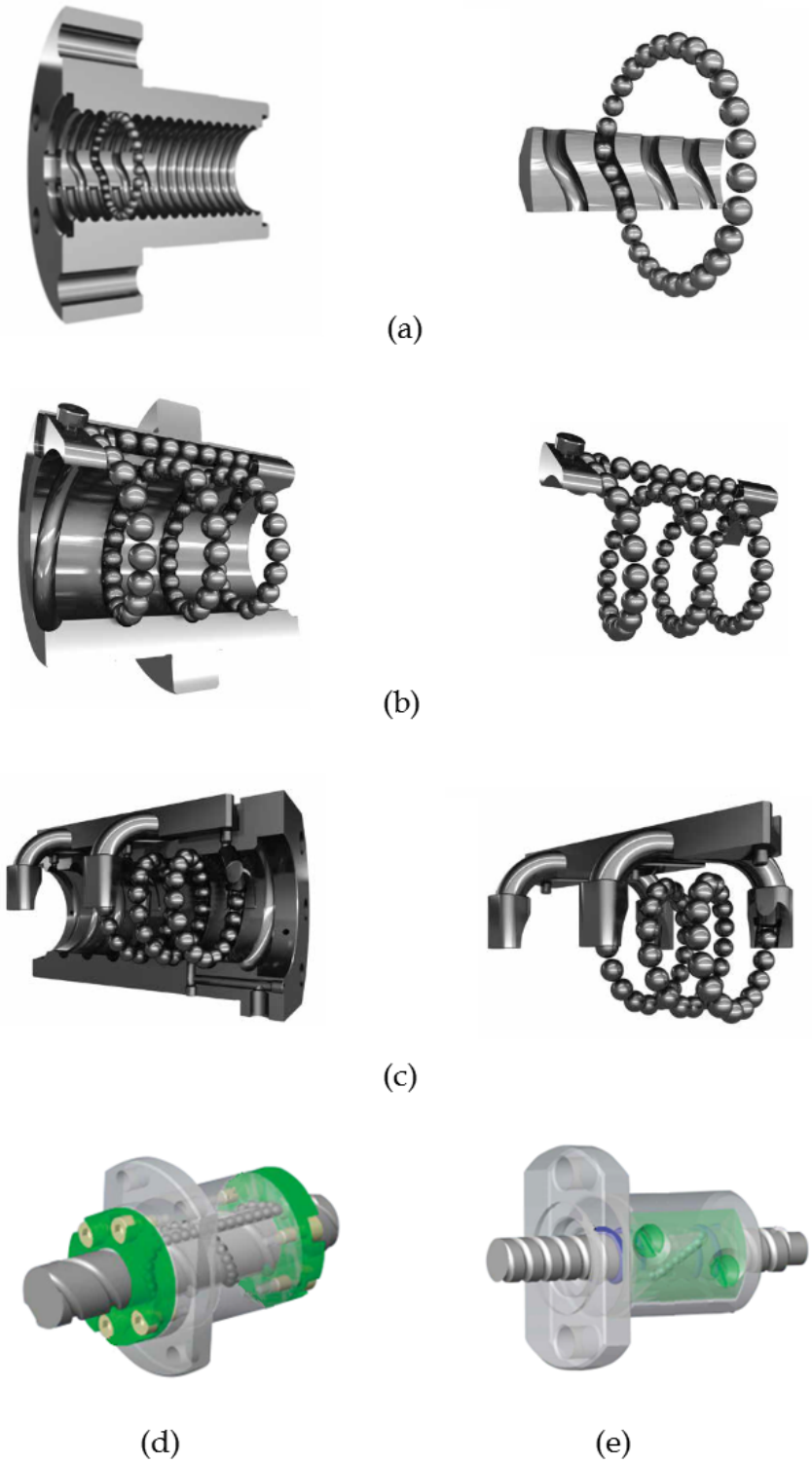

Fig. 3.4 Ball screw return systems [80, 81]: internal return with multiliner (a), internal return with end-deflector (b), external return with tubes/deflectors (c), internal return with end-cap (d), external return with return plate (e).

system can be applied with single and multi–starts BSs and for a wide range of leads. This recirculation system is the most common for application with no special requirements of space and vibration intensities. Usually, more than one tube is adopted and, thus, multiple sphere circuits are present, with the correspondent above mentioned advantages. The presence of the return tubes creates a not negligible imbalance in the mass distribution and can cause uneven load distribution on the spheres depending on their angular location.

If the tubes are incorporated within a plate instead of being fixed singularly with bolts, as in the previous case, the return system is that shown in Fig. 3.4e. The return–plate system is in between an internal and external recirculation and it has the advantage to allow smoother operations than the external tube solution.

3.2 Backlash and preload

The backlash is intrinsically present in a BS due to the machining process and the need of the spheres to move within the grooves without excessive friction. The main effect of the backlash is an uncontrolled movement of the driven element (e.g. the nut assembly in a rotating screw shaft driving BS) in the axial direction without a correspondent rotation of the driving element (e.g. the screw shaft). This phenomenon worsens the positioning accuracy and precision and creates vibrations and impacts that can rapidly deteriorate the BS performance. In particular, for flight control applications, the backlash issue is not insignificant since an uncontrolled movement of the control surface can cause flutter effects and destabilise the aircraft asset.

For this reason, the BS is usually preloaded. Applying a preload causes a slightly lower efficiency, due to the higher contact forces between spheres and grooves, but it increases the BS assembly stiffness and compensates for the backlash. The preload level must be decided according to the application: indeed, a low preload might be cancelled by the operative external force restoring the axial play, while a too high value would increase the friction and cause overheating for high speed conditions, which in turns would affect the positioning accuracy and the life of the component [82, 83]. According to [84], the preload level shall be greater than the maximum expected external force divided by a factor $2^{3/2} = 2.83$: this guarantees that, even with the maximum external load, the detachment between the rolling elements of the

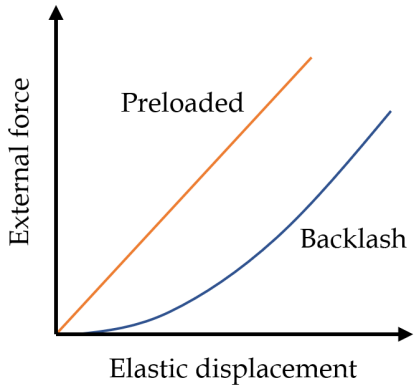

Fig. 3.5 Qualitative comparison of external force vs axial displacement curves for a ball screw with backlash and preload.

unloaded nut and the grooves does not occur. If the maximum external load is high, the preload force could result too elevated, therefore usually its value is limited and should not overcome $\sim 10\%$ of the dynamic load rate specified in the manufacturer's catalogue [78].

A qualitative comparison between the force–deformation curves for a BS with and without a preload is depicted in Fig. 3.5. Different preload methods can be applied to eliminate the backlash:

- double nut with spacer (O configuration);
- double nut with spacer (X configuration);
- single nut with lead shift;
- single nut with lead shift for multi–start BSs;
- single nut with oversized spheres.

The most common method is to use two nuts inserting a spacer ring (or a spring) between them: if the spacer acts to separate the nuts the generated preload is in the *O* configuration (Fig. 3.6a), while it is in the *X* configuration if it tries to close them (Fig. 3.6b). The *X* or *O* configurations take their name from the direction of the load on the spheres, shown in Fig. 3.6 with the dashed lines. Each nut bears the load in only one direction.

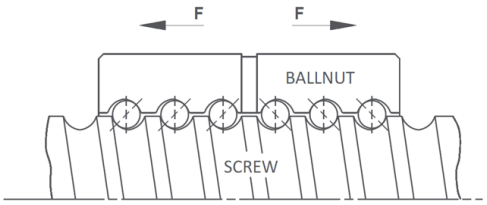

(a) Double nut with spacer (O configuration).

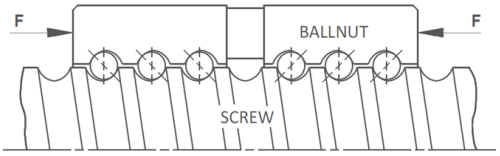

(b) Double nut with spacer (X configuration).

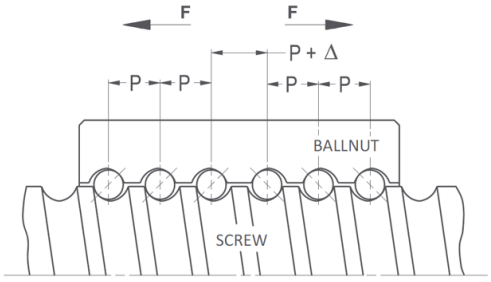

(c) Single nut with lead shift.

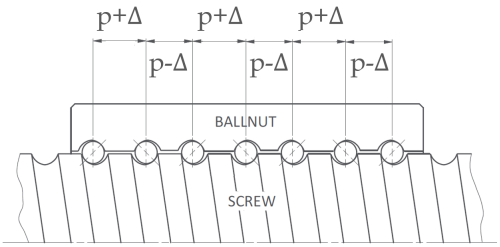

(d) Single nut with lead shift for multi-start BSs.

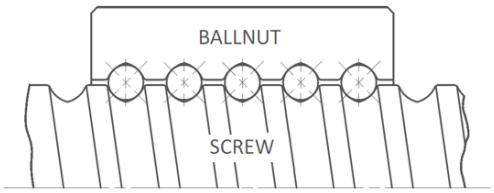

(e) Single nut with oversized spheres.

Fig. 3.6 Ball screw preload methods [77].

Another way to apply a preload is to appositely insert an error Δ in the lead p on one of the groove turns of the nut body, while keeping the screw shaft groove nominal, as explained in Fig. 3.6c. This generates a compression state on the spheres, which try to elongate the screw shaft as a reaction to their compression. Therefore, the load is oriented as in the *O* configuration preload method explained before. The rigidity and load capacity of the BS assembly with this solution are significantly lower than those with other solutions since only half of the spheres effectively bear the external force for each loading direction.

If the BS is multi–start, each of the balls circuits can have a lead error with opposite sign from one circuit to the other. As a result, all the spheres of the same circuit are compressed in one direction, opposite to the direction of the spheres of the other circuit, as shown in Fig. 3.6d.

The last method implies the employment of oversized spheres forced within the screw and nut grooves: the generated interference eliminates the backlash. The

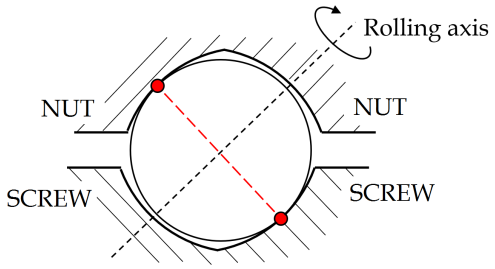

(a) Rolling condition with two contact points.

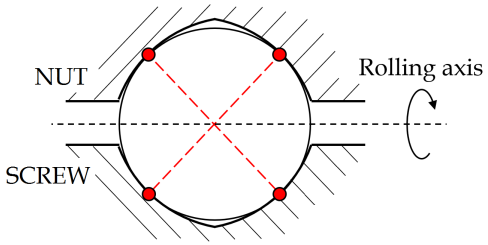

(b) Rolling condition with four contact points.

Fig. 3.7 Ball screw rolling conditions. All preload methods imply two contact points (a) except for the oversized balls method which generates four contact points (b).

preload value can be adjusted selecting the appropriate diameter of the balls. This method requires very tight manufacturing geometric tolerances and therefore it is not usually adopted for normal applications.

The first four preload methods are characterised by two points of contact between each sphere and the grooves. In ideal conditions, these two points are aligned on a line inclined by 45° to optimise the contact pressures and the BS efficiency. The rolling axis of each sphere is then perpendicular to this line, as shown in Fig. 3.7a. With oversized spheres, each ball touches the grooves in four points (Fig. 3.7b): gross sliding occurs in the contact points and the spheres move away from the ideal pure rolling condition. For this reason, this method can be used only in presence of lubrication and for moderate speeds.

A comparison of preloads methods is reported in Tab. 3.1, where the scores range goes from – – (very bad) to ++ (very good).

Table 3.1 Comparison between preload methods.

	Double nut	**Lead shift**	**Oversized balls**
Load capacity	+	− −	+
Stiffness	++	− −	+
Cost	−	+	+
Dimension	− −	+	+
Friction	−	+	− −

3.3 Lubrication

As in ball bearings, the lubrication of BSs is an important aspect that must be carefully taken into account to optimise the performance and extend the mechanism's life. The presence of a lubricant between the spheres and the grooves is paramount since, under the action of the contact load and rolling speed, it creates a thin layer that separates the contacting surfaces and reduces friction, wear and the temperature rise.

The lubrication can be performed either with oil or grease, depending on the average rotating speed of the application, screw diameter and working temperature. Grease lubrication is adopted in case of low rotational speed or for screw with ceramic spheres, which produces little wear debris. In case of high speed applications or low operating temperature it is recommended to use lubricants with low base oil viscosity, while for high speeds, high load or high temperature, greases with high base oil viscosity are more suited.

A grease is a semisolid lubricant and it is composed by a base oil mixed with a solid matrix, the thickener, whose concentration determines the grease consistency. In general, grease lubrication is preferred in BSs since it simplifies the design of the machine avoiding the oil recirculation, filtering and cooling system. Furthermore, the dual–phase nature of greases greatly reduces oil leakages since the grease matrix performs itself an internal sealing action and helps in avoiding the entrance of contaminants. The principal features of different greases, depending on the nature of the thickener and base oil, are summarised in Tab. 3.2, reported from [85].

Table 3.2 Main features of the principal rolling machines greases (from [85]).

Grease thickener	Base oil	Temperature range [°C]	Resistance to ageing	Anticorrosive properties	Water resistance	Remarks
Calcium *	Mineral oil	-20/+50	Good	Good with additives	Very stable, water-repellent	Good sealing action against water, no absorption of leakage water
Sodium	Mineral oil	-10/+120	Good	Good	Unstable	Emulsifies with water but may liquefy
Lithium *	Mineral oil	-20/+120	Very good	Good with additives	Stable up to approx. 90 °C	Emulsifies with little water but softens with more water, universal rolling bearing grease
Lithium *	Synthetic oil	-60/+130	Very good	Good with additives	Stable up to approx. 90 °C	Low-temperature grease; also good for high speeds; low friction
Calcium complex *	Mineral or synthetic oil	-25/+130	Very good	Good with additives	Very stable	Multipurpose grease for high temperatures and loads
Sodium complex	Mineral or synthetic oil	-30/+140	Very good	Good with additives	Water-repellent	Suitable for high temperatures and loads
Barium complex	Mineral or synthetic oil	-30/+140	Very good	Good with additives	Stable up to approx. 90 °C	Suitable for high temperatures, load, and speeds (depending on base oil)
Polyurea *	Mineral or synthetic oil	-30/+175	Very good	Good with additives	Stable	Suitable for high temperature, loads, and speeds
Microgel *	Mineral oil	-20/+150	Very good	Good with additives	Stable	Suitable for high temperature, loads, and low speeds
Bentonite	Mineral oil	-20/+200	Very good	Good with additives	Very stable	Suitable for high temperature, loads, and low speeds

* Also available as EP grease.

In this thesis a Lithium – Synthetic oil grease has been considered due to its wide range of operating temperature and its diffusion for rolling components such as bearings and power screws [85, 86]. More details will be given in Chapter 6.

3.4 Failure modes

The failure modes of BSs can be divided in three main categories, depending on the subcomponent on which it originates:

- global failure mode;
- rolling element failure mode;
- return channel failure mode.

The last type of failures is strictly related to the BS component, while the first two are typical also of roller screws.

The global failure modes involve distributed degradations, such as wear and corrosion, or failure of the entire component, such as those coming from buckling and shock loads.

Wear is a complex mechanism involving various types of degradations, such as adhesion, abrasion and corrosion. In general, wear effect are mating surfaces wreck (Fig. 3.8a), increased friction, temperature rising, energy loss, increased backlash, degraded positioning precision, increased vibrations and impact contacts between spheres and grooves [43]. Among the factors that can accelerate this process the most dangerous and influencing ones are the entrance of foreign particles, the presence of wear debris, mounting misalignments, aggressive environment and degraded or severely starved lubrication [87, 88]. Wear is more relevant in high speed applications since the slip motion between the internal component is higher [89].

Shock loads are impulsive overloads that could happen throughout the operative life of the BS and that can lead to a quickly failure of the mechanism. High but not excessive loads can create permanent indentations of the spheres on the grooves with a consequent increase of vibration levels and performance degradation (Fig. 3.8b). Overloads can also cause the breakage of the screw shaft (Fig. 3.8c). Indentation can also originates from the intrusion of metal flakes in the contact regions.

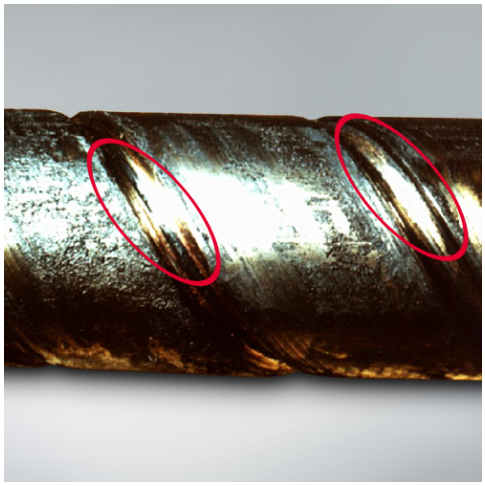

(a) Wear of the screw raceway.

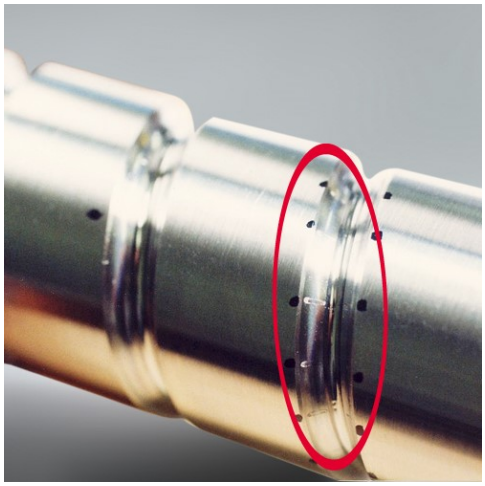

(b) Indentation of the screw raceway.

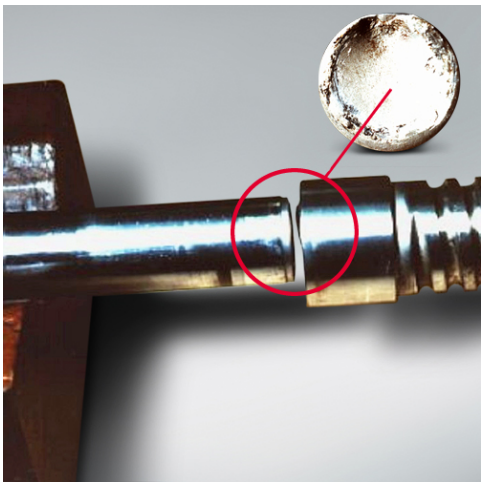

(c) Screw shaft end breakage.

(d) Flaking/spalling of the screw raceway.

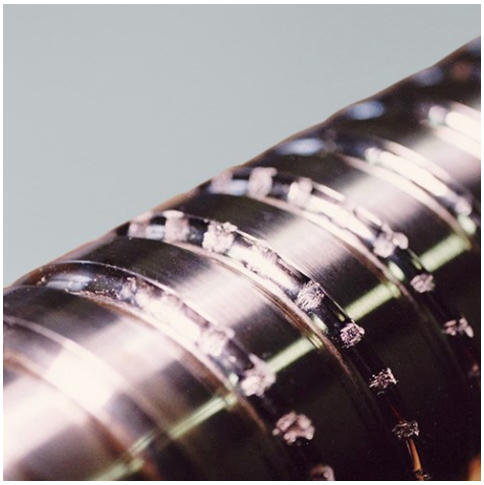

(e) Fretting on the screw raceway.

(f) Breakage of ball recirculation parts.

Fig. 3.8 Ball screw failures[1].

Buckling happens when the axial load exceeds the critical threshold specified in the ISO 3408 [84, 90] depending on the screw size and on the combination and types of supports. This elastic instability can lead to high local overloads and to a global failure of the mechanism. In a properly designed actuator, this condition rarely happens: it is mainly caused by mounting errors.

Flaking, spalling and fretting are degradations typical of the components with rolling elements, such as bearings, ball screws and roller screws.

Flaking and spalling degradation processes are similar to those of bearings, and they are inevitable with the ageing of the BS. They start developing from indentations or corrosion pits created by shock loads, or contaminant and water entrance. Locally, the contact stress increases over the material limit, causing the spall to progress and the formation of metal flakes that separate from the grooves (Fig. 3.8d). The produced debris enter the lubricant and contribute to increase the abrasive wear, producing new indentation points which, in turn, trigger new spall progressions. The damaged surfaces create increased friction and local overheating, that degrades the lubricant favouring the progression of corrosive wear and amplifying a self–exciting degradation process. Flaking and spalling are the major responsible for the increase of vibrations, which can damage not only the BS but also the surrounding components.

Fretting is a local damage that originates on the raceways when the BS is actuated with relatively small amplitude displacement, under high loads, or in presence of excessive vibrations. The grooves wear locally (Fig. 3.8e) and the formed metal debris contribute to increase the wear rate. Because of the small amplitude oscillations the lubricant can be almost completely absent in the contact.

A failure mode typical of BSs is that involving the only component present only in this kind of mechanism: the return channel. It is a critical component of the BSs since it is a preferential site of debris accumulation and the deflector is subjected to high frequency fatigue due to the repeated impacts with the balls that need to be diverted from the grooves. The higher the rotational speed, the larger the impact forces and the vibration level [91]. When the speed exceeds the permissible speed specified by the BS manufacturer, the return channel can plastically deform [92], causing the seizure of the sphere circuit, in case of multiple circuits, or leading to the

[1] Images retrieved from NSK website https://www.nskamericas.com/en/services/troubleshooting/ball-screws.html

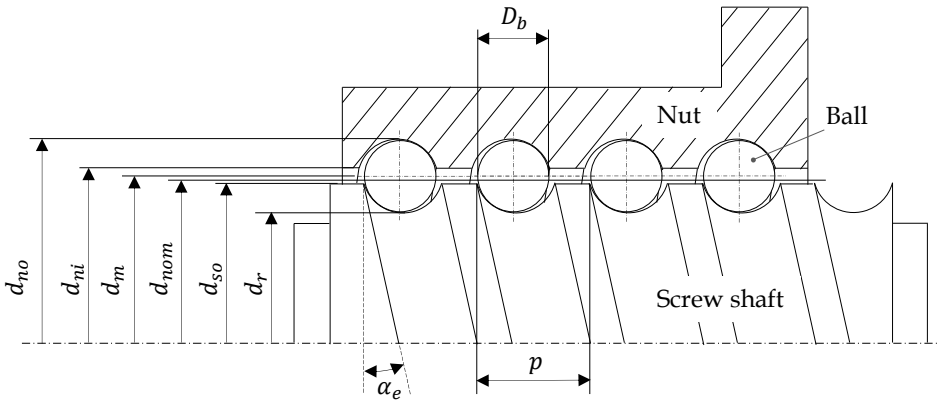

Fig. 3.9 Geometrical definitions of ball screws.

jam of the entire BS, in case of a single circuit. If the excessive speed is maintained, cracks incept in the root of the deflector tongue and progress with the ball impacts until a final breakage which leads to a complete jam (Fig. 3.8f).

In literature there is a lack of information about the fault–to–failure progression in time due to the complexity of BSs investigations, given their closed and compact nature [53]. Figure 3.8 shows a collection of photographs of failed BSs due to the previously cited failure mechanisms, taken from the NSK website[1].

3.5 Geometry

In this section, the ball screw geometry will be described from a mathematical point of view, providing the background and naming conventions that will be adopted and recalled in the following chapters.

3.5.1 Terminology

As already said, the BS is composed by a screw shaft, one or two nuts, several balls, seals and the return inserts, as can be seen in Fig. 3.1. Figure 3.9 shows the main diameters of a BS, according to the ISO 3408-1 [93]:

- d_r is the root diameter of the screw shaft;

- d_{so} is the outer diameter of the ball screw shaft;
- d_{nom} is the nominal diameter of the BS, a value used for designation positioned between the pitch circle diameter and the BS shaft outer diameter;
- d_m is the pitch circle diameter and contains the centres of the balls in contact with the grooves in the theoretical contact points;
- d_{ni} is the internal diameter of the nut;
- d_{nr} is the nut outer diameter of the nut;
- D_b is the balls diameter;
- α_e is the helix angle;
- p is the lead.

3.5.2 Reference systems

Considering the bodies as perfectly rigid, their position can be described using a unique reference frame. Considering a right–hand threaded BS, to describe the position of the screw shaft and of a generic sphere, three coordinate systems (CS) are introduced, shown in Fig. 3.10:

- $Ox'y'z'$ is the global inertial CS, fixed in space;
- $Oxyz$ is the screw shaft CS, with the z axis aligned along the screw shaft axis;
- $Btnb$ is the Frenet–Serret CS, whose centre B is located on the helix, with the t axis tangent to it, the n axis directed perpendicularly toward the screw shaft axis z and the b axis perpendicular to t and n axes to create a right handed CS.

The $Oxyz$ CS rotates with the screw shaft and it is supposed that $z \equiv z'$. The rotation angle with respect to the global CS is Ω and therefore the rotation matrix between these two CS can be written as

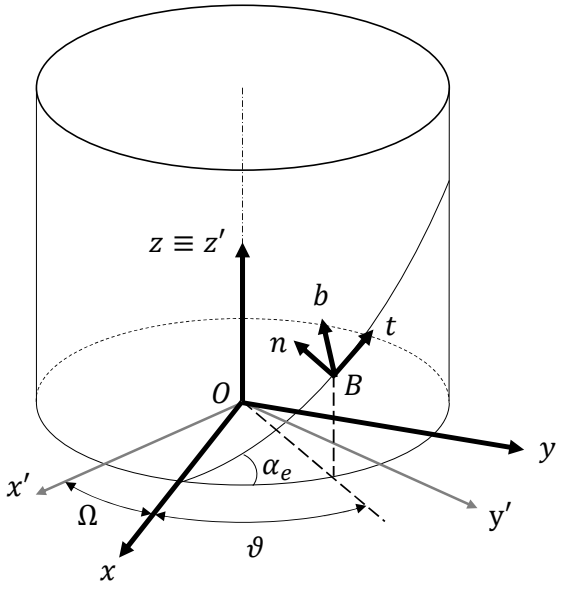

Fig. 3.10 Ball screw reference systems [94].

$$\begin{bmatrix} x' \\ y' \\ z' \end{bmatrix} = \mathbf{T}_1 \begin{bmatrix} x \\ y \\ z \end{bmatrix}$$
$$\mathbf{T}_1 = \begin{bmatrix} \cos(\Omega) & -\sin(\Omega) & 0 \\ \sin(\Omega) & \cos(\Omega) & 0 \\ 0 & 0 & 1 \end{bmatrix} \tag{3.1}$$

The Frenet–Serret CS identifies the ideal position of the centre of one of the spheres. Its location with regard to the screw shaft CS $Oxyz$ can be identified by the azimuth angle ϑ, knowing the helix angle α_e, as

$$\begin{bmatrix} x \\ y \\ z \end{bmatrix} = \mathbf{T}_2 \begin{bmatrix} t \\ n \\ b \end{bmatrix}$$
$$\mathbf{T}_2 = \begin{bmatrix} -\cos(\alpha_e)\sin(\vartheta) & -\cos(\vartheta) & \sin(\alpha_e)\cos(\vartheta) \\ \cos(\alpha_e)\cos(\vartheta) & -\sin(\vartheta) & -\sin(\alpha_e)\cos(\vartheta) \\ \sin(\alpha_e) & 0 & \cos(\alpha_e) \end{bmatrix} \tag{3.2}$$

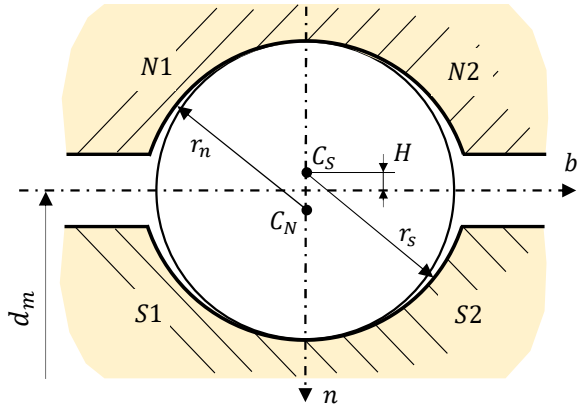

(a) Circular profile.

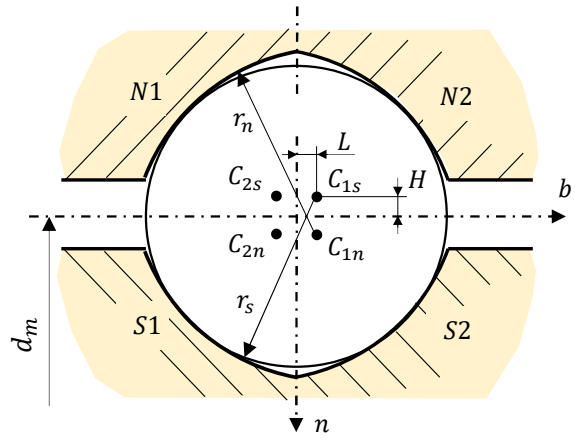

(b) Gothic arch profile.

Fig. 3.11 Groove profiles on a section normal to the thread.

The position vector $\mathbf{R}^O_{B/O}$ of B with regard to O (subscript), expressed in the $Oxyz$ CS (superscript), can be written as a function of ϑ as

$$\mathbf{R}^O_{B/O} = r_m \begin{bmatrix} \cos(\vartheta) & \sin(\vartheta) & \vartheta \tan(\alpha_e) \end{bmatrix}^T \tag{3.3}$$

3.5.3 Grooves profile

Observing a section normal to the thread, the groove profile can be identified (Fig. 3.11): it can be either circular (or round) or with a gothic arch shape (or ogival). In the latter, each raceway is composed by two circular half grooves, whose centres of curvature are offset by a quantity L, called *ogival offset*, along the b axis

with regard to the *n* axis of the *tnb* CS: this parameter determines the gothicity of the profile. The depth of the groove inside the screw shaft or the nut is imposed by the *centre radius offset H*, which is an offset of the curvature centres from the pitch circle diameter line along the *n* axis of the *tnb* CS. The curvature centres of the four half grooves are C_{1s}, C_{2s}, C_{1n} and C_{2n}, where the subscripts refer to the half grooves names of Fig. 3.11. S_1 is the screw half groove located in the forth quarter of the *tnb* CS, S_2 in the first quarter, N_1 in the third quarter and N_2 in the second quarter.

The curvature radius of the screw half grooves is r_s while r_n is that of the nut raceway. The ISO 3408-1 [93] defines two conformity factors f_s and f_n that relate respectively r_s and r_n to the ball diameter D_b as $r_{s,n} = f_{s,n} D_b$.

The circular profile (Fig. 3.11a) is a particular case of the gothic arch profile (Fig. 3.11b), in which $L = 0$ and $C_{1s} \equiv C_{2s} \equiv C_S$, and $C_{1n} \equiv C_{2n} \equiv C_N$. Therefore, in this thesis a gothic arch groove profile has been considered.

The gothic arch profile allows to optimise the BS efficiency, maintaining the contact angles (see Sec. 3.5.4) close to the optimal value. In addition, the gothic arch profile is the only profile on which it is possible to apply the oversized balls preload method.

3.5.4 Contact angle

The performance of the BS mechanism and its efficiency depend on the direction on which the normal contact forces are exchanged between spheres and grooves.

The ISO 3408-1 [93] defines as contact angle *"the angle between a plane perpendicular to the ball screw shaft axis and the resultant of the forces transmitted by a ball track to a rolling element"*. For an optimal efficiency, it should be close to 45° [95].

The ISO definition is sufficient to perform the global design of the BS following the formulations presented in the standard, but it is not completely precise if a detailed analysis has to be carried out. Indeed, two points remain vague:

- the ISO definition does not consider the helix angle and treats the BS as a bearing, on which the plane normal to the thread contains also the bearing symmetry axis;

- even if the helix angle is neglected, the *"resultant of the force transmitted by a ball track to a rolling element"* includes also the tangential forces, which make the force resultant vector to not lie in the same plane on which the screw shaft is contained, leading to a not univocally defined angle in space between a 3D vector and a plane.

In this thesis, following the classical definition commonly adopted in literature [96–98], with the term *contact angle* α it is intended the angle between the normal force exchanged between and the sphere and the raceway and the n axis of the Frenet–Serret CS: with this definition, both the n axis and the force vector lie in the same $n-b$ plane, normal to the thread in B.

A simple relationship between the contact angle α defined in the plane normal to the thread and the contact angle α_{ISO} defined in a plane containing the screw axis can be easily obtained. Figure 3.12a shows a generic sphere, with its centre in B on the Frenet–Serret CS, the plane Π_1 $(n-b)$ normal to the thread in B (red) and the plane Π_2 $(n-b_z)$ used by the ISO 3408-1, containing the screw axis z. Bt_znb_z is a temporary CS, centred in B with the b_z axis parallel to the screw axis z. From the definition of the Frenet–Serret CS, the n axis is the same for both the CSs and the $Btnb$ CS is rotated by an angle α_e around it with regard to Bt_znb_z.

Cutting the sphere with the planes Π_1, Π_2 and the plane $t-b$ the slice of Fig. 3.12b is obtained. The surface containing A, B, C and D lies on Π_1, while that containing A, B, C', C", D' and D" belongs to Π_2. γ_2 and γ_3 are the curves originated by the intersection of the sphere surface with respectively Π_1 and Π_2: γ_2 coincides with γ_3 if the latter is rotated by an angle α_e around n. γ_1 is the projection of γ_3 on Π_2.

Given a contact point D on the sphere surface, the contact angle α on the plane normal to the thread Π_1 is $\widehat{\mathrm{ABD}}$. To represent the same contact angle on the the plane Π_2 it is possible to image to rotate the surface ABD around the edge $\overline{\mathrm{AB}}$ by an angle α_e. D ends up in D" on Π_2 and $\widehat{\mathrm{ABD"}}$ equals α.

Following the prescription of the ISO and observing the system along $-\hat{t}$, i.e. looking everything projected on the Π_2 plane, the angle between the point of contact on which the *"resultant of the forces transmitted by a ball track to a rolling element"* and the *"plane perpendicular to the ball screw shaft axis"*, represented by n on Π_2,

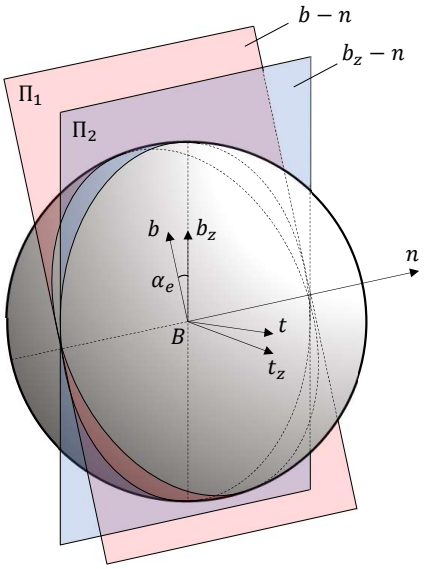

(a) Planes on sphere.

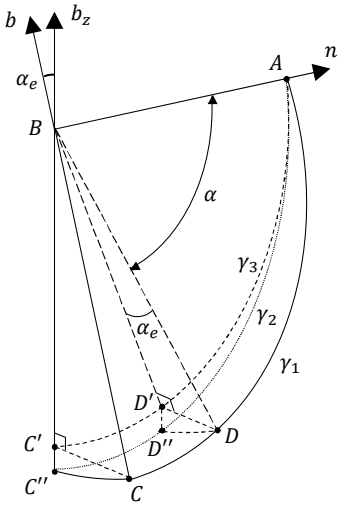

(b) Sphere slice between the planes.

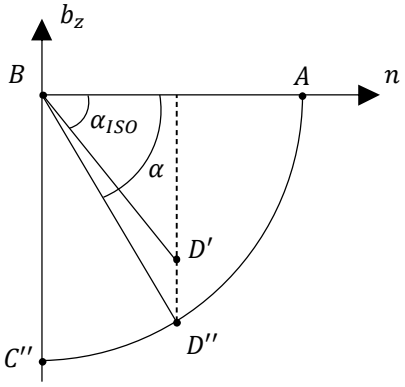

(c) Sphere slice between the planes looking along $-\widehat{t}$.

Fig. 3.12 Sphere section with the planes containing the screw axis (blue) and the plane normal to the thread (red).

is $\widehat{\text{ABD'}}$ since the dashed line in Fig. 3.12c represent the locus of points occupied by the projection D' of D on Π_2.

From Fig. 3.12 it can be seen that $\overline{\text{BD'}} = \overline{\text{BD}}\cos(\alpha_e) = r_b\cos(\alpha_e)$ and that

$$\overline{\text{BD''}}\cos(\alpha) = \overline{\text{BD'}}\cos(\alpha_{ISO}) \tag{3.4}$$

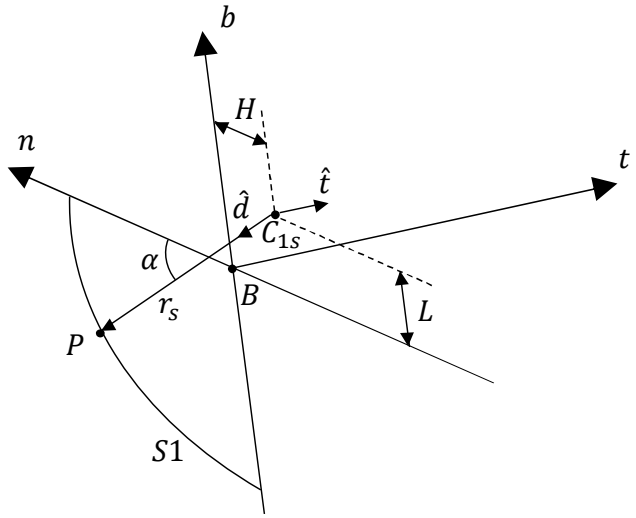

Fig. 3.13 S1 groove in the *tnb* coordinate system.

therefore the relationship between the real contact angle α on Π_1 and the contact angle seen projecting on Π_2 described by the ISO can be written as

$$\alpha = \arccos\Big[\cos(\alpha_e)\ \cos(\alpha_{ISO})\Big] \tag{3.5}$$

The contact angle α coincides with α_{ISO} for $\alpha_e = 0$. In the following chapters, for contact angle it is always intended α on Π_1.

3.5.5 Mathematical formulation of the grooves geometry

The position vector of C_{1s} with regard to to B in the *Btnb* CS is

$$\mathbf{R}^{B}_{C_{1s}/B} = \begin{bmatrix} 0 & -H & L \end{bmatrix} \begin{bmatrix} \widehat{\mathbf{t}} \\ \widehat{\mathbf{n}} \\ \widehat{\mathbf{b}} \end{bmatrix} \tag{3.6}$$

Observing Fig. 3.13, the position vector of a generic point P, belonging to the half groove S1, with regard to to B can be expressed in the *Btnb* CS as

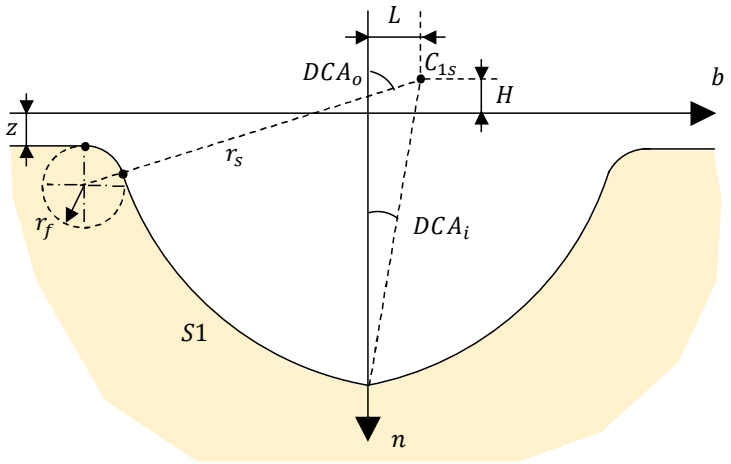

Fig. 3.14 Design containment angles of the groove profile.

$$\mathbf{R}^{B}_{P/B} = \begin{bmatrix} 0 & -H + r_s\cos(\alpha) & L - r_s\sin(\alpha) \end{bmatrix} \begin{bmatrix} \widehat{\mathbf{t}} \\ \widehat{\mathbf{n}} \\ \widehat{\mathbf{b}} \end{bmatrix} \tag{3.7}$$

The contact angle α is the angle on $n-b$ between the segment connecting P and C_{1s} and n.

Considering the coordinates of B with regard to O (Eq. 3.3) expressed in $Oxyz$ and the rotation matrix T_2 (Eq. 3.2), the position vector of the point P with regard to O in $Oxyz$ can be written as

$$\mathbf{R}^{O}_{P/O} = \begin{bmatrix} H\cos(\vartheta) + r_m\cos(\vartheta) - r_s\cos(\alpha)\cos(\vartheta) + L\sin(\alpha_e)\sin(\vartheta) + \\ \qquad - r_s\sin(\alpha)\sin(\alpha_e)\sin(\vartheta) \\ H\sin(\vartheta) + r_m\sin(\vartheta) - L\sin(\alpha_e)\cos(\vartheta) - r_s\cos(\alpha)\sin(\vartheta) + \\ \qquad + r_s\sin(\alpha)\sin(\alpha_e)\cos(\vartheta) \\ L\cos(\alpha_e) + r_m\vartheta\tan(\alpha_e) + r_s\cos(\alpha_e)\sin(\alpha) \end{bmatrix}^{T} \begin{bmatrix} \widehat{\mathbf{t}} \\ \widehat{\mathbf{n}} \\ \widehat{\mathbf{b}} \end{bmatrix} \tag{3.8}$$

A similar procedure can be followed to obtain the description of the other half grooves, considering that for S2 $n_{C_{2s}} = -H$ and $b_{C_{2s}} = -L$ Eq. 3.6, for N1 $n_{C_{1n}} = H$

and $b_{C_{1n}} = L$, for N2 $n_{C_{2n}} = H$ and $b_{C_{2n}} = -L$ and that for the nut grooves the curvature radius r_s must be replaced with r_n.

Equation 3.8 describes every point of the half groove S1 with regard to the screw shaft CS, depending on the azimuth angle ϑ and the contact angle α. The latter can vary between the inner and outer design containment angles DCA_i and DCA_o, shown in Fig. 3.14, which are the contact angle values limiting the effective arch of the raceways on which it is possible to have a contact:

$$DCA_i = \arcsin\left(\frac{L}{r_s}\right) \tag{3.9}$$

$$DCA_o = \arccos\left(\frac{H + r_f + z}{r_s + r_f}\right) \tag{3.10}$$

Figure 3.14 shows the fillet radius r_f of the raceway edge and the distance z between the pitch circle diameter line and the outer surface of the screw shaft.

Screw shaft groove curvatures

In order to calculate the hertzian stress in the contact points the principal curvatures of the mating bodies are required. Calling the sphere and the groove respectively as body 1 and 2, the two principal curvatures of the sphere are trivial and equal to

$$\rho_{11} = \rho_{12} = \frac{1}{r_b} \tag{3.11}$$

For what concerns the grooves of the screw shaft, one of its principal curvature is

$$\rho_{22} = -\frac{1}{r_s} \tag{3.12}$$

on the plane normal to the thread.

The other principal curvature is directed along a plane perpendicular to $n - b$, defined as the plane Π containing the versor $\widehat{t}$ and the points P and C_{1s} (for the half groove S1). It is essentially the curvature of the intersection curve γ of Fig. 3.15 on the plane Π. The aim of the following pages is therefore to obtain an expression for γ.

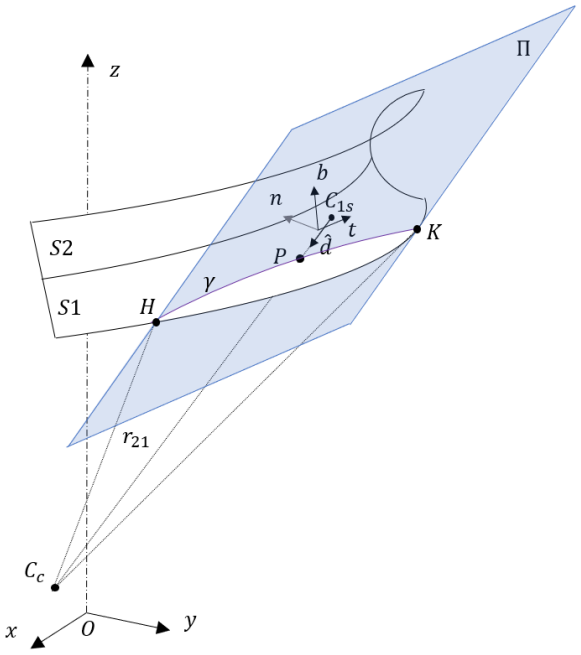

Fig. 3.15 Intersection between the half groove S1 and the plane Π.

The versor $\widehat{d}$ in Figs. 3.14 and 3.15 identifies the direction of the segment connecting the groove secondary curvature centre C_{1s} and the contact point P, and its expression is

$$\widehat{\mathbf{d}} = \cos(\alpha)\,\widehat{\mathbf{n}} - \sin(\alpha)\,\widehat{\mathbf{b}} \tag{3.13}$$

where $\widehat{n}$ and $\widehat{b}$ are the versors of respectively the n and b axes.

The position vector of a generic point P on the plane with regard to O in $Oxyz$ can then be written as

$$\mathbf{R}^{O}_{P/O|\Pi} = \mathbf{R}^{O}_{C_{1s}/O} + l_1\widehat{\mathbf{t}} + l_2\widehat{\mathbf{d}} \tag{3.14}$$

where

$$\mathbf{R}^{O}_{C_{1s}/O} = \mathbf{R}^{O}_{B/O} + \mathbf{T}_2\mathbf{R}^{B}_{C_{1s}/B} \tag{3.15}$$

The superscripts B and O in the previous equations represent the CS in which the vector components are expressed, i.e. respectively the $Btnb$ and $Oxyz$ CSs.

Equating Eq. 3.14 with Eq. 3.8, the expression of the intersection curve γ between S and Π with regard to O in $Oxyz$ can be obtained, function of ϑ, α, l_1 and l_2 with only one independent variable.

$$\mathbf{R}^{O}_{P/O|S1} = \mathbf{R}^{O}_{P/O|\Pi} \tag{3.16}$$

Once the point P where the curvature has to be calculated is fixed and identified by ϑ_P and α_P, the parametric expression of γ which passes through P can be obtained in a variational form, imposing

$$\begin{aligned} \vartheta &= \vartheta_P + \Delta\vartheta \\ \alpha &= \alpha_P + \Delta\alpha \end{aligned} \tag{3.17}$$

where ϑ_P and α_P are the values of the azimuth and contact angle in P.

Inserting Eq. 3.17 in Eq. 3.16 a non–linear implicit problem composed by the following set of equations is obtained:

$$\begin{aligned} &HC_{\Delta\vartheta}C_{\vartheta} - HS_{\Delta\vartheta}S_{\vartheta} + r_m C_{\Delta\vartheta}C_{\vartheta} - r_m S_{\Delta\vartheta}S_{\vartheta} + LC_{\Delta\vartheta}S_{\alpha_e}S_{\vartheta} + \\ &\quad + LS_{\Delta\vartheta}C_{\vartheta}S_{\alpha_e} - r_s C_{\Delta\vartheta}C_{\Delta\alpha}C_{\alpha}C_{\vartheta} + r_s C_{\Delta\vartheta}S_{\Delta\alpha}S_{\alpha}C_{\vartheta} + \\ &\quad + r_s C_{\Delta\alpha}S_{\Delta\vartheta}C_{\alpha}S_{\vartheta} - r_s S_{\Delta\vartheta}S_{\Delta\alpha}S_{\alpha}S_{\vartheta} - \\ &\quad + r_s C_{\Delta\vartheta}C_{\Delta\alpha}S_{\alpha}S_{\alpha_e}S_{\vartheta} - r_s C_{\Delta\vartheta}S_{\Delta\alpha}C_{\alpha}S_{\alpha_e}S_{\vartheta} - \\ &\quad + r_s C_{\Delta\alpha}S_{\Delta\vartheta}S_{\alpha}C_{\vartheta}S_{\alpha_e} - r_s S_{\Delta\vartheta}S_{\Delta\alpha}C_{\alpha}C_{\vartheta}S_{\alpha_e} - \\ &\quad + HC_{\vartheta} - r_m C_{\vartheta} + l_2 C_{\alpha}C_{\vartheta} - LS_{\alpha_e}S_{\vartheta} + \\ &\quad + l_1 C_{\alpha_e}S_{\vartheta} + l_2 S_{\alpha}S_{\alpha_e}S_{\vartheta} = 0 \end{aligned} \tag{3.18a}$$

$$\begin{aligned} &HC_{\Delta\vartheta}S_{\vartheta} + HS_{\Delta\vartheta}C_{\vartheta} + r_m C_{\Delta\vartheta}S_{\vartheta} + r_m S_{\Delta\vartheta}C_{\vartheta} - LC_{\Delta\vartheta}C_{\vartheta}S_{\alpha_e} + \\ &\quad + LS_{\Delta\vartheta}S_{\alpha_e}S_{\vartheta} - r_s C_{\Delta\vartheta}C_{\Delta\alpha}C_{\alpha}S_{\vartheta} - r_s C_{\Delta\alpha}S_{\Delta\vartheta}C_{\alpha}C_{\vartheta} + \\ &\quad + r_s C_{\Delta\vartheta}S_{\Delta\alpha}S_{\alpha}S_{\vartheta} + r_s S_{\Delta\vartheta}S_{\Delta\alpha}S_{\alpha}C_{\vartheta} + r_s C_{\Delta\vartheta}C_{\Delta\alpha}S_{\alpha}C_{\vartheta}S_{\alpha_e} + \\ &\quad + r_s C_{\Delta\vartheta}S_{\Delta\alpha}C_{\alpha}C_{\vartheta}S_{\alpha_e} - r_s C_{\Delta\alpha}S_{\Delta\vartheta}S_{\alpha}S_{\alpha_e}S_{\vartheta} - r_s S_{\Delta\vartheta}S_{\Delta\alpha}C_{\alpha}S_{\alpha_e}S_{\vartheta} - \\ &\quad + HS_{\vartheta} - r_m S_{\vartheta} + LC_{\vartheta}S_{\alpha_e} - l_1 C_{\alpha_e}C_{\vartheta} + l_2 C_{\alpha}S_{\vartheta} - l_2 S_{\alpha}C_{\vartheta}S_{\alpha_e} = 0 \end{aligned} \tag{3.18b}$$

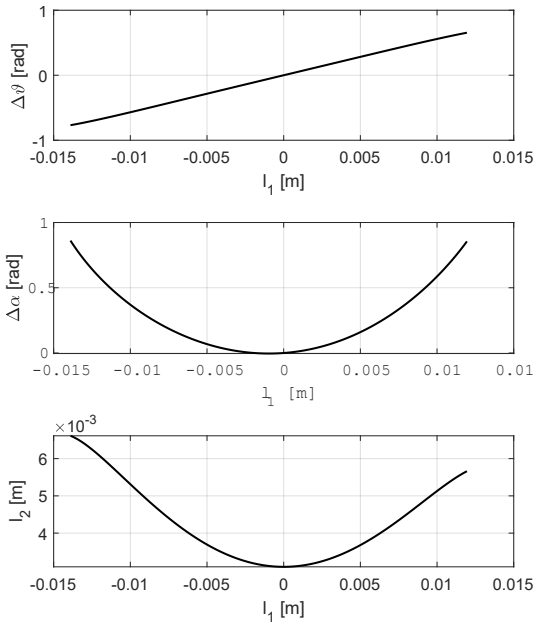

Fig. 3.16 Numerical solution of the set of Eqns. 3.18 for a screw with r_m = 20 mm, r_b = 3.175 mm, α_e = 9.043°, H = 0.078×10^{-3} mm, L = 0.055×10^{-3} mm and a contact angle $\alpha = 60°$.

$$\Delta\vartheta r_m T_{\alpha_e} - r_s C_{\Delta\alpha} C_{\alpha_e} S_\alpha - r_s S_{\Delta\alpha} C_\alpha C_{\alpha_e} - l_1 S_{\alpha_e} + l_2 C_{\alpha_e} S_\alpha = 0 \tag{3.18c}$$

where C_x, S_x and T_x are compact notations for the trigonometric functions $\cos(x)$, $\sin(x)$ and $\tan(x)$.

An explicit solution of Eq. 3.18 cannot be found, therefore it has been solved numerically assuming l_1 as independent variable and using the Levenberg–Marquardt method [99]. To accurately describe the shape of γ, the solution has been calculated in each point of a fine mono–dimensional mesh with size 5×10^{-4} m. The extreme values of l_1 from which to start and finish the mesh corresponds to those point on which α reaches the DCA_o, correspondent to the points H and K in Fig. 3.15.

Each of the points describing the curve γ on Π (Eq. 3.14) is characterised by the pair (l_1, l_2). The third component of the coordinates obtained by Eq. 3.14 is null, thus the bidimensional curve γ

$$\gamma := \quad l_2 = f(l_1) \tag{3.19}$$

Table 3.3 Values of the parameters of Eq. 3.20.

Parameter	**Value**
a_1	1.0091×10^{0}
a_2	1.8975×10^{0}
a_3	7.1416×10^{-6}
a_4	2.8783×10^{0}
a_5	2.3380×10^{-1}
a_6	3.9180×10^{0}
a_7	4.1160×10^{-1}

has been interpolated with a 9$^{\text{th}}$ order polynomial, using the Bisquare robust linear least–square fitting method and whitening the data in order to avoid an ill–conditioned Vandermonde matrix in the fit calculation, obtaining a coefficient of determination $R^2 \geq 0.9996$. Only a small part of γ around P has been considered for the fitting in order to obtain more accurate results, since the shape of the function far from the central point P becomes more difficult to be interpolated with a 9$^{\text{th}}$ order polynomial and, specially, are of little interest in the calculation of the curvature in P. The shapes of $\Delta\vartheta(l_1)$, $\Delta\alpha(l_1)$ and $l_2(l_1)$ are shown in Fig. 3.16 for a screw shaft with $r_m = 20$ mm, $r_b = 3.175$ mm, $\alpha_e = 9.043°$, H = 0.078×10^{-3} mm and L = 0.055×10^{-3} mm.

To obtain the curvature and the position of the curvature centre C_c depicted in Fig. 3.15, this polynomial has been derived twice and the value of the function in $l_1 = 0$ has been calculated, correspondent to the curvature in P.

This procedure has been carried out 180 000 times, calculating the curvature value for all the different combinations of the constructive parameters in the ranges $\alpha_e = 0° \div 75°$, $\alpha = 10° \div 70°$, $r_m = 6 \div 50$ mm, L = $0 \div 0.39$ mm and H = $0 \div 0.39$ mm. The balls radius has been considered as a dependent parameter, function of r_m according to the commercial standards [78, 100].

The resulting dataset has been inserted in the Eureqa® software and a fitting equation has been obtained to describe the curvature radius as an explicit function of the constructive parameters:

$$\begin{aligned} r_{cs}(r_m, r_b, \alpha, \alpha_e, L) &= a_1 r_m e^{\sigma_1 - a_7 \sin^{a_2}(a_3\alpha^{a_4})} - r_b - L a_4^{\sigma_1} \\ \text{with} \qquad \sigma_1 &= \alpha_e^{a_2} + a_3\alpha^{a_4} + \alpha_e \tan(a_5\alpha_e^{a_6}) \end{aligned} \tag{3.20}$$

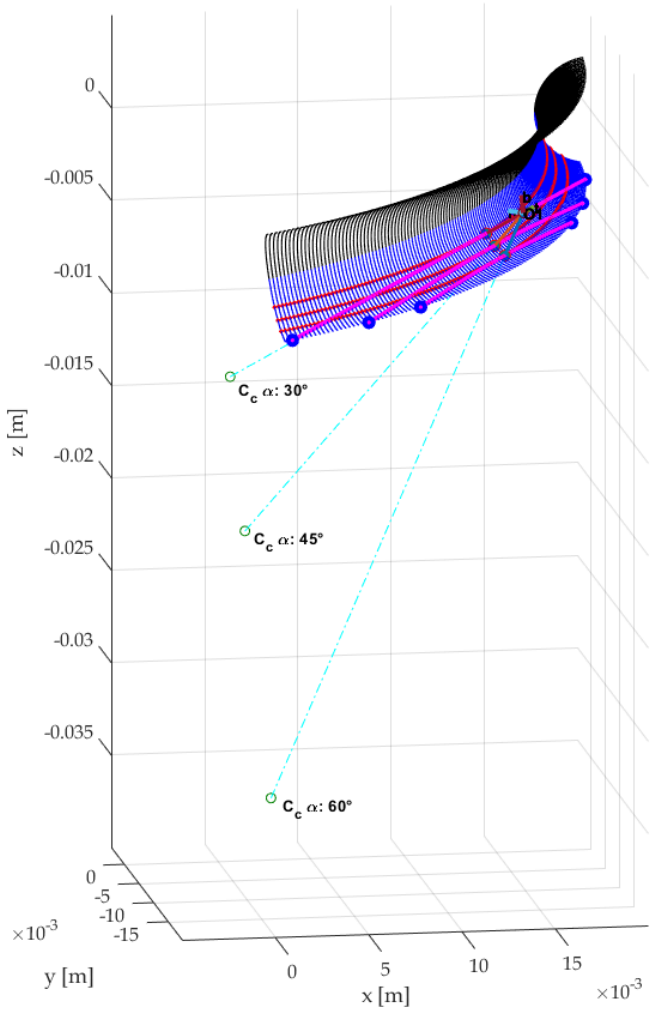

Fig. 3.17 Numerical intersection of S1 with Π and curvature centres for a screw with r_m = 20 mm, r_b = 3.175 mm, α_e = 9.043°, H = 0.078×10^{-3} mm, L = 0.055×10^{-3} mm and contact angle $\alpha = 30°, 45°, 60°$.

where r_{cs}, r_m, r_b and L are in [m], α_e in [rad] and α in [deg]. The values of the constants $a_1 \ldots a_7$ of Eq. 3.20 are listed in Tab.3.3. Equation 3.20 presents a coefficient of determination $R^2 \geq 0.9999$, a mean squared absolute error of 2.33×10^{-6} m and a maximum relative errors < 2%.

Figure 3.17 depicts the results of a purely numerical reconstruction of a quarter of turn of a screw shaft raceway, correspondent of the visualization of Fig. 3.15. The S1 half groove is shown in blue, while the S2 in black. Three γ curves, obtained following the above described procedure of solution of Eqns. 3.18, are shown in

pink for three values of the contact angle α (30°, 45° and 60°). A typical shape of the curve γ on the plane Π is shown in the third subplot of Fig. 3.16. The electric blue dots are the limit points on which the contact angle reaches the DCA_o value. The locations of the curvature centres C_c are represented and it can be noted that the higher the contact angle, the higher the curvature radius and the further the curvature centre from the contact point.

Most of the articles in literature adopt the ISO 3408-4 [84] formula for the curvature of the screw shaft, which defines the curvature radius neglecting the helix angle, as if it was a bearing [73], as

$$r_{cs,ISO} = \frac{r_m - r_b \cos(\alpha)}{\cos(\alpha)} \tag{3.21}$$

The comparison between the numerical solution of Eqns. 3.18, the results of Eq. 3.20 and Eq. 3.21, varying the helix and contact angles, is shown in Fig. 3.18 for a screw with r_m = 20 mm, r_b = 3.175 mm, H = 0.078×10^{-3} mm and L = 0.055×10^{-3} mm.

It can be seen from Fig. 3.18a that the curvature radius r_{cs} increases with both the contact angle and the helix angle and the increase with regard to the contact angle is more pronounced for high helix angle values. For $\alpha_e \to 0$ the proposed new formula (Eq. 3.20) converges to the literature formula (Eq. 3.21) since $\alpha_e = 0$ is the contact condition of a bearing. The relative error with regard to the numerical solution is less than 2%, as depicted in Fig. 3.18c. The literature formulation relative error, shown in Fig. 3.18b, increases with the helix angle, while it does not show a significant dependence on the contact angle.

Normal BSs have a contained helix angle, usually less than 20°, therefore the relative error committed using the literature formula instead of the real value is in the order of 10-15%. Nevertheless, different typologies of BSs exist for high speed applications, with helix angles even up to 58.4° (d_{nom} = 25 mm and p = 80 mm). For these values, using the literature formula leads to a relative error of almost 75%, against the maximum 2% of the proposed approach.

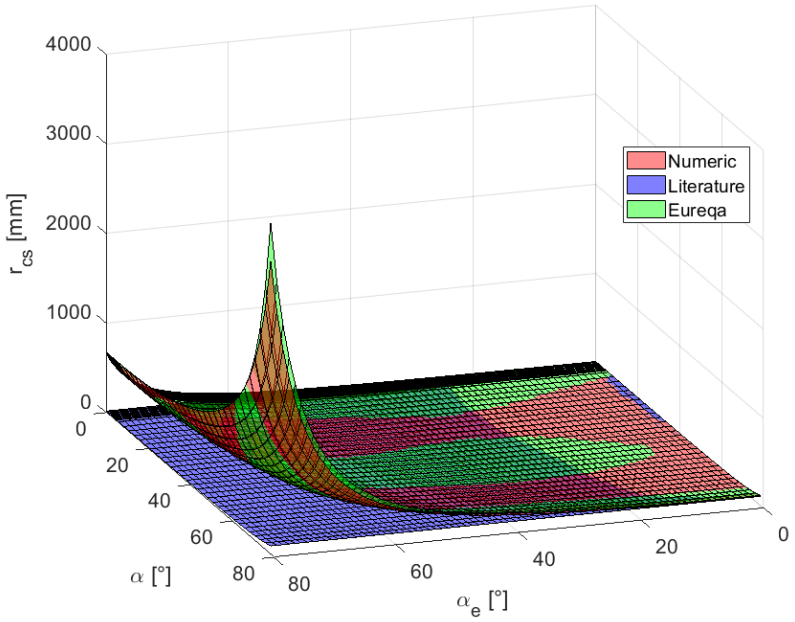

(a) Curvature radius 3D comparison.

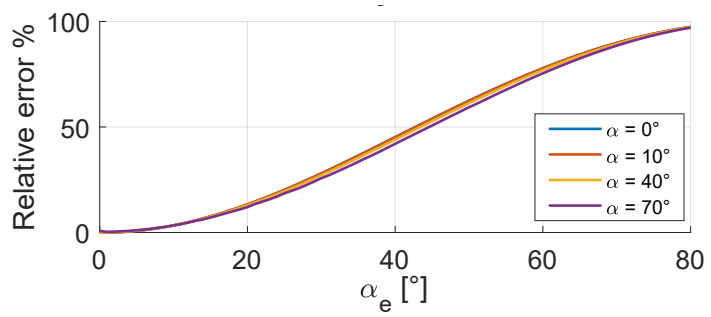

(b) Relative error % between the literature formula and the numerical solution.

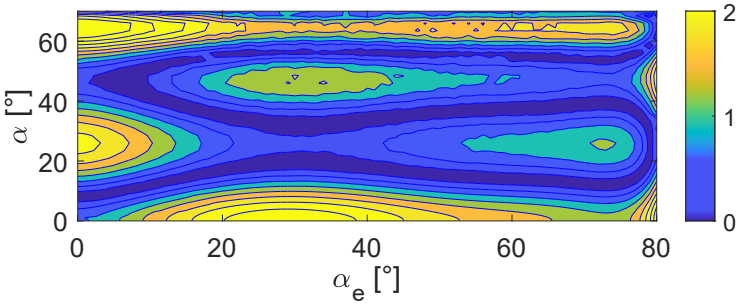

(c) Relative error % between the proposed formula and the numerical solution.

Fig. 3.18 Screw curvature radius comparison varying α and $alpha_e$ for a screw with r_m = 20 mm, r_b = 3.175 mm, H = 0.078×10^{-3} mm and L = 0.055×10^{-3} mm

Nut groove curvatures

The same approach can be followed to obtain en expression for the first curvature radius r_{cn} of the nut raceway. The second curvature, as for the screw shaft, is

$$\rho_{22} = -\frac{1}{r_n} \tag{3.22}$$

The procedure can be applied with no difference to the half groove N1 or N2: N1 is considered here. Reminding that for N1 the position vector of the secondary curvature centre with regard to B in *Btnb* CS is

$$\mathbf{R}^{B}_{C_{1n}/B} = \begin{bmatrix} 0 & H & L \end{bmatrix} \begin{bmatrix} \widehat{\mathbf{t}} \\ \widehat{\mathbf{n}} \\ \widehat{\mathbf{b}} \end{bmatrix} \tag{3.23}$$

Eq. 3.14 becomes

$$\mathbf{R}^{O}_{P/O|\Pi} = \mathbf{R}^{O}_{C_{1n}/O} + l_1\widehat{\mathbf{t}} + l_2\widehat{\mathbf{d}} \tag{3.24}$$

where

$$\mathbf{R}^{O}_{C_{1n}/O} = \mathbf{R}^{O}_{B/O} + \mathbf{T}_2\mathbf{R}^{B}_{C_{1n}/B} \tag{3.25}$$

and applying Eqns. 3.16 and 3.17, the equation set 3.18 reads

$$\begin{aligned} & HS_{\Delta\vartheta}S_{\vartheta} - HC_{\Delta\vartheta}C_{\vartheta} + r_mC_{\Delta\vartheta}C_{\vartheta} - r_mS_{\Delta\vartheta}S_{\vartheta} + LC_{\Delta\vartheta}S_{\alpha_e}S_{\vartheta} + \\ & \quad + LS_{\Delta\vartheta}C_{\vartheta}S_{\alpha_e} + r_sC_{\Delta\vartheta}C_{\Delta\alpha}C_{\alpha}C_{\vartheta} - r_sC_{\Delta\vartheta}S_{\Delta\alpha}S_{\alpha}C_{\vartheta} - \\ & \quad + r_sC_{\Delta\alpha}S_{\Delta\vartheta}C_{\alpha}S_{\vartheta} + r_sS_{\Delta\vartheta}S_{\Delta\alpha}S_{\alpha}S_{\vartheta} - \\ & \quad + r_sC_{\Delta\vartheta}C_{\Delta\alpha}S_{\alpha}S_{\alpha_e}S_{\vartheta} - r_sC_{\Delta\vartheta}S_{\Delta\alpha}C_{\alpha}S_{\alpha_e}S_{\vartheta} - \\ & \quad + r_sC_{\Delta\alpha}S_{\Delta\vartheta}S_{\alpha}C_{\vartheta}S_{\alpha_e} - r_sS_{\Delta\vartheta}S_{\Delta\alpha}C_{\alpha}C_{\vartheta}S_{\alpha_e} + \\ & \quad + HC_{\vartheta} - r_mC_{\vartheta} - l_2C_{\alpha}C_{\vartheta} - LS_{\alpha_e}S_{\vartheta} + \\ & \quad + l_1C_{\alpha_e}S_{\vartheta} + l_2S_{\alpha}S_{\alpha_e}S_{\vartheta} = 0 \end{aligned} \tag{3.26a}$$

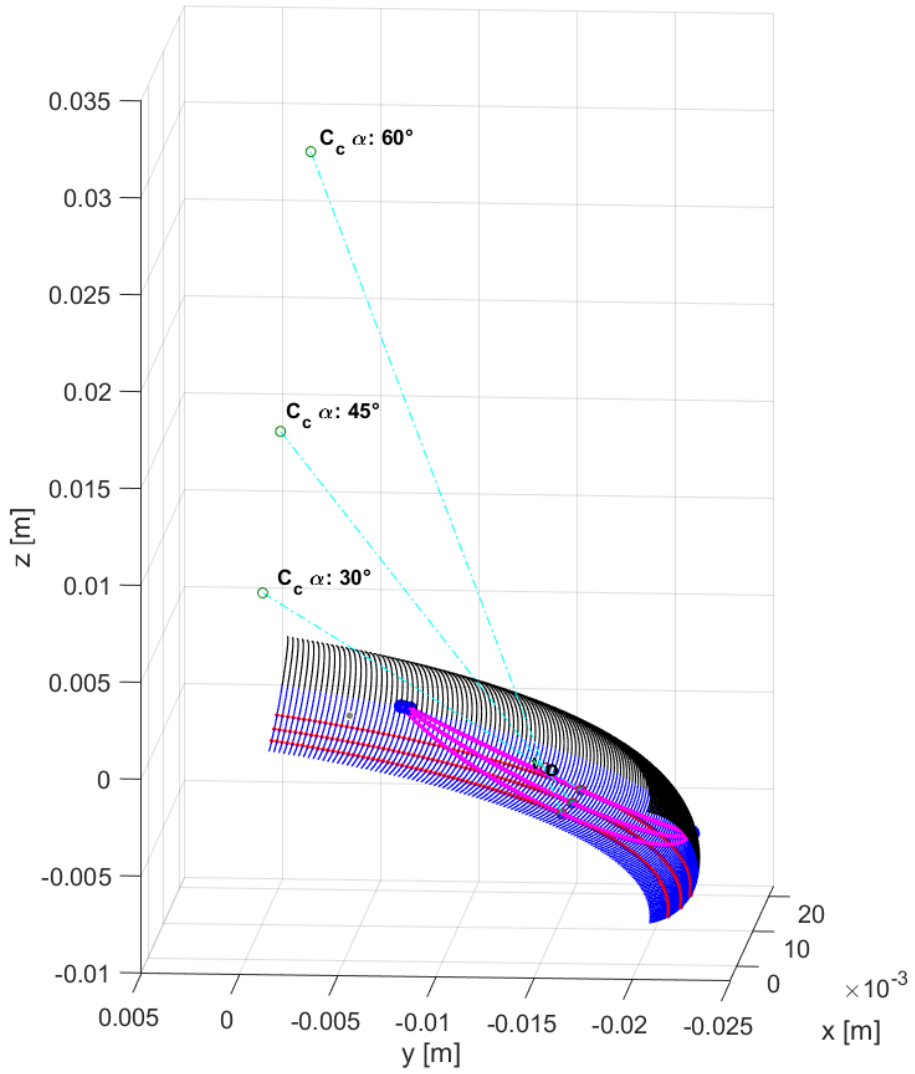

Fig. 3.19 Numerical intersection of N1 with Π and curvature centres for a screw with r_m = 20 mm, r_b = 3.175 mm, α_e = 9.043°, H = 0.078×10^{-3} mm, L = 0.055×10^{-3} mm and contact angle $\alpha = 30°, 45°, 60°$.

$$
\begin{aligned}
&-HS_{\Delta\vartheta}C_\vartheta - HC_{\Delta\vartheta}S_\vartheta + r_mC_{\Delta\vartheta}S_\vartheta + r_mS_{\Delta\vartheta}C_\vartheta - LC_{\Delta\vartheta}C_\vartheta S_{\alpha_e} + \\
&\quad + LS_{\Delta\vartheta}S_{\alpha_e}S_\vartheta + r_sC_{\Delta\vartheta}C_{\Delta\alpha}C_\alpha S_\vartheta + r_sC_{\Delta\alpha}S_{\Delta\vartheta}C_\alpha C_\vartheta - \\
&\quad + r_sC_{\Delta\vartheta}S_{\Delta\alpha}S_\alpha S_\vartheta - r_sS_{\Delta\vartheta}S_{\Delta\alpha}S_\alpha C_\vartheta + r_sC_{\Delta\vartheta}C_{\Delta\alpha}S_\alpha C_\vartheta S_{\alpha_e} + \\
&\quad + r_sC_{\Delta\vartheta}S_{\Delta\alpha}C_\alpha C_\vartheta S_{\alpha_e} - r_sC_{\Delta\alpha}S_{\Delta\vartheta}S_\alpha S_{\alpha_e}S_\vartheta - r_sS_{\Delta\vartheta}S_{\Delta\alpha}C_\alpha S_{\alpha_e}S_\vartheta + \\
&\quad + HS_\vartheta - r_mS_\vartheta + LC_\vartheta S_{\alpha_e} - l_1C_{\alpha_e}C_\vartheta - l_2C_\alpha S_\vartheta - l_2S_\alpha C_\vartheta S_{\alpha_e} = 0
\end{aligned}
\tag{3.26b}
$$

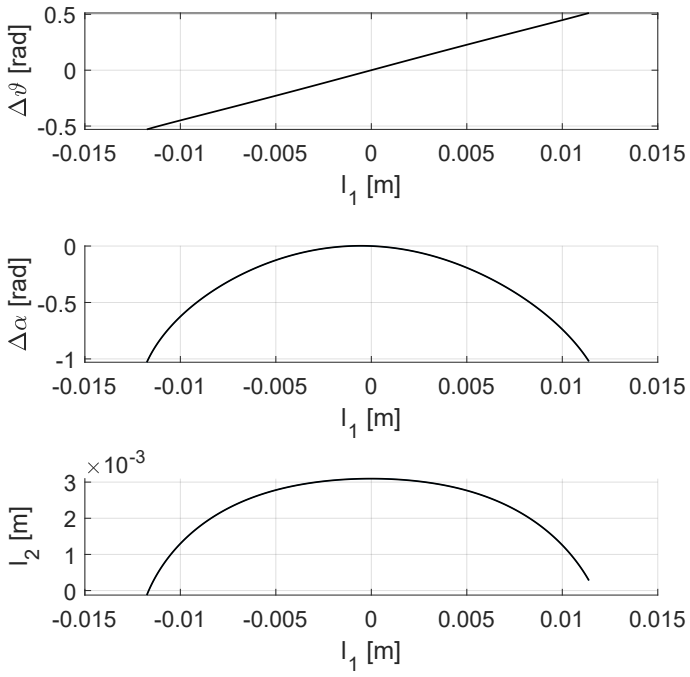

Fig. 3.20 Numerical solution of the set of Eqns. 3.26 for a nut with r_m = 20 mm, r_b = 3.175 mm, α_e = 9.043°, H = 0.078×10^{-3} mm, L = 0.055×10^{-3} mm and a contact angle $\alpha = 60°$.

$$\Delta\vartheta r_m T_{\alpha_e} - r_s C_{\Delta\alpha} C_{\alpha_e} S_\alpha - r_s S_{\Delta\alpha} C_\alpha C_{\alpha_e} - l_1 S_{\alpha_e} + l_2 C_{\alpha_e} S_\alpha = 0 \tag{3.26c}$$

As for the screw shaft, solving the Eqns. 3.26 the intersection of N1 with the plane Π is found, shown in pink in Fig. 3.19 for three different contact angles equal to 30°, 45° and 60°. The extreme points, represented with electric blue dots, are those limit points where the contact angle α reaches the DCA_i. The shape of the γ curve on Π can be observed in Fig. 3.20 as $l_2 = f(l_1)$ together with the solutions for $\Delta\vartheta$ and $\Delta\alpha$.

A database of curvature radii with regard to the constructive parameters has been obtained as previously done and, through the Eureqa® software the following explicit fitting formula has been extracted:

$$\begin{aligned} r_{cn} = b_1 - r_b - \sigma_2 \tan^2(\alpha_e) \arcsin\left(b_3 + b_4 \alpha r_m + L\sqrt{\sigma_2}\right) + \\ - b_5 r_m (1 + \tan^2(\alpha_e)) - b_4 r_m \sigma_2 \alpha \\ \text{with} \qquad \sigma_2 = (b_2 \alpha)^{b_2 \alpha} \end{aligned} \tag{3.27}$$

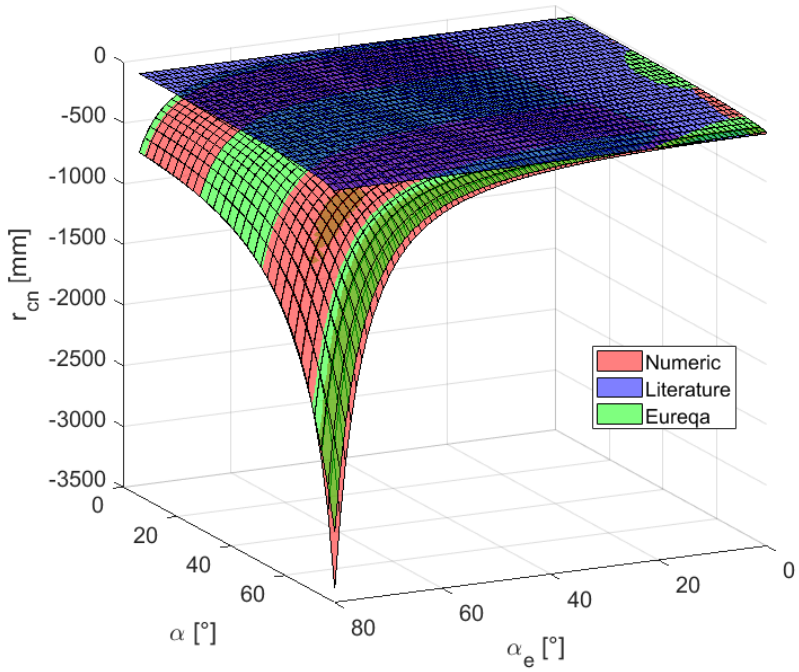

(a) Curvature radius 3D comparison.

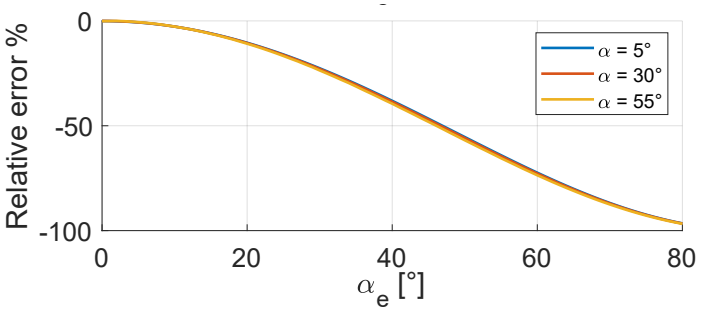

(b) Relative error % between the literature formula and the numerical solution.

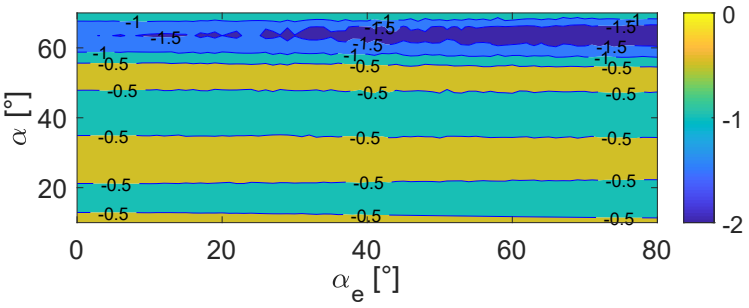

(c) Relative error % between the proposed formula and the numerical solution.

Fig. 3.21 Nut curvature radius comparison varying α and α_e for a nut with r_m = 20 mm, r_b = 3.175 mm, H = 0.078×10^{-3} mm and L = 0.055×10^{-3} mm

Table 3.4 Values of the parameters of Eq. 3.27.

Parameter	Value
b_1	-2.479$\times 10^{-5}$
b_2	2.860$\times 10^{-2}$
b_3	1.124$\times 10^{-4}$
b_4	6.937 $\times 10^{-3}$
b_5	9.695 $\times 10^{-1}$

where r_{cs}, r_m, r_b and L are in [m], α_e in [rad] and α in [deg]. The values of the parameters $b_1 \dots b_5$ are listed in Tab. 3.4. A comparison between the results of this formula and those of the literature formula [84]

$$r_{cn,ISO} = -\frac{r_m + r_b \cos(\alpha)}{\cos(\alpha)} \tag{3.28}$$

is shown in Fig. 3.21 for a nut with $r_m = 20$ mm, $r_b = 3.175$ mm, H = 0.078×10^{-3} mm and L = 0.055×10^{-3} mm. Fig. 3.21a depicts a three–dimensional representation of the comparison of r_{cn} with regard to the helix and contact angles. Contrary to the curvature radius of the screw shaft grooves, which is positive, r_{cn} is negative since the curvature centre lies outside the body of the nut (Fig. 3.19). The magnitude of r_{cn} increases with higher helix and contact angles and the higher the helix angle the greater the increase ratio with regard to to the contact angle. It can be noted from Fig. 3.21c that the proposed fitting formula (Eq. 3.27) presents a relative error contained within approximately 1% except for peaks <2% for $\alpha > 60°$. On the contrary, ignoring the helix effect, Eq. 3.28 presents a relative error almost entirely dependent on the helix angle α_e, as for the screw shaft in Fig. 3.18b.

3.5.6 Summary

In this chapter the BS mechanism has been introduced and its main features and characteristics have been presented. The BS geometry has been mathematically described and new formulae to calculate the curvature radii of the screw and nut raceways have been proposed to obtain more accurate results with respect to the commonly adopted literature formula which ignores the helix angle and the groove profile gothicity.

Chapter 4

Ball screw state of art

4.1 Introduction

The BS mechanism has been identified as one of the major contributor to the jamming risk of an EMA and therefore it has been selected as the topic of the current research.

This chapter presents a review of the state of the art in the field of BS investigation including the major contributions from the first articles in 1963 until the most recent in 2020. Most of the models analyse the BS from a static or quasi static point of view and, from the best of the author's knowledge, very few detailed dynamic model have been presented in literature so far.

4.2 Internal experimental investigations

Due to the intrinsic complexity of investigation, experimental analyses of what happens within the BS component are very difficult. Only few researches have been published in which experiments have been carried out only in very simplified scenarios. Chen et al. [101] exploited a non contact measuring system using an optical projector to investigate the contact angles formed at the sphere/screw interface when a sphere is pressed on the screw shaft not considering it inside the nut body.

Barranger et al. [102] studied the 3D stress distribution in a casting epoxy resin model of a bearing using the scattered light photoelasticity in order to verify the experimental method before to move to the more complex geometry of a BS.

Unfortunately, the results did not match those obtained from the FEM analysis of the same specimen. Thus, in the following they studied the stress and displacement distribution on the spheres of a single nut gothic arch BS using a plane 2D section [103] . The results agreed well with those from the FEM model, finding that the distribution of load on the spheres is not uniform: the load borne by each sphere decreases with the distance from the point of application of the external force. Therefore most of the force are supported by the first row, which is the more loaded. This analysis does not consider the effect of the helix angle and the complex 3D interactions between the spheres and the grooves, and therefore it is not fully representative of the real contact conditions.

4.3 Kinematics and preload

Despite the BS mechanism has been used since the first years of the last century, its inherent complexity of investigation led the first theoretical investigations to be carried out only after several decades of usage, in 1963, with the first studies of Levit [96, 104] followed by Drozdov [105]. Since the mechanism kinematics is similar to that of ball bearings, extensively studied by Harris [106, 73, 74], they adapted the bearings formulation to the BS case assuming no slip conditions in the contact points.

In 1994 Lin et al. [97] demonstrated that the assumption of no slip condition between the spheres and the grooves of previous studies [96, 104, 105] was unreliable because slip always occurs at least in one contact point due to the helical path. Using the results of Harris and Lundberg [106, 74, 107] they inserted in their model the effect of elastic deformations to find the pattern of constant sliding lines in steady state condition.

Hu et al. [108] arrived to the same conclusion analysing the kinematics of the BS via the slide to roll ratio (SRR, see Chapter 6), finding that the compresence of pure rolling conditions in both contact points with the screw and the nut is impossible, except for the trivial case of zero angular speed.

Gnanamoorthy et al. [109, 110] found that the SRR is a crucial parameter for the useful life of contact components, since low SRRs imply low sliding speed and low wear and consequently a longer operative life.

In a companion paper, Lin et al. [95] applied the results of [97] and presented three methods to obtain the mechanical efficiency of a single nut not preloaded BS in order to ease the design process. They developed first a simple quasi static model, then a steady state model and an approximated closed–form solution. The spheres are always considered in contact with the grooves and the contact angles at the screw and nut interfaces are imposed to be equal. This assumption made necessary to hypothesize the presence of a second minor contact point with the nut in order to equilibrate the centrifugal force acting on the spheres. Being the solution of the steady state set of equations not straightforward and thus not suitable to be easily employed during the design phase, they simplified it finding a closed–form expression to calculate the mechanical efficiency. With this formula the optimal combinations of contact and helix angles to obtain the maximum efficiency were investigated and it was found that this condition can be reached with contact angles close to 45° (>40°) and helix angles <45°. The self braking capability and load capacity were studied as well, with the results that the latter increases with decreasing helix angles. Consequently, maintaining the maximum efficiency design condition, it is not possible to increase the load capacity with the helix angle, therefore the only possibility is to increase the screw nominal diameter.

Huang et al. [111] employed a medial axis transformation to find the contact stresses in the contact points and the contact angles, without considering the presence of friction and lubrication.

In 2003, Yoshida et al. [112] analysed the ball motion and the load distribution in a double nut BS with external recirculation and circular groove. The motion of the ball was based on the raceway control theory introduced by Jones [113]. The normal forces between sphere and grooves were calculated according to the Hertzian theory while the tangential friction forces were obtained integrating the lubricant shear stress within the Hertzian contact area. Oil lubrication was considered and the Eyring rheology model was adopted together with the Barus equation for the viscosity dependence on pressure (see Chapter 6). The contact angles with the screw and the nut grooves were modelled as load dependent, as in [74, 98]. They found that an increase of the screw speed causes an increase in the screw contact angle and a decrease in the nut contact angle since the centrifugal force makes the contact force with the nut to rise. The load distribution across the spheres can be flattened arranging the position of the recirculation tubes symmetrically with regard to the screw axis, compensating for the mass disequilibrium.

A major contribution to the theoretical analysis of the BS mechanism comes from Wei et al. [98], who enhanced the work of Lin et al. [97], proposing a flow chart to iteratively solve the set of equations to calculate the mechanical efficiency, taking into account friction, variable contact angles, gyroscopic effects, different normal forces at the nut and screw interfaces, elastic deformations and lubricant drag force. The developed approach required the assumption of the angular displacement and elastic deformations due to the external forces and did not consider the preload effect because a single nut BS was investigated. Similarly to Yoshida et al. [112], the friction forces were obtained by the integration of the shear stresses in the Hertzian contact footprint but no lubricant rheology model was employed, and, instead, the second Amontons' friction law was considered inserting two constant coefficients of friction, different for the screw and nut contact points. Although no lubrication model was used for the friction forces, a force applied in the ball's centre of mass was considered, correspondent to the drag force of a sphere moving inside a lubrication bath. The tendencies of the contact angles with the screw speed of [112] were confirmed and the difference between the two angles diminishes with the applied external load. A higher external force causes higher contact loads and, therefore, an increased gripping force of the spheres on the raceways, which results in decreasing SRRs. Also the gyroscopic angle is affected by both the speed and the external load, showing respectively a growing and reducing trend with respect to these two quantities. Despite the results obtained by Lin et al. [97], they found that the mechanical efficiency is strongly influenced by the helix angle.

Wei et al. [114] enhanced their model in [98] introducing a detailed description of the friction forces in presence of oil lubrication. The pressure distribution was approximated with the Hertzian dry paraboloids and the viscosity dependence on pressure was described with the Roelands equation (see Chapter 6). The analysis was carried out on a single nut double–cycled BS operating at low speed and preloaded with an offset in the pitch of the central thread of the nut. As in the previous paper, the contact angles were considered different for the screw and nut contact and dependent on the load. The mechanical efficiency results with and without lubrication were compared with experimental data. While their model predicted an efficiency drop when the external load approaches the preload value, the same behaviour was not markedly replicated by experimental data coming from a healthy BS. A more similar trend seemed to be present for worn BSs. They found that the external load should be greater than 2.8 times the preload value to operate with high efficiency, and that the

lubrication strongly contributes to the reduction of the frictional forces and therefore to the rise of the mechanical efficiency.

Wei and Lai [89] extended the research of [114] to single nut double–cycled BSs, preloaded with pitch offset on the nut and operating at high speed. As in the previous paper, the assumptions of equally loaded spheres holds. Gyroscopic effects, load dependent contact angles and elastic deformations were considered. It was assumed that each contact point has one pure rolling point and that the closer this point to the centre of the contact ellipse the less slip motion. They found that increasing the initial contact angle leads to a reduced slippage and frictional torque and, eventually, to the increase of the mechanical efficiency and an attenuated wear, as reported by Zhou et al. [115]. This consideration can be useful in case of high speeds or high loads, such as those created by inertial forces generated during high acceleration/deceleration phases. They experimentally verified the revolution speed of the spheres found in [98], using the ball passing frequency detected with an accelerometer placed close to the spheres inlet in the recirculation tube. The efficiency results of their model, obtained for high speed BSs, were instead compared with experimental data from another paper obtained testing the screw at very low speeds.

The kinematics of high speed BS was investigated also by Xu et al. [116], who developed a model to describe the slipping of the spheres in the contact areas, assuming each sphere always in contact in only one point with each groove and an equal distribution of the external force among the balls. Considering load dependent variable contact angles with the screw and the nut and gyroscopic effect they found that the slipping motion is caused by the combination of ball spin and orbital motion. Since the slipping causes negative effects, such as friction and wear increase, they found that it can be reduced increasing the contact and helix angle or decreasing the screw diameter.

Verl and Frey [82] analysed another way of preload, experimentally evaluating the actual preload generated with a thickness between the two nuts, as the screw speed varies. They found that the actual preload and the drag torque increase with the screw angular speed with respect to the static value, specially in high speed applications. The reason for the increase of pretension was attributed to the centrifugal force effects, which pushes the spheres towards the nut, creating additional elastic deformations. They developed a more comprehensive formula to calculate the equivalent load to be used for more accurate life estimation. A new prototype of BS with improved

characteristics was developed by the authors [117] for high demanding applications, with a passive overload mechanism which avoids the over preloading negative effects such as excessive friction, wear and heat generation.

The influence of the preload on the no–load drag torque was studied by Zhou et al. [118] both from a theoretical and experimental point of view. A quasi static formulation was formulated exploiting the kinematics analysis from [95], assuming the sliding speed, and therefore the friction forces, to be oriented only along the rolling direction tangent to the helix. Following the prescriptions of the ISO 3408-3 [119], the experimental test were conducted with low speed (<100 rpm) on a double nut preloaded BS in absence of external load. The developed test bench was studied to allow different preload forces to be imposed through the rotation of drums, which compress a set of disk springs. The separating force of the springs was measured by means of three equally circumferentially disposed load cells. They found that the classic commonly used formula, suggested by manufacturers [77, 78] overestimates the preload no–load drag torque because it does not consider the contact angle effect or the friction coefficient. Thus, a new formulation was proposed, which accounts for these parameters, and it was verified by experimental measures for different values of preload.

A third method of preload is described in [120] by Cuttino et al. who exploited oversized balls alternated with smaller balls as spacers. This solution involves four contact points for each ball. In such a way, the backlash is eliminated but the stresses on the contacts, the friction forces and frictional heating increase. They investigated the non–linearities of the feeding torque, without axial load, on a single nut gothic arch BS with such a preload.

A simplified bidimensional analysis on four point preload was carried out recently by Lin et al. [121]. Basing on rigid body assumption and Coulomb friction, they studied the rolling/sliding behaviour of the spheres when this preload method is applied. The conditions for which slip creates were examined and a slip indicative factor was formulated to describe the slipping conditions in the four contact points. The slip was found to occur only in the point with the smallest value of the parameter. A sensitivity analysis on the friction was carried out with respect to misalignments, manufacturing errors and external load, all factors contributing to the friction loss.

Cuttino and Dow [120] based their work on those of Mindlin [122] and Lubkin [123] and developed a theoretical approach to the contact of a sphere with grooves

with elliptic contact areas, to take into account the correlation between the torque on a sphere and its angular displacement. An analytical equation was constructed fitting the results of several finite element simulations. The results were employed in the investigation of the non–linear torque in a four point preloaded BS [124], which was found to be originated by the rolling friction between spheres and raceways. A map of torque with regard to screw angular displacement was obtained and verified experimentally.

4.4 Positioning accuracy and thermal errors

The results of Cuttino et al. [120, 124] can be exploited to improve the control of a BS drive system. BSs are wide spread in the manufacturing sector, in fact most of the feed axes include a BS drive positioning system. For this reason, several studies have been carried out to determine and study the micro and nano–positioning capabilities of BSs, together with innovative control strategies, since it is well known that BSs performance and duration depend on the design and control parameters [125, 126].

Mi et al. [127], basing on the Hertz's theory, investigated the influence of the preload on the static and dynamic stiffness of a preloaded double nut ball screw installed in the spindle nose drive system of a horizontal machining centre. Validating the results with FE analysis, they found that an increase in the preload can produce a growth of the natural frequencies but at the same time a decrement of dynamic stiffness, and then of the dynamic performance. The preload level should be selected accurately to guarantee the correct functionality and positioning precision of the machine.

Otsuka and Jiro [128] compared the characteristics of three lead screws: a double nut precision BS, a single nut rolled BS and a sliding screw. It was revealed that the BSs are more sensitive than the sliding screws and, therefore, more suitable for feed drive axes. In fact, sliding screws show a non–linear elastic behaviour within a range of few micrometres due to stick–slip.

Nakashima et al. [129] proposed to perform a macro–positioning of the nut rotating the screw and, subsequently, to obtain the micro–positioning through the elastic deformation of the balls due to preload variation, exploiting a piezoelectric crystal, which can also be useful to detect preload changes during normal operations.

Fukada et al. [130] experimentally demonstrated that the non–linear behaviour on nano–positioning is due both to the preloaded ball screw and the support bearings which mix in a complicate way. Conversely of previous studies, which had investigated the micro and nano–positioning behaviour analysing the relationship between the motor current and the final displacement of the nut [131], the acquired experimental data was fitted with a viscous–elastic–plastic equivalent model for deformation problems of solid materials with the goal to isolate the different element contributions to the total friction torque.

Another important aspect that should be considered when designing BS drive system for machining tools is the thermal effect. In fact, specially for long time operations, frictional effects heat the BS causing thermal deformations that can deteriorate the positioning accuracy and lessen the mechanism axial stiffness due to a thermal preload loss.

In order to reduce the thermal positioning error, Min et al. [132] developed a thermal FE model to investigate the temperature distribution in a BS feed drive system considering bearings, roller guides and the motor as heat sources. The frictional heat generated in the BS was considered to be equally transferred into the screw shaft and the nut and the heat sink property of the supports was taken into account. The convection parameters were estimated experimentally, conducting test at 2000 rpm in regime of forced convection. The temperature distribution was investigated using a contactless infrared thermometer reading the temperature in different points of the system every 10 minutes and studying the evolution of the temperature distribution in time.

A similar approach was followed by Kodera et al. [133] who experimentally investigated the temperature distribution with an optical system in order to estimate the thermal elongation and the positioning precision.

When a complex FE model is built, in order to obtain reasonably and meaningful results, it is paramount to choose the correct parameters and boundary conditions. With this aim, Maier et al. [134] conducted experimental tests on a single nut preloaded BS in absence of motion to extract such parameters and they formulated an equivalent conductance to be inserted into the FE model. The results of this model can then be inserted into the control scheme of the feed axis to compensate for the thermal positioning errors.

Ahn et al. [135] developed a robust state observer to evaluate in real time the temperature distribution of the BS system and the heat sources intensity starting from few punctual measures. This information were included into the control loop to avoid positioning thermal errors.

Using a lumped mass simple model, Kamalzadeh et al. [136] developed a robust control strategy to compensate for the thermal errors and to improve the insensibility of the double nut BS drive positioning system to thermal effects. This methodology was focused on the case of a BS drive without a linear direct position measuring system, when only the rotative encoder on the screw shaft is available. This method was able to compensate also for positioning errors due to variable external forces, guides friction increase and variations of the transported mass, being these detected as equivalent thermal errors.

Horejs [137] studied the preload and positioning accuracy evolution due to non steady heat sources in bearings. In fact, he developed a FE thermo–mechanical model of the feed axis and performed a closed loop FE analysis in time, linking the frictional heat produced in the bearings to the borne axial load. At each iteration the thermal deformation was calculated with the mechanical model and, therefore, the axial load on the bearings, and the relative generated heat flows, were obtained. Successively, these heat flows were used as input for the thermal model and so forth until a steady state condition was reached. The results were confirmed by experimentally measuring the temperature distribution on the BS and the elastic deformations of bearings under the thermal loads. The tests were performed at different screw speeds and the results showed that the major temperature increase in the BS was concentrated in the bearing location and on the screw shaft section on which the nut passed during the test.

The positioning accuracy is influenced, besides from the frictional behaviour for very short displacements and thermal errors, also from the elastic nature of the components, specially in case of high frequency motions in which the natural frequencies, and the corresponding vibration modes of the system, are excited. To capture this aspect, several researchers have modelled the screw with non–lumped formulations.

Vicente et al. [138] built an high–frequency dynamic model of a BS drive to investigate the first three natural frequencies and related mode shapes of the BS varying the transmission ratio of the kinematic chain and the carriage position. The

model was composed by both lumped and non–lumped parameters. They found that the transmission ratio is an important parameter to determine the torsional/axial coupling and the natural frequencies' variation.

Zaeh et al. [139] created a FE model of the entire BS drive to study the vibration spectrum, considering the nut as a rigid body. To improve the simulation performance, they applied modal order reduction techniques to the complete model. The spheres' mass and dynamics were ignored and the balls were represented as equivalent springs oriented according to the contact angles values, considered constant and equal for the screw and nut interfaces. They considered the lateral dynamics, but their model was not able to capture the correlation between the lateral, torsional and axial dynamics.

Varanasi and Nayfeh [131] created a BS model with distributed inertia and reduced it through the Galerkin procedure to obtain a low–order model, in order to study the closed loop control system dynamics of a BS drive feed axis with the aim of compensating the dynamic elastic effect to improve the positioning accuracy.

Duan et al. [140] investigated the effect of the table stiffness on the positioning accuracy of a twin preloaded double nut BS drive feed axis. A FE model was built to study how the coupling effect of the table influenced the natural frequencies of the entire twin system. The model results were inserted into a simple lumped masses model to study the control implications of the joint stiffness.

Du et al. [141] analysed the effect of deformations at contact areas on the static and dynamic stiffness of a BS drive. The results indicated that the link between the deformation and the force in the contact points is not linear and depends on the contact angle and the material properties.

Brecher et al. [142] proposed a methodology to calculate the static stiffness of a double nut preloaded BS drive, adapting the calculating approach originally developed for spindle bearing systems. The shaft was approximated as a sequence of beams and the massless spheres were replaced with non–linear Hertzian springs. The resulting force–displacement curves matches with the experimental data validating the proposed approach.

Chen and Tang [143] studied the static stiffness of a double nut preloaded BS. The massless spheres were considered as non–linear springs according to the Hertzian theory, oriented on the basis of the load dependent contact angles, calculated as in [74, 98]. The results highlighted that the contact angle is a key factor in determining

the contact stiffness of the BS and that, even if a purely axial load is applied on the nut, the contact force distribution on the spheres is not uniform, due to the elastic deformation of the internal components: in fact, the first row of spheres bears most of the load while, from the fourth row on, the contribution of the spheres on the load capacity becomes very low.

4.5 Load distribution

The same conclusions of Chen and Tang [143] on the load distribution were reached in the study of Mei et al. [144], in which a reduced order of the BS was developed considering geometric errors on the spheres' dimensions. Only the axial flexibility of the screw shaft, the spheres and the nut body were considered. Hypothesising that the geometric error were concentrated in the spheres only and assuming a constant contact angle of 45° not influenced by geometric errors, the load on each sphere was analysed and a non uniform distribution was found in static conditions, with a decreasing trend from the first sphere towards the last one. The effect of spheres' geometric errors on the load distribution was investigated: positive geometric errors lead to higher loading and to the redistribution of the remaining load on the other spheres. Similar results were found also in [103].

Zhen et al. [145] performed a quasi–static analysis to estimate the fatigue life of a BS under low rotational speed and a mix of radial and axial load. No slipping between sphere and grooves were assumed and centrifugal and gyroscopic torques were neglected. The sphere revolution speed was calculated ignoring the helix angle, as if the system was a bearing. They used the static formulation of Mei et al. [144] to consider the load distribution on the spheres in non static conditions. They found that radial load causes a stronger inhomogeneity on the load distribution and that geometric errors, varying the load distribution, influence the operative life of the BS.

Mei's model [144] was further enhanced by Xu et al. [146] introducing the effect of variable load dependent contact angles and the helix angle, which plays an important role on the load distribution. In fact, they found that its uniformity decreases as the pitch angle increases, causing a less stable load distribution. Nevertheless, only axial deformability was considered and geometric errors were treated as axial dimensional errors. Therefore, the multi–directionality of the interaction of geometric errors, elastic deformations and contact forces was not present.

The monotonically decreasing load distribution with the sphere distance from the point of application of the external load found in [144, 146] was a consequence of having considered only the axial deformability of the BS. Okwudire [147] improved this analysis considering the lateral dynamics of the BS, coupling the axial, lateral and torsional flexibility of the screw shaft in static conditions. A Timoshenko beam–shape function was adopted to describe the screw shaft deformability, increasing in such a way the precision on the natural frequencies calculation, while the nut was regarded as rigid and the massless spheres as non–linear Hertzian springs. The model FRF was verified experimentally confirming the model validity and that the lateral dynamics cannot be ignored in the design of a high acceleration ball screw, because it influences the positioning precision.

In [148] Okwudire enhanced his model with an improved screw/nut interface formulation, considering also the portion of the screw shaft within the nut as a flexible element.

In [149] Okwudire used the previous article's results to investigate the torque induced bending vibrations of the BS. The results showed that the coupling effect between bending, torsional and axial dynamics depends upon the design of the nut body, and, in particular, on the entry and exit angles of the spheres into the recirculating elements. This consideration allows the vibrations to be minimised by design.

Even if a BS is typically subjected to only axial load and torque on the screw shaft, their combination produces an appreciable lateral bending deformation due to the helical geometry of the races. Lin et al. [150, 151] further improved the Okwudire's model [149] investigating how this lateral deformation influences the static load distribution in a preloaded BS with oversized spheres, even in presence of geometric errors. The screw shaft was represented as a FE beam and it was connected to the nut through a stiffness matrix with non–linear Hertzian elements. Contact angles were considered variable and dependent on the load. The results of the reduced order model agreed very well with those coming from a full FE model and highlighted a not uniform and not monotonically decreasing load distribution because of lateral bending, thought a purely axial load was applied.

These studies on the load distribution did not take into account the temperature effect, since in static condition it is supposed to remain constant. On the other hand, in dynamic conditions, it plays an important role in the load distribution,

according to the results presented by Oyanguren et al. [152, 153]. Similarly to [137], they developed a thermo–mechanical model but, instead of studying the BS thermal elongation effects on the load and frictional heat generation of the supporting bearings, they studied the effect of the thermally induced deformations on the load, stress and strain distributions and on the preload level. A 3D FE thermal model of a preloaded double nut BS with external recirculation channels was created with some simplifications to speed up the simulations, such as ignoring the screw shaft thread in the part of the screw shaft outside the nut, the local refinement of the mesh close to the contact points, or the representation of the spheres using Rolling Contact Springs (RoCS) elements. The deformability of the spheres was included in these non–linear springs. The heat flux within the BS was generated by the rolling element motion, in addition to the heat flux created by the supporting bearings. The radiation was neglected while convection parameters were increased by 15% to match experimental data and to take into account the turbulences generated by the non-ideal geometry of the nut assembly and of the screw thread. The equivalent friction coefficient was determined from experimental data using the motor torque signal. The test bench was composed by a double nut assembly with adjustable preload, which was measured by means of six load cells. The temperature distribution was acquired through a thermographic camera and several thermocouples. Two simulation strategies were compared: the not updated heat and the updated heat approaches. In the first one, the preload and stresses were calculated with the mechanical model starting from the temperature field obtained as input from the thermal simulation: a sequence of thermal simulations was carried out and the correspondent preload variation was observed. The second method implied the modification of the heat generated in the source points in the thermal model according to the loads obtained from the mechanical model. To diminish the computational cost, this update was performed every five iterations. The results demonstrated that this second methodology allowed to replicate the experimental outcomes more accurately. Both the theoretical and experimental investigation's results highlighted that, the preload rose a little in the running–in phase and then decreased even to 60% of the static value after 100 minutes as a consequence of the BS temperature rise of 28 °C. The initial preload increase was due to the initial different axial deformation of the screw shaft with regard to the nut. In steady state conditions, indeed, the radial deformation of the nut becomes prevalent and the preload decreases. It was shown also that, being the first rows of spheres more loaded, during the temperature transient these spheres are

subjected to a greater heating. This leads to a local deformation which more evenly redistributes the load across the various rows of spheres. Therefore, assuming a static distribution of the load [144, 151] for dynamic operative conditions, specially if extended in time, is not a valid assumption.

4.6 Preload monitoring

Several investigations have been carried out on the health monitoring of BS drive systems [154–156], specially on the preload monitoring since it is an important factor in determining the axial stiffness and positioning accuracy.

Li et al. [157], considering a purely experimental data–driven method, proposed a systematic methodology to detect the loss of preload and demonstrated that BSs are components on which it is possible to apply prognostic and health monitoring techniques. Comparing sensor–less and sensor–rich strategies, they stated that the features based on the torque signal can be successfully used for fault diagnosis and incipient failure identification but they are not sufficient and not robust to assess the residual useful life. On the contrary, vibration based features, such as those extracted in [158, 159], are more suited to predict the remaining life but they are less sensitive to the instantaneous fault inceptions detection. As a result, if sensors are available, a combination of both types of signals would be a good solution.

Feng et al. [160, 161] developed a cost–effective tiny sensing system embedded into the nut body, composed by a MEMS accelerometer and a SMD Pt-100 temperature sensor. With a data–driven approach, they successfully tried to detect the different preload values from the power spectrum density of the vibrations and from the temperature rise.

Nguyen et al. [162, 83] proposed a preload monitoring technique based on the natural frequency evaluation of a double nut preloaded BS. The axial stiffness of the BS drive can be calculated as the combination of the bearings, screw shaft and nut stiffnesses [84]. Within a normal range of preload, the axial stiffness of the nut can be related to the preload level. The stiffness of the screw shaft depends on the nut position. Therefore, on the basis of a simplified lumped mass model with four state variables, namely the motor and BS rotations and the table and BS linear displacements, a map between the preload and the first natural frequency was

obtained. A methodology to monitor the preload on line during normal operations was developed: when the machine is subjected to transients, due for example to accelerations/decelerations or variable loads, the algorithm automatically detects the transient and acquires the correspondent nut's position and acceleration and the motor current and estimates the input/output FRF of the system. From the FRF, the frequency peak corresponding to the first natural frequency of the system and, ultimately, the preload level are identified. The experiments demonstrated the effectiveness of such an approach.

4.7 Wear

Wear is a natural phenomenon that happen naturally with the mechanism's ageing. Nevertheless, several factors can accelerate this process, such as excessive speed, excessive preload values, overloads [163], entrance of contaminants or moisture, insufficient or inadequate lubrication and so forth.

Brecher et al. [164] studied, from an experimental point of view, the influence of oil additives on the wear and preload lessening of a double nut preloaded BSs. In absence of axial load, they obtained the no–load drag torque measuring the anti–rotation constraint torque by means of strain gauged flexible beams. A comparison between the results of prolonged wear test on two BSs with and without additives in the lubricants was performed. The preload was evaluated measuring the no–load drag torque and the axial rigidity of the system. They arrived to the conclusion that additives help in preserving the BS limiting the wear of the internal components and guaranteeing a minor preload loss.

A theoretical approach to the wear of BS was introduced by Wei et al. [165], who performed a topographic evaluation of the surface of the BS raceways and the spheres. The obtained data were employed in a micro–contact asperity model, in which the ellipticity ratio of the asperities' contacts was assumed in order to take into account the contact directionality with respect to the surface grinding direction. The quasi-static analysis was carried out under the assumptions of equally loaded spheres and dry contact conditions. The wear was evaluated through an accuracy degradation parameter, representing the axial displacement "loss" due to wear. The surface of the sphere was considered smooth since its roughness was very much lower than that of the grooves. Considering the single asperities as ellipsoids, the

elastic–plastic Hertz theory was applied at the asperity level, while the total contact assumed a probabilistic form, in which the asperities heights were described through a Gaussian probability distribution. They considered each asperity loaded with the same force of the entire macroscopic contact but, actually, each asperity acts as a spring, bearing only part of the total load. The total wear depended on the plastic deformation of the asperities according to a modified Archard theory. The total wear depth was assumed as the wear rate multiplied by the acceleration/deceleration time. The model was validated only in nominal condition analysing only the driving torque. No wear test were carried out to validate the degradation model.

Experimental data of prolonged wear test on a not preloaded BS were obtained by Zhou et al. [115], who proposed also a quasi-static theoretical model. They defined the precision loss rate as the ratio between the total worn volume and the total contact area, while the wear depth was defined as the precision loss rate multiplied by the sliding time. They assumed as major wear area a rectangle with dimensions equal to twice the minor semi–axis of the contact ellipse and to the length of the helical path followed by the spheres. The experimental tests lasted more than 1000 hours, with a complete disassemble and reassemble of the mechanism every 157 hours to mount the BS in a precision measurement system. In the first tens of hours the precision increased due to the running-in process but, successively, a monotonically decreasing trend was shown. According to [89], they found that the precision loss rate increases with greater helix angles and lower contact angles.

Zhao et al. [166] applied the Mei's theory [144] of static load distribution in not static conditions, performing a kinematic wear analysis. The results showed that the wear rate, calculated according to the Archard formula, increases with the operative speed and the load and diminishes with higher contact angles and lower helix angles, in accordance with [89, 115]. Their results were related to the slipping speed but not to the operative condition of the screw under investigation. It resulted that the wear rate increases with the raceways radius and decreases with the ball radius.

Another quasi-static wear degradation model was proposed by Cheng et al. [167] for a circular groove profile BS, neglecting the rolling friction. Adopting the kinematic results from [98, 114] and exploiting the wear model of [115], the theoretical results were compared with the experimental data. Several test were performed for 100 hours with sinusoidal load and fixed speed or vice versa. They found, as already known, that the wear increases with the load and the speed, but, at

low speed and load values, the load has more influence on the wear characteristic while, at high speed and loads, the speed effect prevails.

A complex wear model, based on multi–scale contact mechanics, was established by Liu et al. [168]. The surfaces were characterised by a microtopography and represented mathematically with the fractal geometry theory. The spheres were considered equally loaded and a major wear area was assumed as in [115]. The Hertzian contact parameters were derived by a multi–scale model which determined the elastic–plastic deformations of the single asperities: the highest ones are those subjected to the highest load and which undergo plastic deformations, which is the condition in which there is the highest amount of wear [115]. The experimental test bench was made up of two BSs moving the same table (dual–drive BS drive), where one of the BS was driven by the motor and the other was braked. The wear condition was examined measuring the loss of positioning precision through a laser interferometer. Although the model did not consider the lubrication, and the test rig BSs were lubricated with grease, the theoretical wear time evolution matched the experimental data. An unstable wear behaviour with an increase in the wear rate was observed at the end of the test, after 750 hours.

4.8 Friction

The friction of the BS system has been studied by several authors in order to understand which factors are more influential on this phenomenon or with the aim of construct simple expressions which can be used as reference in the design phase. If a detailed BS friction description is available, it can be used to optimise the design parameters in order to minimise the drag torque and maximise the efficiency.

Olaru et al. [169, 170] developed a friction model of a single nut not preloaded BS and evaluated the mechanical efficiency in quasi-static conditions. Rolling friction, moments due to the groove curvature and to the elastic resistance of the material, sliding friction, spin friction, hydrodynamic rolling forces due to Poiseuille flow and pressure flow of the lubricant were taken into account in the forces and moments equilibrium equations. The contact force between adjacent spheres was considered but as a constant imposed a priori. The contact angles were assumed to be constant and equal for the screw and nut interfaces. The friction coefficient was considered a function of the relative roughness parameter, depending on the lubricant

film thickness, calculated according to the Hamrock–Dowson equation (see Chapter 6). This model clearly shows the contributions of the single actions concurring in the total friction torque, but, unfortunately, no experimental validation were performed for the case of BSs.

Xu et al. [171] analysed the friction of a single nut BS using the creep analysis, taken from the linear theory of Kalker [172–174]. For little creep rates the Kalker's theory was used, while the classic Coulomb friction was used for the case of complete slipping. The load distribution was considered similar to that obtained by Mei [144], but, in this case, it was assumed a priori basing on an empirical formula coming from previous experience of the authors, instead of deriving it from a quasi static equilibrium. The model was verified for what concerns the friction torque with regard to the preload, by means of doubtful experiments without specifying the operative conditions ,such as external load and screw speed. Furthermore, the Kalker theory was born to describe the train wheel–rail interaction and it was developed for dry conditions, whilst the authors compared it with the results coming from lubricated BSs. The results highlighted that, ignoring the spin friction of the spheres, which creates forces perpendiculat to the helical path, would lead to erroneous value of the drag torque and, consequently, of the mechanical efficiency.

Recently, a complete quasi-static analysis and modelling of the friction torque of a double nut not preloaded BS with external recirculation tubes were performed by Oh et al. [175]. Assuming all the spheres evenly loaded, a thermal independent friction coefficient and neglecting the contacts between successive spheres, the model of the friction torque was built: it was composed by different components depending on the preload, the external force and the viscous effect of the lubricant. The rolling friction coefficient was assumed to be dependent on the screw and the load, comprising the hysteresis and sliding friction. The lubricant contribution was dependent on the viscosity, which was obtained by the Vogel–Cameron viscosity–temperature equation and by the Roelands equation for the dependence of the viscosity on the pressure. The contact angles were imposed equal and load independent. The model outcomes were verified by test data coming from an extensive experimental campaign, in which the temperature of the nut was always maintained equal to 40°C with a dedicated heating system or cooling pauses. The drag torque was measured with an instrumented anti–rotation constraint on the nut and the preload could be adjusted compressing a set of disc springs and directly reading the preload value from a toroidal load cell. Another load cell allowed to measure the external load applied by an hydraulic

cylinder. The friction torque generated by the support bearings was calculated with the formulae in literature and directly subtracted from the readings. The acquired signals demonstrated that high preload levels causes high friction torque but smoother operations. On the opposite, if the external load becomes greater than 2.83 times the preload value [90] the operations are not smooth anymore, but always with high friction levels. They found that an increase in the friction torque is caused by a decrease in the balls' diameter or by an increase of the helix angle and the pitch circle diameter, since grater diameters and helix angles imply a larger number of spheres and, therefore, more friction contributions.

4.9 Recirculation impact

The recirculating element is typical of BSs and it is a key component of the mechanism, since it allows the spheres to travel in a closed loop path. A failure of this component would cause a jamming of the entire BS. The most stressed part is the "tongue" of the deflector, which is subjected to high frequency bending fatigue under the action of impact forces, originated by the rolling spheres. In order to not excessively stress the deflector, manufacturers indicate a limit for the parameter $d_{nom}N$, which is an indicator of the impact energy of the spheres on the recirculating element.

Braccesi et al. [176] proposed an elastic–plastic model to analyse the impacts of the spheres with the deflector. The elastic–plastic stress limit of the deflector material was described through an equivalent Hertzian stress value, accounting for the maximum tolerable plastic deformation. As a result, a yielding velocity was defined as a parameter to be used in the design phase to compare different materials with regard to the operative conditions.

A similar analysis was carried out by Hung et al. [92], who investigated the condition for which a fracture of the deflector can occur. Using the same impact formula of [176], the theoretical impact force was calculated. Comparing it with that obtained from a short time transient FE model, it appeared that the latter, considering the wave propagation and the material dynamics, indicated an impact force greater than the theoretical value, which underestimates the real force extent. Furthermore, the FE results highlighted that the location of fault inceptions with the highest

stress levels is the recirculating tongue roots. Thus, to avoid fatigue rupture, design precautions were suggested.

The results of [176] were exploited in the analysis of Zhao et al. [163] who investigated the axial positioning precision loss as a result of a mixture of wear and, specially, overloads. In fact, the latter would cause permanent plastic deformations which affects the precision. Experimental investigations confirmed their model showing that the precision loss of the BS increases with the axial overload magnitude.

4.10 Dynamic models

From the best of the author's knowledge, very few dynamic models have been proposed in literature.

In the light of the criticality of the recirculation part discussed in the previous section, Jiang et al. [177, 178] proposed to replace the rigid joint between the recirculating deflector and the nut body with an elastic connection, in order to limit the impact forces. A multibody dynamic model was created in the MSC ADAMS environment to study the speed of the spheres within the recirculating channel and, consequently, the impact frequency with the recirculating channel was obtained. However, though the interesting multibody approach, the unspecified boundary conditions of the model and the unrealistic simulating conditions made the results doubtful and unreliable.

A very computational intensive model was presented by Liu et al. [179], who studied the effect of the environmental temperature on the drag torque generated by the preload. They created a FE dynamic model in which the lubricant forces and moments were inserted exploiting the formulations proposed by Olaru et al. [169, 170]. Experimental measures for different temperatures and speeds and, only for low rotational speed values, there was an agreement with the FE model's results, which showed a decrease of the drag torque with increasing temperature and decreasing speed. As pointed out in [152, 153], the temperature rise causes the dilatation of the elements, the decrease of the lubricant viscosity, and, therefore, the consequent lessening of the friction torque, at the expense of a greater wear. Due to the high computational cost of such an approach, the simulations were executed for very short time periods, making this approach not so suitable for PHM purposes.

4.11 Summary

This chapter presented, under different points of view, the major contributions to the understanding of the internal behaviour of the BS mechanism presented in literature so far. Hitherto, most of the articles have presented quasi-static or steady state analyses or directly static considerations. Such models calculate the mechanical efficiency without taking into account the inertia of different components. This kind of approach is not capable to describe the transients under arbitrary position commands and load conditions. More complex and complete models have been created to describe the interaction between the axial, torsional and lateral dynamics or to better understand the effect of the screw compliance on the static load distribution. The dynamic models are used to perform modal analyses. Recently, further dynamic models have been developed, which, however, require a very high computational cost or are not capable to describe the behaviour of single components. Preload loss diagnosis methods and thermally induced positioning errors have been investigated.

In the following chapters, the evolution of the high–fidelity dynamic model of a double nut single–cycled preloaded BS developed in this thesis work will be presented. It permits to obtain a better physical understanding of the BS mechanism and to study the system behaviour under normal and abnormal dynamic conditions. This model put the basis for a model–based PHM approach on this components.

Chapter 5

Ball screw dynamic model

5.1 Introduction

In order to develop a prognostic and health monitoring system, one method is to build a mathematical high–fidelity model of the component to understand the system dynamics and to discover a connection between the onset and growth of faults and measurable signals variations. This model must be as much representative as possible of the real behaviour and it must be able to reproduce the principal dynamics involved in the system and in the faults progression into a failures to be employed as virtual test bench. Artificial known defects can be then injected in order to investigate the variations in the output signals.

The first version of the non–linear high–fidelity model of a single–cycle double nut preloaded BS is presented in this chapter [56]. The model is physics based, thus the motion of each component is described by its d'Alambert differential dynamic equilibrium equation, so that the inertial actions are taken into account. It can represent the transition between roll and slip contact behaviour in the spheres/grooves contact points depending on the dynamic conditions. Rolling and sliding friction, preload and external axial force are considered and their effect on the direct mechanical efficiency is evaluated. Normal and tangential forces are calculated by means of a double elasto–backlash model. A sensitivity analysis is performed on the mechanical efficiency under different conditions varying the external force, preload, backlash and friction coefficient.

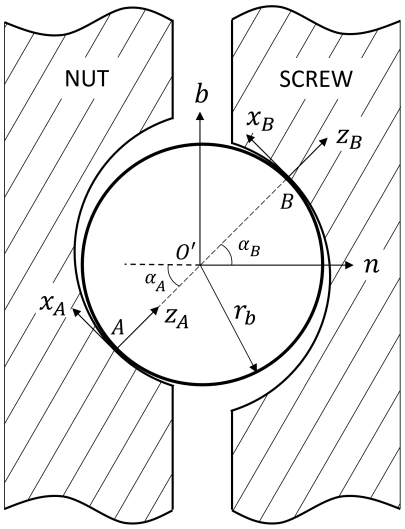

Fig. 5.1 Reference systems on the sphere [56].

5.2 Model description

In addition to the reference systems illustrated in Sec. 3.5.2, two CSs are introduced in the contact points A and B respectively with the nut and the screw shaft. These CSs are centred in the contact points, with the $\widehat{\mathbf{z}}_i$ axis ($i = A, B$) normal to the contact plane and the $\widehat{\mathbf{y}}_i$ axis parallel to the $\widehat{\mathbf{t}}$ axis, as depicted in Fig. 5.1. In A and B the helix angles are respectively:

$$\alpha'' = \arctan\left(\frac{p}{2\pi\left(r_m + r_b\cos\left(\alpha_A\right)\right)}\right) \tag{5.1}$$

$$\alpha' = \arctan\left(\frac{p}{2\pi\left(r_m - r_b\cos\left(\alpha_B\right)\right)}\right) \tag{5.2}$$

It has been assumed a BS system in which the screw shaft can only rotate and the nuts only translate. The preload is obtained inserting a spacer between the nuts, represented by means of a preload force F_{pr}. The contact angles have been assumed constant and both equal to 45°. The friction of supports is neglected to study only the BS performance.

The load is considered to be applied symmetrically with regard to the screw axis, therefore, neglecting geometric errors and the presence of radial forces, each sphere can be considered to bear the same load fraction. Interactions between

adjacent spheres are disregarded. Thus, only one sphere is analysed and dynamically described, considering it as representative of the behaviour of all the others.

The screw shaft rotational dynamic equilibrium equation around the $\widehat{\mathbf{z}}$ axis can be written as:

$$C_m - C_f - C_V - I_S\ddot{\Omega} = 0 \tag{5.3}$$

where C_m is the input torque from the motor, C_f is the friction torque, composed by the rolling friction torque C_{rf} and by the support friction torque, and C_V is the torque obtained from the sum of all reaction forces from the spheres on the screw groove. The latter can be expressed as:

$$C_V = Z\sum_j \left[F_{V,j} + H_{B,j}\cos(\alpha')\right]\left[r_m - r_b\cos(\alpha_B)\right] \tag{5.4}$$

where $H_{B,j}$ is the tangential friction force, along the $\widehat{\mathbf{t}}$ axis, from the spheres belonging to the j-th nut on the screw groove, while $F_{V,j}$ is the contact normal force projected in a direction tangent on the screw shaft and parallel to the $x-y$ plane. Z is the number of effectively loaded sphere, equal approximatively to [105, 180–182]:

$$Z = \lfloor 0.65\, Z_{tot} \rfloor = \left\lfloor 0.6\frac{2\pi r_m n_t}{2r_b\cos(\alpha_e)} \right\rfloor \tag{5.5}$$

A reduced number of spheres have been considered loaded with respect to the total number Z_{tot} because of the presence of the recirculation channel or due to possible geometric errors.

Figure 5.2 illustrates the forces applied on the two nuts. The external force is shown applied on the nut 1 flange, but in the model it is equally subdivided on the two nuts, since the preload is considered as a constant force, instead that as a spring and, therefore, it is not able to transfer the load from one nut to the other.

The total force $F_{Z,j}$ acting on each nut is the sum of all the axial component of the single contact forces of every sphere, represented in red along the helical groove in Fig. 5.2.

The dynamic equilibrium equation of each nut is:

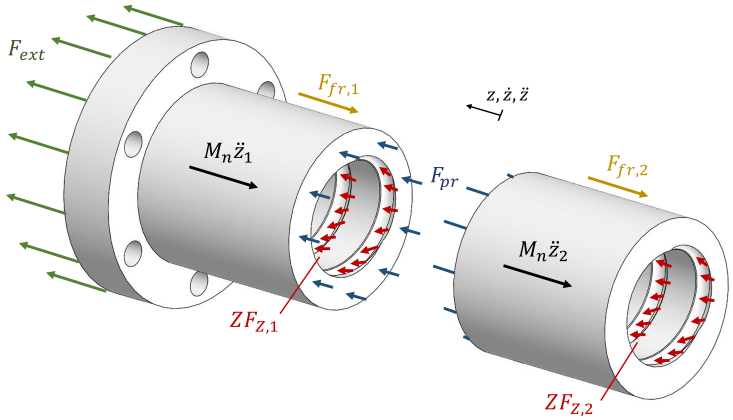

Fig. 5.2 Free body diagram of the nuts [56].

$$ZF_{Z,j} - F_{fr,j} + \frac{F_{ext}}{2} \pm F_{pr} - M_n\ddot{z}_j = 0 \tag{5.6}$$

where the preload sign is positive on the first nut ($j = 1$) and negative on the other ($j = 2$). The support friction on the nut and on the screw is calculated by means of an equivalent Coulomb–Stribeck–viscous friction model [183], but, as previously stated, in this analysis they have been neglected, considering frictionless constraints. Then, the friction force $F_{fr,j}$ expression reduces to:

$$F_{fr,j} = H_{A,j} Z \sin(\alpha'') \tag{5.7}$$

where $H_{A,j}$ is the sum of the components of the tangential force in the contacts between all the spheres and the nut groove along the $\widehat{\mathbf{t}}$ axis.

Referring to Fig. 5.1, only the translational dynamics along the $\widehat{\mathbf{y}}_i$ and $\widehat{\mathbf{z}}_i$ axes and the rotational dynamics around the $\widehat{\mathbf{x}}_i$ axis have been considered. This means that the motion of the sphere has been assumed bidimensional on the rectified cylindrical surface of the screw, along the rectified helical path. Gyroscopic effects and other dynamics have been ignored.

As illustrated in Fig. 5.3, the normal contacts have been represented with spring–damper systems. The rotational motion of the screw sahft, imposed by the motor, is converted in an equivalent motion of the contact point B along the $\widehat{\mathbf{z}}_i$ axis. Each sphere and nut motion is translated into the equivalent motion along the same axis. The resulting BS model presents nine degrees of freedom: the rotation of the screw,

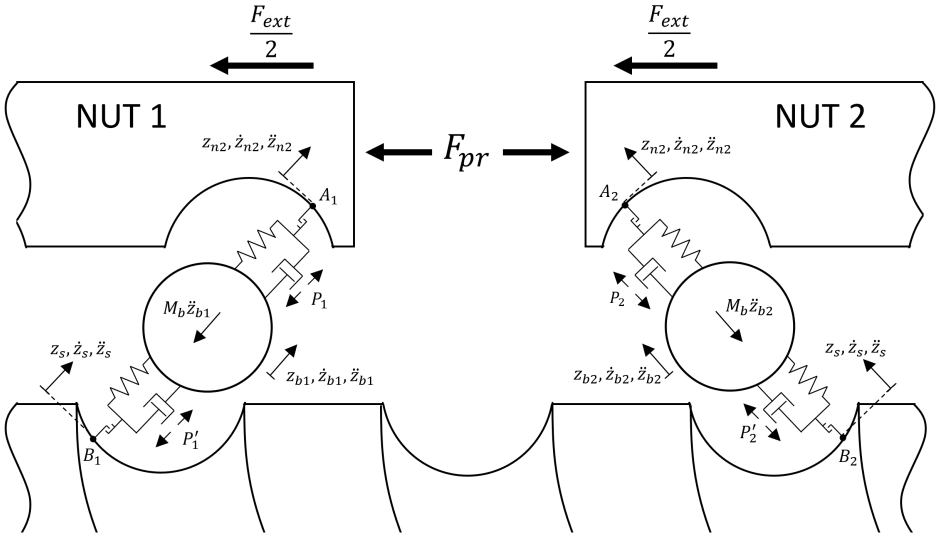

Fig. 5.3 Contact models between spheres, screw and nut. F_{ext} and F_{pr} are parallel to the $\widehat{\mathbf{z}}$ axis [56].

the two translations and one rotation of the two spheres (one for each nut), and the translation of the two nuts. The linear motion of the sphere along the $\widehat{\mathbf{z}}_i$ direction can be obtained by solving the following dynamic equilibrium equation:

$$M_b\ddot{z}_{b,j} + P'_j - P_j = 0 \tag{5.8}$$

The contact forces P'_j and P_j of the sphere respectively with the screw and nut grooves are obtained from the compression of the spring–damper systems along this axis, which is the contact line, connecting the two contact points A and B and the sphere centre. Along $\widehat{\mathbf{z}}_i$ the spheres can have intermittent contact since a double elasto–backlash model has been inserted, according to [181, 182, 184, 185]. The contact forces can then be written as follow:

$$\begin{aligned} P'_j &= \left\{ k\Delta z_{bs,j} + \mathfrak{f}\left[c(\dot{z}_{b,j} - \dot{z}_s), k\Delta z_{bs,j} \right] \right\} \left| H_{c,j} \right| \\ \Delta z_{bs,j} &= (z_{b,j} - z_s) - H_{c,j} \frac{b_{max_z}}{4} \end{aligned} \tag{5.9}$$

$$\begin{aligned} P_j &= \left\{ k\Delta z_{nb,j} + \mathfrak{f}\left[c(\dot{z}_{n,j} - \dot{z}_{b,j}), k\Delta z_{nb,j} \right] \right\} \left| H_{c,j} \right| \\ \Delta z_{nb,j} &= (z_{n,j} - z_{b,j}) - H_{c,j} \frac{b_{max_z}}{4} \end{aligned} \tag{5.10}$$

Since the contact angles are fixed, when the motion is reversed the spring–damper systems undergo tractive forces: therefore, when the contact forces are negative, they must be interpreted as if the contact angles instantaneously have changed from 45° to -45°. To avoid peaks and discontinuities in the contact force due to non null impact velocities at the beginning of the contact event, the function $\mathfrak{f}$ has been introduced together with the coefficient $H_{c,j}$. When the contact force is positive, i.e. when the contact angle is 45°, then $\mathfrak{f} = \min(\cdot)$ and $H_{c,j} = 1$, otherwise $\mathfrak{f} = \max(\cdot)$ and $H_{c,j} = -1$. If the backlash is considered, the situation in which no contacts are actives can be represented with $H_{c,j} = 0$ when $|\Delta z_{nb,j}| < b_{max}/4$, where b_{max_z} is the component along $\widehat{\mathbf{z}}_i$ of the total axial backlash of the BS. Obviously, when the backlash gap is open no force is transmitted.

The equivalent motion z_s of the contact point B, considered belonging to the screw, along $\widehat{\mathbf{z}}_i$ is written as:

$$z_s = -\frac{p}{2\pi}\Omega\cos(\alpha')\sin(\alpha_B) \tag{5.11}$$

while the equivalent motion of the nuts $z_{n,j}$ is linked to their axial translation z_j through the following expression:

$$z_{n,j} = z_j\cos(\alpha'')\sin(\alpha_A) \tag{5.12}$$

From the solution of Eqns. 5.9 and 5.10, the reaction forces of the spheres on the grooves $F_{V,j}$ and $F_{Z,j}$ of Eqns. 5.4 – 5.6 can be obtained as:

$$F_{V,j} = P'_j\sin(\alpha')\sin(\alpha_B) \tag{5.13}$$

$$F_{Z,j} = -P_j\cos(\alpha'')\sin(\alpha_A) \tag{5.14}$$

The rolling motion of the sphere occurs in the $y_i - z_i$ plane, on which it can be assimilated to a sphere rolling between two planes with friction: the plane representing the nut groove is stationary since the nut does not rotate and because the coordinate system y_b used to determine the displacement of the sphere is fixed with the nut [181, 182]. In both contact points there can be either rolling or sliding depending on the operating conditions.

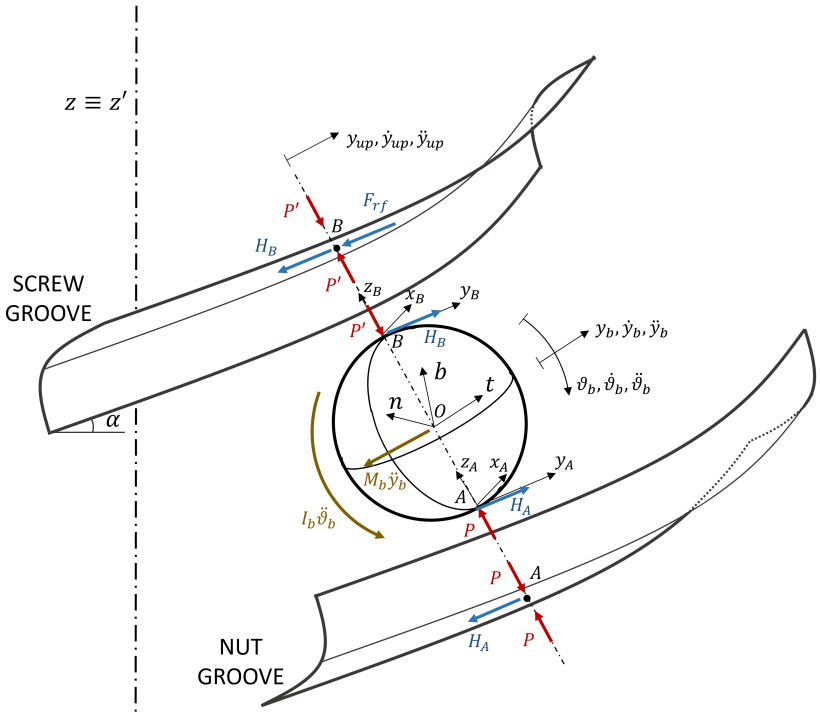

Fig. 5.4 Sphere's free body diagram [56].

Also the rotation of the sphere is governed by the screw motion: the displacement y_{up} (Fig. 5.4) of the screw groove contact point B along the tangential direction $\widehat{\mathbf{t}}$ can be derived from the solution of Eq. 5.3:

$$y_{up} = \frac{p\Omega}{2\pi \sin(\alpha')} \tag{5.15}$$

Simple rotational and translational dynamic equilibrium equations on the $y_i - z_i$ plane can be derived from Fig. 5.4 to calculate the displacement y_b along $\widehat{\mathbf{t}}$ and the angular rotation ϑ_b around $\widehat{\mathbf{x}}_i$.

The tangential friction forces H_A and H_B are obtained from a continuous differentiable formulation proposed by Makkar et al. [186] and already employed in [181, 182, 56]. It expresses the sliding friction coefficient as a function of the relative sliding speed v_{rel}, namely:

$$\mu_{A,B} = g_1 \left[\tanh\left(g_w v_{rel_{A,B}}\right) - \tanh\left(g_3 v_{rel_{A,B}}\right) \right] + \\ + g_4 \tanh\left(g_5 v_{rel_{A,B}}\right) + g_6 v_{rel_{A,B}} \tag{5.16}$$

where $g_1 \dots g_6$ are numerical parameters to adjust the shape of the curve.

The equivalent effect of rolling friction has been represented as an additional tangential force on the screw, F_{rf}, along $\widehat{\mathbf{y}}_i$, which, projected on the $x-y$ plane, creates the component C_{rf} of the friction torque C_f of Eq. 5.3. Adapting the formulation in [187], it can be expressed as:

$$C_{rf} = F_{rf} Z \cos(\alpha')[r_m - r_b \cos(\alpha_B)] \tag{5.17}$$

$$F_{rf} = \sum_j \left(P_j f_{v,j} + P'_j f'_{v,j}\right) \tag{5.18}$$

$$f_{v,j} = f_{v0,j} + f_{v1} \dot{\vartheta}^2_{b,j} \tag{5.19}$$

$$f_{v0,j} = \frac{P_j^{0.26} k_{gc}}{r_b} k_{rf} \tag{5.20}$$

$$f'_{v,j} = f'_{v0,j} + f_{v1} \dot{\vartheta}^2_{b,j} \tag{5.21}$$

$$f'_{v0,j} = \frac{{P'_j}^{0.26} k_{gc}}{r_b} k_{rf} \tag{5.22}$$

The rolling friction u depends on the contact load and on the sphere angular speed, therefore, combining Eqns. 5.18 – 5.22 its value can be written as:

$$u_j = k_{gc} k_{rf} P_j^{0.26} + f_{v1} r_b \dot{\vartheta}^2_{b,j} \tag{5.23}$$

$$u'_j = k_{gc} k_{rf} {P'_j}^{0.26} + f_{v1} r_b \dot{\vartheta}^2_{b,j} \tag{5.24}$$

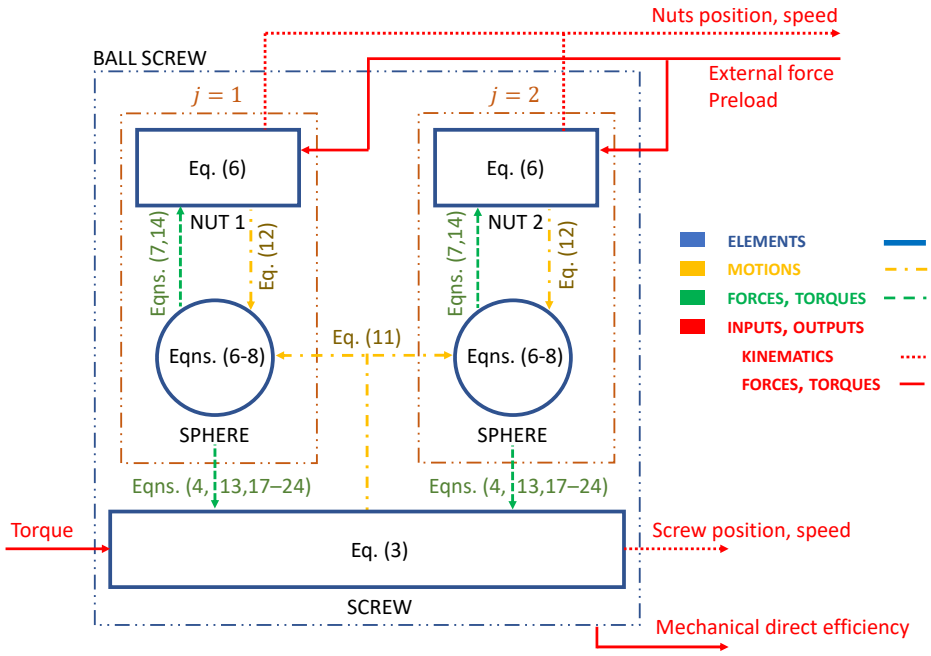

Fig. 5.5 Graphical model implementation [56].

where k_{gc} and f_{v1} are the load and speed dependence coefficients. k_{rf} is a parameter used in the sensitivity analysis to vary the friction effect. For low loads, u is scarcely dependent on the load and the relationship $u \propto P^{0.2}$ is typically used, while for higher load the Gerstener–Coriolis expression $u \propto \sqrt[3]{P}$ is applicable [187]. In this thesis, an average exponent has been selected, equal to 0.26. Because of the local kinetic energy dissipations due to micro–impacts of the material of the sphere when it enters into the contact area, the rolling friction depends on the angular rolling speed $\dot{\vartheta}_b$ squared.

Ultimately, the direct mechanical efficiency has been calculated excluding the inertial effects in order to evaluate it also in dynamic conditions and transients:

$$\eta = \frac{[F_{ext} + M_n(\ddot{z}_1 + \ddot{z}_2)]\dot{z}}{(C_m - I_s\ddot{\Omega})\dot{\Omega}} \tag{5.25}$$

Figure 5.5 shows a graphical implementation of the model: the inputs are the torque on the screw shaft, the preload and the external force, while the outputs are the kinematic quantities of the screw shaft and the nuts. These outputs can be useful if this model is embedded in a more complex model of a general system, e.g. an EMA complete model.

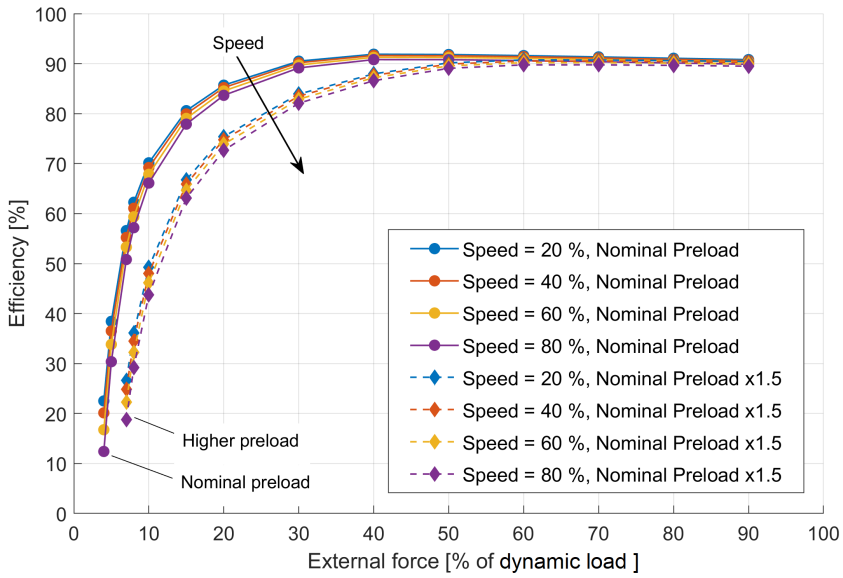

Fig. 5.6 Sensitivity analysis on the mechanical direct efficiency with regard to the external force, screw speed and preload, with $k_{rf} = 1$ [56].

5.3 Mechanical efficiency sensitivity analysis

Sensitivity analyses on the mechanical efficiency have been performed varying the speed, external force, preload, coefficient of friction and backlash with respect to the assumed nominal conditions, summarised in Tab. 5.1. Under the hypotheses of constant contact angles, in previous studies [181, 182] it has been seen that the backlash does not influence the mechanical efficiency in steady state conditions. The nominal external force has been assumed equal to half the BS dynamic load, i.e. 21.72 kN and, consequently, the nominal preload has been assumed, according to the ISO 3408-4:2006 [84], equal to:

$$F_{pr,nom} = \frac{F_{ext,nom}}{2^{3/2}} = \frac{0.5C_a}{2^{3/2}} \tag{5.26}$$

The rotational speed has been varied in the range $0 \div \dot{\Omega}_{cr}$, where $\dot{\Omega}_{cr}$ is the critical speed for transverse vibration, defined as the speed at which the system reaches its first resonance frequency.

The influence of the external force on the direct mechanical efficiency is depicted in Fig. 5.6. For low external force values the mechanical efficiency drops to zero,

Table 5.1 Ball screw parameters.

	Symbol	**Value**	**Units**
Geometrical parameters			
Screw pitch circle radius	r_m	20	mm
Screw lead	p	20	mm
Ball radius	r_b	3.175	mm
Centre radius offset	H	0.2694	mm
Ogival offset	L	0.2694	mm
Screw and nut groove conformity factor	$f_{s,n}$	0.5611	
Screw shaft moment of inertia around $\widehat{\mathbf{z}}$ axis	I_s	980	$\mathrm{kg\,mm^2}$
Loaded turns number	n_t		
Nut mass	M_n	1.3	kg
Total number of spheres	Z_{tot}	63	
Nominal helix angle	α_e	9.043	deg
Nominal contact angle	α	45	deg
Screw, nut and ball elasticity modulus	$E_{s,n,b}$	210	GPa
Screw, nut and ball Poisson modulus	$\nu_{s,n,b}$	0,29	
Axial backlash	b_{max}	10	µm
Performance parameters			
Dynamic load	C_a	43.43	kN
Static load	C_0	95.7	kN
Axial stiffness	k_{ax}	1.27	kN/µm
Critical screw angular speed	$\dot{\Omega}_{cr}$	2400	rpm
Nominal conditions			
Backlash in nominal conditions	$b_{max,nom}$	0	µm
External nominal force	$F_{ext,nom}$	21.72	kN
Nominal preload	$F_{pr,nom}$	7.67	kN

while it increases with growing external force. It presents a peak beyond which the trend is linearly decreasing: this is due to the load dependence of the rolling friction.

Also the screw speed influences the efficiency because the rolling friction coefficient depends on the square of the sphere's angular speed, which is related to the screw speed by known kinematic relationships [98]. Furthermore, also the sliding speed between the sphere and the grooves increases with the screw angular speed, causing increased sliding friction forces.

Another important factor is the preload, which causes an offset in the load to which the sphere is subjected, under the same axial force. Therefore, while the output

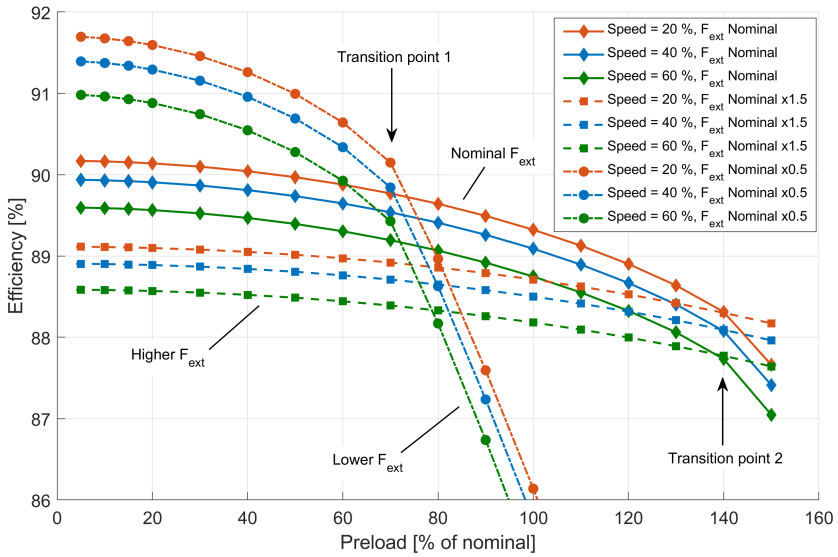

Fig. 5.7 Sensitivity analysis on the mechanical direct efficiency with regard to the preload, varying the screw speed, with $k_{rf} = 1$ [56].

power remains the same, the rolling and sliding friction forces increase, leading to a lower efficiency. The effect of the preload is depicted more in detail in Fig. 5.7. The efficiency has been evaluated varying the preload, for three values of the external force, to which correspond three families of curves in the figure. The external force determines the operative point on the load dependent rolling friction 0.26 power law. The preload variation moves this operative point around its initial value, along the rolling friction power law. Therefore, in the case of high external force, the operative point lays in the flat region of the 0.26 power curve, thus the variation of the preload from its nominal value causes little changes in the rolling friction resistance and the efficiency curve results more flat with regard to the preload values. Vice versa, for low external forces, the direct efficiency is higher for low preloads, but it drops quicker as the preload increases because the operating point lays in the slant part of the power curve.

Looking at Fig. 5.3 , when the preload value approaches $F_{ext}/2$, the spheres of the nut which has the preload force in the opposite direction with respect to the external force are almost unloaded. Hence, all the load is carried by only one nut. This point is indicated in Fig. 5.7 as “transition point”. Higher external force values causes the transition point to appear at higher preload values. For preload values greater than the transition point value, the decreasing trend is almost linear, due to

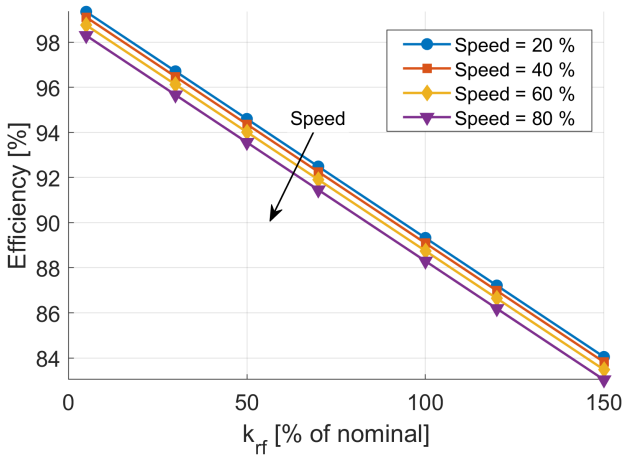

Fig. 5.8 Sensitivity analysis on the mechanical direct efficiency with regard to the friction parameter, varying the screw speed, with nominal preload and external force [56].

the fact that one nut is subjected to basically all the load and thus its operative point lays in the high load flat region of the rolling friction curve. Vice versa, the other nut has the sphere basically unloaded.

Figure 5.8 depicts the mechanical efficiency dependence on the k_{rf} coefficient of Eqns. 5.23 – 5.24, which is the parameter increasing the load dependent component of the rolling friction. The mechanical efficiency decreases linearly with this coefficient, which can be considered as representative of the performance degradation of the BS, such as wear of the grooves or lubricant ageing.

5.3.1 Combined parameter effect

In Fig. 5.9 the results of a multivariate sensitivity analysis are shown, in which three values of the screw speed (20%, 50% and 80% of $\dot{\Omega}_{cr}$) and of the preload (50%, 100% and 200% of $F_{pr,nom}$) have been considered. The external force and k_{rf} are varied continuously respectively in the ranges $0 \div C_a$ and $0.5 \div 2$.

Given a k_{rf} value, the locations of the maximum efficiency points with regard to the external force move to higher external force values for increasing preloads. The higher the k_{rf} coefficient, the more pronounced the peak of the mechanical efficiency. It can be noted that the peak takes place for an external force values approximatively $2^{3/2} = 2.83$ times greater than the considered preload, according to [84]. The slope

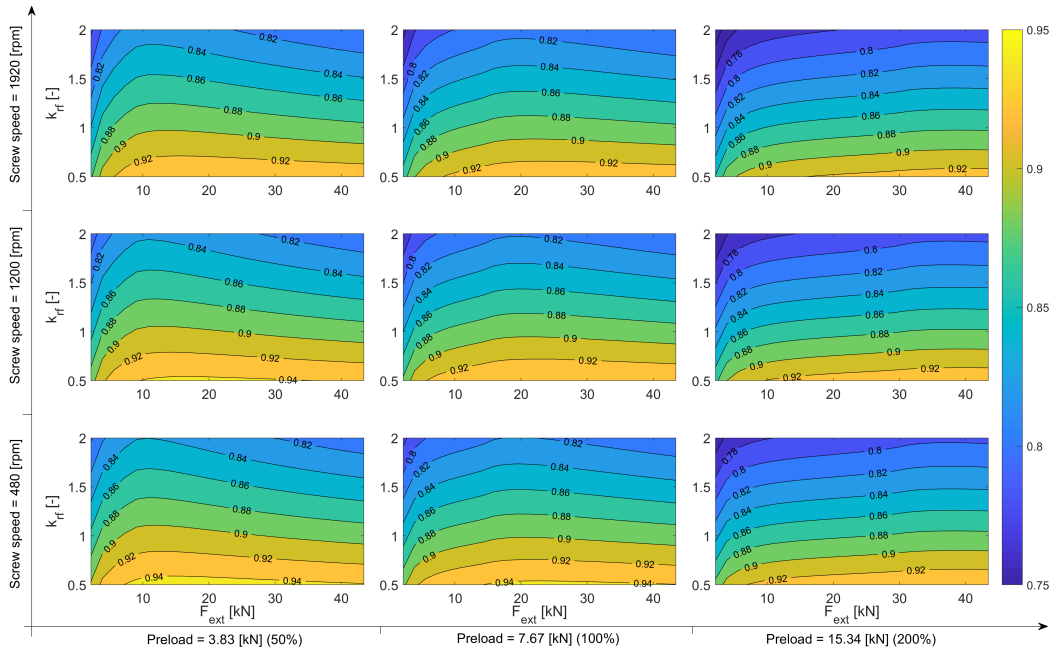

Fig. 5.9 Four-dimensional map of mechanical direct efficiency, with regard to the external force, the preload, the friction coefficient and the screw angular speed [56].

of the linear dependence of the efficiency on k_{rf} is higher for higher preload, while it is almost insensitive to the speed and the external force.

The mutual interaction of the external load and the preload on the mechanical efficiency is shown in Fig. 5.10, obtained for the case of $k_{rf} = 1$ and speed equal to 40% $\dot{\Omega}_{cr}$. For a given external force, the ISO standard [84] prescribes a preload value such that in nominal condition the mechanical efficiency is approximatively the maximum possible. If the external force varies, the mechanical efficiency decreases. Because of the assumptions of equally subdivided external force on the two nuts and constant preload force, it results that it is preferable to have external forces higher than the nominal one, since this would cause a minor efficiency reduction. The region below the straight line of Fig. 5.10 is a low efficiency area in which the efficiency can drop to very low values, and, thus, to be avoided.

For flight control EMAs, the BS component is usually designed to resist to the maximum possible external force, which can be very high, caused by random wind gusts during flight. However, during the majority of its life, the EMA is subjected to much lower loads, i.e. it works in the region below the red line with low efficiencies.

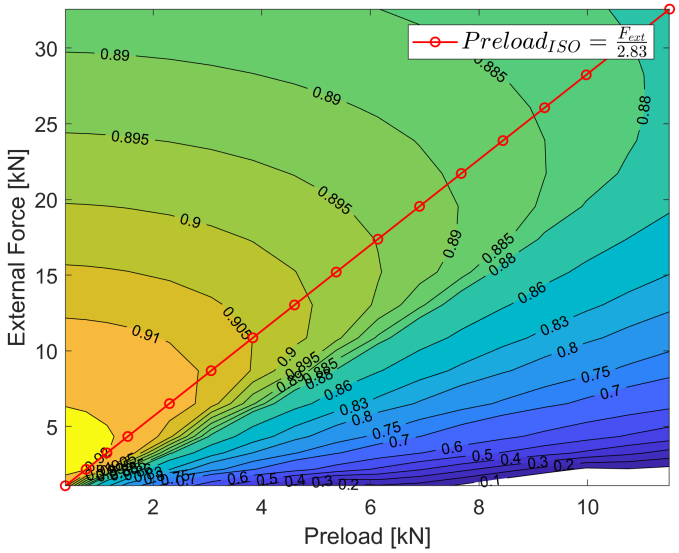

Fig. 5.10 Combined effect of external force and preload on the mechanical direct efficiency, with $k_{rf} = 1$ and $\dot{\Omega} = \dot{\Omega}_{cr}/2$ [56].

Nevertheless, a higher efficiency could be obtained diminishing the preload, varying the nominal working point.

During the life of a BS, due to wear, the preload usually lessens. Thus, according to Fig. 5.10, the efficiency slightly increases, under the same external force. Although in steady state condition this is favourable, a preload decrease would cause dynamic performances reduction, such as the decrease of dynamic stiffness, the insurgence of backlash and higher vibration levels.

From this analysis, it results evident how the mechanical efficiency cannot be used as a unique feature to assess the health status of the BS mechanism, since it depends on several factors and it can assume the same value with different combinations of the influential parameters.

5.4 Friction, backlash and centrifugal force

To highlight the effect of the backlash the BS has been inserted in a closed loop position control system and a sinusoidal position demand has been imposed in absence of preload and external force with different backlash sizes.

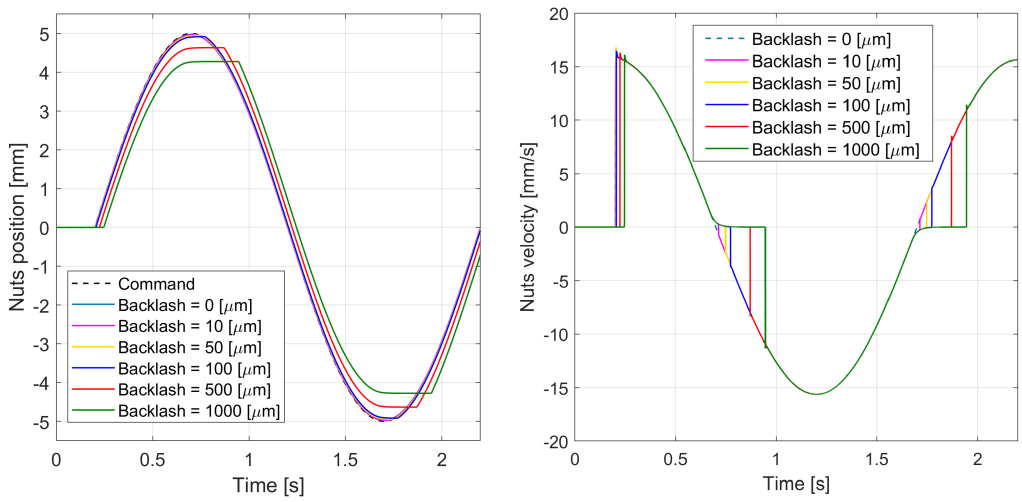

Fig. 5.11 Effect of friction and backlash on a sinusoidal nut displacement command, with no preload, no external force and $k_{rf} = 1$. On the left, the nuts displacement; on the right, the nuts velocity [56].

In Fig. 5.11 the equivalent linear position and speed of the screw shaft and of the nut are shown. It can be seen that the nut trajectory distances from the screw one as the backlash size increases. The friction effect can be seen in the speed inversion points: the nut detaches from the screw and stops earlier, remaining steady under the effect of friction until the backlash gap closes in the opposite direction. At this point, the contact forces rise again and the nut speed is brought back to the screw speed value. When the backlash gap opens the nuts speed drops to zero until the nuts engage again with the screw.

The backlash effect is better emphasized in Fig. 5.12, in which the nut position is plotted against the screw equivalent linear position, showing an hysteresis loops. The area of the loops is proportional to the backlash size. Plotting the nut position versus the screw position, instead of versus the position demand, allows to exclude from the area the effect of the friction and to evaluate only the backlash.

Depending on the preload and external force values, different conditions can arise on the spheres, as depicted in Fig. 5.13. The load direction is represented with a dashed line and the entity of the borne load is qualitatively indicated with SL (small load), NL (no load) or HL (high load). Figures 5.13a and 5.13b show the condition in which only the external force is applied, with no preload: both spheres bear the same load in the same direction. When also the preload is present, the load and

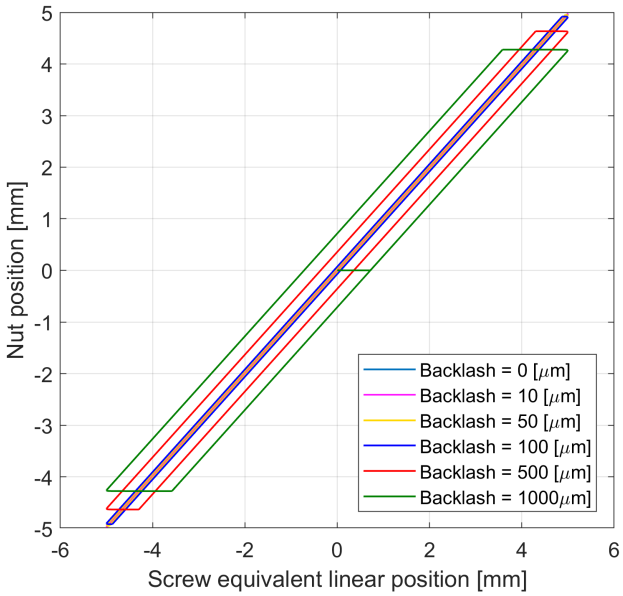

Fig. 5.12 Effect of friction and backlash on the hysteresis loop obtained by a sinusoidal nut displacement command, with no preload, no external force and $k_{rf} = 1$. On the left, the nuts displacement; on the right, the nuts velocity. [56].

direction of the force on each sphere depend on the ratio between the external force and the preload force. If $F_{pr} > F_{ext}/2$ the sphere of the nut 1 bear a high load since the preload and the external force sum up in the same direction, while they subtract on the other sphere, which results lightly loaded (Fig. 5.13c). Instead, if $F_{pr} < F_{ext}/2$ the contact condition of the left sphere remains unchanged, with more load, while the other sphere changes contact direction (Fig. 5.13e). Figure 5.13d depicts the situation with $F_{pr} \simeq F_{ext}/2$, in which only one sphere is heavily loaded while the other is almost unloaded. This is the condition described in Fig. 5.7 for the transition points in the direct efficiency curves. Finally, in Fig. 5.13f the case with preload and no external force is shown, in which both spheres support a small load symmetrically, due to the preload.

The same conditions described in Fig. 5.13 have been simulated and the results are shown in Fig. 5.14. The preload and external force have been applied with a sigmoid function in order to avoid numerical instabilities. The backlash size has been imposed to 0.01 mm and the external and preload forces to their nominal values. In each one of the subplots of Fig. 5.14 the difference between the nut and the screw shaft equivalent linear position is represented and it can be noted that it varies between –0.05 and +0.05 mm. Further discrepancies between the two positions

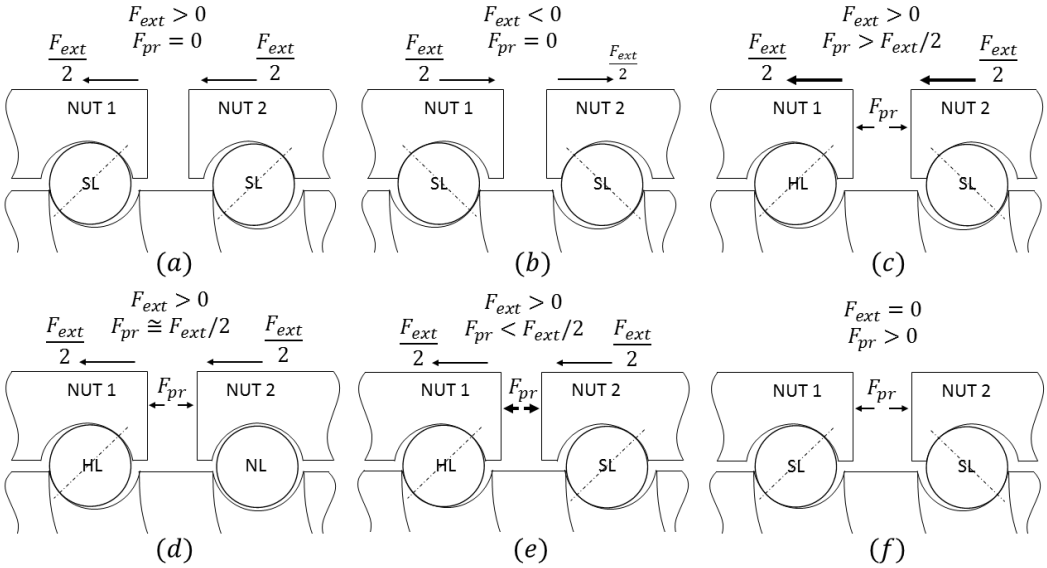

Fig. 5.13 Various loading conditions of the spheres of the two nuts in presence of backlash, depending on the external force and preload (SL: small load, NL: almost no load, HL: high load) [56].

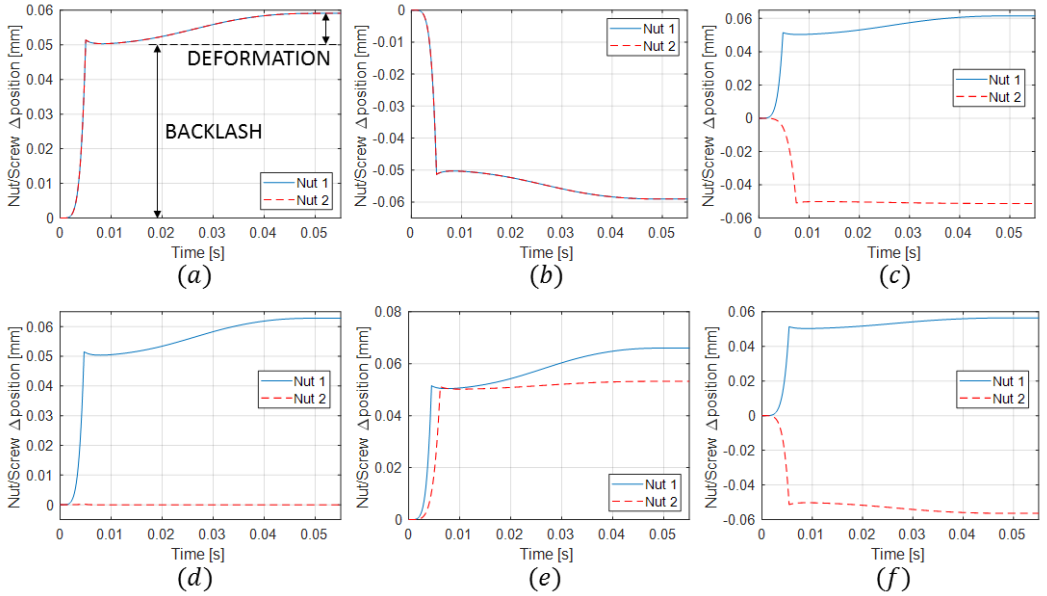

Fig. 5.14 Contact deformations calculated applying constant preload and external force according to loading condition of Fig. 5.13 , in presence of backlash [56].

are given by the elastic deformations in the sphere/groove interfaces, as shown in Fig. 5.14a. As explained above, in Fig. 5.14c the two sphere bear the load in opposite directions, thus the difference in the screw/nut positions assume values with opposite sign. In addition, since the sphere of the nut 2 is lightly loaded, its deformation is smaller than that to which is subjected the sphere of the nut 1. In Fig. 5.14e, the sphere of the nut 2 is almost unloaded, therefore the nut 2 does not move, being in equilibrium between all the acting forces. In every situation, the position difference reaches first suddenly ± 0.05mm, i.e. the backlash gaps closes, and then elastic deformations take place.

The model capability to take into account the backlash is important to be able to model more kinds of faults: the backlash increase can be representative of the grooves wear and it can produce vibrations of the mechanism. The backlash effect and observability depend on the preload, which can be varied as well to represent the preload lessening which can happen during the operative life of a ball screw [160, 188, 162].

5.5 Adherence and sliding in contact points

This model considers either sliding or rolling in both contact points of the spheres with the grooves. The two conditions can occur depending on the normal contact force and the relative sliding speed. The normal contact forces depend on the screw rotational speed. In fact the spheres, besides rolling around their centre, perform a orbital motion around the screw axis. Neglecting gyroscopic effects and imposing both contact angles equal to $\alpha_{A,B} = 45°$, the revolution speed can be estimated as [98]:

$$\omega_{rev} = \frac{1}{2}\dot{\Omega}\left[1 - \frac{r_b}{r_m}\cos(\alpha_{A,B})\right] \tag{5.27}$$

This motion creates a centrifugal force which pushes the spheres towards the nut groove, increasing the contact force in A and diminishing that in B.

Figure 5.15 shows the comparison between Eq. 5.27 and the model results with the sinusoidal position demand depicted in Fig. 5.16a. This command starts at 0.2 [s] and it is multiplied by a sigmoid function which varies from 0 to 1 in 0.8 [s]. The

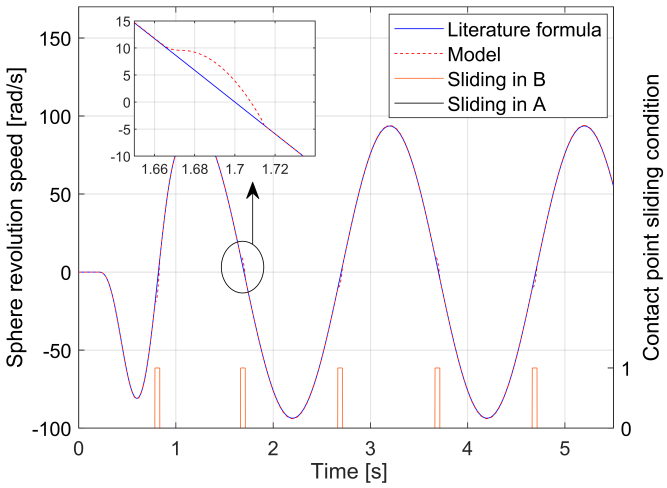

Fig. 5.15 Comparison between the revolution speed of one sphere obtained from the model with the result of the literature formula [56].

external force, preload and backlash are imposed to zero, therefore the contact forces derive only from the inertia effects. In Fig. 5.15 it can be noted that the theoretical and simulated revolution speeds matches very well, except for the instants in which the speed is inverted, highlighted with a boolean flag. In such conditions, as can be seen in Fig. 5.16d, the normal contact force crosses the zero value (which in this model means that the contact angle has changed sign). When this happens the contact pressure is not sufficient anymore to keep a sufficient tangential friction force such that to compensate the sphere inertia and to hinder the sphere to slip. Therefore, slipping occurs until the normal force rises again and the adherence condition is restored.

The slipping occurs in B since the screw is the driving component and since the centrifugal force tends to decrease the contact force in this contact (Fig. 5.16c). With the formulation of the tangential friction force of Eq. 5.16 there is always a little amount of slipping between the surfaces: therefore, if the sliding speed is less than the threshold sliding speed (corresponding to the peak of the friction coefficient), the bodies are considered in adherence and the slipping boolean flag is set to 0. The shape of this function, representing the static and dynamic friction and the Stribeck effect, is qualitatively depicted in Fig. 5.17. The transitions between slipping and adherence are reflected in the peaks of the transmitted tangential friction forces, shown in Fig. 5.16d.

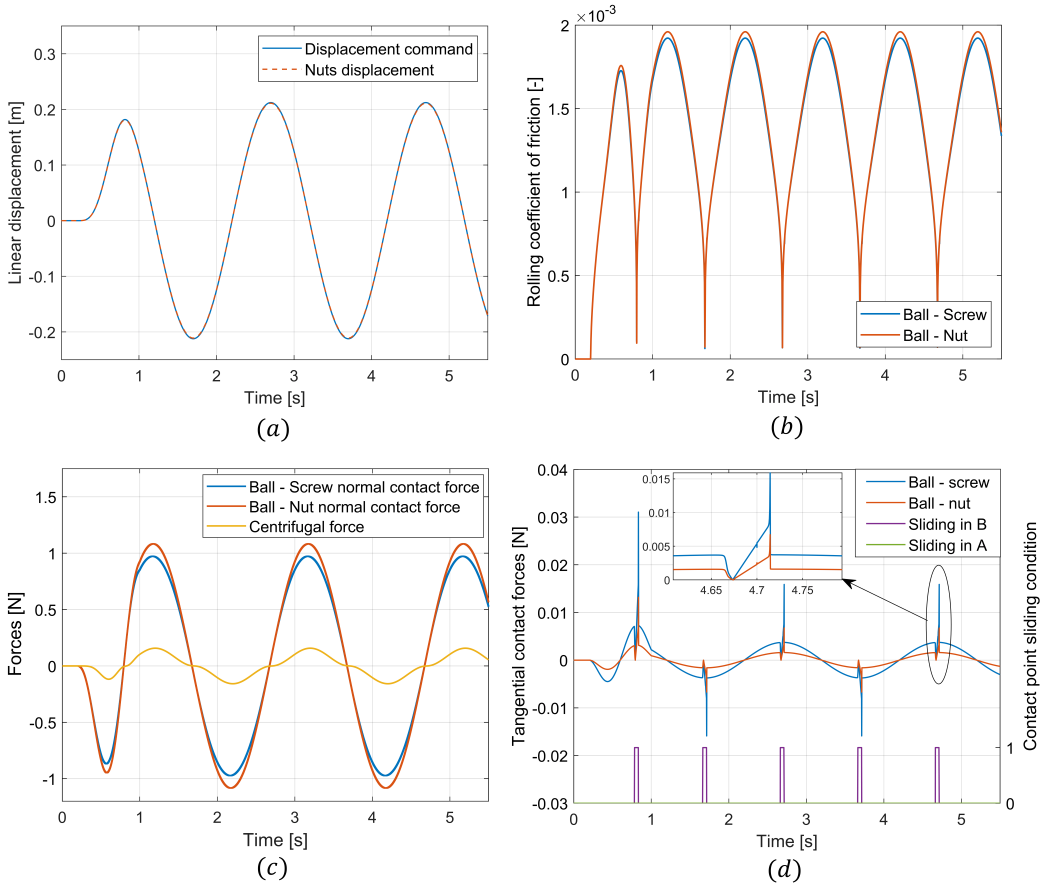

Fig. 5.16 Sinusoidal position command (a), rolling friction coefficient (b), centrifugal forces and contact normal forces (c) and tangential contact forces with Boolean indicator for sliding conditions (d), for nut 1 ($j = 1$) [56].

As for the normal forces, the difference between the tangential friction forces in A and B are due to the presence of the centrifugal force (Fig. 5.16c). Consequently, it influences also the rolling friction coefficients, shown in Fig. 5.16b, which is not constant but depends on the operative conditions. The sign convention for the centrifugal force is the same as for the contact forces: its sign is related to the screw speed sign, but physically it is always oriented along the $-\widehat{\mathbf{n}}$ axis.

Figure 5.17 shows the results of a simulation with the same inputs and conditions used in Fig. 5.16, with, in addition, a non null backlash of 0.05 mm. As in backlash–free conditions, under normal movement the sphere touches both grooves (point 1). However, when the speed inversion point is reached, the sphere and the nut detach from the screw groove and the contact forces drop to zero (point 2) because the contacts become inactive. Due to its inertia, the sphere continue to proceed along the

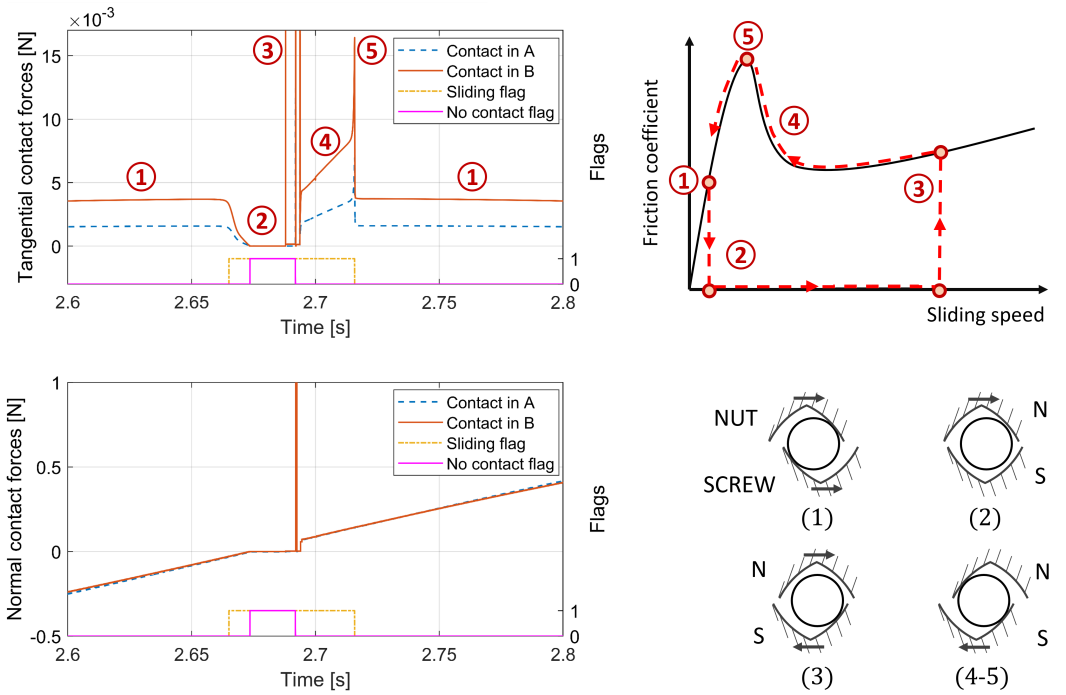

Fig. 5.17 Normal and tangential contact forces during a sphere sliding event at speed inversion point, in presence of backlash [56].

tangential direction and the relative speed increases. No tangential forces are applied on the sphere because of the inactive contacts. When the sphere contacts again with the other side of the groove, it starts to bounce a little between the grooves producing force peaks (point 3). When the grooves tighten, the sphere remains blocked between them and stops bouncing. At this point, the normal contact forces are still low but not null: the sphere starts to slide (point 4), progressively decreasing the relative speed, until it goes below the threshold velocity, passing across the static friction peak force (point 5) and returning in an adherence condition (point 1).

Finally, the effect of backlash and speed inversion on the mechanical efficiency is shown under dynamic conditions. The backlash size has been set to 10 [µm] and the preload to zero in order to highlight the backlash effect. A sinusoidal speed command with 200 [rad/s] amplitude and a frequency of 0.5 [Hz] has been given to the controller, while a sinusoidal external force has been imposed with an amplitude of 5 [kN] and a frequency of 1 [Hz]. Consequently, the torque applied on the screw by the motor shows the same frequency of the external force in order to compensate for it and to make the nut position following the command.

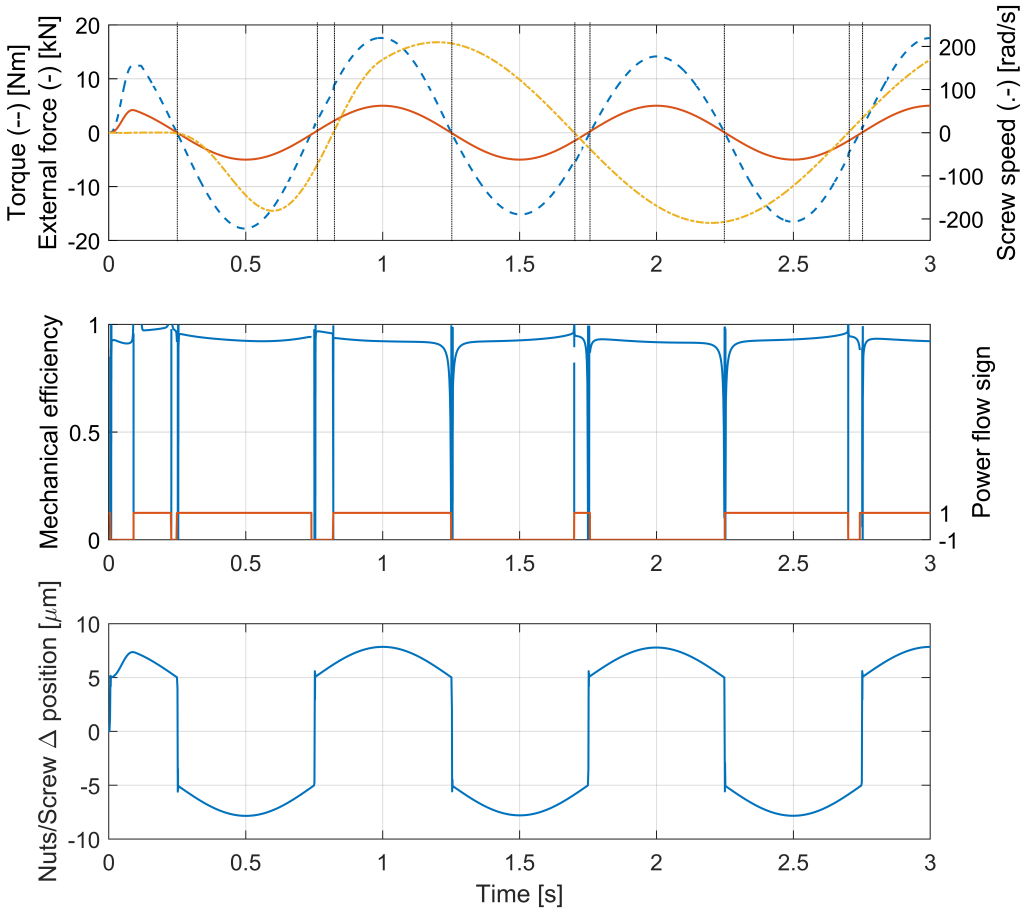

Fig. 5.18 Backlash and speed inversion effects on the mechanical efficiency in dynamics [56].

At each speed or force direction inversion instant, identified by the vertical dashed lines, the mechanical efficiency drops to zero. In these points, also the power flow changes its sign. When the motor is the driver component, it assumes a positive value, while when the motor brakes the action of the external force, it assumes a negative sign.

The external force inversion causes the sphere to change contact orientation, as can be seen from Fig. 5.18. Since backlash is present, for a short time the backlash gap opens and no force is transmitted, thus the mechanical efficiency drops. Moreover, the position difference between the nuts and the screw shows that as the

external force rises, the deformation in the contact areas increases, accordingly to the previous results.

5.6 Summary

A dynamic model of the rotary to linear conversion BS system has been presented in this chapter. The results of a sensitivity analysis on the mechanical efficiency, varying the screw speed, external force, preload and friction have been presented and it has been shown that preload and external force present a non–linear influence. Efficiency maps have been described to identify the efficiency with respect to the combination of nominal preload and external force.

This model introduces into a dynamic model aspects which generally were not considered in literature, such as the backlash hysteresis, friction trends, transients at speed inversions and double contact point sliding behaviour of the spheres in dynamics. Different operative conditions have been analysed, depending on the ratio between the external force and the preload. The effect of the centrifugal force on normal load and sliding/rolling friction forces has been investigated. The mechanical efficiency has been evaluated in dynamic conditions, in presence of backlash, time–variant speed and external force.

It has been found that the mechanical efficiency is not suitable to be used as unique health feature. Model improvements will be described in the next chapters.

The presented model needs to be validated with experimental data to be reliable, therefore a test bench has been designed and it is being currently constructed. Further details will be given in Chapter 9.

Chapter 6

Grease lubrication

6.1 Introduction

In BSs the sliding friction is replaced with rolling friction but, anyway, a little amount of slip always occurs, due to the elastic deformations of the bodies in the contact area and to the kinematics of the mechanism itself. If no lubricant was present, the slip would produce wear on the rolling surfaces and fatigue damage, shortening the life of the component. Lubrication is therefore used to provide a separation of the contacting bodies thanks to the hydrodynamic pressure generated in the lubricant film present at the interface between the two bodies, minimizing wear and friction.

Lubrication can be realised in different ways, including solid coatings, two-phase fluids, gases and so forth. In machine elements it is common to use either oil or grease. Although the oil has some advantages, such as the cooling effect and the transfer of the contaminants away from the contacts due to a continuous recirculation, usually, in components with rolling elements, grease is adopted. It presents a lower cooling effect and it is subjected to ageing, mainly due to oxidation and shearing, but it shows lower friction levels. Moreover, grease reservoirs are created on the sides of the track, replenishing the contact and fulfilling a sealing function forming a barrier against external contaminants entrance. Although the lubricant in the rolling tracks is pushed to the sides by the passage of the spheres, the contacts are constantly replenished by the side grease reservoirs, repairing the lubricant film and extending the component's life.

In general, grease is made up of a base oil in which a thickening agent is dispersed, usually in form of fibres. When this structure is sheared or squeezed, the base oil is released, and the contact lubricated. The grease experiences three main phases during the mechanism's life:

- *churning phase*: at the beginning of the component's life the grease has just been inserted and thus it is evenly distributed inside the component. During this phase it is subjected to a gross flowing pushed by the rolling elements and it accumulates on the groove shoulders, forming the reservoirs in the contact track sides. This phase is characterised by a temperature increase, a greater friction torque and a contact condition which is fully flooded. The lubricant film is composed by both base oil and thickener particles and the film thickness is greater than that expected in fully flooded conditions for base oil only lubrication. The churning phase usually takes up to 24 hours [86], depending on the "channelling" property of the grease and on its consistency [87]. After the churning phase the friction and the temperature decrease, and the normal operative conditions are reached. If the quantity of initially filled grease is excessive it does not find enough space to free the contact track and therefore the temperature and friction remain high, causing oxidation and breakdown of the grease and, eventually, a premature failure of the component. According to [86, 87, 74] approximatively 30% of the internal volume should be filled with lubricant.

- *bleeding phase*: during this phase the lubricant is continuously sheared in the contact and pushed to the sides of the track. Though, the grease reservoirs replenish the contact by bleeding base oil ensuring the presence of a thin film in the contact zones. Further oil replenishment is provided by the grease structure breakdown due to the high shear stresses within the contact, by centrifugal forces, capillary forces and surface tension. Fully flooded conditions occur only in the churning phase: in fact, during most of the life, the contact is starved. According to experimental measurements on rolling bearings [86], the lubricant film is formed by grease only in the very initial part of the mechanism life, while, during the bleeding phase phase and most of the component's life, it is composed by the base oil, fed by the side grease, mixed with some broken thickener fibres. Starvation mainly occurs due to side flow in front of the contact and from within the contact. At the starvation onset both

these contributions are important but, as starvation progresses, the quantity of available lubricant becomes smaller and the only contribution to oil loss remains the elasto–hydrodynamic lubrication (EHL, see Sec. 6.4) pressure induced side flow from the contact areas. The replenishment effect is less effective as the rotational speed increases since the time between successive over rollings becomes shorter. Thus, greases with high bleeding rate are more suitable for high speed applications.

- *severe starvation*: this is the ultimate phase of the component's life and it is characterised by the intermittent presence of a lubricant layer alternated with direct contact of the surfaces, which initiates failures. The grease reservoirs are consumed or the grease is severely oxidized and the replenishment flow is not sufficient anymore to compensate the loss flow. Where the lubricant film breaks down, wear takes place and the temperature rises locally contributing to the lubricant degradation. Usually, additives are present inside the grease to protect the surfaces from damage in case of film collapse. This phase should be avoided through scheduled re–lubrication.

Many concepts in this chapter come from rolling bearing applications but they can be applied to BSs as well since the rolling principle is the same. The basic properties of grease and base oil will be briefly introduced hereinafter. This chapter recalls the main concepts of thin film lubrication theory and introduces the formulations adopted in Chapter 7.

6.2 Lubricant rheology

Rheology is "the study of the deformation and flow of matter" [86] and, therefore, it is the description of the shear rate dependency of the viscosity. In lubrication, the flow properties of the lubricating media, oil or grease, is very important for the lubrication performance. In machine elements, such as rolling bearing and BSs, grease is generally employed: it should not flow, i.e. acting as a visco–elastic material, when it is subjected to low shear stress $\dot{\gamma}$, that is when it is attached to the seals or to the grooves' shoulders. It forms a lubricant reservoir which provides the needed lubrication to the contact areas and, at the same time, performs a sealing action avoiding the lubricant to leakage outside the mechanism: in this situation

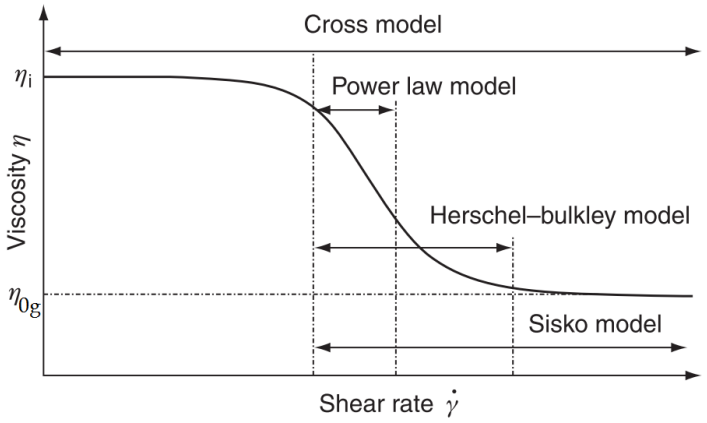

Fig. 6.1 Qualitative representation on a double logarithmic scale of the shear thinning effect of lubricating greases [86].

it is subjected to very low shear rates, in the order of 10^{-6} $[s^{-1}]$ [86]. Whereas, when the grease participates in the contact event, it is subjected to high shear rates (10^{6} $[s^{-1}]$) and it should flow to guarantee an optimal lubrication. This change in grease behaviour is called "shear thinning" and it is typical of greases, which show a strong decrement of the viscosity with increasing shear rates, as shown in Fig. 6.1. This effect can be due to the mutual alignment of the thickener fibres contained inside the grease. For very high shear rates the viscosity value reaches that of the base oil.

Several models are present in literature to describe the shear rate dependence of the grease viscosity (some of them listed in Tab. 6.1), but no model can accurately represent the behaviour on the entire range of shear rates. The most famous will be briefly introduced hereinafter.

For usual share rate values, the viscosity curve can be represented with a reasonably accuracy by means of the Cross model for pseudo–plastic flow [86]:

$$\eta = \frac{\eta_i - \eta_{0g}}{1 + (K\dot{\gamma})^m} + \eta_{0g} \tag{6.1}$$

where η_i and η_{0g} are the grease viscosities at very low and high shear rates. The latter is similar to the viscosity of the base oil η_0, and it can be calculated using the Batchelor's equation accounting for the thickener volume fraction φ [189–191]:

Table 6.1 Most famous rheological models for lubricating grease.

Model	Formulation
Herschel – Bulkley	$\tau = \tau_y + K\dot{\gamma}^n$
Bingham	$\tau = \tau_y + K\dot{\gamma}$
Casson	$\sqrt{\tau} = \sqrt{\tau_y} + \sqrt{K\dot{\gamma}}$
Czarny – Moes	$\sqrt[n]{\tau} = \sqrt[n]{\tau_y} + \sqrt[n]{K\dot{\gamma}}$
Power law (Ostwald – de Waele)	$\tau = K\dot{\gamma}^n$
Sisko	$\tau = K\dot{\gamma}^n + \eta_{0g}\dot{\gamma}$
Palacios	$\tau = \tau_y + K\dot{\gamma}^n + \eta_{0g}\dot{\gamma}$

$$\eta_{0g} = \eta_0(1 + 2.5\varphi + 6.2\varphi^2) \tag{6.2}$$

K and m are constants which depend on the grease, called respectively the consistency and flow index. For $\eta_i \gg \eta_0$ and for medium to high shear rates this model reduces to the Sisko model [86], expressed in terms of shear stress τ as:

$$\tau = K\dot{\gamma}^n + \eta_{0g}\dot{\gamma} \tag{6.3}$$

where $n < 1$ and, for lubricating grease, it can be considered $n \approx 0.5$.

Greases usually exhibit an apparent yield stress at very low shear rates: this behaviour is taken into account adding the term τ_y. Actually, the grease does not have a real yield stress but it flows anyway, but really slowly (creep flow). The majority of greases show a decrease of this value for increasing temperature [86]:

$$\tau_y = \tau_{y0} e^{\frac{T_0 - T}{b} \ln 2} \tag{6.4}$$

where τ_{y0} is the yield stress at temperature $T = T_0$ [°C] and b is a value in °C which determines the decrement rate. For extremely high and low temperatures the yield stress concept does not apply since the grease changes behaviour and becomes, respectively, completely fluid or very viscous.

Adding τ_y to Eq. 6.3, the Palacios and Palacios model is obtained [86]:

$$\tau = \tau_y + K\dot{\gamma}^n + \eta_{0g}\dot{\gamma} \tag{6.5}$$

A simplified version of the Sisko model (Eq. 6.3) can be used when the yield behaviour at low shear stress is not important for the application, obtaining the power law model:

$$\tau = K\dot{\gamma}^n \tag{6.6}$$

The most used model for grease rheology is the Herschel–Bulkley model [86]:

$$\tau = \tau_y + K\dot{\gamma}^n \tag{6.7}$$

This model is relatively simple and correlates well with experimental measurements [86], but it is not suitable for very high shear stress: in these cases Eq. 6.5 should be used, taking into account the base oil viscosity contribution.

Also the grease base oil experiments a viscosity reduction under extreme pressures and shear rates, such as in EHL contacts. The most widely used model for the lubricating oil shear thinning is the Eyring model [86]:

$$\tau = \tau_e \operatorname{arcsinh}\left(\frac{\eta\dot{\gamma}}{\tau_e}\right) \tag{6.8}$$

where η is the reference Newtonian viscosity in [Pas] of an equivalent Newtonian lubricant oil and τ_e is the so called Erying stress, defined as the reference shear stress in [Pa] at which the fluid first starts to behave nonlinearly when stress is plotted against shear strain rate [87, 192].

Several other models have been proposed in literature to describe the rheology of the base oil. Another often used model is the Gecim and Winer model [86]:

$$\tau = \eta\dot{\gamma}\tanh\left(\frac{\tau_L}{\eta\dot{\gamma}}\right) \tag{6.9}$$

where τ_L is the oil limiting shear stress, which strongly depends on pressure p:

$$\tau_L = \tau_{L0} + \xi p \tag{6.10}$$

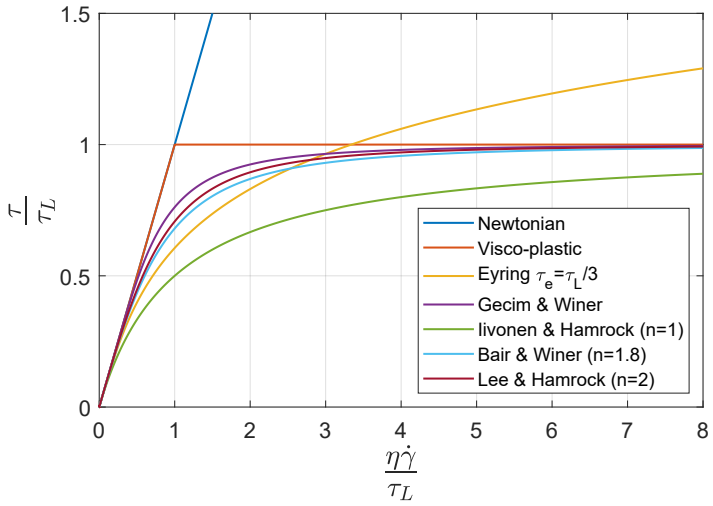

Fig. 6.2 Base oil rheological models non–dimensional comparison.

with ξ the limiting shear stress pressure proportionality constant, usually in the range $0.02 < \xi < 0.15$ according to [86], and τ_{L0} is the limiting shear stress at atmospheric pressure: it has been found experimentally to be in the order of $1 \div 5$ MPa [86]. The latter depends mainly on the contact pressure p but previous studies showed also a small dependence on temperature [193].

All these model have been generalized into the Elsharkawy and Hamrock model [86]:

$$\tau = \tau_L \left[1 + \left(\frac{\tau_L}{\eta \dot{\gamma}} \right)^n \right]^{-\frac{1}{n}} \tag{6.11}$$

where n is an exponent which gives the Lee and Hamrock circular models for $n = 2$, the Bair and Winer logarithmic model for $n = 1.8$ and the Iivonen and Hamrock linear model for $n = 1$. The comparison between these various models is depicted in Fig. 6.2. To compare the various models, it is usually assumed $\tau_L = 3\tau_e$ [86, 87, 192]. It can be seen that the Eyring model is not capable to represent the presence of the limit shear stress: in fact the shear stress increases monotonically with increasing strain rate and therefore it has been sometimes criticised by several authors in recent years. To overcome this issue it has been sometimes saturated to the limiting shear stress value, creating though a discontinuity in the model derivative [192]. The aforementioned models can be integrated into the widely accepted Maxwell model [194, 195]:

$$\dot{\gamma} = \frac{1}{G}\frac{d\tau}{dt} + F(\tau) \tag{6.12}$$

where G is the grease shear modulus, defined in Eq. 6.38. Expressing $F(\tau)$ with the generalized model of Eq. 6.11 leads to:

$$\dot{\gamma} = \frac{\dot{\tau}}{G} + \frac{\tau_L}{\eta}\left[\left(\frac{\tau}{\tau_L}\right)^{-n} - 1\right]^{-\frac{1}{n}} \tag{6.13}$$

or

$$\dot{\tau} = G\dot{\gamma} - \frac{G\tau_L}{\eta}\left[\left(\frac{\tau}{\tau_L}\right)^{-n} - 1\right]^{-\frac{1}{n}} \tag{6.14}$$

Shear thinning influences both the lubricant EHL film thickness and friction, due to the non–Newtonian behaviour of the lubricant. If the lubricant was a Newtonian fluid, the viscosity would be independent from the shear rate.

6.3 Base oil physical properties

The properties of the base oil depend strongly on pressure and temperature and, in the EHL contacts, the pressure can assume values in the order of $1 \div 3$ [GPa]. A commonly used equation for the viscosity is the Barus model [196]:

$$\eta(p,T) = \eta_0 e^{\alpha_{pv} p - \beta(T-T_0)} \tag{6.15}$$

where α_{pv} is the pressure–viscosity coefficient in [Pa^{-1}], p is the average Hertzian contact pressure expressed in [Pa] (see Sec. 7.3), T [K] the oil temperature in the contact and η_0 the base oil viscosity in [Pas] at atmospheric pressure and $T = T_0$ [K]. For lubricating oils $0 \leq \alpha_{pv} \leq 4 \times 10^{-8}$ [Pa^{-1}] and $0.001 \leq \eta_0 \leq 0.1$ [Pas]. Various formulae exist to calculate the α_{pv} value, such as the Wooster formula [87]:

$$\alpha_{pv} = (0.6 + 0.965 \log_{10}(\eta_0 \times 10^3)) \times 10^{-8} \tag{6.16}$$

The temperature–viscosity coefficient β [K^{-1}] can be calculated by the interpolation between two reference points $\eta_{T_{max}}$ and $\eta_{T_{min}}$ [86]:

$$\beta = \frac{-1}{T_{max} - T_{min}} \ln\left(\frac{\eta_{T_{max}}}{\eta_{T_{min}}}\right) \tag{6.17}$$

The Barus model, however, is accurate only for pressures up to 0.5 [GPa]. A more accurate relationship, which describes the viscosity variation with both pressure and temperature, is the Roelands model [86, 196, 197]:

$$\begin{gathered} \eta(p,T) = \eta_0 e^{\alpha^*_{pv} p} \\ \alpha^*_{pv} p = [\ln \eta_0 + 9.67] \left\{ \left(\frac{T-138}{T_0-138}\right)^{-S_0} \left(1 + \frac{p}{p_r}\right)^{Z} - 1 \right\} \end{gathered} \tag{6.18}$$

where α^*_{pv} is the Roelands equivalent pressure–viscosity coefficient and $p_r = 1.962 \times 10^{-8}$ [Pa] is a reference pressure. S_0 is the Roelands temperature–viscosity index, typically in the range $1 \leq S_0 \leq 1.5$ and Z is the Roelands pressure–viscosity index, typically in the range $0 \leq Z \leq 0.8$. S_0 and Z are constants, characteristic for a specific oil, and independent of temperature and pressure. The values of S_0 and Z can be calculated from α_{pv} and β of Eqns. 6.16 and 6.17 as:

$$Z = \frac{p_r \alpha_{pv}}{\left(\ln \frac{\eta_0}{\eta_{dim}} + 9.67\right)} \tag{6.19}$$

$$S_0 = \frac{\beta(T_0 - 138)}{\left(\ln \frac{\eta_0}{\eta_{dim}} + 9.67\right)} \tag{6.20}$$

where $\eta_{dim} = 1$ [Pas].

When the base oil is subjected to high pressure and temperature, also the density varies according to the following formula [86]:

$$\rho(p,T) = \rho_{T_0} \frac{0.59 \times 10^9 + 1.34p}{0.59 \times 10^9 + p} + \alpha_\rho (T_0 - T) \tag{6.21}$$

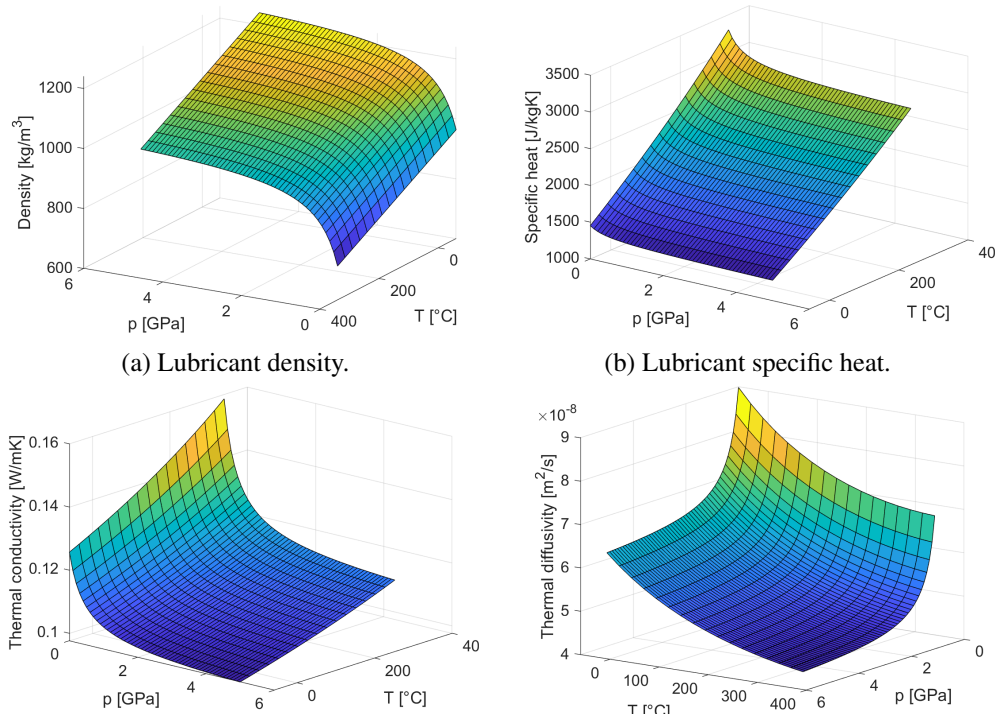

(a) Lubricant density.

(b) Lubricant specific heat.

(c) Lubricant conductivity.

(d) Lubricant diffusivity.

Fig. 6.3 Lubricant properties function of the average Hertzian pressure p and the temperature T.

$$\alpha_\rho = \begin{cases} 0.65 \left[\dfrac{\text{kg}}{\text{m}^3\text{K}}\right] & \text{if} \quad 831 < \rho \leq 950 \left[\dfrac{\text{kg}}{\text{m}^3}\right] \\ 0.60 \left[\dfrac{\text{kg}}{\text{m}^3\text{K}}\right] & \text{if} \quad 950 < \rho < 1000 \left[\dfrac{\text{kg}}{\text{m}^3}\right] \end{cases} \tag{6.22}$$

where ρ_{T_0} is the oil density at $T = T_0$ [K] and p is expressed in [Pa]. The density variation with pressure and temperature for the selected grease, whose characteristics are tabulated in Tab. 6.3, is shown in Fig. 6.3a.

Thermal properties of lubricating oils may be useful when assessing heating effects. The specific heat can be expressed in [kJ/kgK] as [86]:

$$s_h(p,T) = \frac{1.63 + 0.0034T}{\sqrt{s_g}} \tag{6.23}$$

$$s_g = \frac{\rho(p,T)}{\rho_{H_2O_{15.6^\circ\text{C}}}} \tag{6.24}$$

where s_g is the specific gravity, $\rho_{H_2O_{15.6°C}}$ is the density of water at 15.6 [°C] and $\rho(p,T)$ is the density of the oil at pressure p and temperature T [°C] obtained from Eq. 6.21. A typical value for mineral oils is about 1670 [J/kgK] at 20 °C [87]. The specific heat variation with pressure and temperature is shown in Fig. 6.3b.

The thermal conductivity [W/mK] (Fig. 6.3c) can be roughly estimated with the following expression [86]:

$$k_h(p,T) = \frac{0.12}{s_g}(1 - 1.667 \times 10^{-4} T) \tag{6.25}$$

where T is in [°C].

Finally, the thermal diffusivity in [m^2/s] (Fig. 6.3d) can be obtained as

$$\chi(p,T) = \frac{k_h}{\rho s_h} \tag{6.26}$$

where ρ is the lubricant density from Eq. 6.21 and s_h is the specific heat from Eq. 6.23.

6.4 Lubricant film thickness

As previously mentioned, the lubrication goal is to separate the two contacting surfaces creating an enough thick film of lubricant between them. During the churning phase the film is principally composed by grease in fully flooded conditions, but, as soon as the churning phase finishes, the mechanism operates in mild starved conditions and the film is composed mainly of base oil (with few thickening fibres). The film thickness depends therefore on the equilibrium between the oil feed rate and loss rate. The feed rate is mainly determined by the grease reservoir oil bleeding and shear and from the spin motion of the spheres while the loss rate depends on side–flow in the contacts and evaporation. The temperature influences in the same way both rates. Oxidation, polymerization and grease ageing negatively affect the bleeding rate and the quality of the surface separation, due to grease softening.

The EHL lubrication problem can be completely described solving the Reynolds equation describing the fluid flow in narrow gaps (simplification of the more general Navier – Stokes equations)

$$\frac{\partial}{\partial x}\left[\frac{\rho h^3}{12\eta}\frac{\partial p}{\partial x}\right]+\frac{\partial}{\partial y}\left[\frac{\rho h^3}{12\eta}\frac{\partial p}{\partial y}\right]=\frac{\partial(\rho hu)}{\partial x}+\frac{\partial(\rho hv)}{\partial y}+\frac{\partial(\rho h)}{\partial t} \tag{6.27}$$

in combination with the load balance equation

$$F_n=\iint_A p(x,y)dxdy \tag{6.28}$$

the film thickness equation for Hertzian elastically deformable bodies, which takes into account the curvature of the solids and the surface deformations through the Boussinesq integration,

$$h(x,y)=h_0'+\frac{x^2}{2R_x}+\frac{y^2}{2R_y}+\frac{2}{\pi E^*}\iint_A\frac{p(x',y')dx'dy'}{\sqrt{(x-x')^2+(y-y')^2}} \tag{6.29}$$

and considering the dependence of the viscosity on the pressure within the contact, the boundary conditions of cavitation and no wall-slip of the lubricant.

The first two terms on the left side of Eq. 6.27 represent Poiseuille flow, the first two terms on the right side represent Couette flow and the last term represents both the squeeze flow and the local expansion flow resulting from the variation of the density and bodies approach in time. This set of equation can be solved numerically using multigrid methods [198]. Further details and symbols' meaning can be found in [86, 87, 192, 199, 200].

The lubrication is influenced by two major physical effects: the elastic deformation of the solids under the applied load, and the increase in fluid viscosity with pressure. Four main regimes of lubrication can be identified:

- *isoviscous–rigid*: in this regime the elastic deformation of the bodies is negligible with respect to the thickness of the lubrication film and the contact pressure does not lead to significant variation in the fluid viscosity;
- *piezoviscous–rigid*: in this regime the elastic deformation is still insignificant, but the pressure is such that the lubricant's viscosity may change;

- *isoviscous–elastic*: in this regime the elastic deformation of the bodies is comparable with or greater than the film thickness, but the contact pressure is low and the viscosity can be considered constant;
- *piezoviscous–elastic*: in this last regime the elastic deformation is significant, and the high pressure induces lubricant's viscosity variation.

In BSs and ball bearings the elastic moduli are high and the contact pressure can vary between low and very high values (usually up to $1 \div 3$ [GPa]) and, therefore, the contact regime can be considered either isoviscous–rigid (IVR) for low loads or piezoviscous–elastic for high loads. Numerically solving Eqns. 6.27 – 6.29, the film thickness and the pressure profile can be obtained: this operation is fairly computational heavy, therefore in literature several authors performed a bunch of simulations extracting fitting equations in an explicit form to obtain the central and minimum film thickness for several operating conditions.

Due to the hydrodynamic action of the lubricant, the pressure profile changes from the typical Hertzian ellipsoid, as shown in Fig. 6.4. The relative motion between the surfaces builds up a lubricant film and the pressure rises outside the Hertzian contact area in the entry region, slightly enlarging the total contact area. Consequently, the pressure is slightly lower than the Hertzian pressure in the inlet. In the central region the two surfaces remain almost parallel with a film thickness h_c. The viscosity of the lubricant rises with the pressure, thus at the outlet region it decreases causing a film constriction: this is the minimum film thickness h_0. This region is where thre is more probability of having direct asperities contacts (see Eq. 6.50). In correspondence of this constriction, the pressure presents a peak and just after it suddenly drops, sometimes even below the vapour pressure creating a cavitation region. The entity of this peak and of the constriction depends strongly on the lubricant pressure–viscosity characteristic and it is less marked as starvation progresses.

One of the most influential factor in the film creation is the *entrainment speed*, or rolling velociy, i.e. the speed with which the lubricant is swept into the contact. If the peripheral speeds of the two bodies are u_1 and u_2, as shown in Fig. 6.4, the entrainment speed u is the mean of the signed velocities of the two bodies:

$$u = \frac{u_1 + u_2}{2} \tag{6.30}$$

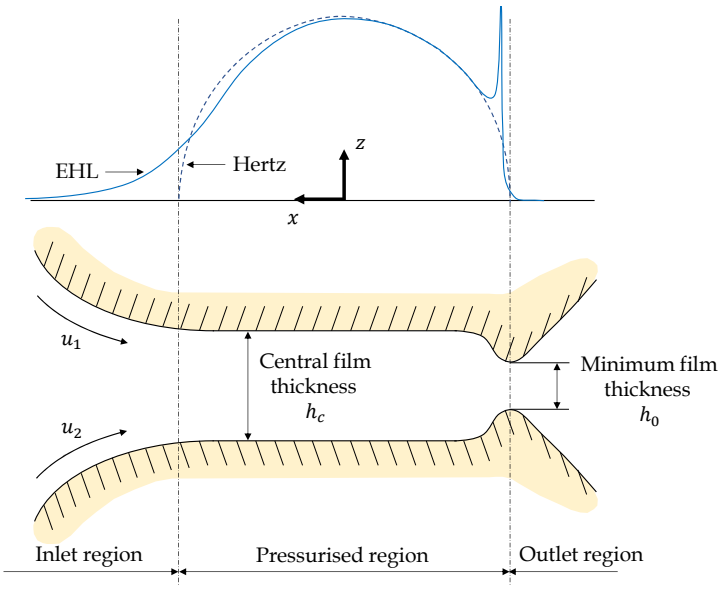

Fig. 6.4 EHL typical pressure distribution and bodies' profile deformation in piezoviscous–elastic regime.

It is not always a simple average of the absolute velocities, but the mean of the surface velocities relative to the theoretical point of contact. Since the lubricant adheres to the surfaces of the bodies, the surface velocity relative to the contact point has to be considered instead of the absolute velocity [201]. If $u_1 \neq u_2$ relative sliding occurs. The ratio between sliding and rolling can be expressed through the slide-to-roll ratio:

$$SRR = \frac{sliding\ velocity}{rolling\ velocity} = 2\frac{u_1 - u_2}{u_1 + u_2} \tag{6.31}$$

where $u_1 - u_2$ is the sliding speed, i.e. the speed of the two surfaces relative to each other. This speed controls the friction and the heat generation but it has very little impact on the film thickness [202]. In case of pure rolling condition $SRR = 0$, $u_1 = u_2$ and the rolling speed is $u = u_1 = u_2$, while in pure sliding $u_2 = 0$ and $SRR = 2$. If the surfaces move in opposite directions, the SRR can assume also greater values.

In the BS system the contacts happen between non–conformal bodies, characterised by two curvature radii r_{ix} and r_{iy} with $i = 1,2$ in the contact points, respectively in the rolling (x) and transverse (y) directions. The contact can thus be reduced to the

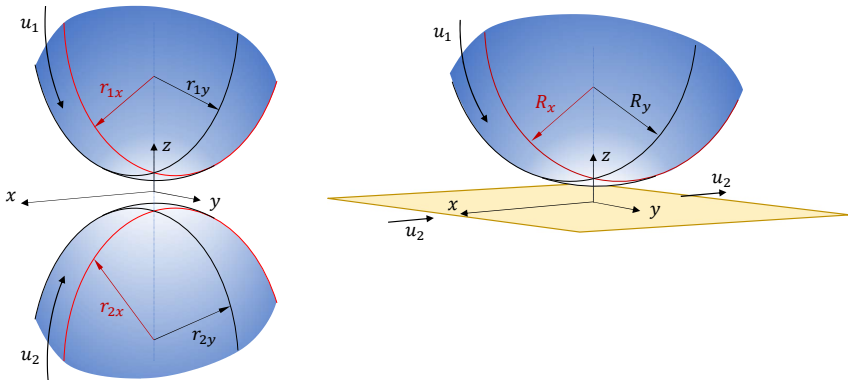

Fig. 6.5 Equivalent curvature radii.

contact of an equivalent body with reduced curvature radii R_x and R_y in the contact point in the same directions, against a flat surface, as depicted in Fig 6.5:

$$\frac{1}{R_x} = \pm\frac{1}{r_{1x}} \pm \frac{1}{r_{2x}} \tag{6.32}$$

$$\frac{1}{R_y} = \pm\frac{1}{r_{1y}} \pm \frac{1}{r_{2y}} \tag{6.33}$$

The most widely used formulae to calculate the central and minimum film thicknesses h_c and h_0 are those developed by Hamrock and Dowson [203]:

$$h_0 = 3.63 R_x U^{0.68} G^{0.49} W^{-0.073} (1 - e^{-0.68\kappa_d}) \tag{6.34}$$

$$h_c = 2.69 R_x U^{0.67} G^{0.53} W^{-0.067} (1 - e^{-0.73\kappa_d}) \tag{6.35}$$

in which U, W, G and κ_d are dimensionless parameters defined as:

$$U = \frac{\eta_{0T} u}{2E^* R_x} \tag{6.36}$$

$$W = \frac{F_n}{E^* R_x^2} \tag{6.37}$$

$$G = \alpha_{pv} E^* \tag{6.38}$$

$$\kappa_d = 1.03 \left(\frac{R_y}{R_x} \right)^{0.63} \tag{6.39}$$

where u is the entraining velocity in [m/s], η_{0T} is the base oil dynamic viscosity at atmospheric pressure and at the oil operating temperature T in [Pas], E^* is the reduced Young modulus in [Pa], defined as

$$E^* = \frac{2}{\frac{1-\nu_1^2}{E_1} + \frac{1-\nu_2^2}{E_2}} \tag{6.40}$$

with E_1, E_2, ν_1 and ν_2 the Young and Poisson moduli of the two contacting bodies. R_x and R_y are the reduced radii of curvature respectively in the rolling and transverse directions expressed in [m] (Eqns. 6.32 and 6.33), α_{pv} is the pressure–viscosity coefficient of Eq. 6.16 in [Pa^{-1}] and F_n is the normal load in [N].

Equations 6.34 and 6.35 apply only to fully flooded conditions and they are accurate only in the piezoviscous–elastic regime for small values of α_{pv}. Nijenbanning et al. [86, 204] developed a central film thickness formula valid for the entire α_{pv} domain and for all the EHL regimes:

$$h_c = R_x \sqrt{2U} \left[\left(H_{RI}^{\frac{3}{2}} + \left(H_{EI}^{-4} + h_{00}^{-4} \right)^{-\frac{3}{8}} \right)^{\frac{2}{3}s} + \left(H_{RP}^{-8} + H_{EP}^{-8} \right)^{-\frac{1}{8}s} \right]^{\frac{1}{s}} \tag{6.41a}$$

$$s = \frac{3}{2} \left(1 + e^{-1.2 \frac{H_{EI}}{H_{RI}}} \right) \tag{6.41b}$$

$$h_{00} = 1.8 \lambda^{-1} \tag{6.41c}$$

$$H_{RI} \approx 145 \left(1 + 0.796 \lambda^{\frac{14}{15}} \right)^{-\frac{15}{7}} \lambda^{-1} M^{-2} \tag{6.41d}$$

$$H_{RP} = 1.29 (1 + 0.691 \lambda)^{-\frac{2}{3}} L^{\frac{2}{3}} \tag{6.41e}$$

$$H_{EI} = 3.18 \left(1 + 0.006 \ln(\lambda) + 0.63 \lambda^{\frac{4}{7}} \right)^{-\frac{14}{25}} \lambda^{-\frac{1}{15}} M^{-\frac{2}{15}} \tag{6.41f}$$

$$H_{EI} = 1.48 \left(1 + 0.006 \ln(\lambda) + 0.63 \lambda^{\frac{4}{7}} \right)^{-\frac{7}{20}} \lambda^{-\frac{1}{24}} M^{-\frac{1}{12}} L^{\frac{3}{4}} \tag{6.41g}$$

where M, L and λ are the Moes' dimensionless groups [204] defined as

$$M = \frac{F_n}{E^* R_x^2} \left(\frac{E^* R_x}{\eta_{0T} u} \right)^{\frac{3}{4}} \tag{6.42}$$

$$L = \alpha_{pv} E^* \left(\frac{E^* R_x}{\eta_{0T} u} \right)^{-\frac{1}{4}} \tag{6.43}$$

$$\lambda = \frac{R_x}{R_y} \tag{6.44}$$

H_{RI}, H_{RP}, H_{EI} and H_{EP} are the film thickness values for the previously described lubrication regimes, respectively the isoviscous–rigid, piezoviscous–rigid, isoviscous–elastic and piezoviscous–elastic. Equations 6.41–6.44 have been obtained for contacts in which the entrainment direction is perpendicular to the major principal axis of the contact ellipse, i.e. $\lambda \leq 1$, which is the case of a sphere in a groove, as in BSs.

The minimum film thickness can be approximated by [86, 87]:

$$h_0 = \frac{3}{4} h_c \tag{6.45}$$

The film thickness is influenced by the local heat generated by lubricant shearing in the inlet zone due to back flow. Murch et al. [205] expressed this influence through a reduction factor C which represents the ratio between the actual and the classical isothermal film thickness from Eq. 6.41:

$$C = \frac{3.94}{3.94 + L_{th}^{0.62}} \tag{6.46}$$

where L_{th} is the thermal loading parameter, defined as:

$$L_{th} = \frac{\eta_{0T} \beta u^2}{k_h} \tag{6.47}$$

where β is defined in Eq. 6.17, u is the entrainment speed of Eq. 6.30 and k_h is defined in Eq. 6.25.

A more comprehensive prediction formula was presented by Gupta et al. [195]:

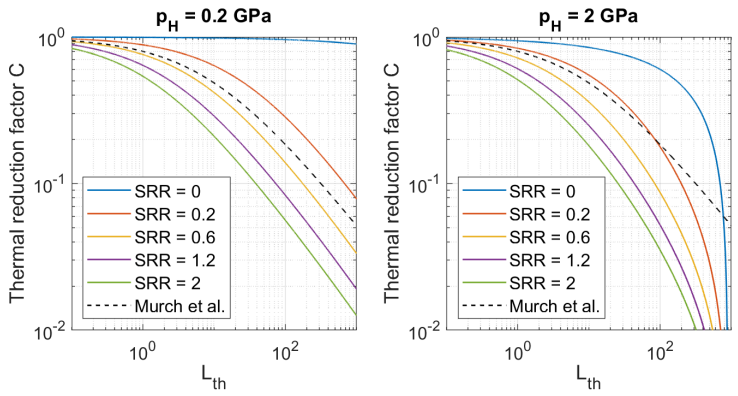

Fig. 6.6 Thermal reduction factor obtained from Eqns. 6.46 and 6.48 with respect to L_{th} for varying SRR and contact pressure.

$$C = \frac{1 - 13.2\left(\frac{p_h}{E^*}\right) L_{th}^{0.42}}{1 + 0.213(1 + 2.23\,SRR^{0.83}) L_{th}^{0.64}} \tag{6.48}$$

where SRR is the slide to roll ratio, defined in Eq. 6.31, and p_h is the maximum Hertzian pressure. The comparison between Eq. 6.46 and Eq. 6.48 is shown in Fig. 6.6 varying the SRR and for two different values of Hertzian pressure.

An interesting feature of lubrication through grease base oil is that, for very low speed, conversely of what happens for oil only lubrication, the film thickness stabilizes and do not fall to zero. This is due to the presence of a thin layer of degraded thickener fibres deposited on the rolling track, as schematically shown in Fig. 6.7, whose height generally varies between $6 \div 80$ [nm] [86, 206]. For this reason, considering Eqns. 6.41 and 6.48, the total film thickness can be expressed as

$$h_{Tc,0} = C h_{c,0} + h_R \tag{6.49}$$

where h_c and h_0 are the central and minimum EHL film thickness calculated basing on the operating conditions (Eqns. 6.41 and 6.45) and h_R is the residual film thickness formed by thickener material.

When the film thickness is of the same order of magnitude of the height of surface asperities, localized contacts between some peaks may take place and mixed lubrication occurs. Tallian [207] proposed a parameter to characterise the film variation as a function of the composite surface roughness:

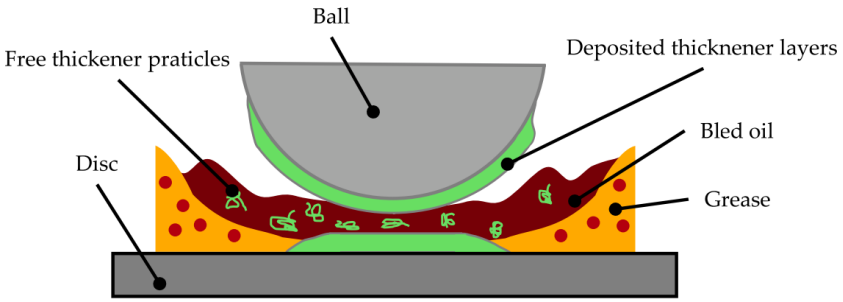

Fig. 6.7 Schematic representation of a contact lubricated by bled oil and thickener fibres [206].

$$\Lambda = \frac{h_{T0}}{\sqrt{\sigma_1^2 + \sigma_2^2}} \tag{6.50}$$

where h_{T0} is the minimum lubricant film thickness and σ_1 and σ_2 are the RMS surface roughness of the two bodies. This parameter is strictly linked with the onset of surface damage [87]. Tallian correlated the parameter with the surfaces' fatigue life. It has been found that for $\Lambda < 1$ wear and smearing occur. For $1 < \Lambda < 1.5$ surface distress can occur, which means spalling and extreme plastic deformation of the asperities which lead to a glazed surface with a new different RMS roughness. For $1.5 < \Lambda < 4$ a little glazing may be possible with minimal wear, while for $\Lambda > 4$ full film EHL lubrication is present and basically no wear occurs.

Experimentally it has been seen that, often, lubricated mechanisms can work well even with $\Lambda \cong 1$ thanks to the establishment of a micro–EHL regime, in which the contact between asperities is mediated by a very thin lubricant film and direct contact is avoided with consequently elastic deformation of the surface peaks [87]. Nevertheless, with increasing load the number of asperities in contact increases and direct contact occurs despite the presence of micro–EHL. In such a condition, called mixed or boundary lubrication, the load is shared between the asperities in direct contact and the lubricant trapped between the surfaces.

The ratio $f(\Lambda)$ between the load F_{n_a} borne by the asperities in direct contact and the total normal force can be expressed, according to [208, 209], with the following load share function:

$$f(\Lambda) = \frac{F_{n_a}}{F_n} = 1 - \frac{1.2\Lambda^{0.64}}{1 + 0.37\Lambda^{1.26}} \tag{6.51}$$

Assuming that the surfaces in contact maintain constant temperature and speed during the integration time step, a simplified approach to calculate the instantaneous temperature increase in the contact zone can be applied [195]. The temperature rise is computed by conduction through the film of the heat generated by the sliding:

$$\Delta T_{EHL} = \frac{\tau h_{Tc} |u_1 - u_2|}{4k_h} \tag{6.52}$$

6.5 Friction

In this section the sliding and rolling friction forces and moments generated at the contact interface in presence of lubricant are introduced.

6.5.1 Sliding friction

The friction depends almost entirely on the properties of the lubricant within the flat central contact region since this part of the film is highly pressurised and thus creates high shear stresses. In this central region, as long as some sliding is present, the lubricant experiences both very high pressures and high strain rates and its response is always highly non-Newtonian.

Sliding friction arises from a difference in the two contacting bodies surface velocities in the contact area. The originated friction force opposes to the relative sliding and acts in opposite directions on the two surfaces. It can results from viscous shear forces in the lubricant or from interface adhesion [210].

In full film conditions, the transmitted friction forces in the contact area are obtained from the integration of the lubricant shear stress over the area of the contact footprint:

$$F_{tEHL} = \int_A \tau dA \tag{6.53}$$

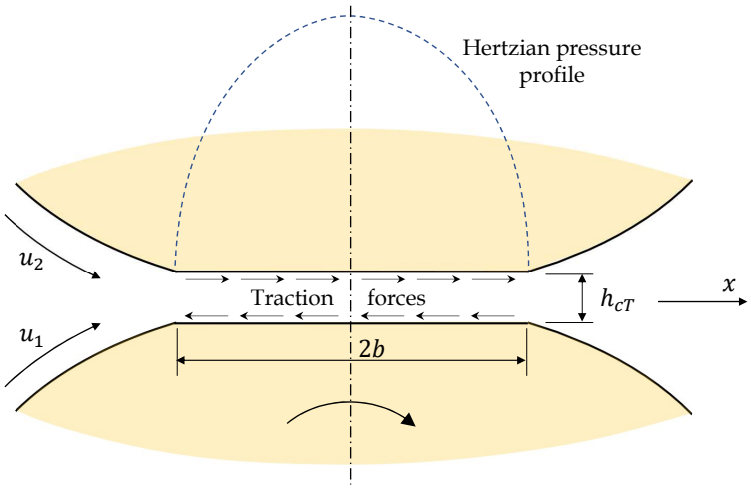

Fig. 6.8 Simplified geometry and generation of friction force in an EHL contact.

In most cases a basic simplification is used: a uniform film thickness is assumed inside the EHL contact and the characteristic end constriction is ignored [87]. Friction has generally been estimated by considering it to be originated simply from Couette shear of a lubricant film between parallel surfaces, having dry Hertzian diameter and thickness estimated from Eqns. 6.41 [210]. These assumptions lead to a contact geometry similar to that assumed in the Grubin theory (Fig. 6.8). In this thesis, such simplifications have been adopted. However, the constriction of the lubricant film at the contact outlet has been considered for possible asperities interactions (Eq. 6.50).

The friction force can be calculated from the lubricant fluid constitutive equation (Eq. 6.11), obtaining

$$F_{t_{EHL}} \simeq \tau(\dot{\gamma})A \tag{6.54}$$

where $A = \pi a_x a_y$ is the contact area calculated according to the Hertzian theory.

If the velocity is a continuous function across the film thickness and there is no slip at the interface between the fluid film and the solid surfaces, the velocity gradient across the film thickness can be approximated by

$$\dot{\gamma} = \frac{\partial u}{\partial h} \cong \frac{u_1 - u_2}{h_{cT}} \tag{6.55}$$

The difference between the actual and the dry Hertzian pressure distribution is less significant as the normal load increases [86, 74]. It is assumed either that the local viscosity remains constant in the EHL contact area or that its average value can be found. In more refined analyses, however, the local variation of viscosity can be included. Under constant load conditions, geometry and lubricant characteristics, the contact area, the local viscosity and film thickness remain almost invariant.

In mixed lubrication conditions, contacts between asperities of the two surfaces may occur. The Tallian parameter of Eq. 6.50 is used to give a probabilistic estimation of the average normal load fraction borne by the asperities contacts, through Eq. 6.51. In mixed lubrication, also the tangential force is partially given by the direct interaction of the asperities [208]. The equivalent friction coefficient μ_{EHL} due to the lubricant shear associated with the full film separation condition can be calculated as:

$$\mu_{EHL} = \frac{F_{t_{EHL}}}{F_n} = \frac{\tau A}{F_n} \tag{6.56}$$

where $F_{t_{EHL}}$ is the tangential friction force due to lubricant shear if all the load was supported uniquely by the lubricant film and F_n is the total normal force. Instead, if all the load was borne by the asperities direct contact, the coefficient of friction would be:

$$\mu_{dry} = \frac{F_{t_a}}{F_n} \tag{6.57}$$

In the mixed lubrication regime the macroscopic equivalent sliding friction μ_s can be expressed as a weighted sum of the friction coefficient μ_{EHL}, due to shearing of the lubricant film, and of the dry friction coefficient μ_{dry} accordingly to the load share function [211]:

$$\begin{aligned} \mu_s &= \mu_{EHL}\left(1 - \frac{F_{n_a}}{F_n}\right) + \mu_{dry}\frac{F_{n_a}}{F_n} \\ \mu_s &= \mu_{EHL}(1 - f(\Lambda)) + \mu_{dry} f(\Lambda) \end{aligned} \tag{6.58}$$

Finally, the total friction force can be calculated:

$$F_t = \mu_s F_n = \mu_{EHL} F_{n_{EHL}} + \mu_{dry} F_{n_a} = \tau A \left(1 - f(\Lambda)\right) + \mu_{dry} F_{n_a} \tag{6.59}$$

where

$$\begin{aligned} F_{n_{EHL}} &= F_n \left(1 - f(\Lambda)\right) \\ F_{n_a} &= F_n f(\Lambda) \end{aligned} \tag{6.60}$$

Therefore, in full film lubrication conditions $f(\Lambda) = 0$, $\mu_s = \mu_{EHL}$ and $F_t = F_{EHL}$, while in completely dry conditions $f(\Lambda) = 1$, $\mu_s = \mu_{dry}$ and $F_t = F_{t_a}$.

6.5.2 Rolling friction

Rolling resistance of a sphere in a groove can be originated from several factors: elastic deformation hysteresis of the two rolling bodies, pivoting effects, curvature effects, roughness and hydrodynamic lubricant resistance caused by the presence of lubricant in the race [212].

The pressure distribution generated in the lubricant film is normal to the contact surfaces, but it is not symmetric along the rolling direction x. In the transversal direction y the pressure distribution is symmetric with respect to the x axis and thus no forces or moments are generated. Researches on the power losses due to the Poiseuille flow in the rolling direction and in the transversal direction showed that the latter is usually very small for wide elliptical contacts and therefore negligible with regard to the power dissipated in the inlet and outlet regions of the contact area [213]. Furthermore, a pressure is generated in the contact inlet, whereas the pressure in the outlet drops towards zero and tangential stresses on the surfaces are created by the pressure induced lubricant viscous flow. This difference in pressure creates a flow of lubricant through the contact, which can be calculated by integrating the Reynolds equations (Eqns. 6.27–6.29).

In a lubricated ball–race contact, depending on the geometry, lubricant viscosity, speed and normal load, the lubricant regime can be a combination of isoviscous–rigid (IVR) and elasto–hydrodynamic (EHD) regimes [214]. Biboulet and Houpert [213]

have expressed the generated hydrodynamic rolling force FR for the IVR and EHL lubrication regimes as:

$$FR_{IVR} = 2.9766 E^* R_x^2 k^{0.3316} W^{\frac{1}{3}} U^{\frac{2}{3}} \tag{6.61}$$

$$FR_{EHL} = 7.5826 E^* R_x^2 k^{0.4055} W^{\frac{1}{3}} U^{\frac{3}{4}} \tag{6.62}$$

These relations depend on the material properties, body geometries and on the dimensionless speed and load parameters, U and W, defined in Eqns. 6.36 and 6.37. k is the dimensionless reduced radius ratio:

$$k = \frac{1}{\lambda} = \frac{R_y}{R_x} \tag{6.63}$$

with R_x and R_y the equivalent radii of curvature in the rolling and transverse directions from Eqns. 6.32 and 6.33.

Equations 6.61 and 6.62 correspond to fully flooded conditions, for which the meniscus distance from the inlet is r_b for the IVR regime and $\approx 10 a_x$ for the EHL regime, where a_x is the half contact width of the Hertzian contact footprint in the direction of motion (the smallest one considering a sphere in a groove).

Previously, Houpert [215] suggested two relationships for the hydrodynamic rolling force FR similar to Eqns. 6.61 and 6.62:

$$FR_{IVR_{Houpert}} = 1.213 E^* R_x^2 k^{0.358} W^{0.364} U^{0.636} \tag{6.64}$$

$$FR_{EHL_{Houpert}} = 2.765 E^* R_x^2 k^{0.35} W^{0.466} U^{0.656} G^{0.022} \tag{6.65}$$

where G is the dimensionless material parameter (Eq. 6.38) and α_{pv} is the piezo–viscous parameter of the lubricant [Pa^{-1}] (Eq. 6.16). These equations correspond to moderately starved conditions in which the rolling resistance due to the lubricant is diminished due to starvation. Indeed, the results of Eqns. 6.64 and 6.65 can be obtained from Eqns. 6.61 and 6.62 with a meniscus distance of about $0.3 r_b$ in the IVR regime and $\approx 3 a_x$ in the EHL regime [216].

The transition between the IVR and the EHL regimes is accomplished using a single parameter M^*, obtained from a curve fitting process on the results of a more complex formulation described in [213, 217]:

$$M^* = 0.5549k^{-0.6029}WU^{-0.75} \tag{6.66}$$

Equations 6.61 and 6.62 can therefore be merged in a single FR value as:

$$FR = \frac{FR_{IVR} - FR_{EHL}}{1 + \frac{M^*}{6.6}} + FR_{EHL} \tag{6.67}$$

which can be rewritten as a sum of the two lubrication regime contributions weighted with the parameter M^*:

$$FR = FR_{IVR}\left(\frac{1}{1 + \frac{M^*}{6.6}}\right) + FR_{EHL}\left(\frac{\frac{M^*}{6.6}}{1 + \frac{M^*}{6.6}}\right) \tag{6.68}$$

The transition described using Eq. 6.67 matches very well with the experimental results presented in literature [211, 216]. The force FR is applied on both the surfaces in the same direction because it is generated by the lubricant flow and its direction is such that it creates a resistant moment on the sphere relative to its rolling direction.

Even in pure rolling contacts, some micro–sliding are present within the contact area, due to the finite size of the footprint, where the speeds of the surfaces do not match exactly [210]. Balan et al. [211, 216] formulated an approximated relationship for the rolling resistant moment around the contact footprint centre caused by rolling elastic hysteresis losses and contact micro–slips:

$$MER = 7.48 \times 10^{-7} r_b^{0.33} F_n^{1.33} \left[1 - 3.519 \times 10^{-3}(k-1)^{0.8063}\right] \frac{\mu_s}{\mu_{s_{dry}}} \tag{6.69}$$

where MER is in [Nm], r_b is the ball radius and μ_s is the average sliding friction coefficient in the contact ellipse, function of the lubrication regime (Eq. 6.58): it reaches its maximum values $\mu_{s_{dry}}$ in dry contact conditions, while it is lower for lubricated contacts. It is assumed that $\mu_{s_{dry}} = 0.11$ [211] at 25 [°C] and its dependence on temperature is specified by an empirical formula (see Sec. 7.4).

Since the race is curved in space, additional micro–slip is present within the contact area and the supplementary resistant moment can be expressed as [211]:

$$MC = 0.0806\mu_s \frac{F_n a_c^2}{R_d} \tag{6.70}$$

where MC is in [Nm], a_c is the major semi-axis of the contact ellipse, which, in the case of a sphere in a groove, is the half width a_y of the contact ellipse in the transverse direction. R_d is the deformed curved surface radius in the same direction:

$$R_d = \frac{2r_b r_{s,n}}{r_{s,n} + r_b} = 2R_y \tag{6.71}$$

where r_s, n is the transverse curvature radius respectively of the screw and nut grooves in the $n-b$ plane.

The total rolling moment is thus the sum of MER and MC. The presence of the lubricant decreases the sliding friction coefficient and thus the MER and MC values, while it makes the hydrodynamic rolling force FR to rise due to the onset of the Poiseuille flow in the gap between the contacting bodies. The lubrication regime affects the rolling resistance moment value since both contributions depend on the sliding friction coefficient μ_s: its value is influenced by the ratio between the thickness of the lubricant film and the combined roughness of the surfaces (Eq. 6.50).

In addition to MER, MC and FR, the component FP of the pressure of the lubricant in the inlet of the contact along the rolling direction, created by the rolling motion of the ball, is considered in [211, 216, 169, 170] and it can be related to the hydrodynamic rolling force FR as [169]:

$$FP = 2FR \frac{R_x}{R_x + r_b} \tag{6.72}$$

A higher pressure is generated in the inlet of the contact because the lubricant is compressed by the rolling and speed effects of the ball. This pressure acts normal to the race and ball surface. The pressure forces on the sphere do not generate a torque but their component FP in the rolling direction opposes to its motion. The components in the other directions are neglected [169, 170]. Thus, the FP forces are considered applied on the sphere centre [169, 170]. Equation 6.72 shows that FP depends on the relative curvature of the two contacting bodies. Figure 6.9 depicts the

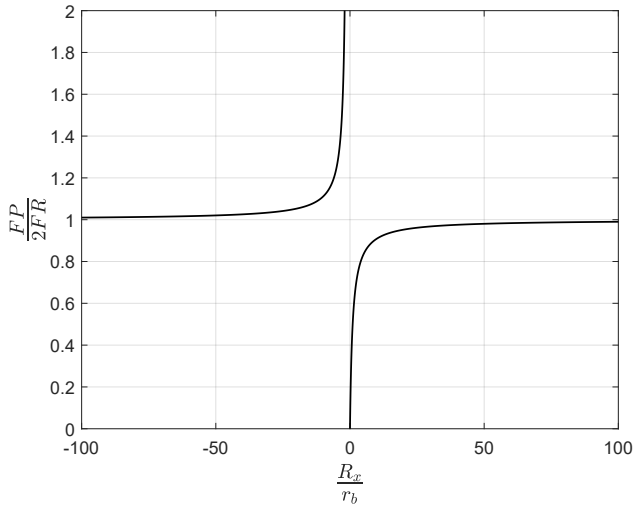

Fig. 6.9 Effect of the contacting bodies curvature ratio on the FP force.

effect of the curvature ratio on the FP force: if the groove is a plane, $FP = 2FR$ as mentioned in [211, 216]. If $\frac{R_x}{r_b} > 0$ both the bodies are convex, as in the ball–screw shaft contact. The volume of the lubricant comprised between the two bodies in the inlet zone becomes bigger for $R_x \to 0$ and so the pressure force becomes lower. If $\frac{R_x}{r_b} < 0$ the groove is concave, as in the ball–nut contact, and therefore for $R_x \to 0$ the inlet volume of lubricant is lower and the generated pressure force becomes higher. The solution has no meaning for $-1 \leq \frac{R_x}{r_b} < 0$ since for these values the groove should be internal to the sphere.

The lubricant forces and moments directions are shown in Fig. 6.10, in which the subscripts *bs* and *bn* simply refer to the ball–screw shaft and ball–nut interfaces. All the calculated resistant moments and forces (MER, MC, FR, FP) oppose to the rolling motion of the sphere on the grooves, therefore they generate a resistant effect also on the screw and the nut. MER and MC act on the same axis of the sphere angular velocity, with opposite sign. This is because the rolling moments direction is dictated by the sphere's rolling direction: indeed, the rotation, with or without sliding, induces a non-uniform normal pressure distribution due to the accumulation of material in the leading edge [87, 88]. The asymmetric pressure distribution resultant generates the rolling resistance moment which finally opposes to the sphere rotational speed around its centre, regardless the direction of sliding or translation of the centre of mass.

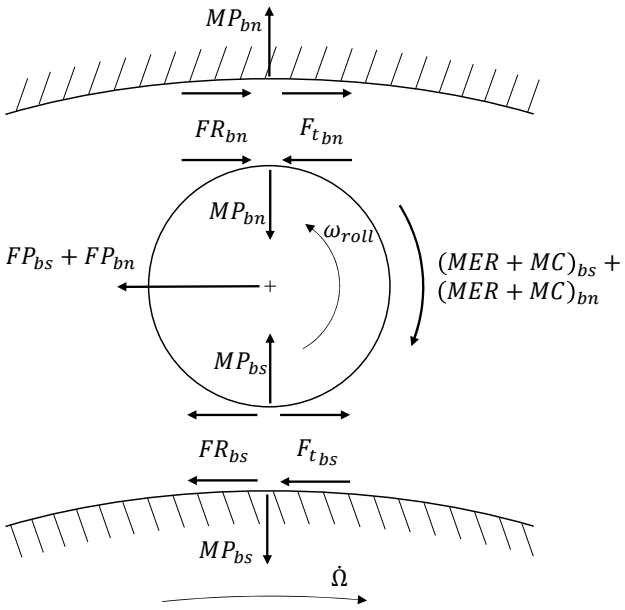

Fig. 6.10 Forces direction on the sphere and the screw and nut grooves.

It is assumed that FR lays in the helix tangential direction since it is due to the lubricant flow through the contact area, which is mainly caused by the motion of the sphere along the helical path. FR is a tangential force applied on the sphere in the contact point and it is oriented in such a way it generates a resistant moment on the sphere concordant with the MER and MC effects. FR is applied on the groove in the same direction, since it is a braking force created by the hydrodynamic effect [211, 214, 216, 169]. FP is applied on the sphere centre opposing to its translational speed.

If mixed sliding–rolling situation occurs, generally the sliding friction predominates but the rolling friction is still present, and it becomes not negligible for quasi–pure rolling conditions.

6.5.3 Spin friction

Spin friction is a particular case of sliding friction, in which the relative angular speed is directed along the common contact normal vector. The friction moment is a function of the global friction parameter μ_s, the normal load F_n and the shape of the contact footprint. It can be approximated with the following expression [216]:

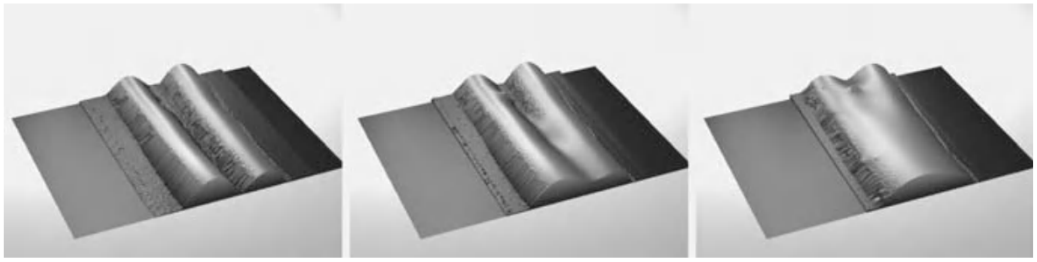

(a) t = 0 s. (b) t = 75 s. (c) t = 135 s.

Fig. 6.11 Effect of replenishment after a single sphere run [86, 218].

$$MP \cong \left[\frac{3}{8} + \left(\frac{3\pi}{16} - \frac{3}{8}\right)\kappa^{-0.945-0.016\ln(\kappa)}\right]\mu_s F_n a_y \tag{6.73}$$

with $\kappa = \frac{a_x}{a_y}$ the ellipticity ratio between the minor contact ellipse half width a_x (in the rolling direction) and the major contact ellipse half width a_y (in the transverse direction).

6.6 Starvation model

As already stated, the mechanism operates for most of its life in mild starved condition. The film thickness in the starved regime is not governed by speed, but by the availability of viscous material in the track due to lubricant re–flow. The lubricant availability in the contact inlet is given by a balance of loss flow and replenishment.

When a sphere passes across the lubricant layer, it leaves a track on it, as shown in Fig. 6.11a, formed by a thin central layer and two lateral ridges [86, 218]. After a certain amount of time, dependent on the viscosity and the bleeding characteristic of the grease, the central part is replenished by the ridges at the sides of the contact restoring the lubricant layer for the next sphere passage (Fig. 6.11b-c).

The replenishment is mainly driven by surface tension and capillary forces [206] but also by the shearing of the grease near the contact which supply further base oil. Accordingly to the experimental measurements performed in literature [86, 88, 218], the full replenishment time is in the order of 10^2 [s].

At low speed the lubricant has the time to replenish the track behind the contact, while, at high speed, this action is limited by the over rolling frequency and starvation

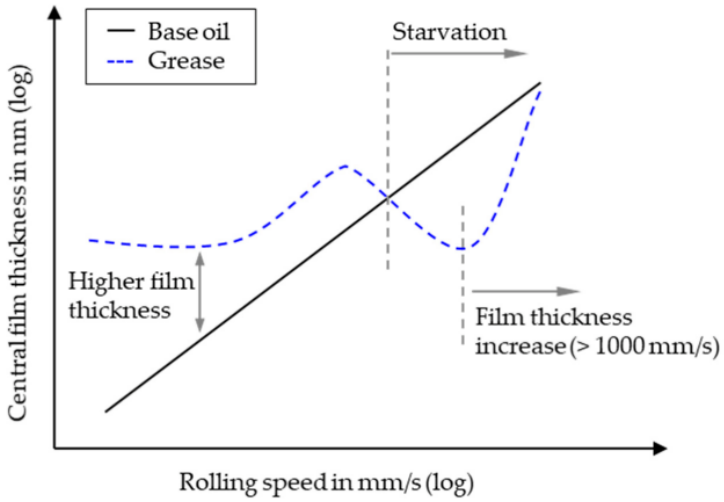

Fig. 6.12 Qualitative representation of the film thickness for fully flooded base oil and starved grease lubricated contacts [206].

occurs. The starvation is more intense with increasing speed since the time between successive over rollings of the spheres on the lubricant becomes shorter and the replenishment from the side of the contact has not the time to restore the lubricant layer.

Throughout the operative life, the effect of replenishment reduces due to the reservoir depletion and modification of grease properties (ageing and oxidation). When the contact inlet is not fully flooded, the contact pressure can build up only where the two lubricant layers on the groove and the sphere merge, reducing the height and modifying the shape of the film within the contact.

As starvation proceeds, the pressure distribution approaches the Hertzian profile [219], making the previous assumption of Hertzian pressure distribution more realistic.

The oil loss by side flow leads to a progressively diminishing film thickness and, when it becomes very thin, severe starvation catches on, characterized by massive wear. This condition should be avoided through the re–lubrication of the mechanism.

Figure 6.12 qualitatively shows the central film height as a function of the rolling speed. It can be seen that, beyond a certain speed threshold, starvation occurs and the film thickness decreases, but, for very high speeds, the centrifugal forces play an important role and push the lubricant towards the contact zone, restoring the film height and attenuating the starvation effects.

Damiens et al. [220], neglecting the effect of replenishment, derived a simple model to calculate the central film thickness reduction in mild starvation with respect to the thickness in fully flooded conditions:

$$\frac{h_{cms}}{h_{cff}} = \frac{r}{\sqrt[\gamma]{1+r^{\gamma}}} \tag{6.74}$$

$$r = \frac{2\tilde{h}_{\infty}}{h_{cff}\bar{\rho}_c} \tag{6.75}$$

where h_{cms} is the central film thickness in mild starvation, h_{cff} is the central film thickness in fully flooded conditions (Eq. 6.41), $2\tilde{h}_{\infty}$ is the thickness of the lubricant layer in front of the contact inlet at a sufficient distance from it to not be subjected to any pressure. $\bar{\rho}_c$ is the ratio between the lubricant density at the maximum Hertzian pressure p_h and the density at the atmospheric pressure in the centre of the contact (Eq. 6.21). γ is the starvation parameter, defined in [220, 221], representing the resistance to side flow. High values of γ mean that most of the oil in front of the contact enters into it, while low values represent the condition in which the oil is pushed to the lateral sides by the sphere motion and the pressure gradient. This parameter is dependent also on the operating condition (the Moes' parameters M and L) and on the ellipticity $\kappa = \frac{a_x}{a_y}$ of the contact area: the more it is squeezed along the transverse direction the more difficult it is, for the oil, to escape laterally from entering the contact, and then the higher γ. An approximated regression expression has been obtained through the software Eureqa® using the few experimental data reported in [219, 220]:

$$\begin{aligned}\gamma \simeq 3.284 + 3.776\kappa r + 0.331\sqrt{\frac{M}{L}}r - 0.5437\kappa - 3.846r + \\ - 2.581r\ln(\kappa) - 0.195\kappa\sqrt{\frac{M}{L}}r^{3.846r+3.846r^2}\end{aligned} \tag{6.76}$$

Figure6.13 shows the data and the linear fitting presented in [219] for different values of r. Equation 6.76 has been obtained fitting the data from these lines and the results are shown in Figs. 6.13a–6.13c. Equation 6.76 is very well correlated with the data showing a $R^2 > 0.99$ and a correlation coefficient of 0.996. The relative

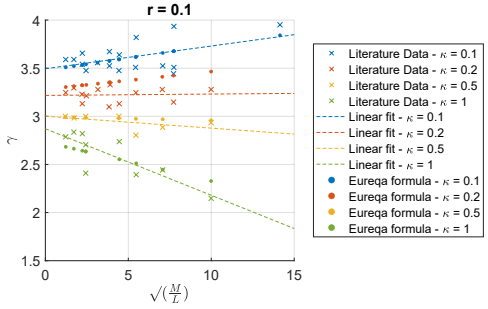

(a) γ values for $r = 0.1$.

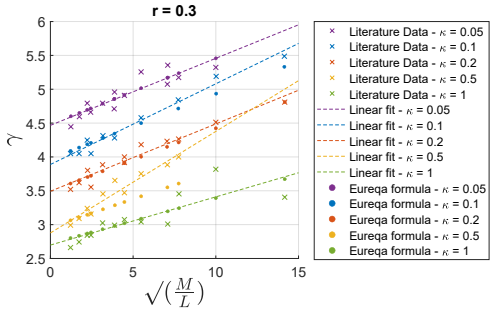

(b) γ values for $r = 0.3$.

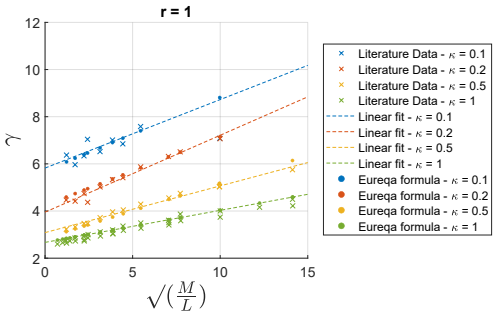

(c) γ values for $r = 1$.

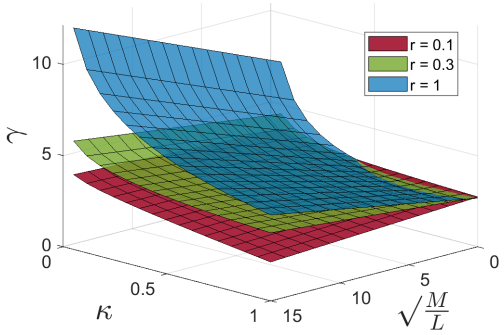

(d) 3D representation varying κ, $\sqrt{\frac{M}{L}}$ and r.

Fig. 6.13 Starvation parameter γ values from [219] and Eq. 6.76 fitting.

errors are reported in Fig. 6.14, from which it can be observed that the maximum relative error is 10.7% for $\kappa = 0.5$ and $r = 0.3$, while the mean and RMS relative errors are only 1.49% and 2.53% respectively.

Figure 6.13d provides a comprehensive three–dimensional view of the γ values with regard to the ellipticity parameter κ, the operating condition parameter $\sqrt{\frac{M}{L}}$ and the starvation ratio r.

Equation 6.74 is valid for one sphere passage over a lubricant layer. For repeated over rollings, typical of roller bearings and BSs, neglecting the replenishment effect and assuming fully flooded film thickness at $t = 0$ [s], Eq. 6.74 can be rewritten as:

$$\frac{h_{cms}}{h_{cff}} = \left(r_0^{-\gamma} + n\right)^{-\frac{1}{\gamma}} \tag{6.77}$$

where r_0 is the ratio of the layer thickness and uncompressed fully flooded film thickness before the first over rolling, for which a good approximation can be $r_0 = 1$ [86], and n is the number of repeated over rollings. In deriving Eq. 6.77 it is assumed

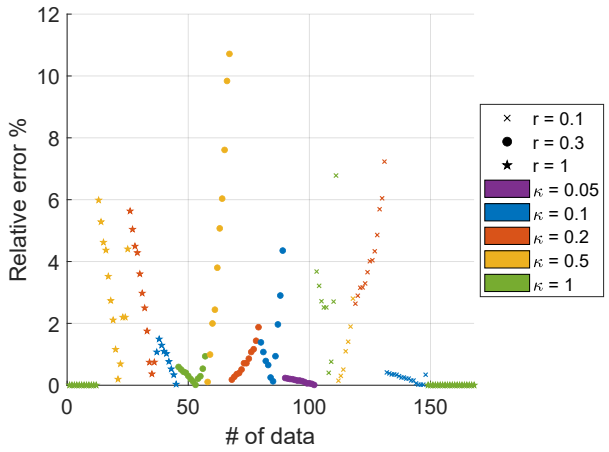

Fig. 6.14 Relative errors between Eq. 6.76 and the linear fitting of the data in [219].

that the oil layer thickness at the exit of the contact is equal to the outlet thickness of the previous over rolling, i.e. $\tilde{h}_{\infty_{(n+1)}} = h_{cms_{(n)}}$. Thus, the film thickness h_{cms} calculated at the previous over rolling is needed in Eq. 6.76 to update the current value of γ modifying r. As starvation proceeds, r decreases and the starvation rate increases since γ diminishes.

When r becomes less than 0.1 the Damien's model does not apply anymore, and it becomes more accurate to use the Van Zoelen model [86, 222] for severely starved contacts. It is assumed that every sphere contributes to the decay of the film thickness in the same way, having the same average side flow over the entire path of the spheres. Considering the value of the film thickness in the contact centre line, the following model can be written:

$$h_{css} = \frac{1}{\sqrt{Ft + h_{c0}^{-2}}} \tag{6.78}$$

$$F \approx \sum_{k=1}^{2z_{eff}} \frac{\pi \bar{\rho}_{c_k}^2 p_{h_k} a_{x_k}}{3 l_t a_{y_k}^2 \eta_0} \left[\left(\frac{\pi \alpha_{pv} p_{h_k}}{2} \right)^{\frac{3}{2}} + 1 \right]^{-\frac{2}{3}} \tag{6.79}$$

where $\bar{\rho}_c = \frac{\rho(p_h)}{\rho_0}$, t is the time passed since starvation started , h_{c0} is the initial central film thickness in fully flooded conditions, p_h is the maximum Hertzian pressure, a_x and a_y are the contact footprint half widths in the rolling and transverse direction respectively, η_0 is the lubricant viscosity at atmospheric pressure and

temperature, α_{pv} is the pressure–viscosity coefficient of Eq. 6.16 and z_{eff} is the number of effectively loaded spheres. The function F is the sum of all the contributes from each sphere–groove contact. l_t is a parameter related to the total track length covered by the lubricant. For a BS, it can be written, following the example in [86], as:

$$\begin{aligned} l_t = \frac{\pi n_t}{\cos\alpha_e}\left[(d_m - D_b\cos(\alpha_s)) + (d_m + D_b\cos(\alpha_n))\right] + \pi D_b z_{eff} = \\ = \frac{2d_m\pi n_t}{\cos\alpha_e} + \pi D_b z_{eff} \end{aligned} \tag{6.80}$$

where n_t is the number of loaded turns in the nut, α_e is the helix angle with p the lead, d_m is the pitch circle diameter, D_b is the sphere diameter, α_s and α_n are the contact angles respectively with the screw and nut grooves, assumed equal for simplicity.

The Damiens and Van Zoelen models can be combined with a smooth transition function to obtain the starved film thickness h_{cs}, as described in [86]:

$$h_{cs} = h_{css} + \frac{h_{cms} - h_{css}}{1 + \left(\frac{n}{n_{tr}}\right)^{m_s}} \tag{6.81}$$

where m_s is a transition parameter, assumed equal to 3 [86], and n_{tr} is the number of over rollings at which the transition happens. It is assumed that the transition occurs for $h_{cs} = c_t h_{cff}$ with $c_t = 0.1$, which means $r = 0.1$. Therefore, substituting this relationship in Eq. 6.77, the transition over rollings value reads:

$$n_{tr} = c_t^{-\gamma} - r_0^{-\gamma} \tag{6.82}$$

In order to correlate the number of over rollings n with the starvation time of Eq. 6.78, it is necessary to know the over rolling frequencies of the spheres and the grooves (see App. A for the derivation), which is a significant parameter affecting the lubricating film formation [206]:

$$f_{sphere} = \frac{|\omega|\, r_m \cos(\alpha_e)}{4\pi r_b}\left[1 - \left(\frac{r_b}{r_m}\cos(\alpha_{sn})\right)^2\right] \tag{6.83}$$

$$f_{screw\ groove} = \frac{|\omega|\cos(\alpha_e)\left(1+\frac{r_b}{r_m}\cos(\alpha_{sn})\right)}{4\arcsin\left(\frac{r_b}{r_m}\cos(\alpha_e)\right)} \tag{6.84}$$

$$f_{nut\ groove} = \frac{|\omega|\cos(\alpha_e)\left(1-\frac{r_b}{r_m}\cos(\alpha_{sn})\right)}{4\arcsin\left(\frac{r_b}{r_m}\cos(\alpha_e)\right)} \tag{6.85}$$

Equations 6.83–6.85 have been obtained using the formulae from [98] assuming the contact angles with the screw and nut groove equal to $\alpha_{sn} = \alpha_s = \alpha_n = 45°$ and neglecting the gyroscopic angles and the contact deformations.

Following the approach in [222], the over rolling rate can be related to the angular speed of the screw by the average over rolling density K_f, expressed in over rollings per radians, as:

$$\begin{aligned} K_f &= \frac{1}{3|\omega|}\left(f_{sphere} + f_{screw\ groove} + f_{nut\ groove}\right) = \\ &= \frac{\cos(\alpha_e)}{12}\left\{\frac{r_m}{\pi r_b}\left[1-\left(\frac{r_b}{r_m}\cos(\alpha_{sn})\right)^2\right] + \frac{2}{\arcsin\left(\frac{r_b}{r_m}\cos(\alpha_e)\right)}\right\} \end{aligned} \tag{6.86}$$

The over rolling rate is then:

$$\frac{dn}{dt} = K_f|\omega| \tag{6.87}$$

The Damiens and Van Zoelen models can then be compared calculating the number of over rollings as the time integral of the over rolling rate, considering that K_f is time invariant:

$$n = \int_{t_0}^{t}\frac{dn}{dt}dt = K_f\int_{t_0}^{t}|\omega|\,dt \tag{6.88}$$

As can be observed in Fig. 6.12, starvation takes place only after a certain rolling speed, due to the insufficient time for replenishment between successive over rollings: the angular speed of the screw correspondent to this threshold condition is $\omega_{s_{th}}$ and it can be assumed equal to the value corresponding to an entrainment speed of 100

mm/s [206]. Considering this phenomenon, in Eq. 6.78 the time t becomes the time passed since the critical speed was reached, and Eq. 6.88 turns into:

$$n = \begin{cases} K_f \int_{t_0}^{t} |\omega - \omega_{s_{th}}| \, dt & n > 0 \\ 0 & n \leq 0 \end{cases} \tag{6.89}$$

where the term $|\omega| - \omega_{th}$ allows to represent the following conditions:

- when $|\omega| < \omega_{s_{th}}$ the time between successive over rollings is long enough to allow the replenishment and therefore the cumulative number n of over rollings is decreased and the lubricant film conditions returns toward very little starved conditions;
- when $|\omega| > \omega_{s_{th}}$ starvation occurs and the film thickness decreases;
- when $|\omega| = \omega_{s_{th}}$ the replenishment and loss flow are in equilibrium and the film thickness remains constant;
- when $|\omega| \gg \omega_{s_{th}}$ a recovery phase of the film thickness has been noted experimentally [206, 223–225], due to shear degradation of the grease close to the track which releases low viscosity material that becomes available for reflow, or to centrifugal forces so large that the lubricant is pushed in the contact track and starvation is slightly attenuated. It has been seen that this happens for entrainment speeds in the order of 1000 [mm/s].

At high temperatures, the starvation threshold speed $\omega_{s_{th}}$ moves to higher speed values since the bleeding property of the grease is promoted by the decrease of the viscosity [226] and the replenishment becomes easier. For the same reason, shear degradation of the grease is favourable for starvation since the consequent grease softening causes the release and reflow of base oil into the track replenishing the contact. In severe ageing conditions the base oil availability is strongly diminished, thus starvation occurs again [223].

The Damien and Van Zoelen models have been developed considering a sphere rolling in steady state conditions at constant speed on a disk and therefore they formulated the equations disregarding the possibility of rolling speed variation. In an EMA BS, the operational profile varies with time: it is indeed likely that the

BS operations are alternated with resting or low speed periods. Thus, during these phases, it is not realistic to consider that the starvation level remains constant, but replenishment will take place and the layer thickness is restored.

6.7 Lubricant degradations

An incorrect or improper lubrication is one of the main causes for fault inception in mechanical components, as well as one of the main factors which affect the fault growth. This generally happen when the lubricant degrades. The most common degradations are: oil oxidation, decomposition, crystallization, emulsion, grease bleeding (starvation), slumping and mechanical ageing [86, 87, 227].

The base oil oxidation is the major cause of failure for lubricants subjected to high temperatures: it consists in the breakdown or rearrangement of the lubricant molecules and it usually occurs when the oil is exposed at ordinary air environment. This process is due to the contaminants, such as sulphur, aromatics, oxygen and chlorine, that remain in the oil after the refining process and that favour the reaction between the oil and the environmental oxygen generating corrosive compounds. This phenomenon can be accelerated by the water presence beside the high temperature.

The effect of oxidation is a reduction in the lubricity properties and of the viscosity (softening) of the lubricant. The reduction of viscosity may cause direct contact between surface asperities and, therefore, local temperature peaks which contribute to further oxide the lubricant.

Accelerated wear is also a consequence, due both to possible direct contact of the surfaces and to the presence of the corrosive compounds. Moreover, the debris generated by the surface wear enter the lubricant, contributing to the wear process and acting also as a catalyst for the oxidation process.

A similar process may occur if no or little oxygen is present and the temperature is very high. The base oil molecules brake down to methane, ethane and ethylene, generally for temperatures well above the flash and flame points. The consequences of this degradation are the same: loss in viscosity and lubricity properties with consequent friction and temperature increase and accelerated wear.

On the other hand, oil crystallization can occur at very low temperatures, below the pour point (the lowest temperature at which the lubricant shows a fluid behaviour).

The result is the formation of crystals which solidify the lubricant and cause the viscosity to rise considerably increasing the risk of jamming. This degradation is generally avoided by design, choosing a lubricant with the appropriate temperature range for the application.

The presence of water degrades the lubricant also at normal temperatures: in fact, if a high content of water is present, it may create an emulsion with the base oil, which has much lower load bearing capacity. This causes the surface to be closer and direct contact may occur, damaging the surfaces. The water entrance can be caused by seals failure or by unexpected environmental conditions. In general, the amount of water needed for the emulsion to occur is higher than that needed to generate a rapid oil oxidation.

As extensively described in the previous section, starvation causes the film thickness to be thinner and the surfaces to touch with consequent wear and local overheating. The loss of the base oil from the grease soap is accelerated by high temperatures, high vibrations and high speeds.

Always at high temperatures, the grease thickeners can melt or soften, loosing the contained oil. As a result the lubricant looses its consistency and lubricity and surface separation is not guarantee anymore.

The grease ages due to shearing and its resistance is identified by the mechanical stability. With the ageing progression the thickeners fibres are ground and the lubricant viscosity decreases. This softening causes, in the end, a film breakdown, similar to slumping, and thus the direct contact of the surfaces with the consequent accelerated wear and contact overheating.

6.7.1 Grease ageing model

To have an optimal separation of the two contacting surfaces, it is necessary that the grease and base oil properties remain constant throughout all the component's life. However, according to the failure modes of the lubricant presented in Sec. 6.7, its physical properties deteriorate with time due to several reasons..

As seen in the Sec. 6.7, the most important causes of lubricant degradation are ageing, due to the mechanical shearing, thickener fibres breakdown, oil loss and chemical reactions caused by oxidation [228]. Chemical deterioration is predominant

Table 6.2 Parameters for grease ageing.

Property	$\mathbf{Y_i}$	$\mathbf{Y_\infty}$	$\mathbf{K_a}$	$\mathbf{m_a}$
Grease viscosity [Pas]	8.9×10^5	0.11	50	0.89
Oil viscosity [Pas]	100%	54%	50	0.89
Grease yield stress [Pa]	83	9.9	660	1.9

at high temperature and low speed conditions whereas physical deterioration is predominant at lower temperature and high speed conditions [86]. For this reason, since the primary flight controls operates with external temperature usually lower than -40°C, ageing degradation has been considered and oxidation has been ignored.

With the lubricant ageing progression, the lubricity properties decrease and the probability to have direct contact between the surfaces, and therefore wear, becomes higher. Zhou et al. [189, 228] developed a model for mechanical grease ageing due to shear. The grease degradation is usually characterised by the loss of its original consistency (softening), possibly yielding leakage from the mechanism and, hence, starvation. The following formula has been developed to describe the variation of a certain property Y with ageing:

$$Y = \frac{Y_i - Y_\infty}{1 + K_a S_g^{m_a}} + Y_\infty \tag{6.90}$$

where Y_i is the initial rheological property value for the fresh grease, Y_∞ is its value for infinitely long shearing time, K_a and m_a are the ageing coefficients, to be fitted on real data if available, and S_g is the generated entropy per unit of lubricant volume due to mechanical shearing $[\mathrm{J/Km^3}]$. The latter depends on the temperature and on the work exerted on the grease by the spheres in every contact area, that is the time integral of the grease frictional shearing forces and the relative speed over the ageing time [229]:

$$S_g = \frac{1}{V_{lub} \times 10^9} \int \sum_{k=1}^{2z_{eff}} \frac{F_{t_{EHL}} |u_1 - u_2|}{T} dt \tag{6.91}$$

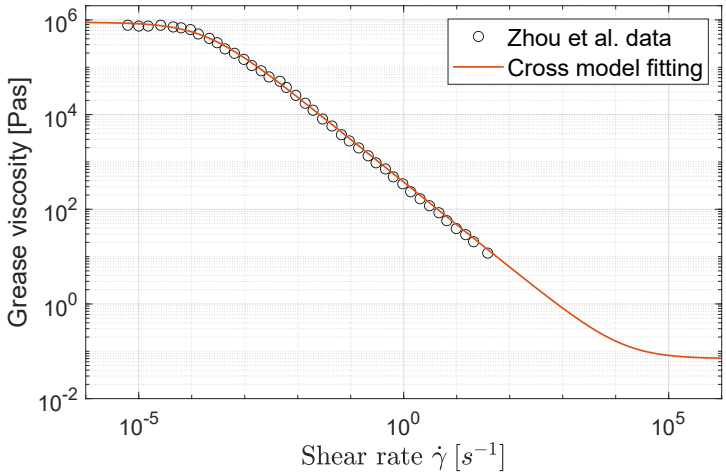

Fig. 6.15 Cross model (Eq. 6.1) fitting on Zhou et al. [189] data for the Li/SS grease with the properties in Tab. 6.3.

where $F_{t_{EHL}} |u_1 - u_2|$ is the mechanical power on the grease expressed in $[\mathrm{W/m^3}]$, T is the lubricant temperature in [K] and V_{lub} is the grease volume inside the BS in $[\mathrm{m^3}]$, which usually should be approximately the 30% of the free internal volume.

The generation of entropy represents a dissipative process which makes the grease microstructure to collapse [189]. The process is composed by two phases with different degradation rates: initially the grease is subjected to a fast ageing rate, in which the fibrous structure is destroyed, and, after that, the deterioration process slows down and the rheology of the grease becomes stable and degrades almost constantly with the generated entropy [189].

The considered rheological parameters mainly influenced by ageing are the grease and base or bled oil viscosity and the grease yield stress [223]. The values reported in Tab. 6.2 has been retrieved and adapted from literature [189, 230].

6.8 Grease properties

In this thesis a lithium 12–hydroxystearate–thicknened grease has been considered, since this type of grease is widely adopted in many applications due to its wide temperature range applicability, relatively good mechanical stability, water–resistant characteristics and low cost [86, 189].

Table 6.3 Properties of the considered grease.

Property of Li/SS	**Value**
Base oil	Mineral oil (semi-synthetic)
Thickener agent	Lithium
NLGI grade	2
Mass fraction of thickener	0.17
Volume fraction of thickener	0.16
Grease viscosity at high shear rate [Pas]	0.1091
Grease density @ 25 °C [kg/m^3]	920
Base oil viscosity @ 25 °C [Pas]	0.07
Base oil viscosity @ 80 °C [Pas]	0.0045
Base oil density @ 25 °C [kg/m^3]	910
Bled oil viscosity @ 25 °C [Pas]	0.08
Bled oil viscosity @ 80 °C [Pas]	0.0051
Zero–shear–rate grease viscosity @ 25 °C [Pas]	8.9×10^5
Transition shear rate $\dot{\gamma}_c$ [s^{-1}]	1.4×10^{-4}
Grease yield stress @ 25 °C [Pa]	83
Storage modulus G' [Pa]	7.67×10^4
Base oil limiting shear stress τ_L [Pa]	2.5×10^6
Limiting shear stress pressure constant ξ	0.06
Yield shear stress temperature parameter b [°C]	50
Derived parameters	
Base oil temperature–viscosity coefficient β [K^{-1}]	0.05
Bled oil temperature–viscosity coefficient β [K^{-1}]	0.05
Base oil Roelands temperature–viscosity index S_0	1.1422
Bled oil Roelands temperature–viscosity index S_0	1.1208
Base oil Roelands pressure–viscosity index Z	0.6658
Bled oil Roelands pressure–viscosity index Z	0.6687
Base oil pressure–viscosity coefficient α_{pv} [Pa^{-1}]	23.805×10^{-9}
Bled oil pressure–viscosity coefficient α_{pv} [Pa^{-1}]	24.365×10^{-9}

The properties of this lubricant, denoted as Li/SS, are summarized in Tab. 6.3 [86, 87, 189, 230, 231]. The consistency and flow indexes of the Cross model (Eq. 6.1) for the grease viscosity have been estimated fitting the data in [189]: the fitting results is shown in Fig. 6.15.

6.9 Summary

This chapter presented the main concepts about grease lubrication reporting the state of the art of investigations on this topic. The various formulations have been experimentally verified in the correspondent papers using ball on disc tribometers, and can be considered reliable. However, the application of these formulations to the case of a BS of an EMA would require further experimental validations and, possibly, the construction of a dedicated test bench to investigate the effect of different lubricant typologies and with different degradation levels on the contact friction and lubricant film's condition. Nevertheless, at least for cylindrical and roller bearings, Kanazawa et al. [232] demonstrated that the tribometer's results, represented by the formulations presented in this chapter, provide a quantitative representation of the real friction forces and power losses arising in full bearings, and can then be used to obtain a fast and economic estimate of the grease lubrication performance on real components.

It has been stated that, after the initial churning phase, the grease lubrication can be assimilated to bled oil lubrication with replenishment. The BS operates most of its life in mild starved conditions due to the high over rolling frequency of the spheres on the track. Therefore, a mathematical model for mild and severe starvation has been introduced. Formulations for sliding and rolling friction have been described for full film and mixed lubrication. The most common degradations of the lubricant have been described and the ageing model has been explained. The formulations presented in this chapter will be used in the multibody model of Chapter 7.

Chapter 7

Multibody ball screw model

7.1 Introduction

The dynamic model presented in Chapter 5 can describe the motion of a sphere within the grooves, automatically switching between adherence and slipping in both contact points depending on the operating conditions. Nevertheless, its motion is represented as unidimensional along the rectified helix, the three–dimensional interaction with the grooves is ignored and the helix torsion effect is neglected. The sphere is assumed to have maximum one contact point with each raceway, even if intermittent contact is considered. Furthermore, the contact angles are the same for screw and nut interfaces and imposed equal to 45°. The interaction between adjacent spheres is ignored and ideal joints are considered both for the screw shaft supports and the anti–rotation constraint of the nut. Moreover, the friction curve is described using an equivalent empirical formulation which is not capable of taking into account the complex non–linear rheology of the lubricant and the effect of the temperature. In addition, since all the spheres are considered equally loaded, the effect of geometric errors on the load distribution cannot be represented.

In order to overcome the aforementioned limitations, a new model, described in the present chapter, has been created in the Simscape Multibody environment. This allowed to move the formulation from unidimensional to three–dimensional. Simscape Multibody allows to describe the bodies with an acausal object–oriented programming language: the dynamic equations are inserted in their standard form and, depending on which signals are available as input information, they are automat-

ically reformulated in a suitable form such that the requested output can be obtained. Each body or component is individually represented and their interconnections reflect the real world interactions and define the underlying dynamic equations. In such a way, the model design can start from the real structure of the physical system. The full dynamics of each component is automatically taken into consideration, including gyroscopic and inertial effects.

Simscape Multibody is provided with basic built–in contact libraries which allow to represent the contact between elementary shapes, such as spheres, cylinders, cones and planes. Unfortunately, these libraries are not sufficient to describe the complex geometry contact between a gothic arch helical groove and a sphere. Therefore, a custom three–dimensional contact model has been formulated to compensate for this lack [94].

Currently, the presence of the recirculation path has not been inserted yet, therefore the model considers an endless helical path composed by the two grooves, in which the spheres continuously move: this obviously involves that, after a certain angle of rotation of the screw shaft, they come out from the nut body and continue to roll in the virtual helix. This situation can also be imagined as a BS with an infinitely long nut. This assumption does not create any issue for what concerns the friction and efficiency values as well as the motion of the spheres and the contact forces. Instead, the reaction forces and torques on the ground and the acceleration of the screw and the nut on the x and y axis are affected by this hypothesis.

In this thesis, a rotating screw and a translating nut have been considered, but this model allows every possible combination to be simulated, such as rotating nut and translating screw or even fixed screw with rotating and translating nut or vice versa.

7.2 Model topology

In this model, all the six degrees of freedom of each body are considered. The screw shaft and the nut are constrained to the ground (the global fixed frame defining an inertial coordinate system) according to the type of application which is simulated (see Sec. 7.6). Instead, independently on the typology of constraints, the spheres maintain always their six degrees of freedom and their motion is defined uniquely by

the fact to be trapped between the helical grooves: therefore their motion depends on the contact forces with the raceways.

All the bodies are considered rigid, thus each one can be described by only one CS. The screw CS, as described in Sec. 3.5.2, is $Oxyz$ and it has the z axis coincident with that of the global CS $O'x'y'z'$: this is not a model limitation but just an assumption to simplify the result analyses, since the BS is the only component simulated. Even if the screw shaft was placed and oriented differently, no changes would be necessary in the model to calculate the contact forces, since only the relative speeds and positions between the contacting bodies are needed.

If a sufficiently smooth groove surface is assumed, namely a surface on which the minimum local curvature radius is grater than the ball radius, each sphere is always in contact with only one point for each half groove. In particular, if the ideal geometry of the grooves, corresponding to the mathematical formulations presented in Sec. 3.5.5, is assumed, in every point of the curve obtained from the intersection of the groove with the $n-b$ plane normal to the thread, at least one of the lines tangent to the groove surface in that point is parallel to the $\widehat{\mathbf{t}}$ axis of the Frenet–Serret CS.

Under these assumptions, it is possible to reduce the order of the problem from a three–dimensional to a bidimensional contact problem on the $n-b$ plane: the basic idea is, at each time step, to construct the geometry representing the four half grooves on the $n-b$ plane around the circle representing the sphere on the same plane. In general, the centre F of the sphere does not coincide with the centre B of the Frenet–Serret CS lying on the ideal helix, contrary to the ideal description adopted in the previous version of the model (5). Thus, for each time step of simulation, given the current position of F, the corresponding ideal point B on the helix can be identified, belonging to the same $n-b$ plane: it is the reference point to construct the groove geometry and, for each time step, it is considered belonging to the screw shaft or to the nut body, depending on which contact is being described. Below, the contact with the screw shaft grooves is explained. The procedure to obtain the formulation for the contact with the nut is straightforward following the same steps.

At the beginning of the simulation, each sphere has its position defined by the initial set of coordinate with respect to the world frame. In order to describe the contact, the relative position $\mathbf{R}^{O}_{F/O}$ and speed $\mathbf{v}^{O}_{F/B}$ of the centre of the sphere F with respect to the screw shaft are needed. These quantities are directly provided by Simscape trough the built–in block Transform Sensor. Anyway, they could be easily

obtained just having the absolute position and speed of both bodies expressed in the global reference system.

By referring to Fig. 3.10, the position of a sphere with respect to the screw CS can be identified by the absolute value of the azimuth angle θ. To eliminate the periodicity of the trigonometric functions, it can be calculated as

$$\vartheta(t) = \int_{t_0}^{t} \frac{x_{F/O}(t)\dot{y}_{F/O}(t) - \dot{x}_{F/O}(t)y_{F/O}(t)}{{x_{F/O}}^2(t) + {y_{F/O}}^2(t)} dt + \vartheta_0 \tag{7.1}$$

where $x_{F/O}(t)$ and $y_{F/O}(t)$ are the coordinate of F with respect to B in the $Oxyz$ CS, and ϑ_0 is the initial azimuth angle defined by the initial position:

$$\vartheta_0 = \vartheta(t=0) = \arctan\left(\frac{y_{F/O}(0)}{x_{F/O}(0)}\right) \tag{7.2}$$

The position of F with respect to B can be expressed in the *Btnb* CS as

$$\mathbf{R}^B_{F/B} = \mathbf{T}_5\left(\mathbf{R}^O_{F/O} - \mathbf{R}^O_{B/O}\right) \tag{7.3}$$

where $\mathbf{R}^O_{B/O}$ is defined in Eq. 3.3 and $\mathbf{T}_5$ is the inverse matrix of Eq. 3.2:

$$\mathbf{T}_5 = \mathbf{T}_2^{-1} \tag{7.4}$$

The Transform Sensor block provides also the rotation matrix $\mathbf{T}_{OF}$, which can be used, together with $\mathbf{T}_5$, to obtain the rotation matrix from the sphere CS (F), which is centred in the sphere centre F and continuously rotates with the progression of the simulation, to the Frenet–Serret CS (B):

$$\mathbf{T}_{BF} = \mathbf{T}_5\mathbf{T}_{OF} \tag{7.5}$$

Since B belongs to the screw shaft for each time step, and the relative linear and angular speed of F with respect to O, given by the Transform sensor block, is the same for each point belonging to the screw shaft body, considering the revolutionary motion of B around $\widehat{\mathbf{z}}$, the following equalities can be formulated:

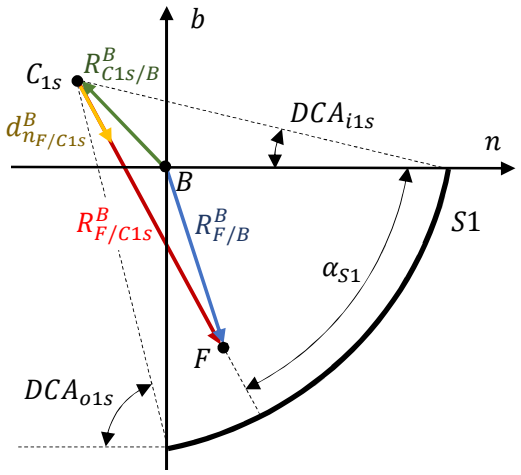

Fig. 7.1 Position vectors on the normal plane.

$$\mathbf{v}^O_{F/O} = \mathbf{v}^O_{F/B} = \mathbf{v}^O_{F/C_i} \qquad \mathrm{i} = 1s, 2s \tag{7.6}$$

$$\boldsymbol{\omega}^O_{F/O} - \boldsymbol{\omega}^O_{B/O} = \boldsymbol{\omega}^O_{F/B} = \boldsymbol{\omega}^O_{F/C_i} \qquad \mathrm{i} = 1s, 2s \tag{7.7}$$

In the following, only the contact with the half groove S1 will be described in detail. Equations 7.6 and 7.7 can be expressed in the Frenet–Serret CS applying the transformation matrix $\mathbf{T}_5$ of Eq. 7.4.

The normal force between the sphere and the circular half groove is always directed along the the common normal in the contact point, i.e. the direction connecting the curvature centres of the two bodies C_{1s} and F. Referring to Fig. 7.1, the versor identifying this direction can be written as

$$\mathbf{d}^B_{n_{F/C_{1s}}} = \frac{\mathbf{R}^B_{F/C_{1s}}}{|\mathbf{R}^B_{F/C_{1s}}|} \tag{7.8}$$

with

$$\mathbf{R}^B_{F/C_{1s}} = \mathbf{R}^B_{F/B} - \mathbf{R}^B_{C_{1s}/B} \tag{7.9}$$

where $\mathbf{R}^B_{C_{1s}/B}$ is the position of the S1 half groove curvature centre defined in Eq. 3.6.

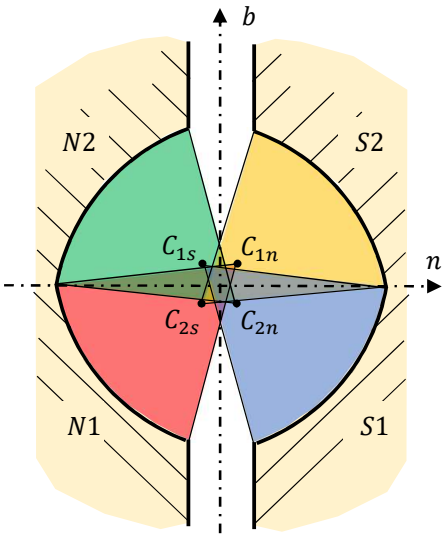

Fig. 7.2 Half grooves contact activation areas.

The translational speed normal to the contact, along $\mathbf{d}^B_{n_{F/C_{1s}}}$, can be expressed by

$$\mathbf{v}^B_{n_{F/C_{1s}}} = \left(\mathbf{v}^B_{F/C_{1s}} \cdot \mathbf{d}^B_{n_{F/C_{1s}}}\right) \mathbf{d}^B_{n_{F/C_{1s}}} \tag{7.10}$$

Observing Fig. 7.1 the contact angle can be identified, calculated as

$$\alpha_{S1} = \arctan\left(\frac{-\mathbf{R}^B_{F/C_{1s}} \cdot \widehat{\mathbf{b}}}{\mathbf{R}^B_{F/C_{1s}} \cdot \widehat{\mathbf{n}}}\right) \tag{7.11}$$

In order to reduce the computational time, the contact model calculations for each half groove are performed only if the contact existence conditions are met, namely:

$$\begin{cases} DCA_{i1s} \leq \alpha_{S1} \leq DCA_{o1s} \\ |\mathbf{R}^B_{F/C_{1s}}| \geq r_s - r_b \\ \mathbf{R}^B_{F/C_{1s}} \cdot \widehat{\mathbf{n}} \geq 0 \end{cases} \tag{7.12}$$

The second condition defines the inner contact between two spheres, one inside the other. Therefore, to avoid that the sphere accidentally and unrealistically "mathematically touches" the rest of the circumference defining S1 outside the DCA boundaries, the third condition has been added. This can happen because of the

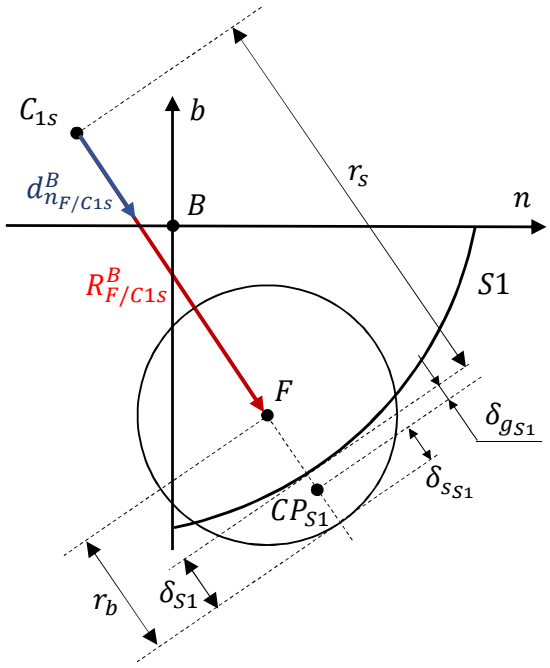

Fig. 7.3 Contact interpenetration and contact point location.

properties of the `arctan` function. Figure 7.2 shows the areas in which the half groove contact models are activated: e.g. the blue area in the case of contact with S1.

The normal contact force is calculated starting from the rigid body interpenetration (see Sec. 7.3), as shown in Fig. 7.3: the contact point CP_{S1} does not lie exactly on the unloaded groove profile because of the elastic deformations $\delta_{g_{S1}}$ and $\delta_{s_{S1}}$ respectively of the groove and the sphere. Therefore, the position of CP_{S1} with respect to the screw origin O, expressed in *Oxyz*, can be written as:

$$\mathbf{R}^O_{CP_{S1}/O} = \mathbf{T}_2 \mathbf{R}^B_{CP_{S1}/B} + \mathbf{R}^O_{B/O} \tag{7.13}$$

where

$$\mathbf{R}^B_{CP_{S1}/B} = \mathbf{R}^B_{CP_{S1}/C_{1s}} + \mathbf{R}^B_{C_{1s}/B} - \frac{MER + MC}{F_{n_{S1}}} \widehat{\mathbf{t}} \tag{7.14}$$

$$\mathbf{R}^B_{CP_{S1}/C_{1s}} = (r_s + \delta_{g_{S1}})\, \mathbf{d}^B_{n_{F/C_{1s}}} \tag{7.15}$$

The last term of Eq. 7.14 represents the change of position of the centre of the pressure distribution in the direction of rolling, due to rolling friction. *MER* and *MC* are the moments responsible for the rolling friction (Eqns. 6.69 and 6.70) and $F_{n_{S1}}$ is the normal contact force magnitude (see Sec. 7.3).

The speed of the contact point CP_{S1}, considered belonging to the sphere, with respect to C_{1s} and expressed in *Btnb*, is

$$\mathbf{v}^B_{CP_{S1}/C_{1s}} = \left(\boldsymbol{\omega}^B_{F/C_{1s}} \times (r_b - \delta_{s_{S1}})\,\mathbf{d}^B_{n_{F/C_{1s}}}\right) + \mathbf{v}^B_{F/C_{1s}} \tag{7.16}$$

The component of the speed along the common normal can be written as

$$\mathbf{v}^B_{n_{CP_{S1}/C_{1s}}} = \left(\mathbf{v}^B_{CP_{S1}/C_{1s}} \cdot \mathbf{d}^B_{n_{F/C_{1s}}}\right)\mathbf{d}^B_{n_{F/C_{1s}}} \tag{7.17}$$

Due to the helix torsion the spheres have always a non-null tangential sliding speed in at least one contact point, which can be expressed using Eqns. 7.16 and 7.17 as

$$\mathbf{v}^B_{t_{CP_{S1}/B}} = \mathbf{v}^B_{CP_{S1}/C_{1s}} - \mathbf{v}^B_{n_{CP_{S1}/C_{1s}}} \tag{7.18}$$

The versor identifying the direction of the sliding speed of the sphere with respect to the screw is simply

$$\mathbf{d}^B_t = \frac{\mathbf{v}^B_{t_{CP_{S1}/B}}}{|\mathbf{v}^B_{t_{CP_{S1}/B}}|} \tag{7.19}$$

and it can be used to identify the direction of the tangential friction force.

The spin velocity of the sphere has been defined positive if oriented along the contact common normal coming out from the groove, as depicted in Fig. 7.4:

$$\boldsymbol{\omega}^B_{spin_{S1}} = -\boldsymbol{\omega}^B_{F/C_{1s}} \cdot \mathbf{d}^B_{n_{F/C_{1s}}} \tag{7.20}$$

The rolling speed is the angular speed vector perpendicular to the common normal and lying on the $n-b$ plane:

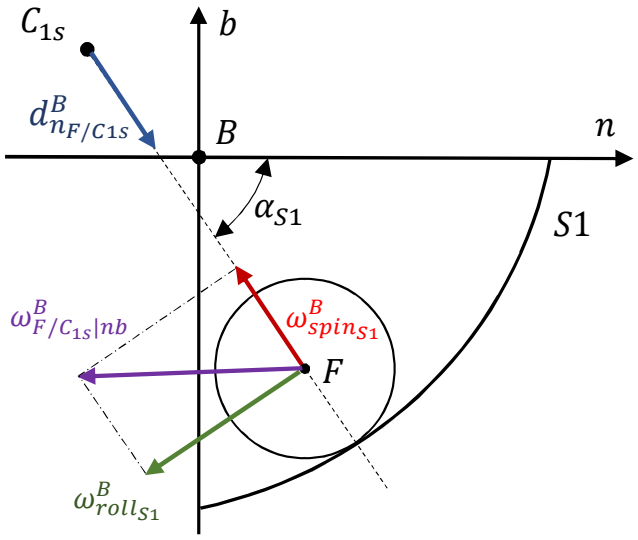

Fig. 7.4 Roll and spin velocities of the sphere.

$$\boldsymbol{\omega}^B_{roll_{S1}} = -\frac{1}{r_b}\mathbf{v}^B_{CP_{S1}/F} \times \mathbf{d}^B_{n_{F/C_{1s}}} \tag{7.21}$$

where $\mathbf{v}^B_{CP_{S1}/F}$ is the component directed along $\widehat{\mathbf{t}}$ of the peripheral speed of the sphere in the contact point CP_{S1}:

$$\mathbf{v}^B_{t_{CP_{S1}/F}} = \left(\boldsymbol{\omega}^B_{F/C_{1s}} \times (r_b - \delta_{s_{S1}})\,\mathbf{d}^B_{n_{F/C_{1s}}}\right) \cdot \widehat{\mathbf{t}} \tag{7.22}$$

Using Eqns. 7.9, 7.10 and 7.18 the normal and tangential forces $F_{n_{S1}}$ and $F_{t_{S1}}$ in the contact point are calculated according to the normal and friction contact models, described in Secs. 7.3 and 7.4. Being $\mathbf{v}^B_{t_{CP_{S1}/B}}$ the sliding speed of the sphere with respect to the screw shaft, the friction force $F_{t_{S1}}$ is directed along $-\mathbf{d}^B_t$ on the sphere and in the opposite direction on the screw. Therefore, the total force acting on the sphere centre F, expressed in the sphere CS F, results

$$\mathbf{F}^F_{sphere} = \mathbf{T}^{-1}_{BF}\left(-F_{n_{S1}}\mathbf{d}^B_{n_{F/C_{1s}}} - F_{t_{S1}}\mathbf{d}^B_t\right) \tag{7.23}$$

while the torque vector acting on the sphere, expressed in the sphere CS F, is

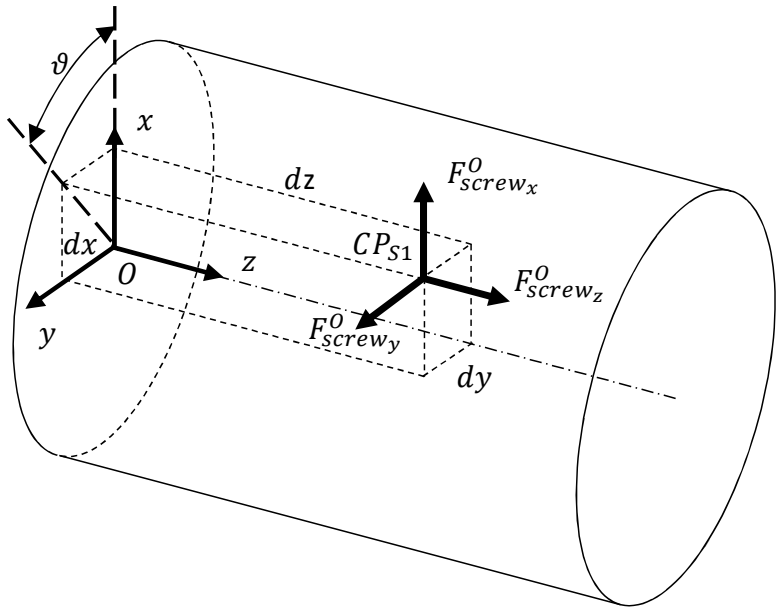

Fig. 7.5 Contact force component on the screw shaft.

$$\begin{aligned}\mathbf{M}^F_{sphere} = \mathbf{T}^{-1}_{BF}\Big[(r_b - \delta_{s_{S1}})\,\mathbf{d}^B_{n_{F/C_{1s}}} \times \left(-F_{t_{S1}}\mathbf{d}^B_t\right) + \\ -(MER + MC)\,\mathbf{d}^B_{\omega_{roll}} + MP\,\mathbf{d}^B_{n_{F/C_{1s}}}\Big]\end{aligned} \tag{7.24}$$

where $\mathbf{d}^B_{\omega_{roll}}$ is the versor of $\boldsymbol{\omega}^B_{roll_{S1}}$.

The same forces of Eq. 7.23 are applied with opposite sign on the screw shaft:

$$\mathbf{F}^O_{screw} = \mathbf{T}_2\left[F_{n_{S1}}\mathbf{d}^B_{n_{F/C_{1s}}} + F_{t_{S1}}\mathbf{d}^B_t\right] \tag{7.25}$$

Looking at Fig. 7.5, the moment generated by the total contact force vector $\mathbf{F}^O_{screw}$ on the screw shaft can be written as

$$\mathbf{M}^O_{screw} = \mathbf{F}^O_{screw} \times \mathbf{R}^O_{CP_{S1}/O} - \mathbf{T}_2\left(MP\,\mathbf{d}^B_{n_{F/C_{1s}}}\right) \tag{7.26}$$

where dx, dy and dz in Fig. 7.5 represent the three components of $\mathbf{R}^O_{CP_{S1}/O}$.

As can be seen from Eqns. 7.14 and 7.26, while the rolling friction effect created by *MER* and *MC* is applied as pure moment on the sphere, on the screw shaft it is represented by the displacement of the contact point CP_{S1} in the direction of rolling: thus the screw sees the contact forces applied on the displaced CP_{S1}, out of the normal plane $n-b$ along the $\widehat{\mathbf{t}}$ axis.

7.3 Normal contact model

The normal contact force is calculated starting from the rigid bodies interpenetration δ_i, as depicted in Fig. 7.3, and from the approaching speed. The total normal force is obtained modelling the contact with a spring and a damper in parallel:

$$F_{n_i} = F_{nk_i} + F_{nd_i} \tag{7.27}$$

where $i =$ S1, S2, N1, N2. According to the Hertzian theory, the elastic component can be written as

$$F_{nk_i} = K_H \delta_i^{\frac{3}{2}} \tag{7.28}$$

where K_H is the Hertzian stiffness expressed in $[\mathrm{N/m^{3/2}}]$. The energy dissipation which occurs during the deformation of the material is modelled through a damping element, which contributes to the total contact force with the following component:

$$F_{nd_i} = \begin{cases} F_{nk_i} & \text{if} \quad F_{nd_i} \geq F_{nk_i} \\ -F_{nk_i} & \text{if} \quad F_{nd_i} \leq -F_{nk_i} \\ C_H \dot{\delta}_i & \text{otherwise} \end{cases} \tag{7.29}$$

where $\dot{\delta}_i = |\mathbf{v}^B_{CP_i/C_i}|$ (Eq. 7.16) and C_H is the damping coefficient. As can be observed in Eq. 7.29, the damping component is saturated to the elastic value component, similarly to the elasto–backlash model presented in Chapter 5. This is to avoid force discontinuities in the beginning of the contact event due to non–zero approaching speed values and to avoid negative attracting forces between the bodies in the separation phase of the contact: in fact F_{n_i} cannot be negative.

F_{n_i} is defined as a repulsive only force, therefore the normal force vector is concordant with $\mathbf{d}^B_{n_{F/C_{1s}}}$ on the groove and discordant on the sphere and tends to separate the bodies. According to the second condition of Eq. 7.12, the interpenetration can assume only positive values:

$$\delta_i = |\mathbf{R}^B_{F/C_{1s}}| + r_b - r_s \geq 0 \tag{7.30}$$

The saturations of Eq. 7.29 and Eq. 7.30 together guarantee that the normal force is non–zero only if the interpenetration is positive (occurring contact) and that it vanishes in non–contact conditions. The contact model of Eq. 7.27 acts applying a sort of penality regularization of the normal contact constraint, where the force magnitude is a function of the constraint violation (the interpenetration).

Antoine et al. [233] proposed an explicit non recursive method to calculate the Hertzian contact quantities, adopted in this thesis because suitable to be inserted in a dynamic model. In order to make the simulation time shorter, all the formulae presented in this section have been pre–calculated and embedded in few maps (Look Up Table blocks on Simulink), linking the contact deformation to the normal force, pressure and contact footprint dimensions.

Known the geometries of the two contacting bodies, called generally body 1 and 2, the principal curvatures can be defined: in the case of a sphere and a helical gothic arch groove they have already been introduced in Sec. 3.5.5.

The equivalent modulus of elasticity is

$$E^*_h = \left[\frac{1-\nu_1^2}{E_1} \frac{1-\nu_2^2}{E_2} \right]^{-1} \tag{7.31}$$

The combination of the two contact geometries is usually defined with the following two parameters:

$$\sum \rho = \rho_{11} + \rho_{12} + \rho_{21} + \rho_{22} \tag{7.32}$$

$$F_\rho = -\frac{\left[(\rho_{11}-\rho_{12})^2+(\rho_{21}-\rho_{22})^2+2\cos(2\omega_h)(\rho_{11}-\rho_{12})(\rho_{21}-\rho_{22})\right]^{\frac{1}{2}}}{\sum\rho} \tag{7.33}$$

where ω_h is the angle between the planes of relative principal curvatures of the two bodies.

The relative principal curvatures can be obtained from

$$A = \frac{\sum\rho}{2}\left(1+F_\rho\right) \tag{7.34}$$

$$B = \frac{\sum\rho}{2}\left(1-F_\rho\right) \tag{7.35}$$

According to the Hertzian theory, the ellipticity parameter κ_h can be related to the geometrical parameters through the following implicit equation [74]:

$$F_\rho = \frac{\left(\kappa_h^2+1\right)E(\kappa_h)-2K(\kappa_h)}{\left(\kappa_h^2-1\right)E(\kappa_h)} \tag{7.36}$$

where $K(\kappa_h)$ and $E(\kappa_h)$ are respectively the elliptic integrals of first and second kind, which, in the canonical form, read:

$$K(\kappa_h) = \int_0^{\frac{\pi}{2}}\left[1-\left(1-\frac{1}{\kappa_h^2}\right)\sin^2\phi\right]^{-\frac{1}{2}}d\phi \tag{7.37}$$

$$E(\kappa_h) = \int_0^{\frac{\pi}{2}}\left[1-\left(1-\frac{1}{\kappa_h^2}\right)\sin^2\phi\right]^{\frac{1}{2}}d\phi \tag{7.38}$$

These integrals can be expressed in an approximated form, committing a maximum absolute error $< 2\times10^{-8}$, as [234]:

$$\begin{aligned} K(m) \simeq &\left(a_0+a_1m_1+a_2m_1^2+a_3m_1^3+a_4m_1^4\right)+ \\ &+\left(a_5+a_6m_1+a_7m_1^2+a_8m_1^3+a_9m_1^4\right)\ln\left(\frac{1}{m_1}\right) \end{aligned} \tag{7.39}$$

Table 7.1 Coefficients of the elliptical integrals approximation formula (Eqns. 7.39 and 7.40).

Coefficient	Value	Coefficient	Value
a_0	1.38629436112	b_0	1
a_1	0.09666344259	b_1	0.44325141463
a_2	0.03590092383	b_2	0.06260601220
a_3	0.03742563713	b_3	0.04757383546
a_4	0.01451196212	b_4	0.01736506451
a_5	0.5	b_5	0.24998368310
a_6	0.12498593597	b_6	0.09200180037
a_7	0.06880248576	b_7	0.04069697526
a_8	0.03328355346	b_8	0.00526449639
a_9	0.00441787012		

$$E(m) \simeq \left(b_0 + b_1 m_1 + b_2 m_1^2 + b_3 m_1^3 + b_4 m_1^4\right) + \\ + \left(b_5 m_1 + b_6 m_1^2 + b_7 m_1^3 + b_8 m_1^4\right) \ln\left(\frac{1}{m_1}\right) \tag{7.40}$$

where $m_1 = 1 - m$, therefore $m = 1 - \kappa_h^{-2}$ and $m_1 = \kappa_h^{-2}$. The coefficients of Eqns. 7.39 and 7.40 are reported in Tab. 7.1.

It has to be pointed out that Eqns. 7.39 and 7.40 are only valid for $0 \leq m_1 \leq 1$, which means $\kappa_h \geq 1$. Thus, to consider all the possible values of the ellipticity parameter, the following equations are used [233, 234]:

$$K(\kappa_h) = \begin{cases} K\left(m = 1 - \kappa_h^{-2}\right) & \kappa_h \geq 1 \\ \kappa_h K\left(m = 1 - \kappa_h^2\right) & \kappa_h < 1 \end{cases} \tag{7.41}$$

$$E(\kappa_h) = \begin{cases} E\left(m = 1 - \kappa_h^{-2}\right) & \kappa_h \geq 1 \\ \frac{1}{\kappa_h} E\left(m = 1 - \kappa_h^2\right) & \kappa_h < 1 \end{cases} \tag{7.42}$$

Instead of solving Eq. 7.36 to find κ_h, an approximate solution can be used [233]:

$$\kappa_h = \left(\frac{B}{A}\right)^{\gamma_h} \tag{7.43}$$

valid for $1 \leq B/A < 10^{10}$ and where

Table 7.2 Coefficients of the ellipticity parameter approximation formula (Eq. 7.44).

Coefficient	Value	Coefficient	Value
μ_1	$4.02274361 \times 10^{-1}$	μ_5	4.2678878×10^{-1}
μ_2	3.7491752×10^{-2}	μ_6	4.2605401×10^{-2}
μ_3	7.4855761×10^{-4}	μ_7	9.0786922×10^{-4}
μ_4	2.1667028×10^{-6}	μ_8	2.7868927×10^{-6}

$$\gamma_h = \frac{2}{3}\left(\frac{1+\mu_1 X^2+\mu_2 X^4+\mu_3 X^6+\mu_4 X^8}{1+\mu_5 X^2+\mu_6 X^4+\mu_7 X^6+\mu_8 X^8}\right) \tag{7.44}$$

In Eq. 7.44, $X = \log_{10}(B/A)$ in order to make the equation valid even if A and B are interchanged [233]. The parameters' values of Eq. 7.44 are reported in Tab. 7.2.

Once the values of A, B and κ_h are obtained, respectively from Eqns. 7.34, 7.35 and 7.43, the semiaxes dimensions of the contact footprint and the contact stiffness can be calculated:

$$a = a^* \left(\frac{3F_{n_i}}{2(A+B)E_h^*}\right)^{\frac{1}{3}} \tag{7.45}$$

$$b = b^* \left(\frac{3F_{n_i}}{2(A+B)E_h^*}\right)^{\frac{1}{3}} \tag{7.46}$$

$$K_H = \frac{2^{\frac{5}{2}}E_h^*}{3\left(\delta_i^*\right)^{\frac{3}{2}}(A+B)^{\frac{1}{2}}} \tag{7.47}$$

where a^*, b^* and δ^* are respectively the dimensionless semimajor and semiminor axes of the contact ellipse and the dimensionless contact deformation [233]:

$$a^* = \left(\frac{2\kappa_h^2 E(\kappa_h)}{\pi}\right)^{\frac{1}{3}} \tag{7.48}$$

$$b^* = \left(\frac{2E(\kappa_h)}{\pi\kappa_h}\right)^{\frac{1}{3}} \tag{7.49}$$

$$\delta^* = \frac{2K(\kappa_h)}{\pi}\left(\frac{\pi}{2\kappa_h^2 E(\kappa_h)}\right)^{\frac{1}{3}} \tag{7.50}$$

The average Hertzian pressure is simply

$$p = \frac{F_{n_i}}{\pi ab} \tag{7.51}$$

and the maximum Hertzian pressure is $p_h = \frac{3}{2}p$.

According to the notation adopted in Chapter 6, for BSs the semimajor axis of the contact footprint is directed in the transverse direction of motion and thus $a = a_y$ while, vice versa, the semiminor axis is disposed in the rolling direction and therefore $b = a_x$.

The total contact deformation δ_i is composed by the deformation of the two contacting bodies δ_{i_1} and δ_{i_2}, as depicte in Fig. 7.3, which are related to the material properties as [235, 236]:

$$\delta_i = \delta_{i_1} + \delta_{i_2} \tag{7.52}$$

$$\delta_{i_j} = \frac{3\left(1-\nu_j^2\right)F_{n_i}K(m)}{2\pi a E_j} \qquad j = 1,2 \tag{7.53}$$

The contact stiffness K_H is not a constant value but it varies with the contact angle, as shown in Fig. 7.6, since the groove first principal curvature depends on the contact angle (Eqns. 3.20 and 3.27).

The damping coefficient C_H of Eq. 7.29 has been assumed to vary with the contact stiffness to maintain stable the damping ratio, according to the following law:

$$C_H = b_h\sqrt{K_H} \tag{7.54}$$

where b_h is a proportional coefficient.

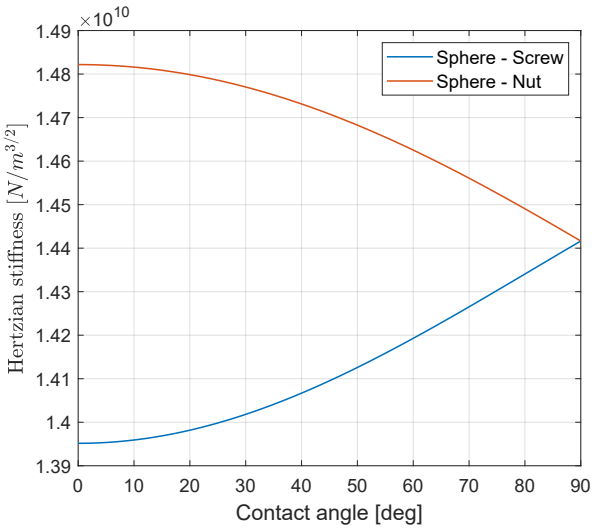

Fig. 7.6 Variation of the Hertzian contact stiffness with the contact angle.

7.4 Friction model

Two models have been developed to calculate the tangential forces exchanged between the contacting bodies:

- equivalent empirical model;
- lubrication model.

Depending on what is the goal of the simulation, one of the two can be chosen. The first model represents the dependence of the friction coefficient on the sliding speed with an equivalent function: this model requires less computational time to be evaluated. The second model is more computational intensive but it provides a more detailed description of the contact in presence of lubrication. The empirical model allows to save approximatively the 53% of the time for the same simulation.

7.4.1 Empirical

The friction coefficient curve is similar to that described in Eq. 5.16 but, because of the complexity of the parameter tuning, the formulation has been replaced by

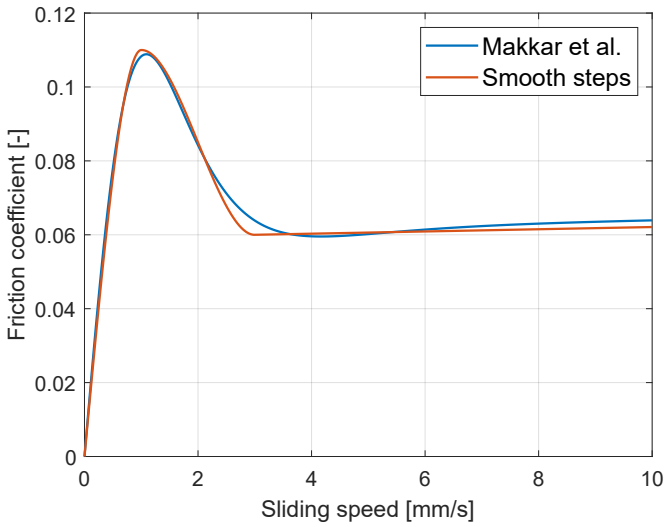

Fig. 7.7 Comparison of friction coefficient models.

$$\mu = \begin{cases} \text{step}\left(v_{rel}, -v_{st}, -\left(\mu_{st} - \mu_v v_{st}\right), v_{st}, \mu_{st} - \mu_v v_{st}\right) + \mu_v v_{rel} & \text{if} \quad 0 \leq v_{rel} \leq v_{st} \\ \text{step}\left(v_{rel}, v_{st}, \mu_{st} - \mu_v v_{st}, v_{dyn}, \mu_{dyn} - \mu_v v_{dyn}\right) + \mu_v v_{rel} & \text{if} \quad v_{rel} > v_{st} \end{cases} \tag{7.55}$$

where $v_{rel} = |\mathbf{v}^B_{t_{CP_{S1}/B}}|$ (Eq. 7.18) is the magnitude of the relative sliding speed, v_{st} is the static friction threshold speed, v_{dyn} is the dynamic friction threshold speed and μ_v is the viscous coefficient. The smooth step function can be expressed as:

$$\text{step}\left(x, x_0, f_0, x_1, f_1\right) = \begin{cases} f_0 + \left(f_1 - f_0\right)\left[3\left(\frac{x-x_0}{x_1-x_0}\right)^2 - 2\left(\frac{x-x_0}{x_1-x_0}\right)^3\right] & \text{if} \quad x_0 < x < x_1 \\ f_0 & \text{if} \quad x \leq x_0 \\ f_1 & \text{if} \quad x \geq x_1 \end{cases} \tag{7.56}$$

Equation 7.55 describes a continuously differentiable curve without discontinuities as a combination of two smooth steps and a straight line representing the viscous effect. This model, as the previous one [186], requires an always present little amount of sliding to transmit a tangential force: the bodies are considered in the adherence condition if the sliding speed is lower than the set threshold value v_{st}, corresponding to the peak in the coefficient of friction in which it assumes the static

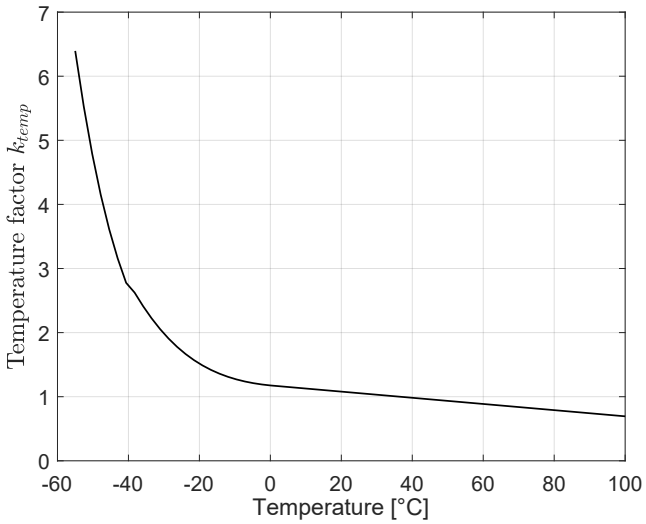

Fig. 7.8 Temperature dependence of the friction coefficient multiplicative factor.

value μ_{st} . For higher speeds, the friction coefficient decreases to the dynamic value μ_{dyn}, qualitatively describing the transition from boundary to full lubrication, and then it increases again linearly due to the viscous effect.

This model reproduces the Coulomb, Stribeck and viscous effects which are usually exhibited by mechanical systems in presence of lubrication. The comparison between the shape of the friction coefficient curves with the two formulations is depicted in Fig. 7.7.

According to the Amonton's second law of friction, the magnitude of the friction force is proportional to the magnitude of the normal force through the friction coefficient. The latter depends only on the relative speed and does not vary with the normal load.

To take into account the temperature effect, the friction coefficient is scaled by a multiplicative factor, shown in Fig. 7.8, which assumes the following expression [58]:

$$k_{temp} = \begin{cases} e^{\sum_{i=1}^{6} k_{Ti}(T-40°\mathrm{C})^i} & T \leq 0°\mathrm{C} \\ k_{T7} - k_{T8}T & 0°\mathrm{C} < T < 40°\mathrm{C} \end{cases} \tag{7.57}$$

where T is in [°C] and the parameters' values are reported in Tab. 7.3.

Table 7.3 Coefficients of the temperature dependent friction formula (Eq. 7.57).

Coefficient	**Value**	
	$T < 40^{\circ}\mathrm{C}$	$T < 40^{\circ}\mathrm{C}$
k_{T1}	-1.231×10^{-2}	-1.531×10^{-2}
k_{T2}	-5.869×10^{-4}	-5.606×10^{-4}
k_{T3}	-6.119×10^{-6}	-6.181×10^{-6}
k_{T4}	2.749×10^{-8}	2.374×10^{-8}
k_{T5}	-6.868×10^{-11}	-3.181×10^{-11}
k_{T6}	-2.767×10^{-12}	-3.250×10^{-12}
k_{T7}	6.875×10^{-1}	6.875×10^{-1}
k_{T8}	-1.563×10^{-3}	-1.563×10^{-3}

The spin friction MP and the rolling friction moments MER and MC are modified in order to not generate torques even when the speed is null, i.e. multiplying the values obtained from Eq. 6.73 and Eqns. 6.69 and 6.70 respectively by $\tanh\left(\frac{\omega_{spin}}{\omega_{spin,th}}\right)$ and $\tanh\left(\frac{\omega_{roll}}{\omega_{roll,th}}\right)$, where $\omega_{spin,th}$ and $\omega_{roll,th}$ are two threshold values to be selected sufficiently small to make the residual slipping speed negligible but not too small to cause integration issues for the solver.

7.4.2 Lubricated

The lubricated friction model uses the formulae presented in Chapter 6 to obtain the sliding friction force and the other friction components. The lubricant quantities are calculated hypothesizing that each sphere moves principally in the direction tangent to the helix. Therefore, from the point of view of the lubrication model, only the motion of the spheres along the $\widehat{\mathbf{t}}$ axis is taken into account, since the prevalent one. Nevertheless, the sliding friction opposes also to the slipping of the sphere on the other directions.

Referring to Eqns. 7.6 and 7.22, the entrainment speed can be obtained as the average speed of the two contacting surfaces (see Chapter 6):

$$\mathbf{u}_{S1}^{B} = \frac{1}{2}\left(\mathbf{v}_{t_{CP_{S1}/F}}^{B} + \mathbf{v}_{F/C_{1s}}^{B} \cdot \widehat{\mathbf{t}}\right) \tag{7.58}$$

The formulae presented in Chapter 6 must be implemented in the dynamic model in order to calculate the forces and moments acting on the contacting bodies for each contact. At each time step of simulation, the kinematic quantities of the matching bodies are known from the integration of the equations of motion at the previous time step, as well as the material and lubricant properties and the operating temperature. Hereinafter the calculation procedure implemented in the model is described.

1. Input parameter: surface speeds, temperature, normal force, material and lubricant properties.
2. Calculate the entrainment speed (Eq. 7.58) and the *SRR* (Eq. 6.31).
3. Solve the Hertzian problem calculating the two half widths of the contact footprint a_x (Eq. 7.45) and a_y (Eq. 7.46), and the contact pressure p and p_h (Eq. 7.51).
4. Update the lubricant properties $\eta(p,T)$ (Eq. 6.18), $\rho(p,T)$ (Eq. 6.21) and $k_h(p,T)$ (Eq. 6.25) basing on average contact pressure and temperature.
5. Calculate Moes and thermal parameters M, L, λ (Eqns. 6.42–6.44) and L_{th} (Eq. 6.47).
6. Calculate the central and minimum film thickness h_c (Eq. 6.41) and h_0 (Eq. 6.45).
7. Calculate the thermal reduction factor C (Eq. 6.46 or 6.48).
8. Calculate the total central and minimum film thickness (Eq. 6.49).
9. Calculate the lubricant shear rate (Eq. 6.55).
10. Update the limiting shear stress τ_L basing on average Hertzian pressure (Eq. 6.10).
11. Calculate the shear stress in the lubricant film (Eq. 6.11).
12. Calculate the Tallian parameter Λ (Eq. 6.50) and the load share function $f(\Lambda)$ (Eq. 6.51).
13. Calculate the total tangential friction force (Eq. 6.59).
14. Calculate the total friction coefficient in mixed lubrication μ_s (Eq. 6.58)

15. Calculate the rolling friction transition parameter M^* (Eq. 6.66).

16. Calculate the rolling friction moments MER (Eq. 6.69), MC (Eq. 6.70), MP (Eq. 6.73) and the friction forces FR (Eq. 6.67) and FP (Eq. 6.72).

17. Calculate the temperature rise in the contact due to lubricant shear ΔT_{EHL} (Eq. 6.52).

Considering the actions of the lubricant, Eq. 7.23 becomes

$$\mathbf{F}^F_{sphere} = \mathbf{T}^{-1}_{BF}\left[-F_{n_{S1}}\mathbf{d}^B_{n_{F/C_{1s}}} - F_{t_{S1}}\mathbf{d}^B_t + (FP-FR)\widehat{\mathbf{t}}\right] \tag{7.59}$$

where FP and FR are applied only on the $\widehat{\mathbf{t}}$ axis because of the simplifying assumptions of the lubricant model (see Chapter 6).

Analogously, Eq. 7.24 becomes

$$\begin{aligned}\mathbf{M}^F_{sphere} = \mathbf{T}^{-1}_{BF}\Big[&(r_b-\delta_{s_{S1}})\,\mathbf{d}^B_{n_{F/C_{1s}}} \times \left(-F_{t_{S1}}\mathbf{d}^B_t - FR\widehat{\mathbf{t}}\right) + \\ &-(MER+MC)\,\mathbf{d}^B_{\omega_{roll}} + MP\,\mathbf{d}^B_{n_{F/C_{1s}}}\Big]\end{aligned} \tag{7.60}$$

The force FP does not create a moment on the sphere since it is considered applied on the centre of the sphere because its effect on the moment is already considered by the change of position of the centre of the pressure distribution [215].

$$\mathbf{F}^O_{screw} = \mathbf{T}_2\left[F_{n_{S1}}\mathbf{d}^B_{n_{F/C_{1s}}} + F_{t_{S1}}\mathbf{d}^B_t + (FP-FR)\widehat{\mathbf{t}}\right] \tag{7.61}$$

According to Fig. 6.10, in case of contact with the nut half grooves, the FP force acts in the same direction both on the sphere and on the groove, thus Eq. 7.61 becomes:

$$\mathbf{F}^O_{nut} = \mathbf{T}_2\left[F_{n_{S1}}\mathbf{d}^B_{n_{F/C_{1s}}} + F_{t_{S1}}\mathbf{d}^B_t - (FP+FR)\widehat{\mathbf{t}}\right] \tag{7.62}$$

7.5 Sphere to sphere contact model

The contact and friction between adjacent spheres is taken into account. The models to calculate the normal and friction forces between the spheres are the same explained in Secs. 7.4.1 and 7.4.2. Though, the relative position and velocity calculation is much easier than for the sphere/groove interaction since both the bodies have simple geometries.

7.6 Constraints

The constraints have been considered as ideal as a first approximation but they can be replaced by bushings without any changes in the model. The results presented in the next sections have been obtained considering an ideal revolute joint on the lower extremity of the screw and an ideal prismatic joint on the nut. This joints combination leaves only the rotational degree of freedom to the screw shaft and only the translational degree of freedom to the nut. The prismatic joint is an ideal representation of an anti–rotation device, which could be for example composed by one or two linear guides, as depicted in Fig. 7.9. The friction of the linear guides or the supporting bearing have been inserted in the simulations of Sec. 7.9.3 with an equivalent formulation [136, 140, 181, 182], dependent only on the relative speed:

$$F_{fr,supp} = \left[F_{frd} + (F_{frs} - F_{frd})e^{-a_{lfr}|\dot{z}_{nut}|}\right] \text{sign}(\dot{z}_{nut}) + b_{lfr}\dot{z}_{nut} \tag{7.63}$$

where F_{frs} is the static Coulomb friction, F_{frd} is the dynamic friction, a_{lfr} and b_{lfr} are two constants to modify the shape of the curve.

Analogously, the bearings' friction torque can be expressed as:

$$T_{fr,supp} = \left[T_{frd} + (T_{frs} - T_{frd})e^{-a_{rfr}|\dot{z}_{nut}|}\right] \text{sign}(\dot{z}_{nut}) + b_{rfr}\dot{z}_{nut} \tag{7.64}$$

The screw shaft is moved by an electric motor, which, for the moment, is represented by a simple transfer function since it is not the main object of the

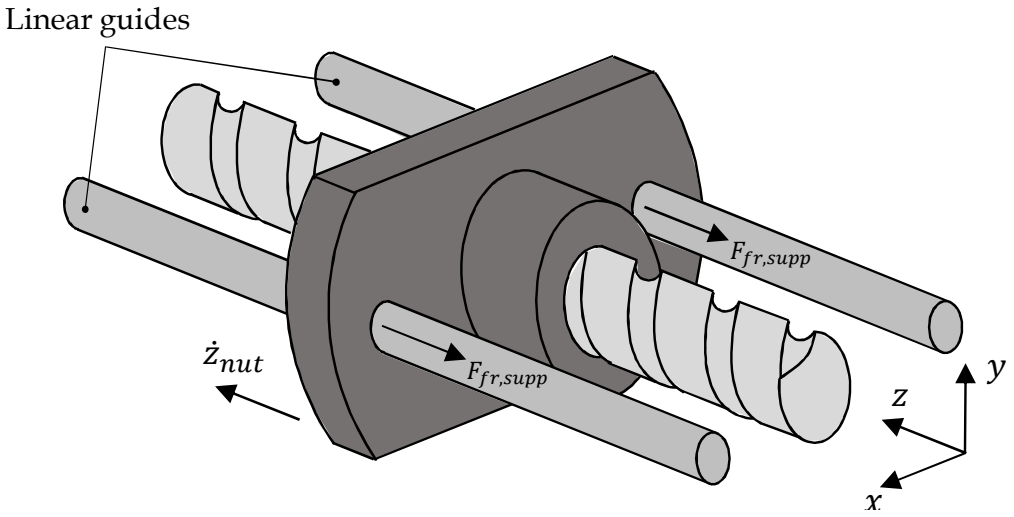

Fig. 7.9 Linear guides on the nut.

investigation. The motor applies a torque on the screw shaft and the linear position and velocity of the nut are the feedbacks for respectively the position and speed control loops. The PI controller commands the motor depending on the error between the feedback and the set. On the nut, an external force acts as load disturbance: it has been considered to be axial with the screw shaft but it could also be applied eccentrically.

7.7 Thermal model

The thermal flux per unit of contact area [$\mathrm{W/m^2}$] generated by the shearing of the lubricant can be obtained as:

$$q_{lub} = \tau |u_1 - u_2| \tag{7.65}$$

while that generated from the direct contact of asperities depends on the Péclet number, according to [87].

The relative weight of the two contribution on the total flux generated in the contact is determined by the load share function $f(\Lambda)$ which indicates how much area is in direct contact for mixed lubrication conditions.

The fluxes coming from each contact are the inputs to the thermal model, which describes the time evolution of the temperature of each single body and, therefore, determines the temperature of the lubricant layer at each time step. It is important since the lubricant properties are temperature dependent. Furthermore, if a direct contact between asperities occurs the flash temperature can reach very high values, generating a high thermal flux which causes a rapid increase in the lubricant temperature and a deterioration of the viscosity and the load capacity of the film thickness, causing a self-exciting degradation process.

Currently, the time evolution model of the components' temperature is not implemented yet, but it will be developed soon. The current model considers a constant operating temperature of the lubricant and the bodies, not influenced by the friction heat.

Depending on the temperature, the thermal deformation of the bodies are taken into account. Applying the coefficient of thermal expansion in three dimensions to the spheres and the gothic arch grooves of the screw shaft and nuts the following expressions are obtained:

$$r_b(T) = r_{b,ref} + \alpha_{Tlin}\left(T - T_{ref}\right) \tag{7.66}$$

$$L(T) = L_{ref} - 3.043 \times 10^{-9}\left(T - T_{ref}\right) \tag{7.67}$$

$$H_{screw}(T) = H_{ref} + 9.528 \times 10^{-8}\left(T - T_{ref}\right) \tag{7.68}$$

$$H_{nut}(T) = H_{ref} - 9.679 \times 10^{-8}\left(T - T_{ref}\right) \tag{7.69}$$

$$r_s(T) = r_{s,ref} + 2.012 \times 10^{-8}\left(T - T_{ref}\right) \tag{7.70}$$

$$r_m(T) = r_{m,ref} + \alpha_{Tlin}\left(T - T_{ref}\right) \tag{7.71}$$

$$p(T) = p_{ref} + \alpha_{Tlin}\left(T - T_{ref}\right) \tag{7.72}$$

where the reference temperature correspondent to the nominal geometric dimensions is 20 [°C] and $\alpha_{Tlin} = 12 \times 10^{-6}[\mathrm{K}^{-1}]$ is the steel coefficient of thermal expansion.

It can be noted that the centre radius offset H varies with different rates for the screw and nut raceways due to their different radial distance from the screw shaft axis. Since the temperature currently does not vary during the simulation, also the geometrical dimensions remain constant.

The coefficients of Eqns. 7.67–7.70 are typical of the ball screw characterised by the dimensions listed in Tab. 7.5.

7.8 Degradation models

Two degradation models have been inserted: the lubricant ageing (described in Sec. 6.7.1) and the abrasive wear model, which is described hereinafter.

The flowchart shown in Fig. 7.10 graphically shows the calculation procedure followed to obtain the friction forces and moments in a lubricated contact, explained in Sec. 7.4.2, with the addition of the lubricant starvation and wear and ageing degradation models. The time variant inputs are coloured in cyan, the constants in pale salmon and the degradation models in olive green.

7.8.1 Wear

Abrasive wear is modelled with the commonly used Archard equation [237], which expresses the abraded volume as:

$$V_w = K_w \frac{F_n L_w}{H_w} \tag{7.73}$$

where L_w is the travelled distance during the abrasion, H_w is the hardness of the softer material (equal to $\simeq 1$ [GPa] for steel) and K_w is the Archard's wear constant. In case of metal on metal contact, the latter assumes the values tabulated in Tab. 7.4.

In order to be implemented in the dynamic model, Eq. 7.73 can be rewritten as

$$V_w = \int_{t_0}^{t} K_w \frac{F_n v_{rel}}{H_w} dt \tag{7.74}$$

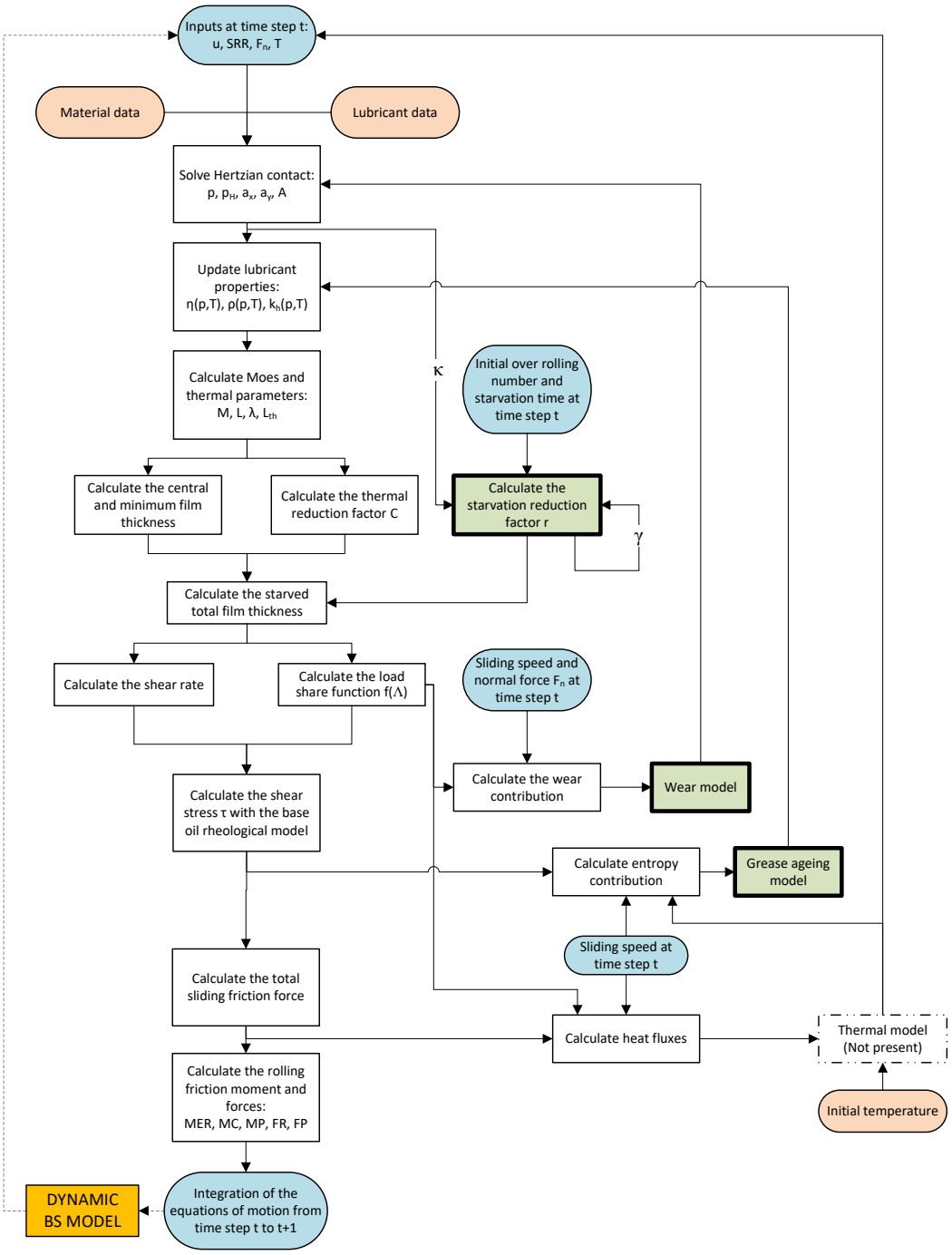

Fig. 7.10 Lubrication model flowchart with degradations.

Table 7.4 Archard's wear coefficients for steel–steel contact.

Symbol	Lubrication	Value
K_{lub}	Yes	1.6×10^{-9}
K_{dry}	No	1×10^{-3}

where, similarly to Sec. 7.4.1, $v_{rel} = |\mathbf{v}^B_{t_{CP_{S1}/B}}|$ is the relative speed of the surfaces.

The Archard's wear coefficient is a parameter whose value includes the probability of interaction of the asperities depending on the film thickness, i.e. it depends on the Tallian parameter Λ. Therefore, it can be expressed as

$$K_w = K_{lub} + \left(K_{dry} - K_{lub}\right) f(\Lambda) \tag{7.75}$$

It is assumed that the total wear volume, obtained as the sum of the single contact abraded volumes, is distributed along an abrasion area in general interested by wear, similarly to [115]. The abrasion area is different from time step to time step and for the screw and nut grooves. Indeed, it is calculated as a rectangle with the major side equal to the length of the helix on which the spheres move and the minor side equal to the mean of the instantaneous contact footprint half widths in the transverse directions with respect to the $\widehat{\mathbf{t}}$ axis:

$$A_{w_{ij}} = \sum_{k=1}^{Z} a_{yk_{ij}} l_i \quad \text{with} \quad i = S, N \quad j = 1, 2 \tag{7.76}$$

where Z is the number of sphere actually in contact (as in Chapter 5). Since each sphere can have intermittent contacts with each half groove, its contribution is considered only if the interpenetration is grater than zero. Therefore, each half groove can be subjected to different wear extents, depending on the operative conditions. The length of the track interested by wear $l_{s,n}$ can be written as:

$$l_{s,n} = \frac{2\pi \left(r_m \mp r_b \cos\left(\alpha_{sn}\right)\right) n_t}{\cos\left[\arctan\left(\frac{p}{2\pi(r_m \mp r_b \cos(\alpha_{sn}))}\right)\right]} \tag{7.77}$$

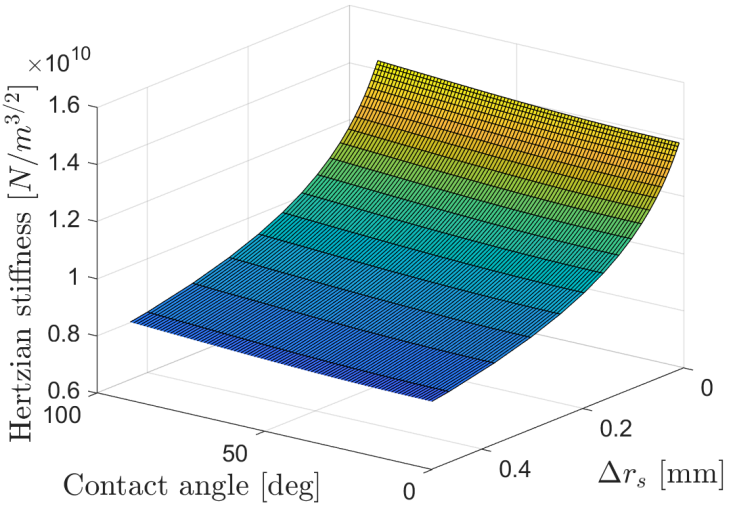

Fig. 7.11 Variation of the sphere–screw Hertzian contact stiffness with the contact angle and the wear depth.

where n_t is the number of helix turns occupied by the spheres. The $+$ and $-$ are referred respectively to the nut and the screw contact points, and it is assumed $\alpha_{S1} = \alpha_{S2} = \alpha_{N1} = \alpha_{N2} = \alpha_{sn} = 45°$.

Therefore, the radial amount of material lost in the wear process for the screw and the nut grooves can be approximated as:

$$\begin{aligned} \Delta r_{s_{Sj}} &= \frac{V_{w_{Sj}}}{A_{w_{Sj}}} \\ \Delta r_{n_{Nj}} &= \frac{V_{w_{Nj}}}{A_{w_{Nj}}} \end{aligned} \qquad \text{with} \quad j = 1,2 \tag{7.78}$$

To take into consideration the variability of the groove radii r_s and r_n with wear, some of the formulae of Secs. 7.2 and 7.3 must be modified. Considering that the secondary curvature radius of the S1 groove becomes $r_s + \Delta r_{s_{S1}}$, the contact stiffness becomes dependent also on $\Delta r_{s_{S1}}$ beside the contact angle. Therefore, Fig. 7.6 turns into Fig. 7.11, which shows a decrement in the sphere–screw stiffness with the increase of the wear depth. Consequently, also the contact area dimensions a_x and a_y varies accordingly.

The second contact condition of Eq. 7.12 must be written as:

$$|\mathbf{R}^{B}_{F/C_{1s}}| \geq r_s + \Delta r_{s_{S1}} - r_b \tag{7.79}$$

The position of the contact point with respect to the groove curvature centre expressed in *Btnb* (Eq. 7.15) becomes:

$$\mathbf{R}^{B}_{CP_{S1}/C_{1s}} = (r_s + \Delta r_{s_{S1}} + \delta_{g_{S1}})\,\mathbf{d}^{B}_{n_{F/C_{1s}}} \tag{7.80}$$

Finally, the equivalent radius in the transverse direction R_y (Eq. 6.33) becomes:

$$\frac{1}{R_{y_{S1}}} = +\frac{1}{r_b} - \frac{1}{r_s + \Delta r_{s_{S1}}} \tag{7.81}$$

The same modifications are applied to the other three half grooves.

7.9 Simulation results

In this section, the results of various simulations are shown and analysed in order to highlight the kind of data made available from the model, to understand the dynamic behaviour of the sphere under different conditions and to investigate the performance of the BS mechanism.

All the results in this section, except for Sec. 7.9.2, have been obtained simulating a preloaded double nut BS with the characteristics listed in Tab. 7.5. In every simulation, unless otherwise specified, the gravity has been oriented along $-\widehat{\mathbf{z}}$. The Simscape software allows to visualise the outcome of a simulation in terms of displacements and rotations of each body: in Fig. 7.12 the 3D representation of the model in the initial configuration is shown.

7.9.1 Comparison with literature results

The kinematic results of the model have been verified with the formulae present in literature [98], which are, although, valid only for steady state conditions. Therefore, a constant speed has been imposed to the BS in the dynamic model and the affinity

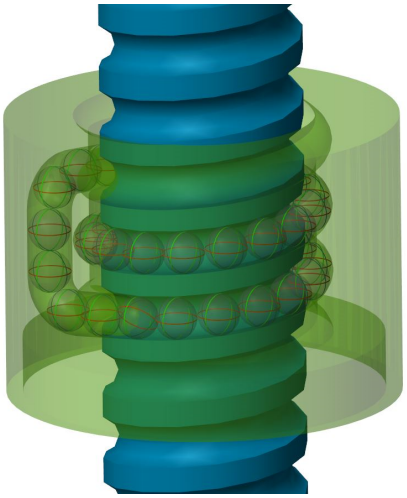

Fig. 7.12 Visual representation of the Simscape multibody model.

of the results have been evaluated only in the last part of the simulation, once the system accelerations disappeared.

The comparison outcome, shown in Fig. 7.13, demonstrates a close match between the model and the literature formulas. Figures 7.13a and 7.13b depict respectively the revolution speed ω_m of the considered sphere with regard to the ground and the spinning speed ω_R with regard to the screw shaft.

Wei et al. [98] expressed these velocities as:

$$\boldsymbol{\omega}_R = \begin{bmatrix} |\boldsymbol{\omega}_R|\cos(\beta)\sin(\beta') \\ -|\boldsymbol{\omega}_R|\cos(\beta)\cos(\beta') \\ |\boldsymbol{\omega}_R|\sin(\beta) \end{bmatrix}^T \begin{Bmatrix} \widehat{\mathbf{t}} \\ \widehat{\mathbf{n}} \\ \widehat{\mathbf{b}} \end{Bmatrix} \tag{7.82}$$

$$\boldsymbol{\omega}_m = \frac{\dot{\Omega}}{1 + \frac{\left[1+\frac{r_b}{r_m}\cos(\alpha_{Nj})\left[\cos(\alpha_{Sj})+\tan(\beta)\sin(\alpha_{Nj})\right]\right]}{\left[1-\frac{r_b}{r_m}\cos(\alpha_{Sj})\left[\cos(\alpha_{Nj})+\tan(\beta)\sin(\alpha_{Nj})\right]\right]}} \widehat{\mathbf{z}} \tag{7.83}$$

where $j = 1,2$ and β and β' are two gyroscopic angles defined in [98] that can be obtained from the simulation data, known the contact angles. The components of the spinning speed, calculated from Eq. 7.82, are shown in Fig. 7.13c.

Finally, the peripheral speed of the sphere in the contact point with the screw shaft groove is represented in Fig. 7.13d and compared with the following literature formula [97]:

Table 7.5 Ball screw parameters.

Geometrical parameter	Symbol	Value	Units
Screw pitch circle radius	r_m	8	mm
Screw lead	p	5	mm
Ball radius	r_b	1.5875	mm
Centre radius offset	H	0.0629	mm
Ogival offset	L	0.0505	mm
Screw and nut groove conformity factor	$f_{s,n}$	0.528	
Screw shaft moment of inertia around $\widehat{\mathbf{z}}$ axis	I_s	9.1893	kg mm^2
Loaded turns number	n_t	1.75	
Nut mass	M_n	0.275	kg
Total number of spheres	Z_{tot}	35	
Nominal helix angle	α_e	5.679	deg
Nominal contact angle	α	45.13	deg
Ball roughness [165]	σ_b	41.56	nm
Grooves roughness [165]	σ_g	11.56	nm
Screw, nut and ball elasticity modulus	$E_{s,n,b}$	210	GPa
Screw, nut and ball Poisson modulus	$\nu_{s,n,b}$	0.29	
Dynamic load	C_a	8.2	kN
Static load	C_0	13	kN
Critical screw angular speed	$\dot{\Omega}_{cr}$	18000	rpm

$$\mathbf{V}_{per_{BS}} = \begin{bmatrix} \dfrac{r_m}{\cos(\alpha_e)}\left(\omega_m - \dot{\Omega}\right) + r_m\dot{\Omega}\cos(\alpha_e) + \\ -r_b\left[\cos\left(\alpha_{Sj}\right)\boldsymbol{\omega}_R\cdot\widehat{\mathbf{b}} - \sin\left(\alpha_{Sj}\right)\boldsymbol{\omega}_R\cdot\widehat{\mathbf{n}}\right] \\ -r_b\sin\left(\alpha_{Sj}\right)\boldsymbol{\omega}_R\cdot\widehat{\mathbf{t}} \\ -r_m\dot{\Omega}\sin(\alpha_e) + r_b\cos\left(\alpha_{Sj}\right)\boldsymbol{\omega}_R\cdot\widehat{\mathbf{t}} \end{bmatrix}^T \begin{Bmatrix} \widehat{\mathbf{t}} \\ \widehat{\mathbf{n}} \\ \widehat{\mathbf{b}} \end{Bmatrix} \tag{7.84}$$

The simulation, from which the results shown in Fig. 7.13 have been obtained, has been performed giving a negative speed smooth step command from 0 to -1000 [rpm]. Consequently, the nut moves in the positive direction of the $\widehat{\mathbf{z}}$ axis, upwards, and the spheres move in the positive direction of the $\widehat{\mathbf{t}}$ axis if observed from the screw shaft, while they move in the negative direction if observed from the ground.

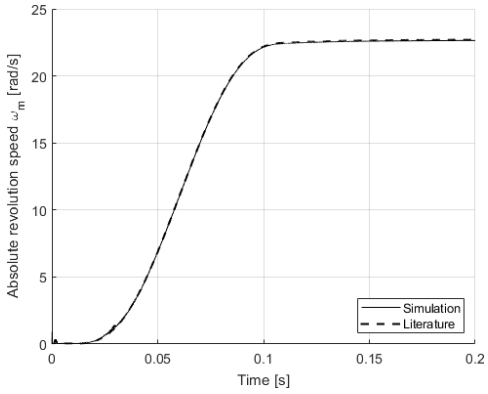

(a) Sphere revolution speed magnitude relative to ground.

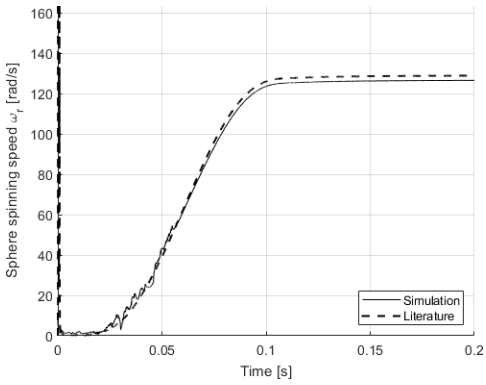

(b) Sphere spin speed magnitude relative to ground.

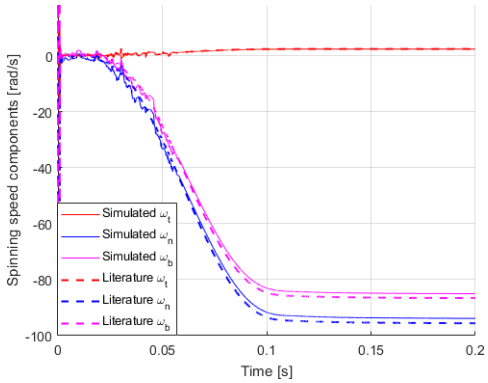

(c) Spin speed components relative to ground.

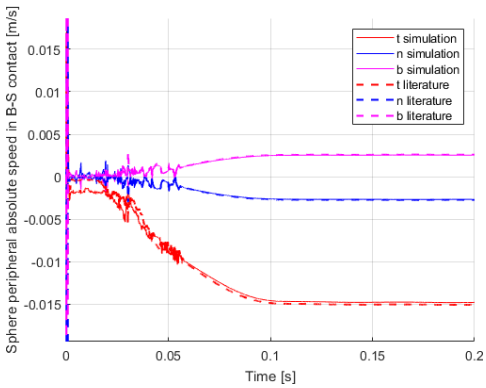

(d) Sphere peripheral speed components relative to ground in the sphere/screw contact point.

Fig. 7.13 Comparison between dynamic model results and literature formulas [98].

The spin speed components on $\widehat{\mathbf{n}}$ and $\widehat{\mathbf{b}}$ axes are both negative, in accordance with the screw rolling motion and the fact that, due to gravity, $S1$ and $N2$ are the active half grooves.

Since the screw shaft is the driving component, its velocity in the contact point is higher than the velocity of the sphere in the same location. Therefore, since the screw speed is negative and since the considered BS has a right-hand helix, the screw surface drags the sphere surface along $-\widehat{\mathbf{t}}$, as shown from the red curve of Fig. 7.13d.

7.9.2 Multiple contact points with the nut groove

In this section, a not preloaded single nut BS with the dimensions of Tab. 5.1 is simulated. Since the elevated number of spheres requires a high simulation time, the empirical friction model has been used in order to speed up the simulation.

The combination of geometrical and friction parameters and have been selected in order to highlight the possibility of a third contact point of the sphere with the grooves [94]. In particular, except for the case of oversized preloaded balls for which the spheres touches every half groove, if a little amount of backlash is present the spheres can only touch in maximum three points. In general, if this happens, it is more likely to have two contact points with the two nut half grooves and only one with one of the two screw half grooves because of the centrifugal force.

A velocity smooth step command is imposed to the screw shaft to go from 0 to 1000 [rpm] from 0.15 [s] to 1 [s], as can be seen in Fig. 7.14. The simulation lasts 1.5 s.

Before the start of the motion, a smooth opposing external force of 1 [kN] is applied on the nut axially from 0.01 [s] to 0.1 [s]. As soon as the external force arises, the controller starts to generate a torque to equilibrate the disturbance, since the screw is still commanded to maintain null speed. Contextually, because of the compression of the system, the contact angles vary a little and remain almost identical since the system is still steady.

At 0.15 [s] the speed command starts and the torque has to be increased as well to overcome the friction. The spheres start to move: the spin speed components on $\widehat{\mathbf{n}}$ and $\widehat{\mathbf{b}}$ rise while that along $\widehat{\mathbf{t}}$ remains very small. This means that the sphere spin speed lies almost entirely on the $n-b$ plane, as shown in Fig. 7.15a. The components on $\widehat{\mathbf{n}}$ and $\widehat{\mathbf{b}}$ are similar in magnitude because the contact angle is almost 45°.

At approximately 0.55 [s], the speed becomes so high that the centrifugal forces pushes the spheres outwards, towards the nut, until a third contact point is created. This originates a sudden friction force in the just created contact, which destabilises the motion of the sphere. The original contact angles of $S2$ and $N1$ diverge and that of $N2$ arises. At the same time, the input torque increases and the mechanical efficiency presents a drop. The spin speed vector aligns almost entirely along $-\widehat{\mathbf{b}}$ to accommodate the new contact conditions, as can be seen in Fig. 7.15b.

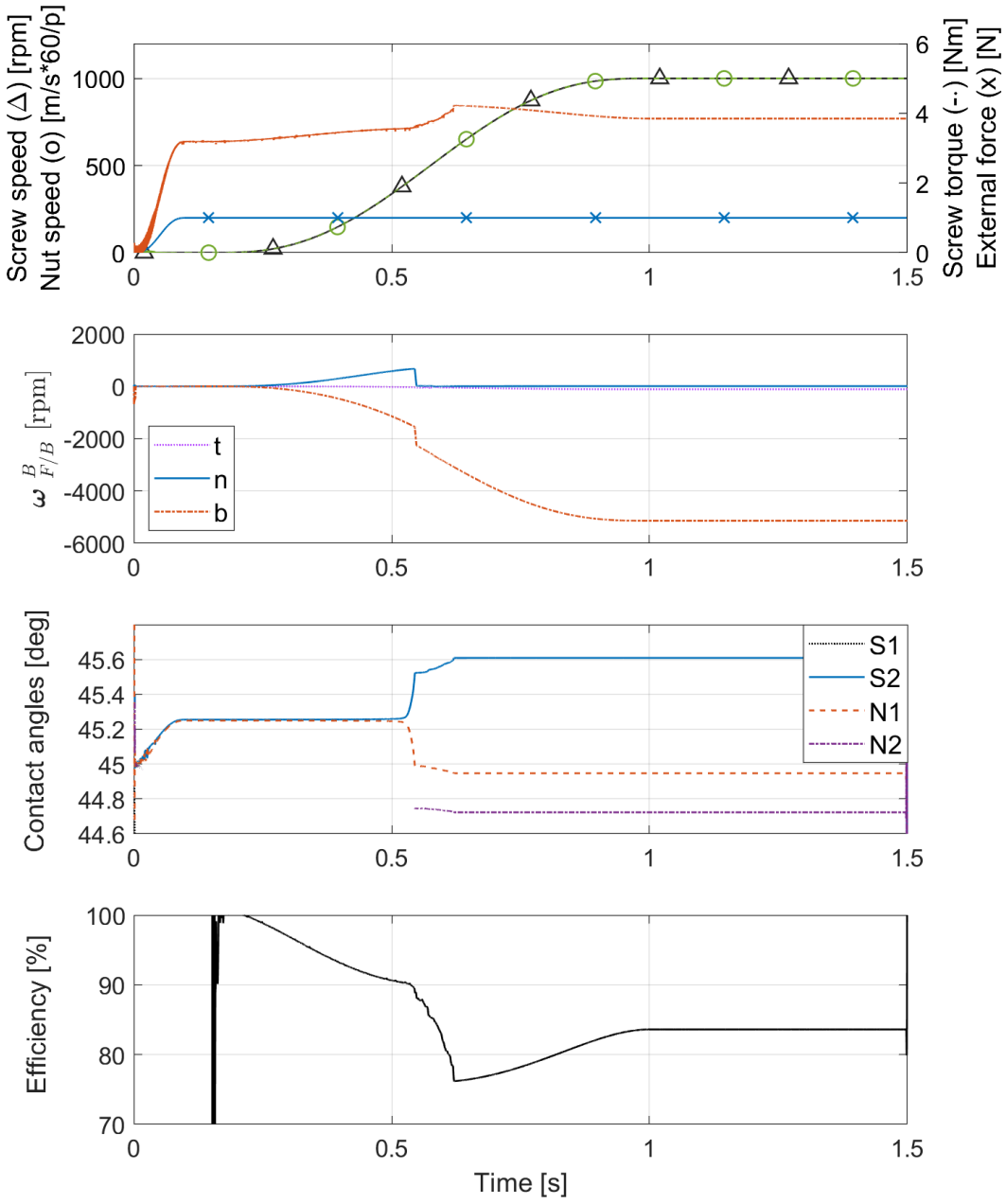

Fig. 7.14 Simulation results with three contact points [94].

Finally, when the speed reaches the set value, the system finds a new equilibrium condition and the mechanical efficiency slightly recovers. The presence of a third point causes more sliding and friction in every contact point, therefore the mechanical efficiency shows a value of $\approx 84\%$, smaller than the usual values.

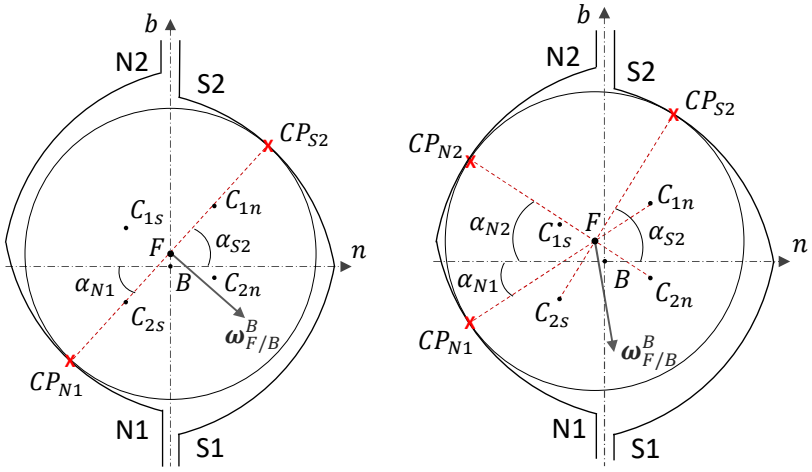

(a) Two contact points. (b) Three contact points.

Fig. 7.15 Contact angles and spin velocity with a third contact point [94].

7.9.3 Backlash

This section aims to put in evidence the dynamic characteristics of the model and to investigate the behaviour of the internal components in presence of a backlash of 0.05 [mm].

The BS is driven by an electric motor, controlled through a closed loop speed PI controller. A 5 [Hz] sinusoidal speed command with amplitude of 500 [rpm] has been imposed to the controller. As in Chapter 5, the command has been multiplied by a smooth step from 0 to 1 to avoid discontinuities. An external force of 1 [kN] has been applied smoothly from 0.25 to 0.3 [s]. Since the BS is simulated vertically, the weight of the nut keeps the backlash gap always closed if sufficient acceleration is not imposed. To overcome this problem, that would hinder the backlash observability, the support friction has been added according to the equations in Sec. 7.6: a total static and dynamic friction of 100 [N] and 70 [N] respectively have been considered.

The screw and nut equivalent axial displacements are shown in Fig. 7.16a, in which the effect of the backlash and friction can be observed in the stationary points when the speed is reversed. The effect is more visible if the speed plot is observed (Fig. 7.16b). In the first three null speed points, at 0.05 [s], 0.1 [s] and 0.2 [s], while the screw shaft speed follows the command, the nut speed stops at zero until the backlash gap is closed and the axial force overcomes the static friction of the supports.

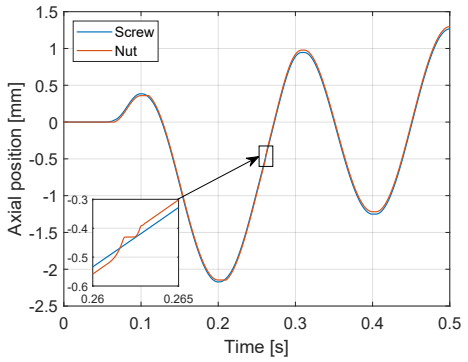

(a) Axial displacement.

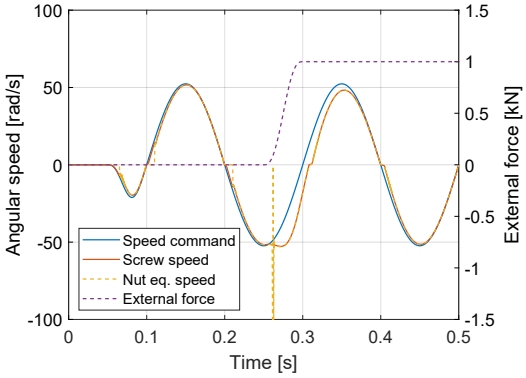

(b) Angular speeds.

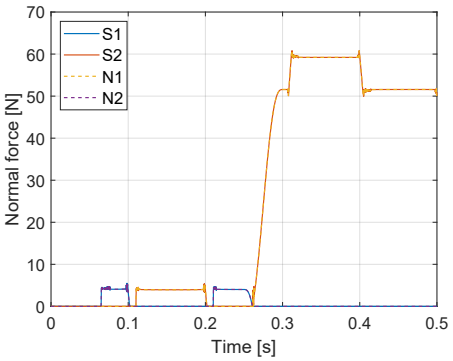

(c) Normal contact force.

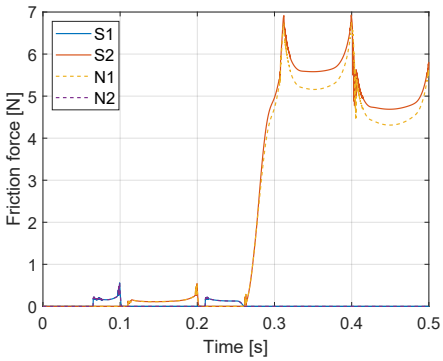

(d) Friction contact force.

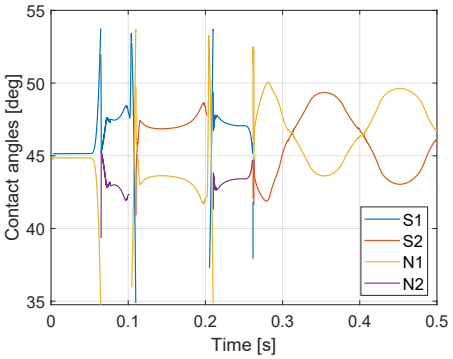

(e) Contact angles.

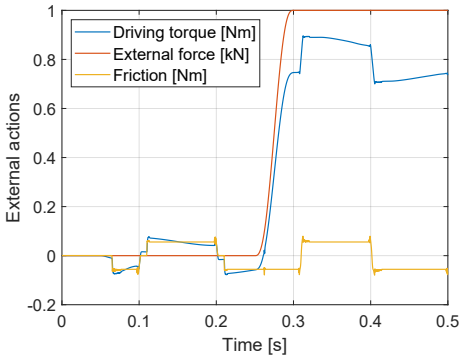

(f) Input torque, friction torque and external force.

Fig. 7.16 Sinusoidal speed command with 0.05 [mm] axial backlash, no preload and external force.

Indeed, looking at Fig. 7.16c, between the vanishing of the contact forces on two half grooves and the rise of those on the other two half grooves, there is a no force gap which identifies the moments in which the nut is steady and the screw is reversing the motion, within the open gap. The intervention of the static friction in

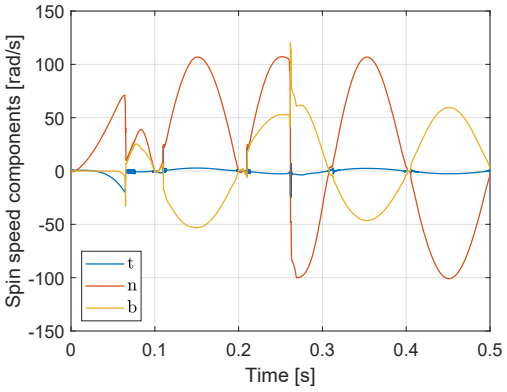

(a) Sphere spin speed.

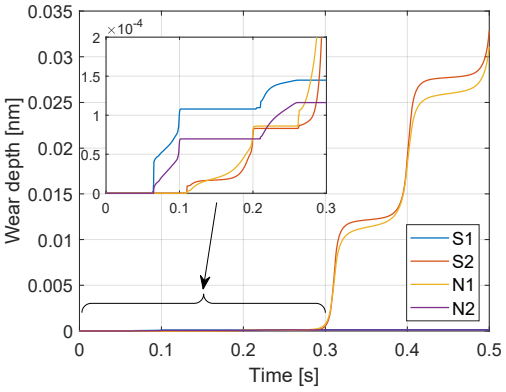

(b) Wear depth.

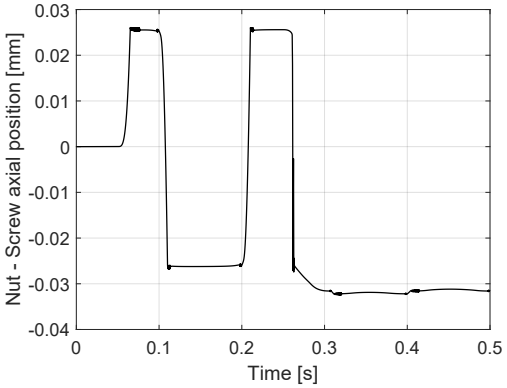

(c) Axial position difference between nut and screw.

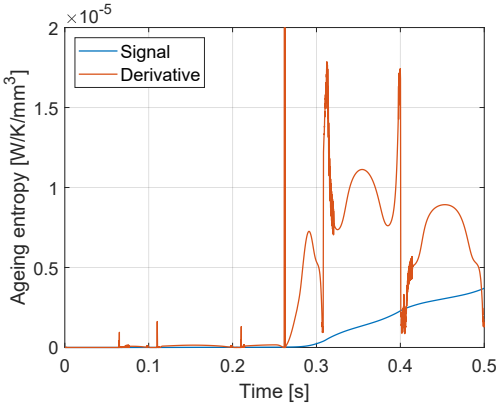

(d) Ageing entropy.

Fig. 7.17 Sinusoidal speed command with 0.05 [mm] axial backlash, no preload and external force (continued).

these instants can be seen from the friction forces in Fig. 7.16d, which exhibit force peaks in proximity of the stops.

When the screw speed is negative, the nut velocity is positive and the $S1$ and $N2$ half grooves are active, as can be seen from Figs. 7.16c and 7.16e. In the latter, the contact angles vary with the speed and the load and the screw contact angle is higher than the nut contact angle in absence of external load. The mean value remains approximately 45°, as in the case of rest state in the first 0.05 [s] of simulation.

Figure 7.17a shows the spin speed components of the considered sphere with respect to the ground. It can be observed that, for example, when the screw speed is positive and the active half grooves are $S2$ and $N1$, the component along $\widehat{\mathbf{n}}$ is positive and that along $\widehat{\mathbf{b}}$ negative: this means that the spin speed is oriented in the fourth quadrant, equivalently to the condition indicated in the scheme of Fig. 7.15. The

component along the $\widehat{\mathbf{t}}$ axis, due to the helix torsion, is always present but very small, in accordance with previous researches [98, 114, 89].

Until no external force is applied, the motor has to provide just the torque necessary to overcome the internal and support friction (Fig. 7.16f). The torque, external force and friction cause the backlash gap to open alternatively in both directions, depending on the sign of the external action. In Fig. 7.17c the difference between the nut and the equivalent screw position is depicted. Once the gap is closed without external force, i.e. when this value reaches the maximum or minimum, the elastic deformation is negligible with respect to the gap size, while it becomes considerable when the external force is present, i.e. from 0.25 [s] on.

When the external force is applied, the gap closes and remains closed for both displacement directions. While before the torque was always driving, from 0.25 [s] on, in presence of the external force, it drives the BS only for negative nut speeds and it acts as a brake for positive nut speeds. Indeed, the applied force is positive and it tries to drag the nut in the positive direction of the $\widehat{\mathbf{z}}$ axis. As soon as it is applied, the controller makes the torque to rise to compensate the disturb and then it continues to oscillate around this mean value to generate the sinusoidal motion, as shown in Fig. 7.16f. Due to the controller delay in responding to the disturbance, both the screw and nut speeds are slightly retarded with respect to the command (Fig. 7.16b).

The contacts are polarised by the application of the external force and $S2$ and $N1$ become the only two active half grooves: the $S2$ and $N1$ normal and friction forces rise while the other two decrease definitively (Figs. 7.16c and 7.16d). The support friction effect becomes even more visible in Fig. 7.16d. The contact angle angles on $S2$ and $N1$ oscillate around a mean value greater than the previous one, since it depends on the external force.

The application of the external force causes greater elastic deformations at the interfaces, as can be seen in the second part of Fig. 7.17c.

Concurrently, the wear depth of the active half grooves augments with the load and exhibits particular growths when the speed is reversed due to the increased temporary sliding speed between the sphere and the grooves. Also the lubricant is subjected to ageing and the entropy production is increased proportionally to the friction force and the sliding speed. In fact, Fig. 7.17d depicts the generated entropy

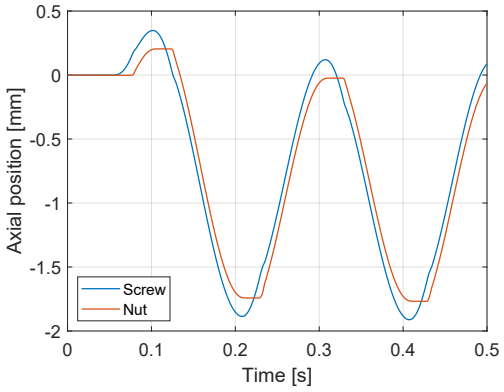

(a) Axial displacement.

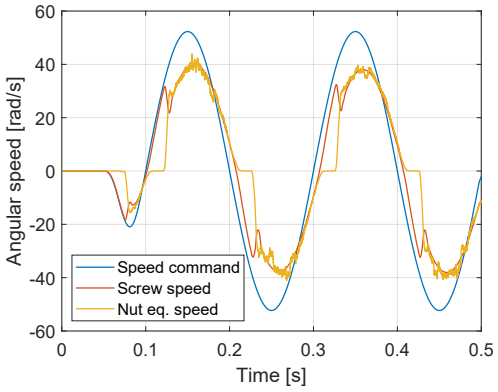

(b) Angular speeds.

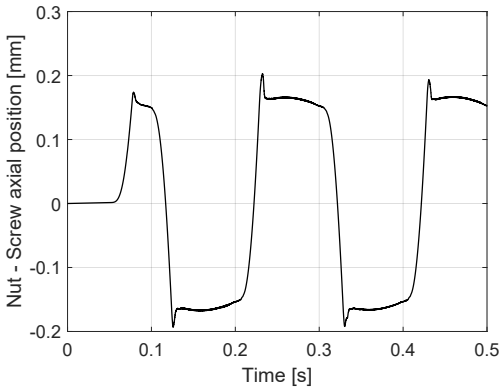

(c) Axial position difference between nut and screw.

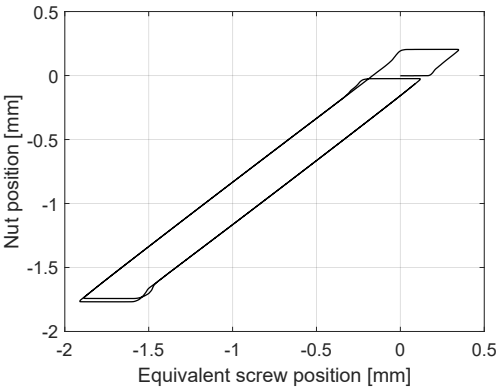

(d) Backlash hysteresis.

Fig. 7.18 Sinusoidal speed command with 0.3 [mm] axial backlash, no preload and external force (continued).

and its derivative in time, which shows the peaks in correspondence to the speed reversing points.

Similar graphs are shown in Fig. 7.18 for the case of a greater axial backlash of 0.3 [mm], value which can be observed in Fig. 7.18c. If the nut position is plotted against the equivalent screw axial position the backlash can be visualised by means of an hysteresis loop (Fig. 7.18d): the area enclosed in this loop is proportional to the backlash size and it depends also, in some extent, on the friction.

The application of a preload can produce the same effect of the external force in the second half of the simulation and maintain the backlash gap closed. A very short simulation has been carried out to show the axial deformation of the nut when a preload is applied. The screw shaft has been imposed as fixed and a triangular wave

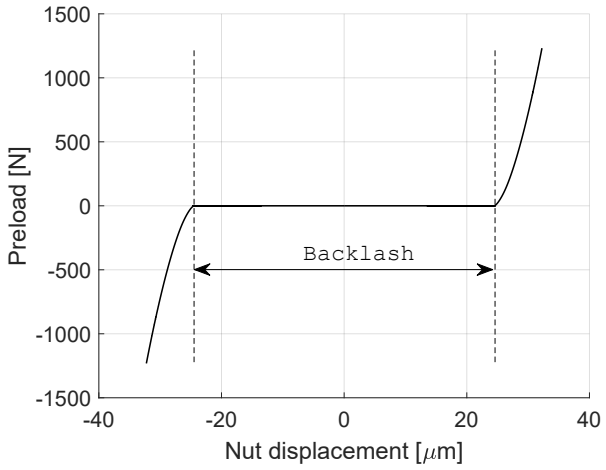

Fig. 7.19 Preload versus nut displacement with 0.05 [mm] backlash.

preload has been applied. The result in presence of a backlash gap of 0.05 [mm] is shown in Fig. 7.19.

7.9.4 Geometric errors

In previous paragraphs the following assumptions have been made:

- the bodies are rigid;
- an ideal revolute joint on the screw and a prismatic joint on the nut have been imposed for the moment;
- the groove geometry is ideally smooth.

Under these assumptions the load distribution on the spheres is uniform. However, if only one hypothesis is removed the load distribution becomes uneven (see Chapter 8).

In this analysis the screw speed of a BS with 25 spheres has been led to a regime condition at a constant speed of 500 [rpm], with a preload of 1800 [N] and an external force of 1000 [N], and the load distribution has been evaluated. Though, a geometric error in the radius has been added to each sphere, according to the error distribution in Fig. 7.20.

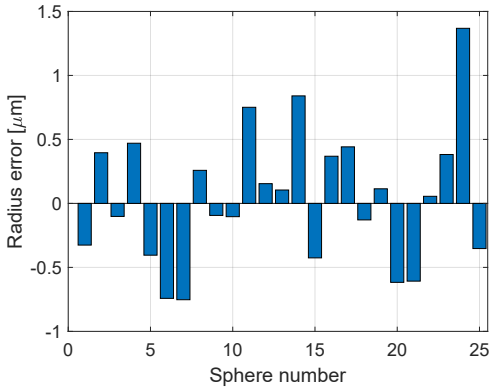

Fig. 7.20 Random radius error distribution on the spheres.

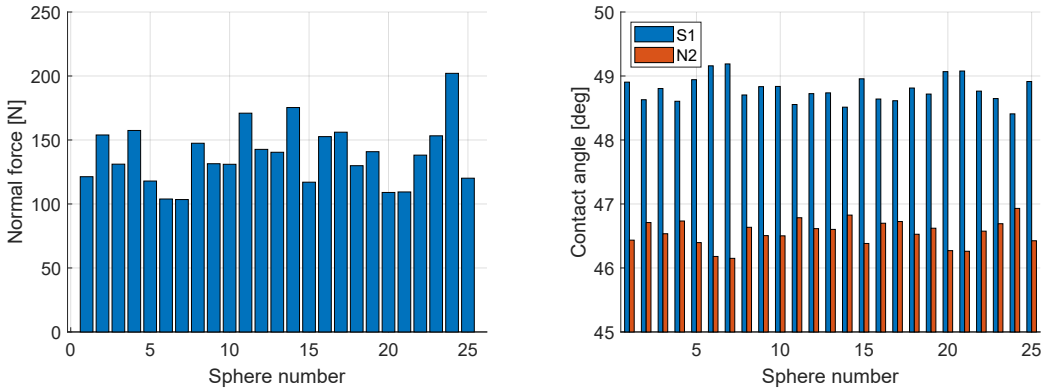

(a) Normal contact force distribution.

(b) Contact angles distribution.

Fig. 7.21 Sphere radius error effect on load distribution.

The resulting load and contact angles distributions are shown respectively in Fig. 7.21a and 7.21b. It can be observed that, as expected, the spheres with positive errors bear a higher load and vice versa. Since the radius errors are not too high, also the spheres with the minimum radii, such as the spheres number 6 and 7, are loaded. In fact, if the geometric error was too negative, the reaction forces given by the other loaded spheres could equilibrate the external force causing a deflection of the nut too small to load also the smaller spheres, which would remain unloaded.

It can be noted also that, in Fig. 7.21b, the more loaded the spheres, the closer the contact angles with the screw and nut grooves.

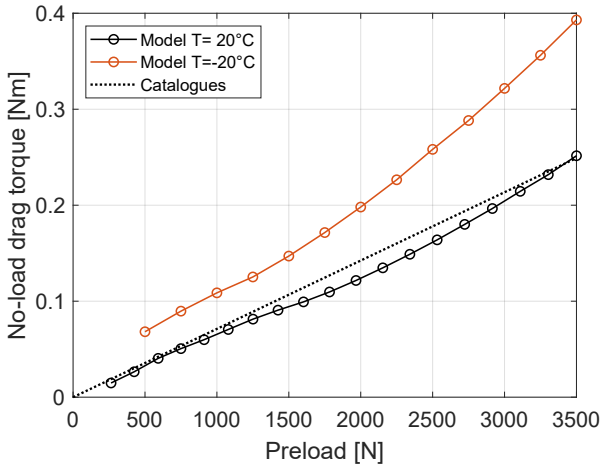

Fig. 7.22 Preload influence on the no–load drag torque for 500 [rpm] and two different temperatures.

7.9.5 No-load drag torque

The influence of the preload on the drag torque without external load is investigated in this section. Various parameters' dependences on the preload have been analysed for preload values up to 3500 [N].

Each point of Figs. 7.22–7.24 has been obtained as a mean of the analysed quantity for 0.3 [s] at constant speed of the BS. The screw shaft speed has been set to -500 [rpm], corresponding to a linear speed of the nuts of 41.7 [mm/s], with no load disturbance. The different behaviour of the BS at normal and low temperature has been investigated running the simulations for 20 [°C] and –20 [°C]. Since the gravity acts on $-\widehat{\mathbf{z}}$, and the nuts are moving along $+\widehat{\mathbf{z}}$, the only active half grooves are $S1$ and $N2$: thus, only their quantities are shown.

The manufacturers catalogues gives an estimation of the no–load drag torque using the following formula [78, 81, 80]:

$$T_{drag_0} = \frac{0.05 p F_{pr}}{2\pi\sqrt{\tan(\alpha_e)}} \tag{7.85}$$

which describes a linear correlation with the preload force F_{pr}.

The comparison between Eq. 7.85 and the model results at 20 [°C] and –20 [°C] is shown in Fig. 7.22. It can be observed that, at 20 [°C], the model drag torque

matches the catalogue formula estimation, but, for low temperatures, the friction increases and Eq. 7.85 underestimates the friction torque.

Figure 7.23 shows the various quantities involved in the contact, obtained from one random sphere. It is not granted that every sphere presents exactly the same values for each signal, but, because of the absence of external load and geometric errors and the presence of the prismatic joint on the nut assembly, reasonably all the spheres bear the same load and present the same trend of the investigated signals, besides the friction between adjacent spheres.

Since the screw speed is not excessive and the pitch circle diameter is small, the centrifugal force does not play an important role ($\approx 2[\mathrm{N}]$). In fact, in Fig. 7.23a it can be seen that the normal contact forces on $S1$ and $N2$ are almost equal. Nevertheless, the friction forces are different for the screw and nut grooves (Fig. 7.23b) because of the friction coefficient, depicted in Fig. 7.23c. As expected, the low temperature causes an increase of the frictional forces, observable also in Figs. 7.24a–7.24f.

It is worth to be highlighted that, in the contact point with the screw groove, the friction is slightly higher than in the contact point with the nut groove. This is due to the dimensions of the contact areas which depends on the curvature radii of the grooves. In fact, as shown in Fig. 7.23f, the contact area created on $N2$ is greater than that on $S1$, thus the contact pressure on the screw shaft is higher (Fig. 7.23e) and, therefore, the viscosity of the lubricant film increases, creating higher shear stress (Fig. 7.24a). The shear stress, however, is also influenced by the lubricant film thickness, which depends on the lubricant viscosity as well. Therefore, the shear stress increase derives by a balance of the two effects caused by the rise in viscosity: the shear stress lowering effect of thicker film, and the increasing effect of the viscosity itself.

Moreover, the film thickness determines also the probability of interaction between the asperities of the two surfaces, identified by the Tallian parameter (Eq. 6.50). In Fig. 7.24b, the Λ values can be observed: due to the higher viscosity, the film thickness on $S1$ is higher than on $N2$. However, this difference is more marked for low temperatures, due to the non–linear dependence of the lubricant viscosity with pressure for different temperatures described by the Roelands expression (Eq. 6.18). As a consequence, despite the friction increase due to higher viscosity, the wear of the grooves is substantially avoided in the case of low temperature since the BS operates in full film lubrication. On the contrary, at 20 [°C], the speed is not sufficient

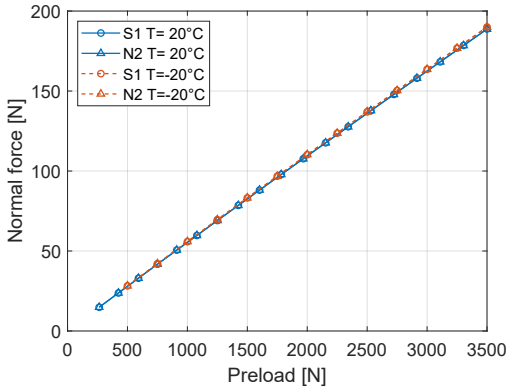

(a) Normal contact force.

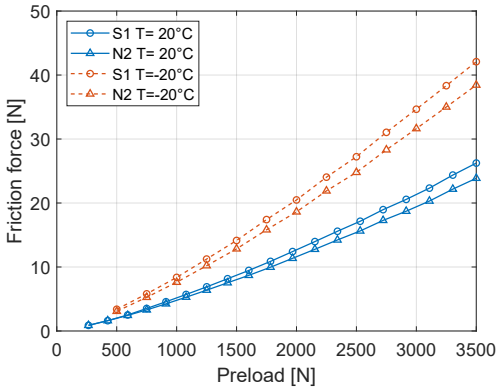

(b) Friction contact force.

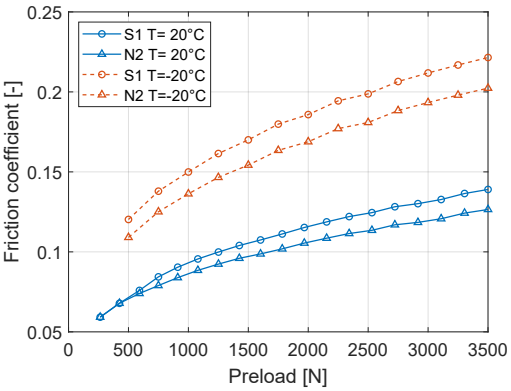

(c) Coefficient of friction.

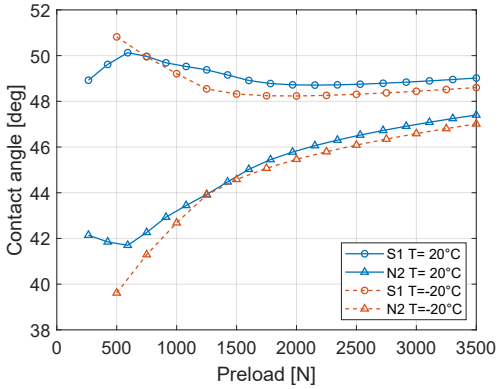

(d) Contact angles.

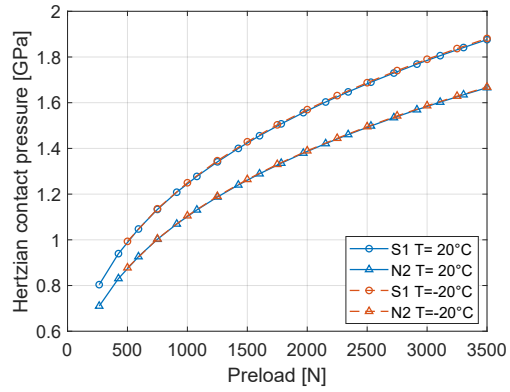

(e) Contact pressure.

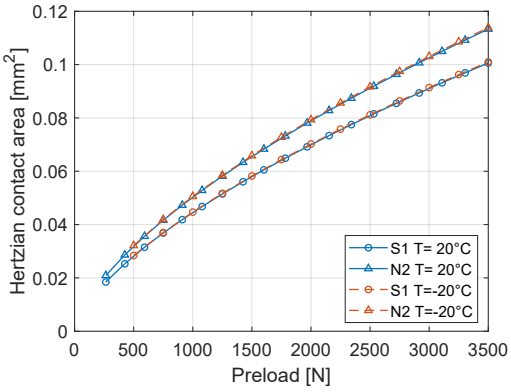

(f) Contact footprint area.

Fig. 7.23 Preload influence on contact model quantities for 500 [rpm] and no load for two different temperatures.

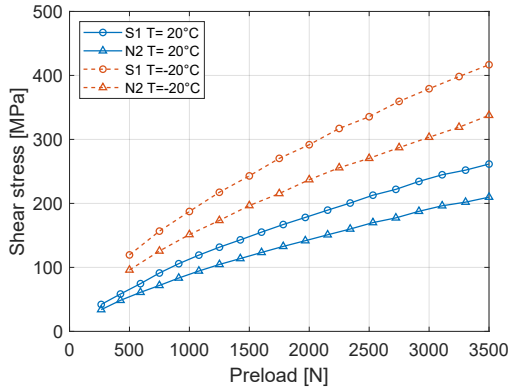

(a) Lubricant shear stress.

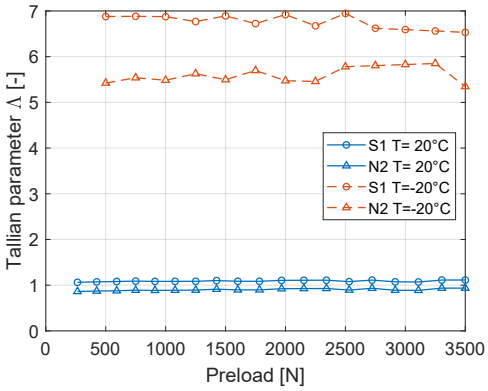

(b) Tallian parameter.

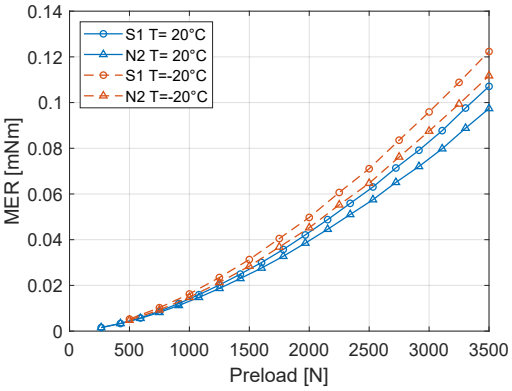

(c) MER moment.

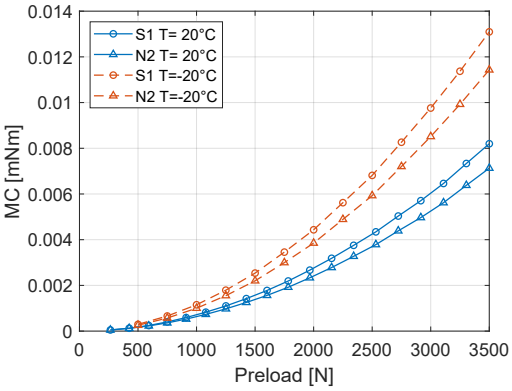

(d) MC moment.

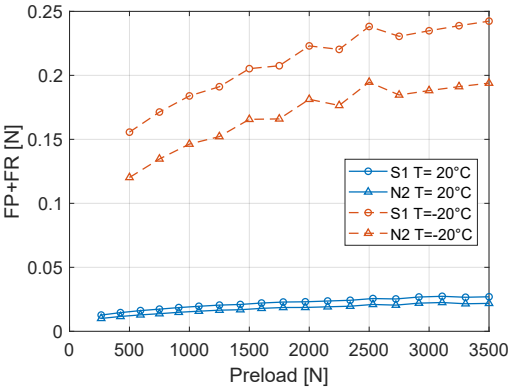

(e) FP and FR forces.

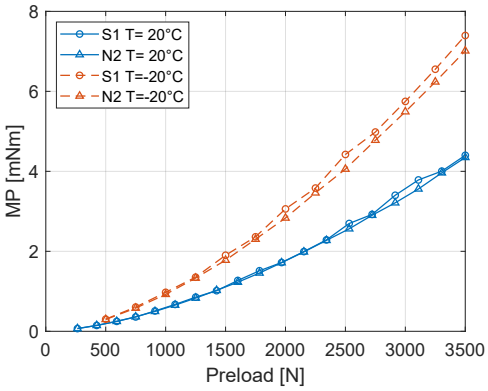

(f) MP moment.

Fig. 7.24 Preload influence on lubrication model quantities for 500 [rpm] and no load for two different temperatures.

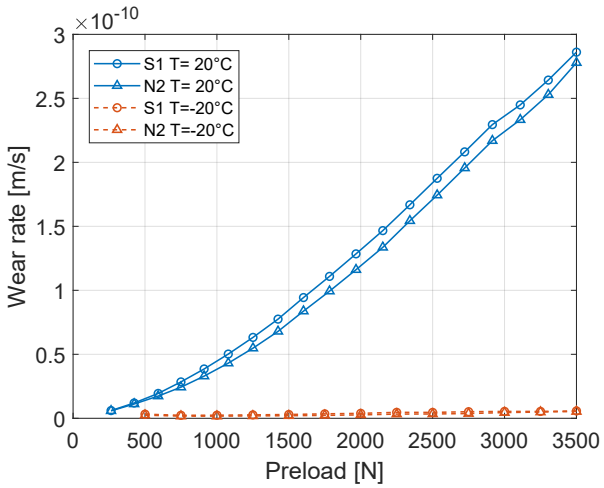

Fig. 7.25 Preload influence on the wear rate for 500 [rpm] and two different temperatures.

to create an enough thick film with this kind of lubricant and, therefore, the BS operates in mixed lubrication condition. The wear rates, expressed as the worn depth per second, are shown in Fig. 7.25 for the contacts with the screw and nut grooves.

The lubricant forces and the rolling and spin moments increases with the preload and with the lower temperature, as can be seen in Figs. 7.24c–7.24f.

Finally, the contact angles vary according to the normal force applied on the sphere, depending on the elastic deformations [74, 98], as shown in Fig. 7.23d. The contact angle with the screw increases with the axial load, represented by the preload in this case, while the contact angle with the nut groove decreases. However, the mean angle rises with the preload increase.

7.9.6 Ageing

The lubricant is a very important factor in the life duration of BSs since it determines the separation of the contacting surfaces, preserving them from advanced wear. In this section, how the ageing of the lubricating grease affects the overall behaviour of the entire mechanism is investigated.

The main effect of ageing are the diminish of the lubricating viscosity and consistency and the decrease of the grease yield stress (Sec. 6.7.1). However, it has been stated that BSs operates most of their life in mild starved conditions, where the lubricating media is essentially the base oil. Therefore, only the viscosity reduction

Table 7.6 Legend codes for ageing analysis.

Ageing		**Speed**		**External force**	
Code	[%]	Code	[rpm]	Code	[N]
A1	0	w1	–500	F1	–1000
A2	30	w2	–1000	F2	–4000
A3	60	w3	–1500		
A4	80	w4	–2000		
A5	90				

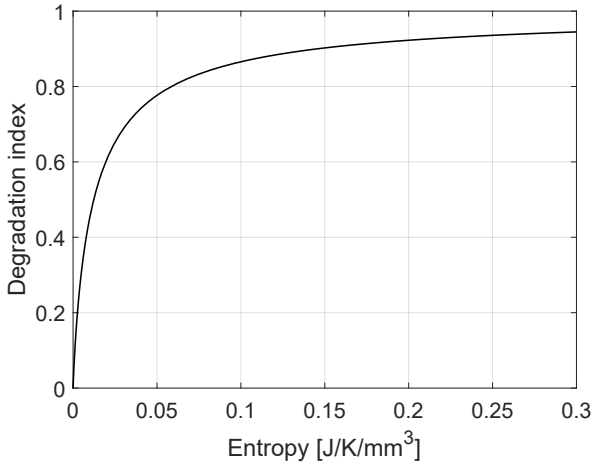

Fig. 7.26 Ageing degradation evolution with generated entropy according to Eq. 6.90 (0: healthy, 1: fully degraded)

has been thoroughly considered. According to Eq. 6.90 and the parameters in Tab. 6.2, the ageing evolution is depicted in Fig. 7.26 and shows an initial elevated degradation rate followed by a stabilization phase. In Fig. 7.26, a degradation index equal to 0 means a completely healthy lubricant, while the value of 1 represents a fully degraded grease.

Several simulations have been carried out to compose the graphs presented in this section. Five degradation levels have been investigated (0%, 30%, 60%, 80% and 90%), and, for each one, four negative speeds have been imposed (–500, –1000, –1500 and –2000 [rpm]) with two external force levels (–1000 and –4000 [N]) and a constant preload of 2000 [N] distancing the nuts. For legends' simplicity, the various conditions have been shortened with abbreviations, listed in Tab. 7.6

From this analysis, an important consideration emerged: the macroscopic instantaneous performance parameters are almost independent on the lubricant ageing

level. In fact, observing Figs. 7.27a, 7.27c and 7.27e it is visible that just the efficiency shows a very little increase with the ageing progression, while the other quantities remain almost unvaried. The efficiency increment is in the order of 0.5%, therefore it cannot be detected during field operations since it would be drown in the measurement noise and uncertainties. Moreover, as stated in Chapter 5, the efficiency is dependent on too many factors and, thus, a variation of its value could be due to several reasons and cannot be attributed uniquely to the lubricant ageing degradation.

This is an important observation from the point of view of fault detection since the signal normally adopted for the BS drive system control are not useful in detecting the lubricant status: direct analyses on the lubricant should be performed to estimate its health state, e.g. analysing the presence and size of dispersed contaminants and metal debris [227].

The speed is an influential factor in determining the efficiency decrease: in Fig. 7.27b the efficiency obtained with the high load (F2) is obviously higher since the friction power loss becomes smaller compared to the output power given by the BS mechanism.

The external load rise implies an offset in the contact angles, as seen also in Fig. 7.16e. Furthermore, as seen in Fig. 7.27d, the contact angle with the screw increases with the speed while that with the nut decreases. This variation with the speed is lower for higher external forces. The contact angles variation causes a geometrical decrease of the efficiency while the normal forces remain almost constant, dependent only on the external load.

The viscosity decrease involves the reduction of the lubricant film thickness, as shown in Fig. 7.28a. The film height is higher for small loads and high speeds, as can be observed in Fig. 7.28b. Consequently, if the lubricant film thickness becomes thinner, also the Tallian parameter decreases (Fig. 7.28c) and, thus, the probability of interaction between bodies' asperities becomes higher. In fact, Fig. 7.28e shows the wear depth rate for varying ageing levels, speeds and loads. The ageing progression leads to an increase of the wear rate, the more marked the more the load increases and the speed decreases.

It is worth to be highlighted that the Tallian parameter decreases from values in the range $5 \div 6$ to $3.5 \div 4.5$, therefore the load share function $f(\Lambda)$ does not change particularly since the lubrication regime remains in the full film lubrication

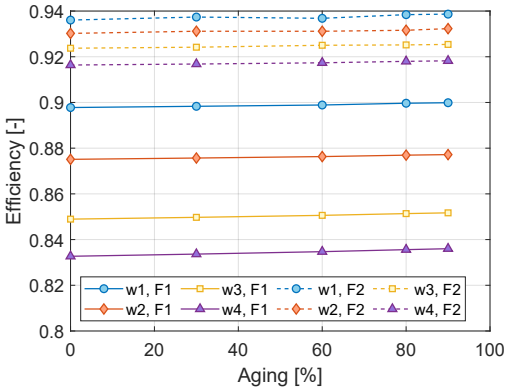

(a) Mechanical efficiency versus ageing level.

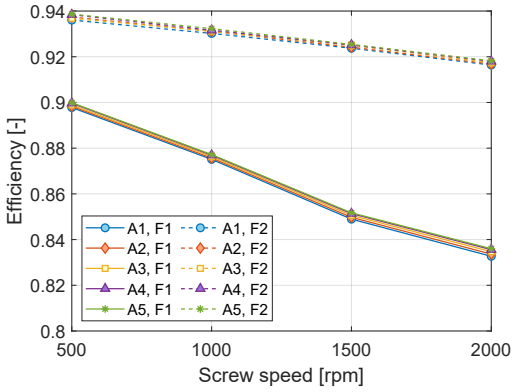

(b) Mechanical efficiency versus speed.

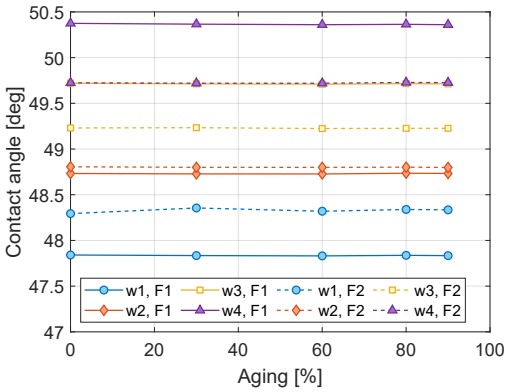

(c) Contact angles vesus ageing level.

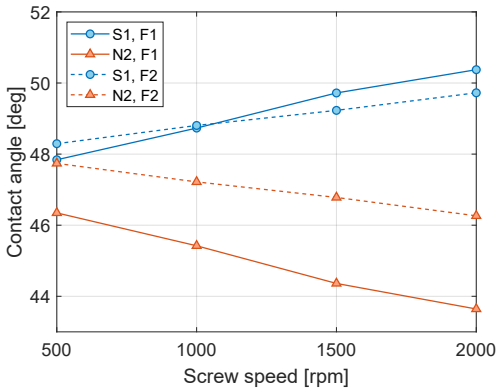

(d) Contact angles versus speed in nominal conditions.

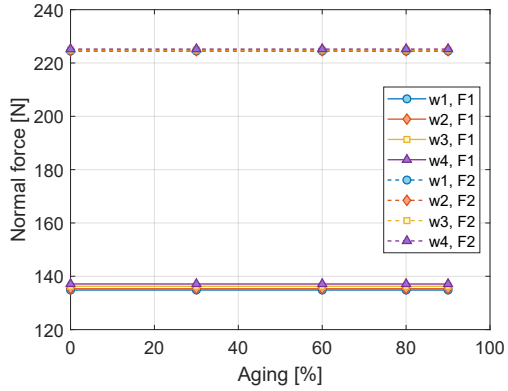

(e) Normal contact force versus ageing level.

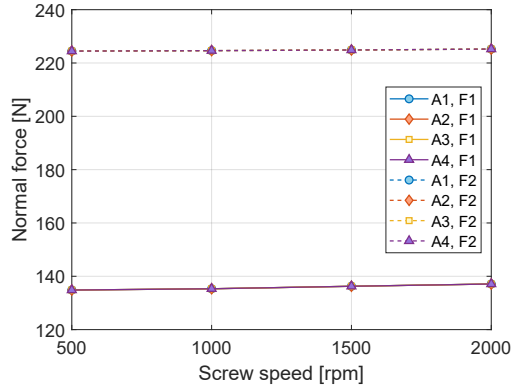

(f) Normal contact force versus speed.

Fig. 7.27 Ageing effect.

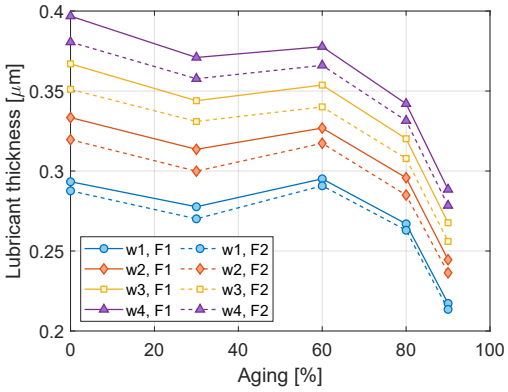

(a) Lubricant film thickness in $S1$ versus ageing level.

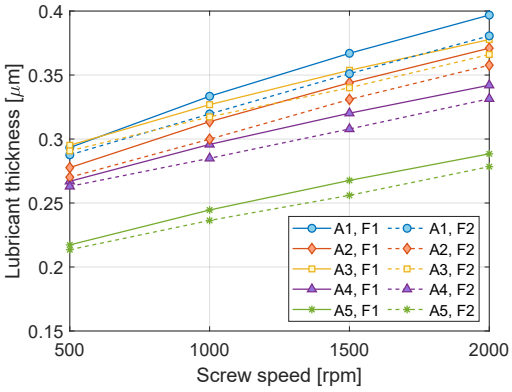

(b) Lubricant film thickness in $S1$ versus speed.

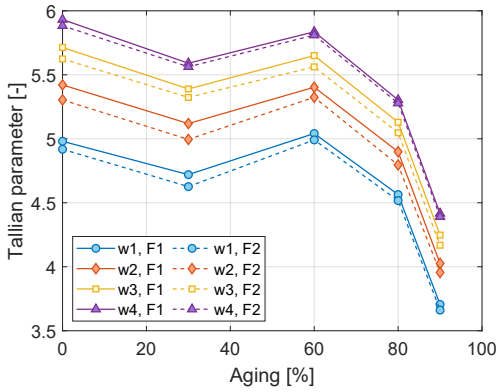

(c) Tallian parameter in $S1$ versus ageing level.

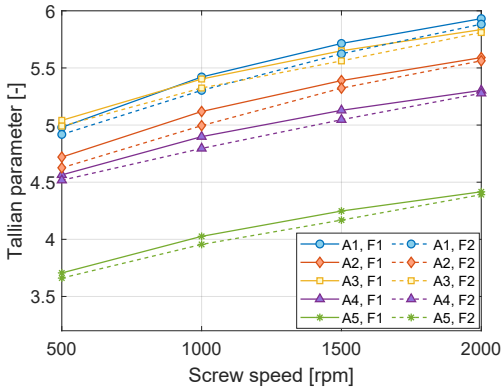

(d) Tallian parameter in $S1$ versus speed.

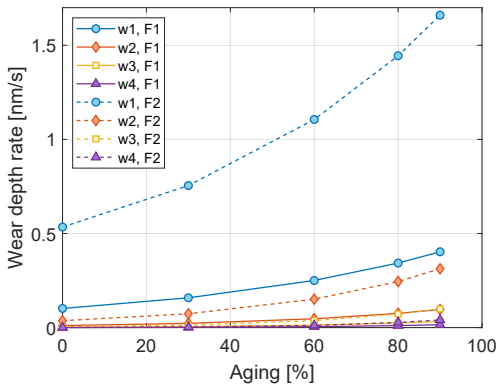

(e) Wear depth rate in $S1$ versus ageing level.

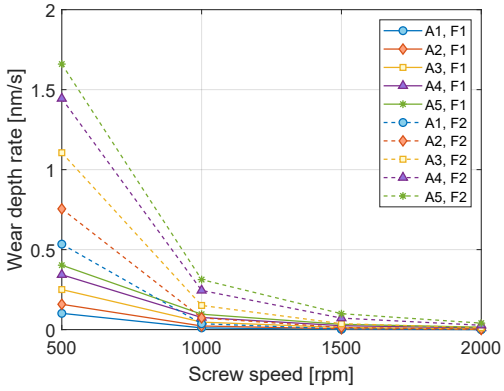

(f) Wear depth rate in $S1$ versus speed.

Fig. 7.28 Ageing effect (continued).

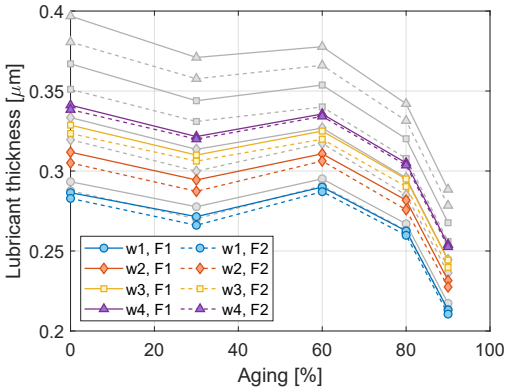

(a) Lubricant film thickness in $S1$ versus ageing level.

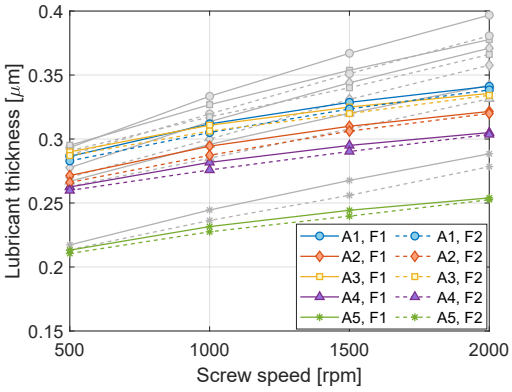

(b) Lubricant film thickness in $S1$ versus speed.

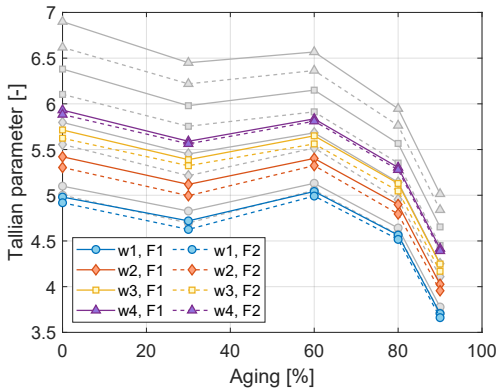

(c) Tallian parameter in $S1$ versus ageing level.

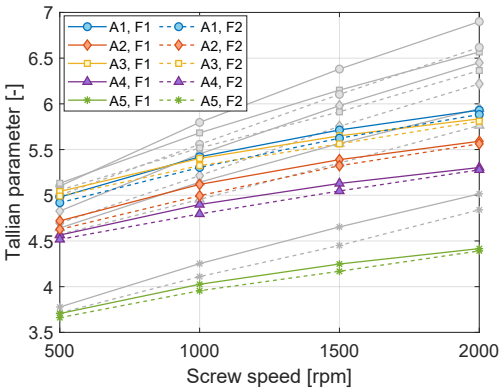

(d) Tallian parameter in $S1$ versus speed.

Fig. 7.29 Effect of starvation on the lubricant film thickness and Tallian parameter.

and, hence, the Archard wear coefficient does the same. Nevertheless, in Fig. 7.28e the wear rate increases: this is due to the increase of viscous shear forces which contributes to augment the worn volume. This is also the reason why the wear rate is more marked as the load increases. In fact, the load generates a dual effect: it reduces the film thickness and, at the same time, it causes also the increase of the frictional forces. The effect of the speed can be seen in Fig. 7.28f: higher speeds lead to higher film thicknesses (Fig. 7.28b), higher relative roughness values (Fig. 7.28c) and, then, lower wear rates (Fig. 7.28f).

Finally, the effect of the lubricant starvation is shown in Fig. 7.29. The lubricant film thickness and the corresponding Tallian parameter values are compared with those obtained if starvation is not taken into account, depicted in light grey. Starvation

causes the film thinning and, thus, the Tallian parameter reduction. This effect is more pronounced for higher speeds due to the greater over rolling frequency.

7.9.7 Jamming

Jamming is a catastrophic failure that can occur in EMAs which causes a sudden drop in actuator performance, such that the electric motor is no longer able to move under the action of the friction actions. This results in the actuator stuck in the last position reached before the jamming occurrence, which can be a very dangerous situation if the EMA is employed as a primary flight control.

Generally, jamming occurs because of the spheres' inability to roll and to transmit the motion. This can happen progressively, e.g. for progressive wear or fatigue, or almost instantaneously, e.g. due to the breakage of the recirculating deflector or to plastic deformations due to overloads, which hinder the correct motion of the spheres.

The latter condition has been simulated and the results are presented in this section. It has been assumed that the BS was driven by an electric motor with a stall torque of 4 [Nm]. A smooth step smooth command has been given as input from 0 to -500 [rpm] between 0.05 [s] and 0.2 [s]. A preload of 1800 [N] has been inserted at 0.02 [s] and this caused the growth of the contact forces between the spheres and the grooves (Figs. 7.30d and 7.30e). At 0.1 [s] an external force of -1000 [N] has been applied, and, consequently, the motor torque rose to equilibrate it (Fig. 7.30b). As in previous sections, the results of a generic sphere are presented to keep the images as clear as possible.

The application of the external force causes the contact angles to distance one from the other (Fig. 7.30c) and the normal and friction forces to increase (Figs. 7.30d and 7.30e).

In the Simscape model the 3D CAD of the screw and nut bodies have been directly inserted in order to make the graphic render more realistic and intuitive when analysing the simulation results (Fig. 7.12). The centres of mass of both the screw shaft and the nut do not lay exactly on the BS axis of symmetry $\widehat{\mathbf{z}}$ but they present a small eccentricity due to their shape: in the screw shaft, this is due to the shaft ends and the thread, while, in the nut, this effect is produced by the presence of the recirculating channel. The eccentricity effect can be seen in the reaction forces

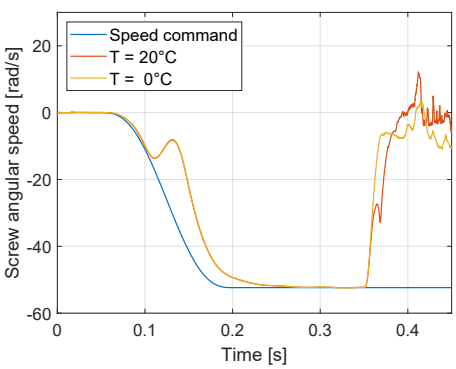

(a) Screw shaft speed.

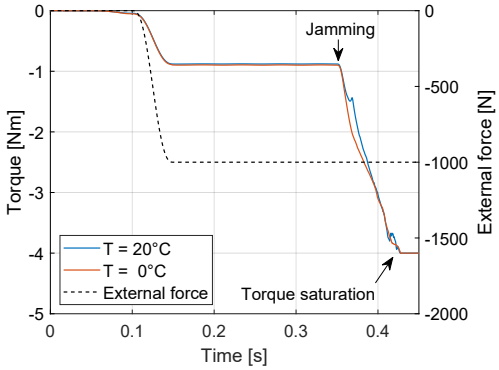

(b) Input torque and external force.

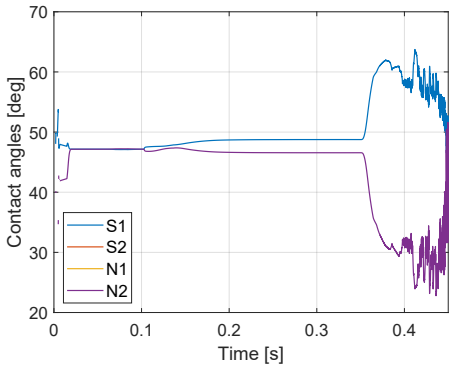

(c) Contact angles.

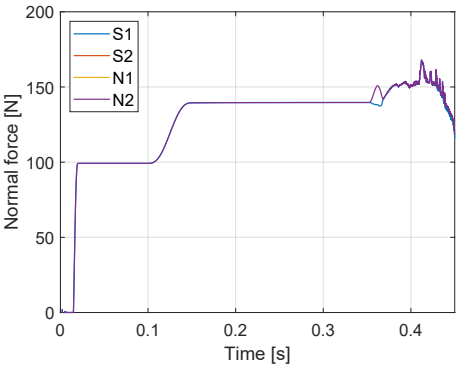

(d) Normal contact force.

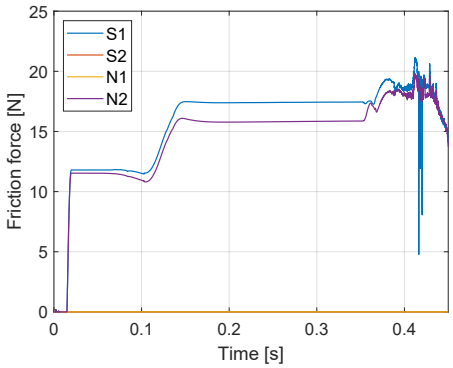

(e) Friction contact force.

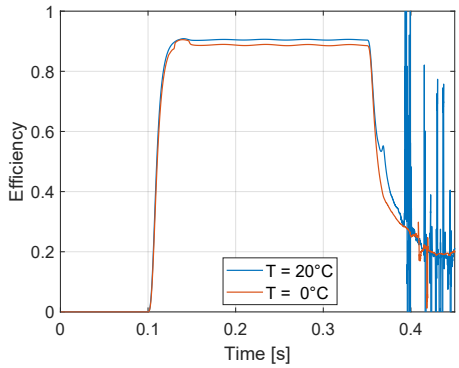

(f) Mechanical efficiency.

Fig. 7.30 Simulation of jamming.

of the screw support shown in Fig. 7.31d. When the external force is applied, the axial constraint force (z component) rises to exactly the value of the external force, while the x and y components start to oscillate with a sinusoidal fashion due to the eccentricity.

As soon as the motion starts, the sphere spin components rise: from Fig. 7.31c it can be seen that the spin speed vector lays almost entirely on the $n-b$ plane normal to the thread, in normal conditions.

Figures 7.31a and 7.31b depict respectively the coordinates of the first three spheres and the translational speed of the first sphere centre of mass with respect to the ground. The x and y components present sinusoidal trends while the z component represents the axial motion of the spheres along the screw axis and, therefore, this signal shape reflects those of the screw and nut angular and linear displacements.

Not being still present the recirculation channel in the present model, the jamming event is modelled by instantaneously sticking one sphere to the nut body at 0.35 [s] by means of three stiff spring–damper systems, one for each direction. This is to represent what happens if the recirculation channel blocks or if the deflector "tongue" brakes: the spheres cannot continue moving along the helical path and the mechanism jams.

In Fig. 7.30b it can be observed that, as soon as the jamming occurs, the actuator torque rises until the motor stall condition is reached. Consequently, the speed drops to zero, the contact angle with the screw increases, that with the nut decreases and the mechanical efficiency, shown in Fig. 7.30f, falls from approximatively 0.92 to 0.2.

When the mechanism is stuck, the torque applied by the motor cannot generate the translation of the nut in the axial direction and, thus, thanks to the anti–rotation reaction torque given by the nut constraints, it traduces to the tendency of the screw to move backwards along $-\widehat{\mathbf{z}}$: the mechanism acts as if the nut was fixed and the screw had both the translational and rotational degrees of freedom. This is what happens in this simulated case in which it can be noted that the support axial reaction force reaches a value of approximatively -5000 [N], which is the linear thrust force corresponding to the stall torque of the motor.

The sphere movement around the screw axis suddenly stops (Figs. 7.31a and 7.31b): the jammed sphere arrests due to the added spring but all the other 24 spheres remain stuck due to the contacts with the adjacent spheres. In steady state motion with unidirectional moving direction, the contact forces between successive spheres are generally low, but, when one sphere blocks, a series of successive impacts between the spheres occur, originating very high forces which can results in plastic deformations leading to worse jamming conditions. This behaviour can be observed

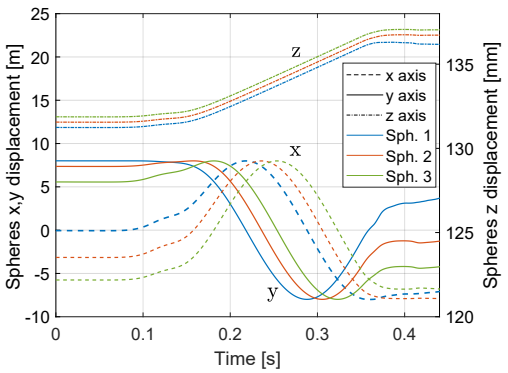

(a) Sphere coordinates relative to ground.

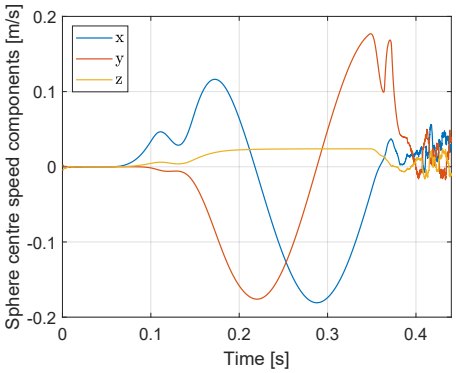

(b) Sphere translational speed relative to ground.

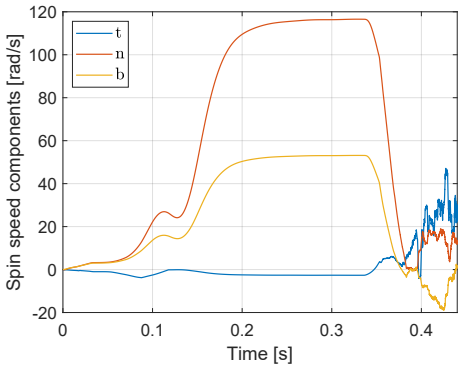

(c) Shpere spin speed relative to the nut.

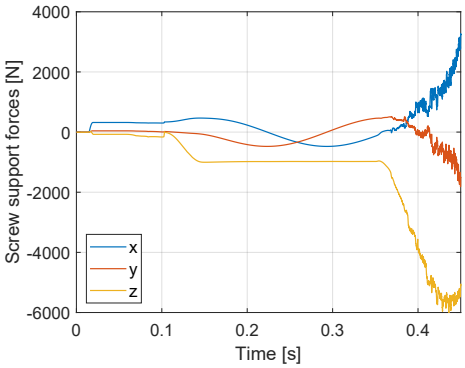

(d) Forces on the screw support.

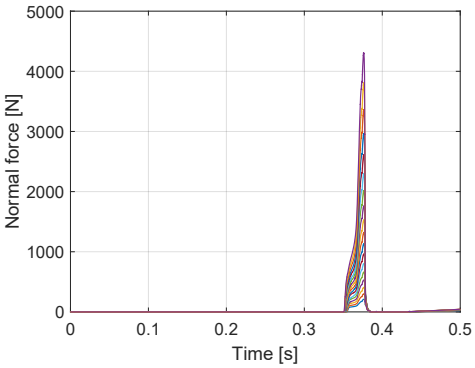

(e) Sphere to sphere contact force.

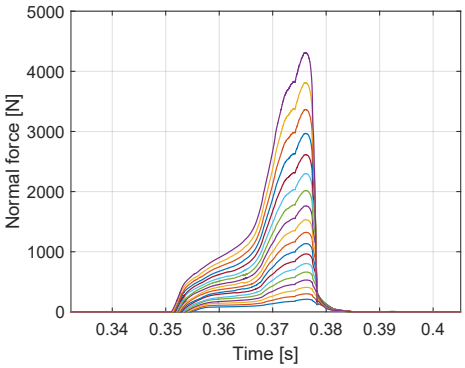

(f) Sphere to sphere contact force (zoom).

Fig. 7.31 Simulation of jamming (continued).

in Figs. 7.31e and 7.31f, where the impact force between the jammed sphere and the following one reaches more than 4000 [N]. The impact force between the successive spheres presents peaks with gradually decreasing intensities because of the equivalent stopping stiffness seen by each sphere, corresponding to the series of the contact stiffness of the already impacted spheres.

7.10 Summary

An new advanced multibody dynamic model of a preloaded BS has been presented in this chapter, enhancing the first model introduced in Chapter 5. The full dynamics of each component is considered and a three–dimensional Hertzian contact model has been developed. The friction forces can be calculated with a low computational cost empirical equivalent model or with a more complex model involving lubrication. Rigid bodies and ideal joints have been considered and the presence of the recirculation has not been modelled so far. The model results have been compared with literature formulae and a close match has been found.

Several simulations have been performed, investigating the possibility of the motion of the sphere with three contact points, the influence of the preload on the no-load drag torque, the relationship between the backlash size, the preload and the friction, the effect of geometric errors and the consequences of lubricant ageing. Eventually, the occurrence of a jamming has been simulated and investigated.

Depending on the geometry, operational speed and friction conditions, the spheres can touch the grooves in three contact points: if this occurs the increased sliding speed generated at each point causes an efficiency decrease and a change in the spin axis orientation of the spheres. In presence of backlash, a preload can avoid undesirables vibrations due to the backlash gap closure. The backlash can be visualised observing the hysteresis loop of the nut displacement relative to the screw rotation. If geometric errors on the spheres are considered, the larger spheres are subjected to higher loads and the load distribution deviates from the ideal one. The wear of the grooves as well as the lubricant ageing depend on the applied load and on the sliding speed of the spheres. Indeed, applying a preload increases the stiffness and compensates the presence of the backlash, but it also increases the drag torque and the wear rate of the loaded half grooves. The lubricant ageing has scarce influence on the measurable macroscopic instantaneous performance signals, such as the torque, the external force, or the kinematic quantities, but it is strictly related to the lubricant thickness and, therefore, to the wear rate of the contacting bodies. Starvation contributes to decrease the film thickness and its effect is more marked for high speed values.

In parallel, a multibody model of a BS has been recently created with a commercial software to investigate the effect of the recirculating channel, and will be presented in Chapter 8.

To be reliable, the model needs to be verified by field measurements. Thus, an experimental test bench has been designed and it is currently under construction, described in Chapter 9.

Chapter 8

Multibody ADAMS model

8.1 Introduction

MSC ADAMS is a commercial multibody software used mainly in the industry during product development to evaluate characteristics of comfort, safety and performance of the studied product.

Among its various characteristics, the ability to describe 3D contacts between arbitrary shaped bodies is the main reason why its use has been included in this work.

A multibody model of the BS has been recently developed within this environment to investigate the effect of the recirculating channel and to acquire knowledge in order to insert this key component also in the Simscape model presented in Chapter 7.

In this chapter, the preliminary model definition is presented and the results of the first simulations are analysed. The use of this software is not intended to replace the previous version of the model but it will be used just as a support in its enhancement.

8.2 Model definition

Before to proceed in assembling the multibody model, the geometry of the BS has to be defined. A BS with the characteristics listed in Tab. 7.5 has been created with the Solidworks CAD software. A render of the geometry is depicted in Fig. 8.1.

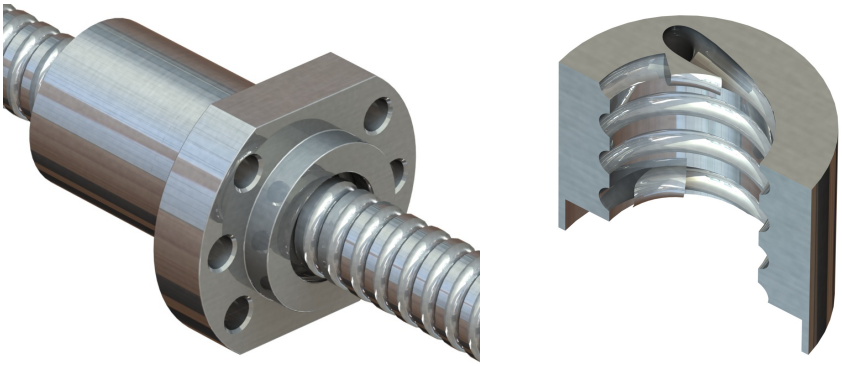

(a) Entire CAD.

(b) Section of the nut with recirculation deflector.

Fig. 8.1 CAD model of a ball screw with nominal diameter of 16 [mm] and 5 [mm] lead.

Fig. 8.2 Multibody model of the ball screw.

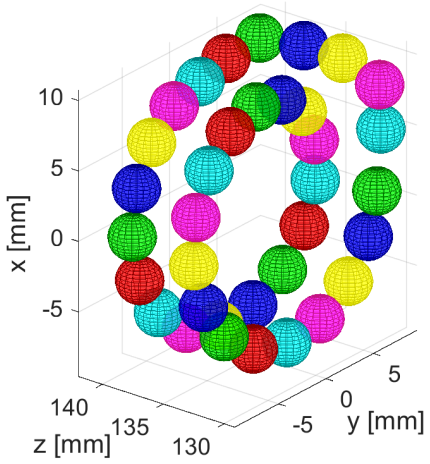

Fig. 8.3 Initial configuration of the spheres.

The shape and the inertial characteristics are the same exploited in Chapter 7 for the Simscape model.

The recirculation system, shown in Fig. 8.1b, has been modelled as an end cap type, with the recirculating channel embedded in the nut body, aligned axially along $\widehat{\mathbf{z}}$ (Fig. 8.2). The exit and entry ways in the recirculation are realised tangentially to the helix direction, as can be seen in Fig. 8.1b.

The BS geometry has been then simplified avoiding unnecessary geometrical features, obtaining the model shown in Fig. 8.2.

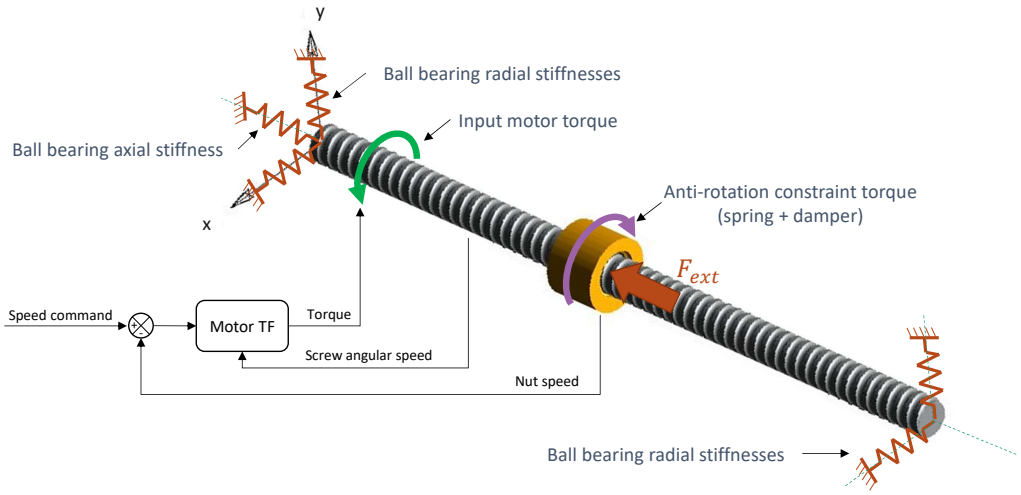

Fig. 8.4 ADAMS ball screw model boundary conditions.

From the CAD model, the actual complete path of the spheres has been extracted. The initial positions of the spheres, depicted in Fig. 8.3, have been defined imposing a tangent condition on adjacent spheres with the centres laying on the path.

As in the Simscape model (Chapter 7), the screw is considered as the rotational element and the nut as the translating one. A PI controller commands an electric motor, which applies a torque on the screw shaft. The speed control loop is closed with the axial speed on the nut, on which an external force is applied.

Flexible supports have been modelled through elastic elements on the $\widehat{\mathbf{x}}$ and $\widehat{\mathbf{y}}$ axes on both shaft ends to represent the support bearings compliance according to [238] (Fig. 8.4). The rear bearing supports also the axial load, while the front bearing is not axially constrained. Analogously, the anti–rotation torque on the nut has been represented with a torsional spring–damper element along the $\widehat{\mathbf{z}}$ axis. The nut is free to tilt around the other two axes and the reaction torque is given by the compression of the internal spheres. Therefore, all the components, including the screw shaft and the nut, have all their six degrees of freedom: no ideal constraints have been imposed.

ADAMS calculates the contact forces between arbitrary shaped bodies either using the Parasolid geometry imported from the CAD or performing a triangular tessellation and applying the RAPID algorithm for contact detection: the first works with an exact boundary representation of the geometry, which makes it highly accurate but also heavily computational intensive, while, with the second method,

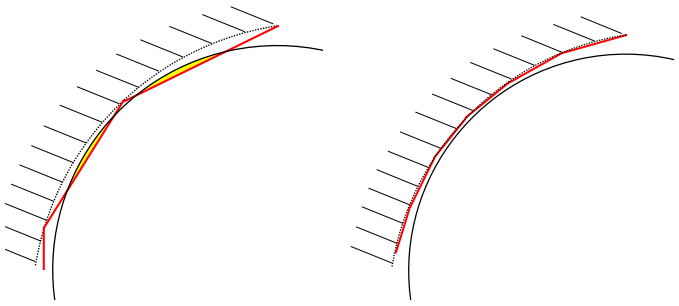

(a) Coarse mesh: yellow areas represent intersections.

(b) Fine mesh: no contact.

Fig. 8.5 Example of geometric artefacts originated by the use of rough tessellation.

a hierarchical representation of the ADAMS model is pre-computed using tight-fitting oriented bounding box trees (OBBTrees), and thus the model is approximated by a series of polygons [239]. The latter has been selected as contact library for simulation time reasons, imposing, though, a tight discretization factor in such a way to represent accurately the small curvatures of the grooves. In fact, if a rough tessellation is adopted, the small geometric tolerances typical of the BS mechanism could be not satisfied, such as the backlash of few microns and the absence of contact force when the backlash gap is open, as Fig. 8.5 exemplifies.

The result of such a tessellation on the screw shaft and on the recirculating deflector is depicted in Fig. 8.6.

8.3 Contact model

To calculate the contact force, ADAMS detects the intersection volume (or volumes, if multiple contact points arise at the same time) between the tessellated rigid bodies and calculates the centroid location and the outward normal vector for each contact point. Thus, the interpenetration used to calculate the contact force is defined as the distance between the nearest points to the centroid on each surface [240].

Two normal contact models are implemented in ADAMS: the Poisson restitution method and the so called Impact method [240]. Both force models result from a penality regularization of the unilateral contact constraint, but the first is more suitable for intermittent contacts and a more accurate representation of the energy

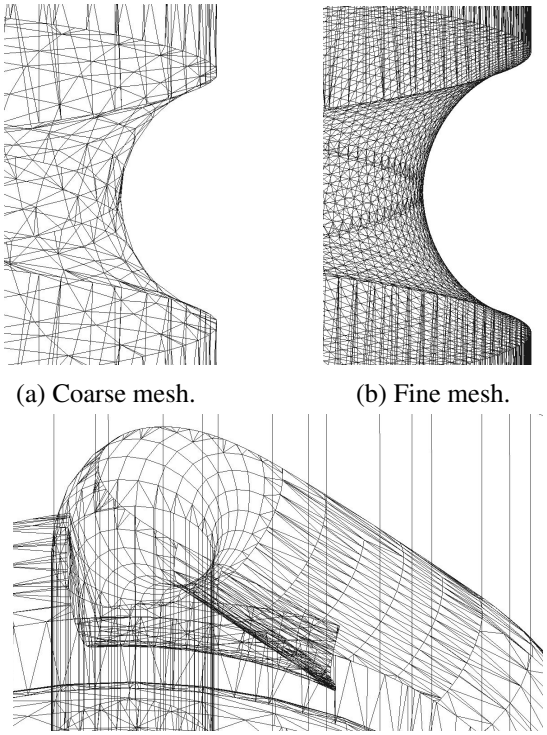

(a) Coarse mesh. (b) Fine mesh.

(c) Recirculating deflector.

Fig. 8.6 CAD model tessellation of MSC ADAMS for contact detection.

loss, while the latter is more robust and much less sensitive to solver error tolerances and it is suitable if many contacts are present.

For this reason, the Impact method has been adopted, which can be written as:

$$F_n = K_{AD} g^e + \text{step}(g, 0, 0, d_{max}, c_{max})\dot{g} \tag{8.1}$$

where K_{AD} and e are the contact stiffness and exponent, calculated from the Hertzian theory with the same approach explained in Sec. 7.3. The damping contribution $c_{max}\dot{g}$ is applied smoothly with the `step` function (Eq. 7.56) since the damping coefficient value changes from 0 to c_{max} when the interpenetration function g goes from 0 to a user defined depth d_{max}. This approach allows avoiding contact discontinuities due to non-null contacting speeds: it is similar to the saturation method presented in Sec. 7.3, with the difference that, in this case, the contact force can also assume negative values (e.g. if a high separating speed occurs when the bodies are already in contact with $g > d_{max}$).

The friction force is calculated by means of a velocity–based model, similar to the model described by Eq. 7.55 but without the viscous linear effect.

According to [240], the spin friction torque, to react to a relative angulare motion about the contact normal axis, is calculated as

$$T_{spin} = \frac{2}{3} r_{cont} F_n \tag{8.2}$$

where the contact area is assumed to be always circular with a radius r_{cont}.

8.4 Integration of the equations of motion

Contacts are discontinuities in the solution of the set of DAE equations describing the model and, therefore, the ADAMS solver uses an heuristic method to predict the occurrence of a contact [240]. If a contact is expected to occur, the solver parameters are updated and the integration time step reduced to avoid solver errors.

The ADAMS software supports several types of solver, explicit and implicit. In this thesis the implicit Hilber–Hughes–Taylor (HHT) solver is chosen since it is the most appropriate solver for stiff models with many contacts and in which the contact force and accelerations are important signals. It behaves like a low pass filter, cutting high frequency spurious oscillations and preserving the low frequency ones. Since in its formulation no divisions by the time step size are present, it is stable for small integration steps. This solver uses a low order integrator, i.e. an integrator which uses low order approximation of the solution in the prediction phase.

In fact, the ADAMS integration process can be subdivided in four parts:

- prediction phase;
- integration phase;
- correction phase;
- post–integration phase.

In the *prediction phase*, a polynomial or a Taylor's series (depending on the solver type) is fitted on a certain number of past values of the solution and it is

used to explicitly estimate a first guess of the solution value in the following time step. The order of the polynomial (defining the *order of the integrator*) generally is variable and depends on the smoothness of the solution, however the HHT integrator works with a fixed order. It is reduced to 1 if an imminent contact is expected, since the solution scarcely depends on the previous values in presence of a discontinuous event such a contact.

In the *integration phase*, the implicit integration algorithm is applied to determine the following state values by means of a quasi–Newton–Raphson method, which starts from the solution value obtained in the prediction phase and continues to iterate until the convergence error falls below the specified threshold value. The method is called *quasi* since the derivative of the Jacobian matrix is not performed at each iteration but following a pre–specified pattern: this in general ensures that the solution satisfy the equation of motion and constraints with more iterations, but more quickly because of the minor number of Jacobian derivations.

In the *correction phase*, the obtained value of the solution is compared with the predicted value and, if the error is sufficiently small the integration moves to the following time step, otherwise the solution is rejected and the process is repeated again with a smaller time step. In case of contacts, the time step is directly reduced basing on the stiffness and damping values of the contact and on the mass of the contacting bodies. The ADAMS software uses always a variable step solver and, thus, if a large number of contacts are present, the simulation time can rise significantly if the correct contact and friction parameters are not chosen appropriately. Depending on the formulation (index) of the corrector, the error control can be performed on displacements, velocity and acceleration or just on the first two. For the HHT integrator, the error control is done on acceleration too.

In the last phase, the solver prepares itself for the next integration deciding the optimal integration time step and prediction order depending on the smoothness of the solution.

In general, ADAMS represents a model with a set of non–linear differential algebraic equations (DAEs). Usually, for mechanical systems, the DAEs system involves the acceleration of the generalised coordinates q, i.e. a formulation with an *index 2*:

$$\begin{cases} \mathbf{M}\ddot{\mathbf{q}} + \boldsymbol{\Phi}_q^T \boldsymbol{\lambda} - \mathbf{Q}(\mathbf{q}, \dot{\mathbf{q}}) = \mathbf{0} \\ \frac{d}{dt}\left(\frac{\partial K}{\partial \dot{\mathbf{q}}}\right)^T - \left(\frac{\partial K}{\partial \mathbf{q}}\right)^T + \boldsymbol{\Phi}_q^T \boldsymbol{\lambda} - \mathbf{Q}(\mathbf{q}, \dot{\mathbf{q}}) = \mathbf{0} \\ \boldsymbol{\Phi}(\mathbf{q}, t) = \mathbf{0} \end{cases} \tag{8.3}$$

where $\mathbf{M}$ is the mass matrix of the system, $\mathbf{q}$ is the generalised coordinate vector, $\boldsymbol{\Phi}$ is the set of configurations and motion constraints (in this case holonomic), K is the kinetic energy of the system, $\mathbf{Q}$ is the external forces vector projected on the direction of $\mathbf{q}$, $\boldsymbol{\lambda}$ is the Lagrange multiplier vector and $\boldsymbol{\Phi}_q = \frac{\partial \boldsymbol{\Phi}}{\partial \mathbf{q}}$ is the gradient of the constraint set at any given state. The first equation represents the translational motion equilibrium, the second the rotational motion equilibrium and the last one the constraint set of equation.

The index of a DAE is defined as the number of time derivatives required to convert a set of DAEs to ODEs (ordinary differential equations) [241]. The DAEs system of Eq. 8.3 can be reduced to a ODEs introducing new equations with new variables representing the velocities:

$$\begin{cases} \mathbf{M}\dot{\mathbf{u}} + \boldsymbol{\Phi}_p^T \boldsymbol{\lambda}_p - \mathbf{Q}_p(\mathbf{p}, \dot{\mathbf{p}}) = \mathbf{0} \\ \boldsymbol{\Gamma} - \frac{d}{dt}\left(\frac{\partial K}{\partial \boldsymbol{\xi}}\right)^T = \mathbf{0} \\ \dot{\boldsymbol{\Gamma}} - \left(\frac{\partial K}{\partial \boldsymbol{\varepsilon}}\right)^T + \boldsymbol{\Phi}_\varepsilon^T \boldsymbol{\lambda}_\varepsilon - \mathbf{Q}_\varepsilon(\boldsymbol{\varepsilon}, \dot{\boldsymbol{\varepsilon}}) = \mathbf{0} \\ \dot{\mathbf{p}} - \mathbf{u} = \mathbf{0} \\ \dot{\boldsymbol{\varepsilon}} - \boldsymbol{\xi} = \mathbf{0} \\ \boldsymbol{\Phi}(\mathbf{p}, \boldsymbol{\varepsilon}, t) = \mathbf{0} \end{cases} \tag{8.4}$$

where the coordinates, Lagrange multipliers and applied force vectors $\mathbf{q}$, $\boldsymbol{\lambda}$ and $\mathbf{Q}$ have been divided in the translational and rotational components, respectively $\mathbf{p}$ and $\boldsymbol{\varepsilon}$, $\boldsymbol{\lambda}_p$ and $\boldsymbol{\lambda}_\varepsilon$, and $\mathbf{Q}_p$ and $\mathbf{Q}_\varepsilon$. $\boldsymbol{\Gamma}$ represents the angular momentum vector while $\mathbf{u}$ and $\boldsymbol{\xi}$ are the two new variables to reduce the index.

The rotational motion equilibrium equation has been divided in two equations, separating the definition of angular momentum, to increase the sparsity of the resulting matrix in order to augment the solution efficiency.

The HHT integrator applies an improved α–method characteristic of the Newmark integration scheme, allowing the error control also on acceleration state while keeping the method stable for every time step. The equation of motion is discretised and a scaling of the force vector is performed: it is composed by the weighted sum of the force at time instant t, scaled by $1+\alpha$, with the force of the previous time step, scaled by α. Namely, $\boldsymbol{\Phi}_p^T \boldsymbol{\lambda}_p - \mathbf{Q}_p(\mathbf{p}, \dot{\mathbf{p}})$ becomes:

$$(1+\alpha)\left[\boldsymbol{\Phi}_p^T \boldsymbol{\lambda}_p - \mathbf{Q}_p(\mathbf{p}, \dot{\mathbf{p}})\right]_t - \alpha\left[\boldsymbol{\Phi}_p^T \boldsymbol{\lambda}_p - \mathbf{Q}_p(\mathbf{p}, \dot{\mathbf{p}})\right]_{t-1} \tag{8.5}$$

The α parameter is a coefficient of the HHT algorithm, which can assume value in the range $-0.3 \leq \alpha \leq 0$.

Further details can be found in literature [240–242].

8.5 Simulation results

As aforementioned, the model has been recently created and it is still under development and investigation. In this section, how the load distribution is influenced by the suppression of the prismatic joint between the screw shaft and the nut is investigated, together with the effect of the recirculating system.

A smooth step command of 5000 [rpm] has been imposed to the controller from 0.1 to 0.2 [s] and, concurrently, a smooth force step of -1000 [N] has been applied on the nut. The presence of the recirculation path allows the true displacements of the sphere to be reproduced. A single nut not preloaded BS with 35 spheres and the characteristics listed in Tab. 7.5 has been considered and simulated.

In Fig. 8.7 a part of the trajectory of one of the sphere with respect to the ground is depicted together with the spin speed vector at each location. It can be observed that the latter is always approximatively oriented with an angle of 45° with respect to the Frenet–Serret coordinate system $\widehat{\mathbf{n}}$ axis (not shown in the figure) for each location of the sphere. Instead, when the sphere enters the recirculation channel, the

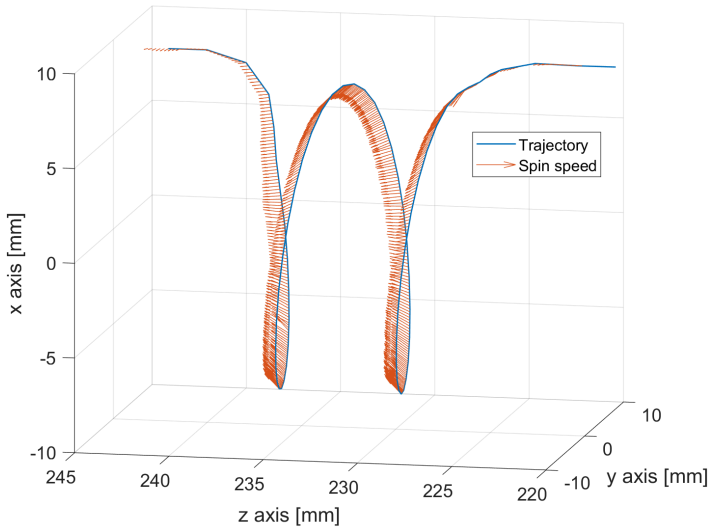

Fig. 8.7 Sphere trajectory and spin speed vector during one complete cycle inside the nut.

spin speed vector direction is not well-defined since the sphere is mainly transported by the surrounding spheres and does not have a principal rolling motion.

The absolute translational velocity components of the sphere's centre of mass with respect to the ground are shown in Fig. 8.8a for the time span in which the mechanism is in regime conditions. The x and y components present a sinusoidal trend since they represent the position of the sphere's projection on a plane normal to the screw longitudinal axis. In fact, the frequency of these sinusoids is related to the revolution speed of the nut ω_m, shown in Fig. 8.8b, whose value matches the theoretical value of –218 [rad/s], according to Eq. 7.83 [98]. The absolute speed of the sphere's centre of mass along the $\widehat{\mathbf{z}}$ axis, while it is within the helical loaded region, is constant for constant speeds of the BS and equal to:

$$v_{CMz,helix} = \frac{p\dot{\Omega}}{2\pi} + \omega_m r_m \tan(\alpha_e) \approx 0.24 \text{ [m/s]} \tag{8.6}$$

where $\dot{\Omega}$ and ω_m are taken with their sign: for positive screw speeds the revolution speed is negative and vice versa.

The recirculating axial channel is realised, for this model, exactly on the location correspondent to an azimuth angle equal to approximatively 45°, therefore, the entry and exit channels are almost aligned with the $\widehat{\mathbf{x}}$ and $\widehat{\mathbf{y}}$ axes. In fact, when the sphere enters into the recirculation, it stops to follow an helical trajectory and moves only

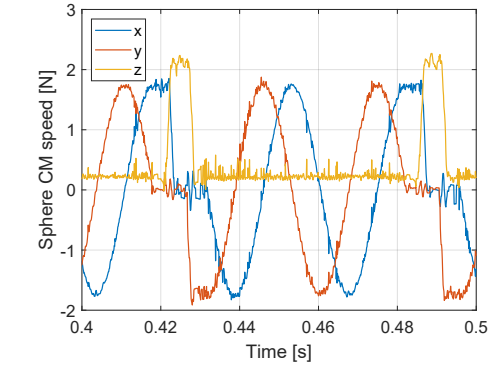

(a) Sphere translational speed relative to ground.

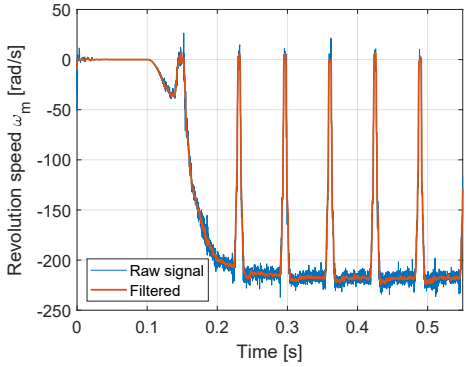

(b) Revolution speed of the sphere.

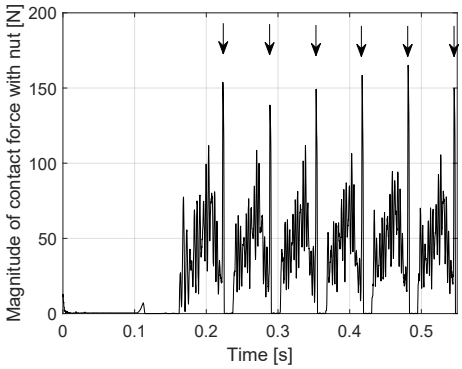

(c) Cotnact force with the nut.

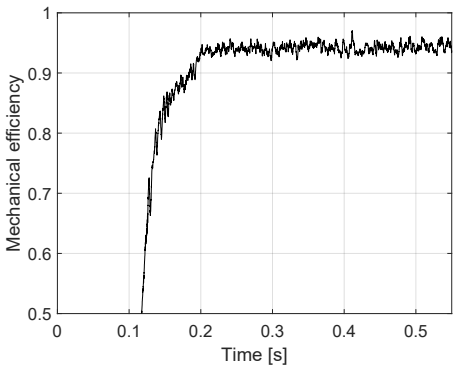

(d) Mechanical efficiency.

Fig. 8.8 ADAMS simulation results for the sphere n.8.

in the x direction, while the speed y components becomes null; when the sphere exits the recirculation it moves almost entirely in the y direction and the speed x component is equal to zero (Fig. 8.8a). Opposite conditions occur for positive speeds of the BS. When the sphere enters in the axial recirculating channel, both the x and y components of the speed are absent since it moves axially with a translational speed equal to:

$$v_{CMz,rec} = \frac{p\dot{\Omega}}{2\pi} + \frac{\omega_m r_m}{\cos(\alpha_e)} \approx 2.16 \text{ [m/s]} \tag{8.7}$$

Obviously, since the x and y components are null, every time the sphere enters in the recirculation its revolution speed ω_m falls to zero, as depicted in Fig. 8.8b. As can be seen from Fig. 8.8a, the model results match very well the expected values. A realistic value of the mechanical efficiency, of approximatively 0.94, can be observed in Fig. 8.8d.

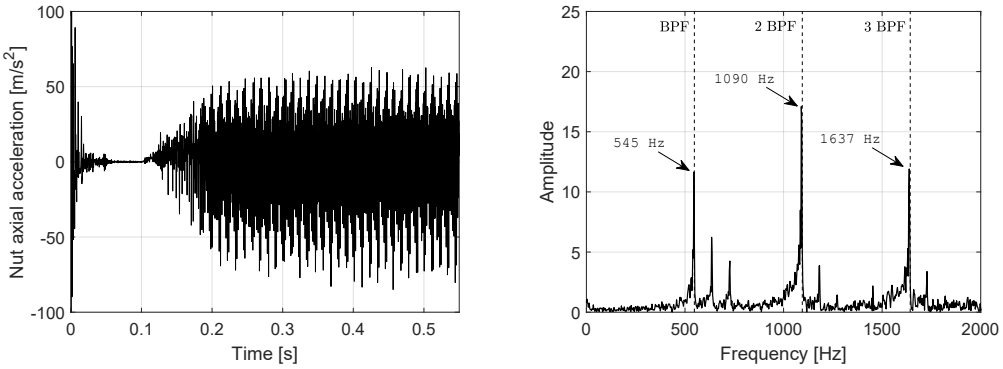

(a) Time domain. (b) Frequency domain.

Fig. 8.9 Nut axial acceleration.

The magnitude of the contact force between one of the spheres and the nut body is plotted in Fig. 8.8c and it can be observed that every time the sphere enters the recirculation path the contact force becomes negligible because the channel is slightly larger that the spheres' diameter to facilitates their passage. Just before the exit, the sphere impacts with the deflector and a spike in the contact force occurs (indicated by the arrows in Fig. 8.8c). These spikes coincide with the zero revolute speed of Fig. 8.8b and occur with the frequency at which one sphere completes the entire circuit.

Because of the removal of the ideal constraints, the nut is free to tilt and oscillates, therefore vibrational analyses can be performed. The axial acceleration of the nut is displayed in Fig. 8.9a. By means of a FFT, the single–sided acceleration amplitude spectrum shown in Fig. 8.9b has been obtained. It presents three peaks at 545, 1090 and 1637 [Hz], very close to the theoretical ball passing frequency (BPF) value and its harmonics. The BPF can be calculated as [89]:

$$BPF = \frac{\omega_m}{\varphi} \tag{8.8}$$

where φ is the difference between the azimuth angle of two adjacent spheres considered tangent. It can be obtained solving the following implicit equation:

$$2r_b - r_m\sqrt{2\left[1-\cos\left(\varphi\right)\right]+\left[\varphi\tan\left(\alpha_e\right)\right]^2} = 0 \tag{8.9}$$

Table 8.1 Theoretical and simulated ball passing frequency values.

Frequency	**Theory** [Hz]	**Model** [Hz]	**Relative error** %
BPF	547.76	545	0.5064
2 BPF	1095.52	1090	0.5046
3 BPF	1643.28	1637	0.3836

The resolution of Eq. 8.9 is performed numerically starting from an approximated formula which slightly overestimates the BPF:

$$BPF \approxeq \frac{\omega_m}{2\pi} \frac{2\pi r_m}{2r_b \cos(\alpha_e)} = \frac{r_m \omega_m}{2r_b \cos(\alpha_e)} \tag{8.10}$$

Solving Eqns. 8.8–8.9, the values of the BPF and its harmonics, listed in Tab. 8.1, have been found to be very similar to those obtained from the simulation, confirming the correspondence of the developed model behaviour with that of the real component.

To analyse the load distribution on the sphere without ideal constraints, three simulations have been carried out giving the same previously explained inputs to the model. The load distributions for two different time instants are shown in Fig. 8.10: Figs. 8.10a and 8.10b have been obtained inserting a positive geometric error of 0.5% on the radius of one of the sphere, Figs. 8.10c and 8.10d show the case in which all the spheres are affected by geometrical errors extracted from an uniform distribution in the range $-0.5 \div 0.5\%$, Figs. 8.10e and 8.10f are related to a case with no geometrical errors but with an eccentricity of 1 [mm] of the external force application point on the nut along the $\widehat{\mathbf{x}}$ axis.

In Fig. 8.10a it can be noted that, when the bigger sphere is circulating in the helical part of the path, it bears a large amount of the load. This causes the nut to tilt exploiting the little backlash present, redistributing the load on all the other spheres and deforming the load distribution from its normal shape, represented in blue. The number of sphere in one turn can be approximated as:

$$N_{sph,1turn} = \frac{\pi r_m}{r_b \cos(\alpha_e)} \approx 16 \tag{8.11}$$

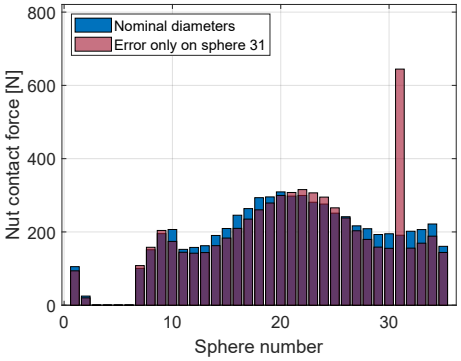

(a) Geometric error on one sphere.

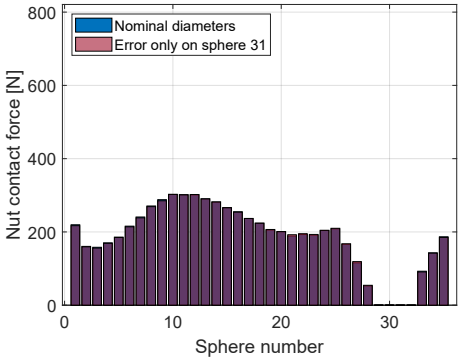

(b) Geometric error on one sphere in the recirculation.

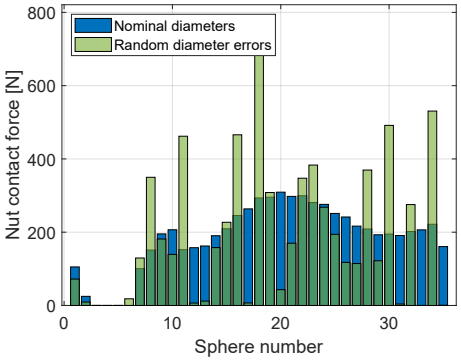

(c) Random geometric errors on the spheres.

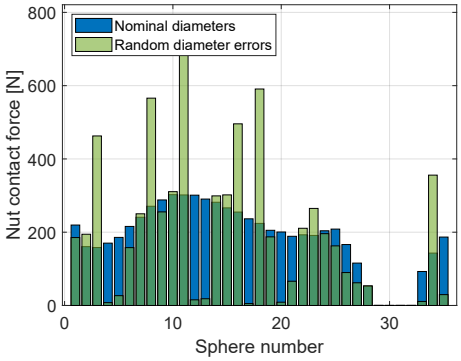

(d) Random geometric errors on the sphere in a different time instant.

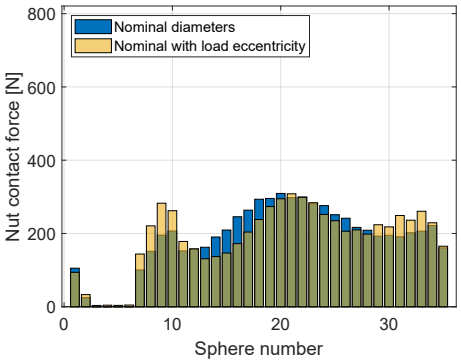

(e) External force eccentricity.

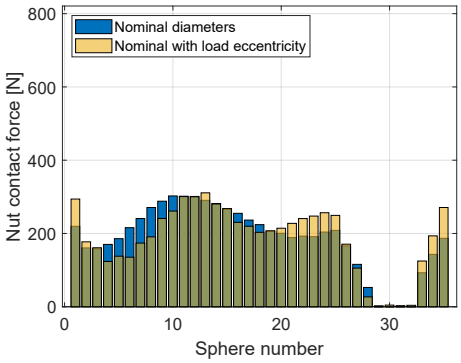

(f) External force eccentricity in a different time instant.

Fig. 8.10 Load distribution on the spheres.

In fact, in Fig. 8.10a, the load distribution describes a sort of sine wave with the maximum peaks outdistanced of 15 spheres. The spheres next to the bigger one are less loaded, while those located at an azimuth angle of π with respect to it receive

more load because of the nut tilting. The distribution returns to the nominal one when the faulty sphere enters into the recirculation, as can be observed in Fig. 8.10b.

The load distribution can be imagined moving in the right direction of Fig. 8.10a as the time passes. This means that the sphere with a low cardinal number enters into the recirculation before than those with high numbers. Indeed, the spheres just on the right of the load distribution gap (representing the spheres in the recirculation) have a slightly higher force value than the others, since they are impacting with the deflector.

If random errors are considered on each sphere, the load distribution is always different from the nominal one: bigger spheres bear higher loads and the nut tilts according to the resultant of all the contacting forces. In particular, it can be noted in Fig. 8.10c that the spheres number 12, 13, 31, 33 and 35 are substantially unloaded since they are surrounded by spheres with increased radius which prevent the nut to touch them and, thus, to transmit load.

Finally, even if no errors are considered, the external load eccentricity can modify the shape of the load distribution. In this situation, the nut tilts under the effect of the external force and, as a consequence, the load on the spheres changes, opposing to the previous cases in which the nut tilts because of the load change on the increased spheres.

It is worth to be mentioned that, looking at Fig. 8.10a, the nominal blue load distribution is not constant even without geometrical errors and applied force eccentricity: this is due to the fact that, because of the presence of the recirculation channel, the nut centre of mass does not lay on the BS symmetry axis and, hence, it tends to tilt and does not distribute its weight equally on every sphere.

8.6 Summary

The ADAMS software offers interesting possibilities, such as the contact detection algorithm and the simulation with flexible bodies [240], but it is oriented to industry, in which, often, the main interest is in the position or velocity of the bodies and there is no interest in the in–depth modelling of the contact conditions with a high level of detail. However, the contact subroutines can be customised to insert user–defined friction and contact laws. Though, this process is not straightforward because of the

closed nature of commercial softwares. For this reason, the default built–in contact models have been currently used.

The BS geometry has been created first in Solidworks and then exported in the Parasolid format in order to be read by ADAMS. The geometry has been simplified and tessellated to allow the contact routines to detect the occurrence of contact events.

Supports' compliance have been modelled with elastic elements: the removal of the prismatic joint on the nut highlighted that the load distribution on the sphere is not uniform neither if an axial constant load is applied, without geometric errors, and the screw shaft and nut flexibilities [144, 151] are disregarded, due to the position of the centre of mass of the nut body out of the BS symmetry axis. The presence of eccentrical external force or geometric errors accentuates the non–uniformity of the load distribution.

The recirculation deflectors are subjected to repeated impacts from the spheres exiting from the helical path, identified by the peaks in the force signal. Analysing the axial acceleration of the nut in the frequency domain, the ball passing frequency has been calculated and it has been found to be very close to the theoretical value, confirming the validity of the present dynamic model.

Further analyses will be carried out in the next future customising the contact models and improving the model fidelity. Depending on the scope of the analysis either the Simscape or the ADAMS model can be used: for example, the latter is more suitable for groove defect injection since the software supports the contact between arbitrary shaped geometries, while the first is more appropriate if friction, detailed contact condition and power loss evaluation are the main scope.

Chapter 9

Experimental test bench

9.1 Introduction

In the previous chapters, mathematical models of the BS mechanism with different levels of detail have been presented and extensively described. However, it is necessary to validate them with experimental measures in order to prove the reliability of the obtained results. In fact, the high fidelity model shall be used as a virtual test bench to investigate prognostic strategies and, therefore, its behaviour must replicate that of a real component both in nominal and faulty conditions.

With this aim, this chapter presents the model–based robust design of the BS drive experimental test bench currently under construction [243]. It is being developed with the goal of validating the results obtained through the theoretical framework and to study the experimental behaviour of a ball screw in presence of few selected fault modes, such as the backlash increase, the preload loss, the lubricant starvation, the presence of a notch on the groove to simulate the pitting and fatigue effect, the wear, and so forth. To have a database of measurements composed by not a unique sample, five identical BSs have been purchased.

Because of the impracticability of the onboard insertion of numerous sensors for EMAs monitoring, the primary objective of this test bench is to asses the observability of the fault modes with the available sensors and to define the measures which would need to be made available in order to perform PHM activities on BSs in ground stations, if not onboard. To do so, a whole set of additional sensors is needed in the test bench, which must be carefully designed to fulfil the requirements. In fact, the

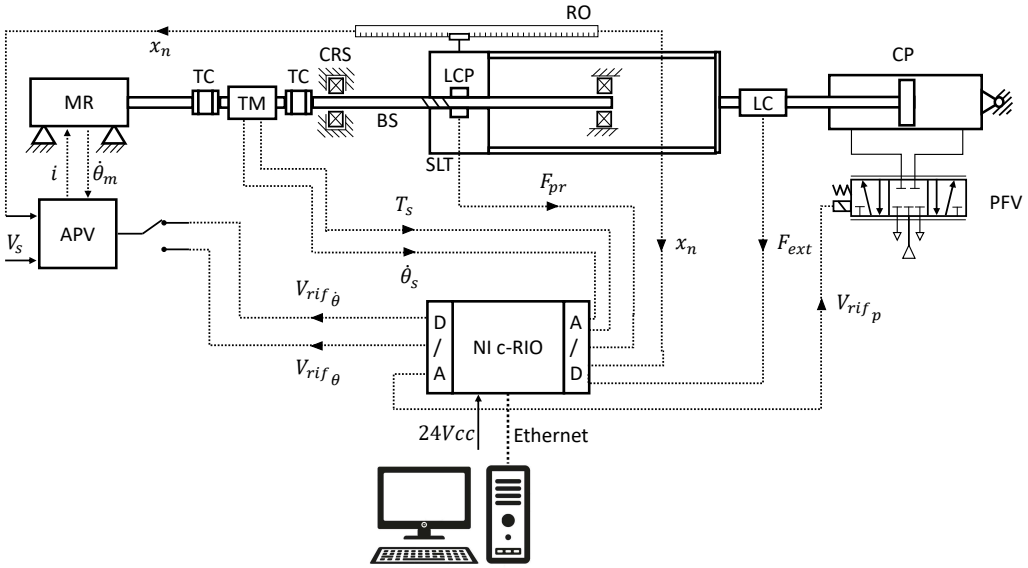

Fig. 9.1 Test bench schematic layout.

sensors' characteristics shall be such as to enable the minimum defects' size to be detectable.

A mathematical model of the entire test bench has been developed to study the influence of the noise introduced by the measuring system and the test procedures on the defects' observability. It helps in the definition of a proper set of features for the PHM system and also in the selection of the appropriate sensors. A Monte Carlo analysis has been performed to verify the robustness of the test bench design against the geometrical and measuring uncertainties unavoidably present.

Though several components are already available, the test bench is still under construction and thus no experimental data are presented in this thesis.

9.2 Layout

Several test bench architectures have been proposed in literature mainly to investigate the precision positioning of BS drive systems for feed drive axes [124, 128–130, 244], to carry out studies aimed to the optimization of the control parameters to compensate positioning errors [136, 245, 246] and to study and develop algorithms for performance evaluations [114, 115, 118, 165].

Table 9.1 Test bench component acronyms.

Component	**Acronym**
Motor–reducer	MR
Motor driver	APV
Torsional coupling	TC
Torque meter	TM
Rear thrust bearing	CRS
Preload load cell	LCP
Nuts assembly	SLT
Ball screw	BS
Linear encoder	RO
External force load cell	LC
Pneumatic cylinder	CP
Proportional pneumatic flow valve	PFV

Only recently, the focus of BS experimental researches moved towards health monitoring analyses, in particular related to preload lessening: in [247] a test bench based on two parallel EMAs is proposed, while a test bench to study the prognosability of balls screws is described in [157]. The study reported in [147] provides an interesting solution based on a shifting table and a fastener to change the value of the preload applied to the ball screw, while significant position measures are taken from a combination of rotary and linear encoders; a similar architecture is described in [161]. A compact design to reduce the preload is reported in [118]. In most applications no load control is performed, but an exception is reported in [248], where a second electric motor is employed to oppose a variable resistant torque to the ball screw.

The designed test bench is composed by the traditional EMA architecture with additional sensors used to discriminate the different faults and defects on the BS mechanism, isolating them from the rest of the test bench. The schematic layout is shown in Fig. 9.1 and the acronyms' meanings are listed in Tab. 9.1. The entire test rig is controlled by a NI c–RIO 9047 which sends the speed or position demands to the electric motor–reducer (MR), and acquires the signals coming from all the installed sensors. Moreover, it performs the control of the external force loop commanding a proportional pneumatic flow valve (PFV), which regulates the flow in the two chambers of a pneumatic cylinder (CP).

The motion is imposed by the electrical brushless motor–reducer, which receives the inputs by its driver (APV): it realises the current, speed and position control loops.

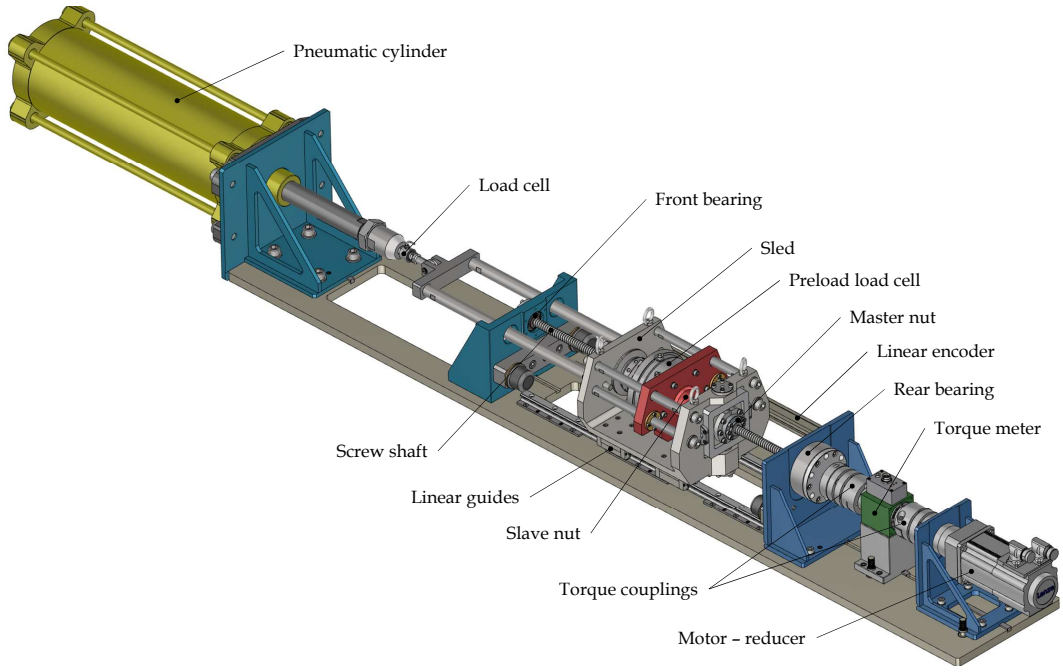

(a) Axonometric view.

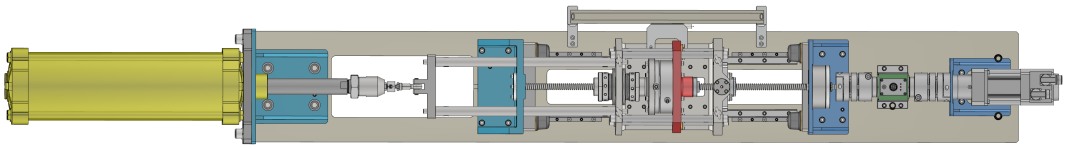

(b) Top view.

Fig. 9.2 Test bench CAD.

The screw shaft of the BS is connected to the output shaft of the reducer through two elastic torque couplings (TC) which are needed to guarantee safety operations and correct measurements to the non–contacting torque meter (TM), compensating possible misalignments. The torque meter measures both the transmitted torque and the screw shaft angular speed, exploiting its built–in encoder disc, and allows to separate the effects on the measured signal caused by the BS from those caused by the upstream components.

The BS preload is performed through two separate nuts which allow it to be regulated and measured from test to test. One of the two nuts (master nut) bears the external load, while the other (slave nut) is used to generate the preload. The BS is supported by two sets of bearings: the one on the motor side (CRS) bears both

Table 9.2 Test bench component list.

Component	**Model**
Electric motor	Lenze MCS09F38
Electric motor driver	Lenze Servo–Drive 9400 High Line
Reducer	Lenze g700–P44
Resolver	Lenze R58 (embedded in the motor)
Linear encoder	ELCIS L–RV1846–320–5–BZ–N–1
Torque meter	BURSTER 8661–5050–V1402
Torsional couplings	RADEX NC 25 DK 2.6
Ball screw	MOOG C5168-19-14-A
Preload load cell	Lorenz Messtechnik Gmbh K–1882
Preload load cell conditioner	Lorenz Messtechnik Gmbh LCV/U10
Ball screw bearings	SKF BSA 201 C
Linear guides	Hiwin RGH20CA
End stroke damper	Angst+Pfister E, 12.2037.1003
Pneumatic cylinder	FESTO DSBG Φ160 mm
Proportional pneumatic flow valve	FESTO MPYE – 3/8
External force load cell	HBM K–U9C–20K0–03M0–Y–S
Control and acquisition hardware	NI c-Rio 9047

axial and radial loads, while the other is not axially constrained to allow free axial deformations. The nuts rotation is prevented by two linear bearing guides.

The external force generated by the pneumatic cylinder is applied on the master nut thanks to two jags (Fig. 9.2) and it is measured by a traction/compression load cell (LC). The linear position of the nuts assembly (sled) is read by a linear optical encoder, whose signal is used both for measure and control purposes.

The CAD of the described entire test bench is shown in Fig. 9.2, while that of the variable preload system is depicted in Fig. 9.3b.

The nuts assembly has been designed with the goal of allowing the preload to be both measured and regulated. It is composed by two sub–assemblies, corresponding to the two nuts, represented in Fig. 9.3. The nut 1 is the master nut and its sub–assembly is composed by two cross beams rigidly connected (the sled body of Fig. 9.3b) on which the external force is applied by the two jags coming from the pneumatic cylinder. The second sub–assembly is that of the nut 2, the slave nut, which is attached to the central crossbeam number 2.

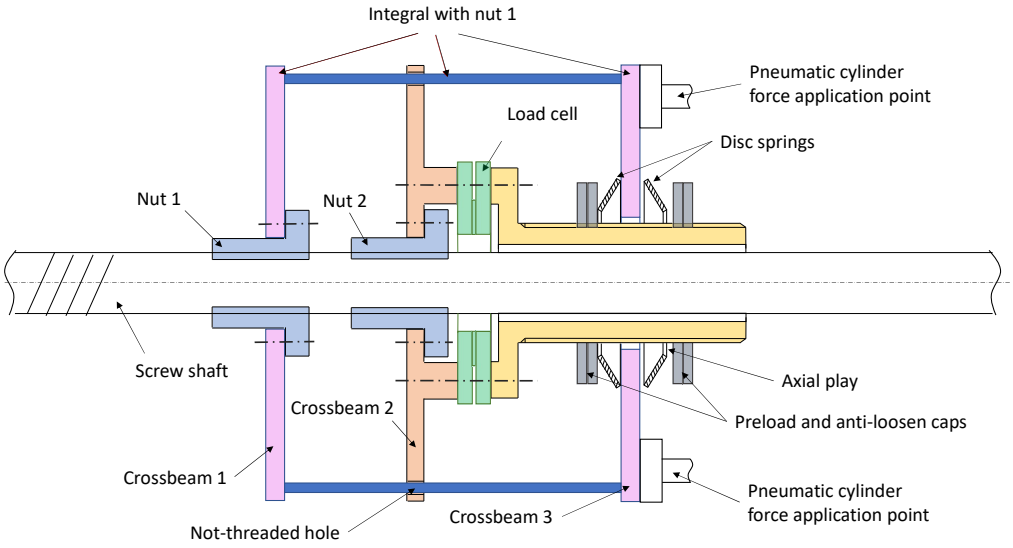

(a) Schematic representation.

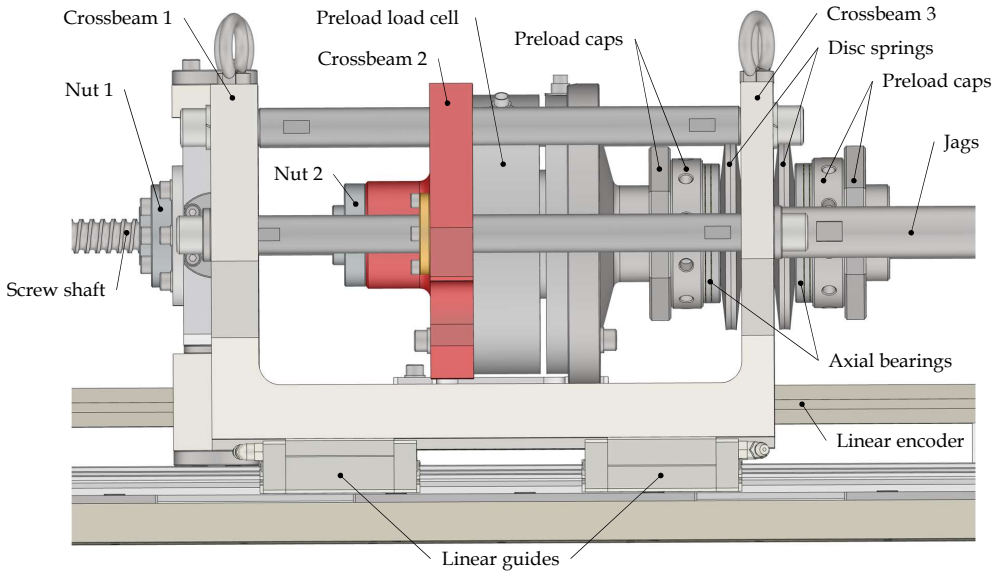

(b) CAD particular.

Fig. 9.3 Variable preload system.

A toroidal load cell connects the crossbeam 2 to a hollow threaded beam, on which two sets of disc (Belleville) springs, axial bearing and preload/anti–loosen caps are screwed. By tightening either one or the other side, an X or O preload configuration can be obtained, respectively moving the nuts closer or further. If no spring set is compressed, the mechanism is left without preload, not compensating for

Table 9.3 Test bench design specifications.

Specification	Value
Nominal linear speed	70 [mm/s]
Linear stroke	300 [mm]
Maximum load	12 [kN]
Minimum detectable linear backlash	1 [µm]

the internal backlash. The axial bearings are needed to allow a fine regulation of the preload by the rotation of the end caps, minimising the friction effect on the manual regulation sensibility. The preload is dynamically read by the traction/compression toroidal load cell, whose shape allows the load cell to be mounted concentrically to the screw shaft, avoiding bending problems and eccentric measures.

The design specifications of the test bench are listed in Tab. 9.3. The list of the components is reported in Tab. 9.2 while the detailed characteristics from the data sheets can be found in Appendix B.

9.3 Mathematical model

9.3.1 Subcomponents models

In this section, the mathematical model of the test bench is presented. It has been developed in the MATLAB&Simulink environment and its structure, depicted in Fig. 9.4, reflects the schematic configuration shown in Fig. 9.1.

Since the scope of this model was to be used in Monte Carlo simulations, equivalent simple formulations have been adopted in order to keep the simulation time as fast as possible.

The position and speed control loops have been modelled taking into account the A/D and D/A conversions and the quantization errors. The current control loop has been modelled with not digitalized (analog) continuous signals, while the position and speed loops are digital.

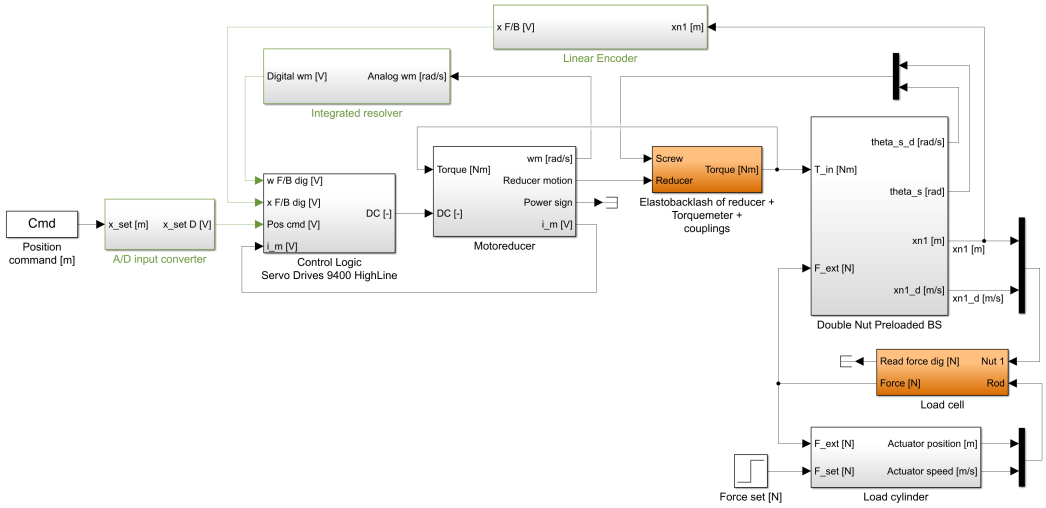

Fig. 9.4 Simulink model main screen.

Electric motor

Although the real component is an brushless three–phase motor, it has been modelled with an equivalent mono–phase circuit:

$$\alpha_{DC} V_s - k_e \tau_{mr} \dot{\vartheta}_r - R_m(T_w)\, i = H_m \frac{di}{dt} \tag{9.1}$$

where α_{DC} represents the duty cycle imposed by the motor drive electronics, V_s is the supply voltage, k_e is the motor velocity constant, τ_{mr} is the reduction ratio, $\dot{\vartheta}_r$ is the reducer output shaft angular speed, H_m is the equivalent motor windings inductance, i is the motor current and $R_m(T_w)$ is the armature equivalent resistance, dependent on the windings temperature T_w. The latter can be calculated from [247]:

$$R_{th}\left[R_m(T_w)\, i^2 - hA_m(T_w - Trif) - \varepsilon\sigma\left(T_w^4 - T_{rif}^4\right)\right] = \tau_w \frac{dT_w}{dt} \tag{9.2}$$

In Eq. 9.2 the windings have been considered as a bulk exchanging heat directly with the ambient at temperature T_{rif}. R_{th} is the thermal resistance, h is the heat transfer coefficient, A_m is the equivalent motor surface area, ε is the surface emissivity, σ is the Stefan–Boltzmann constant and τ_w is the windings time constant.

The current calculated with the electrical domain equation (Eq. 9.1) is the input to solve the mechanical domain equation:

$$J_{mr}\tau_{mr}^2\ddot{\vartheta}_r = \left(k_t i\eta_{mr} - b_{mr}\tau_{mr}\dot{\vartheta}_r\right)\tau_{mr} - T_{fr,mr} - T_{tm} \tag{9.3}$$

where J_{mr} is the equivalent motor–reducer moment of inertia reflected on the motor shaft, k_t is the motor torque constant, η_{mr} is the motor–reducer efficiency, b_{mr} is the damping viscous coefficient, $T_{fr,mr}$ represents the friction torque, calculated with a formulation similar to Eq. 7.64, and T_{tm} is the disturbance torque coming from the reaction of the torque meter. The current of the motor is used to close the current control loop, in which the Hall effect sensors are represented through a simple first order transfer function.

Torque meter

All the force/torque measurement instruments have been modelled as spring–damper systems. The force/torque signal has been used as disturbance for the upstream components and as input for the downstream elements, while it has been digitalised before being saved as simulation result to simulate the measurement noise and the sensor characteristics effect on the read signal resolution.

The torque meter measures both the torque and the angular speed contactless. The torque information is streamed from the rotor to the stator with a refresh rate of 1000 [Hz], therefore some instantaneous torque peaks may be lost during the acquisition: this behaviour has been represented in the model.

The combination of the two torque couplings in series with the torque meter has been reduced to a unique equivalent stiffness, with a small damping effect in parallel to help the integrator. Moreover, the backlash of the reducer has been inserted in this component making it, de facto, an elasto–backlash equivalent to that described in Eq. 5.9 [181, 182, 56].

The torque T_{tm} is calculated from the relative angular position and velocity of the screw shaft relative to the reducer output shaft: it has been used as driving torque on the BS and as reaction force on the motor–reducer.

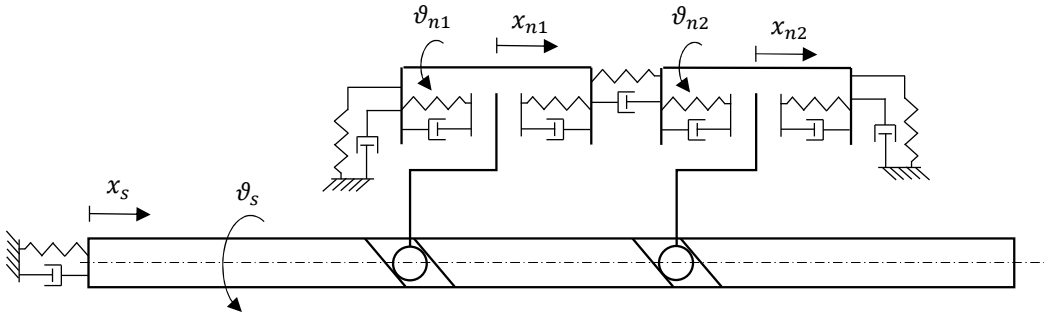

Fig. 9.5 Ball screw equivalent scheme.

Ball screw

This model of a BS is the simplified version of that described in Chapter 5, since the rolling/sliding motion of single spheres is not considered. Nevertheless, the present model includes a simple variable contact angle model, according to [249]:

$$\alpha = \arctan\left[\tan(\alpha_0)\frac{\delta}{2(r_s - r_b)\cos(\alpha_0)}\right] \tag{9.4}$$

where α_0 is the design contact angle, which varies to α due to the contact deformation δ on the plane normal to the thread.

Both the linear and rotational motions of the screw shaft and the nuts are considered (Fig. 9.5), thus the position and speed difference between the equivalents axial linear positions can be expressed as:

$$\begin{aligned} \Delta x_i &= x_s - \frac{p\vartheta_s}{2\pi} - \left(x_{ni} + \frac{p\vartheta_{ni}}{2\pi}\right) \\ \Delta \dot{x}_i &= \dot{x}_s - \frac{p\dot{\vartheta}_s}{2\pi} - \left(\dot{x}_{ni} + \frac{p\dot{\vartheta}_{ni}}{2\pi}\right) \end{aligned} \quad \text{with} \quad i = 1,2 \tag{9.5}$$

where x_s and ϑ_s are the linear and angular positions of the screw shaft, while x_{ni} and ϑ_{ni} are the linear and angular positions of the two nuts.

From the equivalent linear relative position, projected on the plane normal to the thread, the contact force between the spheres and the grooves is calculated for one sphere by means of a double–side elasto–backlash model, under the hypotheses of uniformly distributed load and equal contact angles for the screw and nut interfaces.

As in Sec. 7.3, the contact stiffness has been calculated applying the Hertzian theory taking into account the variability of the groove curvature with the contact angle.

According to [248], the normal contact force P between one sphere and the grooves can be decomposed as:

$$\begin{aligned} F_a &= P\sin(\alpha)\cos(\alpha_e) \\ F_t &= P\sin(\alpha)\sin(\alpha_e) \\ F_v &= P\cos(\alpha) \end{aligned} \tag{9.6}$$

where F_a is the axial component, F_t is the component tangent to the screw shaft on the $x-y$ plane and F_v is the radial component. It is assumed that all the radial components coming from each sphere equilibrates and, hence, they have been not considered.

The axial motion of the screw shaft has been modelled as a simple mass–spring–damper system in which the stiffness is the series of the rear bearing stiffness [238] and the axial stiffness of the screw shaft itself, dependent on the sled position [83], and where the external excitation is represented by the sum of all the contributions of the spheres' contact forces in the axial direction. The rotational motion of the screw shaft can be described through the following expression:

$$(J_s + J_{tm} + 2J_{tc})\,\ddot{\vartheta}_s = T_{tm} - b_s\dot{\vartheta}_s - T_{fr,s} - Z_{eff}F_t \tag{9.7}$$

where J_s, J_{tm} and J_{tc} are respectively the screw shaft, torque meter and torque couplings moment of inertia. b_s is a small rotational damping to help the simulation, Z_{eff} is the actual number of loaded spheres and $T_{fr,s}$ is the Coulomb–Stribeck–viscous friction force with a formulation equivalent to Eq. 7.64.

Also the rotational equilibrium of each nut can be represented with a simple mass–spring–damper system as for the translation of the screw, in which the rotational stiffness is produced by the stiffness of the linear guides and the excitation torque is that created by the sum of the tangential components of the spheres' contact forces. The translational equilibrium equation is simply:

$$M_{ni}\ddot{x}_{ni} = Z_{eff}F_a - F_{nfr} - \xi F_{pr} - \lambda F_{ext} \quad \text{with} \quad i = 1,2 \tag{9.8}$$

where M_n is the mass of the nut, F_{nfr} is the friction force generated by the linear guides (Eq. 7.64), F_{pr} is the preload force, considered positive if separating the nuts, and F_{ext} is the external force. If $i = 1$, i.e. the master nut is considered, then $\xi = \lambda = 1$, otherwise $\xi = -1$ and $\lambda = 0$ for $i = 2$.

Preload load cell

As for the torque meter, the toroidal load cell to measure the preload has been represented as a translational spring–damper system acting between the nuts. Its stiffness is the equivalent value obtained from the series of the Belleville spring set and the load cell. The mass of all the components connected with the slave nut has been reflected on the slave nut mass. The preload force is saturated to zero, since it cannot change sign during a simulation. In fact the preload is generated by the tightening of the disc springs, which create a unidirectional force.

Linear and rotary encoders

The linear and rotary encoders present on the sled and embedded into the torque meter have been described according to [250]. The impulse trains for the A, B and Z tracks are considered: the position has been obtained simulating the clockwise (forward for the linear encoder) and counter clockwise (backward) counters, while the speed has been calculated using either the period or the frequency method depending on the absolute value of the speed [250].

Pneumatic load system

The pneumatic circuit has been represented with the lumped parameter approach proposed in [251]. The controller sends a command to the proportional pneumatic flow valve, which regulates the flow to the two chambers of the actuator. Both subsonic and sonic regimes are considered to describe the mass flow rate passing through the ports:

$$G = \begin{cases} c_v \rho_0 P_u & \text{for} \quad 0 < P_d \leq b_{crit} P_u \\ c_v \rho_0 P_u \sqrt{1 - \frac{\frac{P_d}{P_u} - b_{crit}^2}{1 - b_{crit}}} & \text{for} \quad b_{crit} P_u < P_d \leq P_u \\ -c_v \rho_0 P_u \sqrt{1 - \frac{\frac{P_u}{P_d} - b_{crit}^2}{1 - b_{crit}}} & \text{for} \quad P_u < P_d \leq \dfrac{P_u}{b_{crit}} \\ -c_v \rho_0 P_u & \text{for} \quad P_d > \dfrac{P_u}{b_{crit}} \end{cases} \tag{9.9}$$

where P_u and P_d are the upstream and downstream pressures, ρ_0 is the air pressure in reference conditions, b_{crit} is the critical pressure ratio defining the onset of the sonic regime and c_v is the conductance of the valve, dependent on the spool position and, thus, on the command.

The mass flow rate enters into the chambers, whose continuity equations are:

$$\begin{cases} \dfrac{dP_1}{dt} = \dfrac{G_1 n R T_{i1}}{A_1 (x_{d1}+x) \frac{P_1}{P_{1i}}^{\frac{1-n}{n}}} - \dfrac{P_1 n}{(x_{d1}+x)} \dfrac{dx}{dt} \\ \dfrac{dP_2}{dt} = \dfrac{G_2 n R T_{i2}}{A_2 (x_{d2}+x) \frac{P_2}{P_{2i}}^{\frac{1-n}{n}}} + \dfrac{P_2 n}{(x_{d2}+x)} \dfrac{dx}{dt} \end{cases} \tag{9.10}$$

where P_1 and P_2 are the chambers' average pressures, G_1 and G_2 are the mass flow rates, x is the actuator position, x_{d1} and x_{d2} are the dead volumes coordinates along the cylinder stroke, T_{i1} and T_{i2} are the gas temperatures inside the chambers and R is the universal gas constant. It has been assumed that the air behaves as an ideal gas with P_{1i} and P_{2i} the pressures at the beginning of the assumed isothermal transformation of the gas, characterised by the exponent n.

The two active areas A_1 and A_2 on the two sides of the piston define the net pressure force. Its translational equilibrium equation can be written as:

$$P_1 A_1 - P_2 A_2 - F_{fr,cyl} - c_p \dot{x} = m_p \ddot{x} \tag{9.11}$$

where $F_{fr,cyl}$ is the friction force acting between the piston and the cylinder (Eq. 7.64), c_p is the damping coefficient and m_p is the piston translating mass, composed by the mass of the piston, the rod end and the load cell.

9.3.2 Simulation results

An example of simulation results in nominal conditions obtained with the above described mathematical model of the test bench is shown in Figs. 9.6 and 9.7. Both the ideal physical signals and the measured signals are shown in the relevant plots, in which the latter are affected by measuring electrical noise and by sampling and quantization artefacts introduced by conditioners and acquisition boards.

The position demand given as input to the controller is depicted in Fig. 9.6a together with the system response. A zoom of the signals is shown in Fig. 9.6b where the sampling and quantization effects can be observed.

The error between the position demand and the actual displacement of the nuts assembly is used to generate the speed command for the motor, shown in Fig. 9.6c. Figure 9.6d represents a particular of the system response in correspondence of the end of the sinusoidal part of the command. It can be observed that the resolution of the set is much lower than that of the feedback: this is due to the amplification of the position resolution through the proportional gain of the PI position controller. Indeed, it has been assumed that no interpolation or smoothing of the speed command are performed since no precise information are available yet on the motor driver's internal control logic. Nevertheless, it must be mentioned that the acquisition system has a greater number of bits and, therefore, a much higher resolution of all the signals is obtained for signal analysis purposes.

The quantization of the speed command reflects into the noisiness of the motor current command and, thus, on the motor current itself, shown in Fig. 9.6e. Peaks in the current signal arise in correspondence of the acceleration phases. It can be also noted that, during the sinusoidal part of the motion, the mean current moves from zero to approximatively -0.57 [A] because of the application of an external force step of 4 [kN] at 1 [s], depicted in Fig. 9.7a.

The windings' temperature variation is shown in Fig. 9.6f and it is due to the Joule power losses related to the motor current.

The external force of Fig. 9.7a is obtained commanding the proportional flow valve through the PI controller of the force loop. The error between the imposed set and the force feedback measured by the load cell is used to generate a displacement of the valve spool and, consequently, two flow rates between the two chambers of the pneumatic cylinder, the supply and the drain, shown in Fig. 9.7d. The force

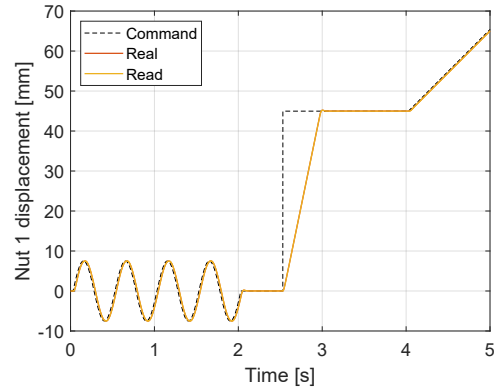

(a) Linear positions.

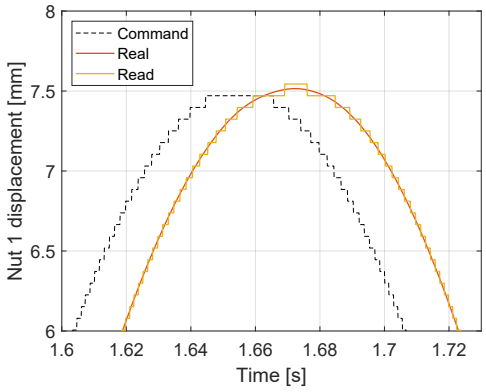

(b) Linear position (zoom).

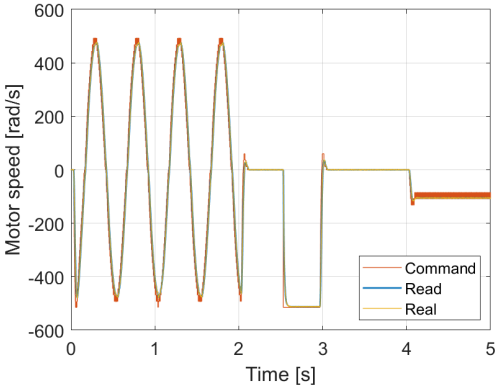

(c) Motor speeds.

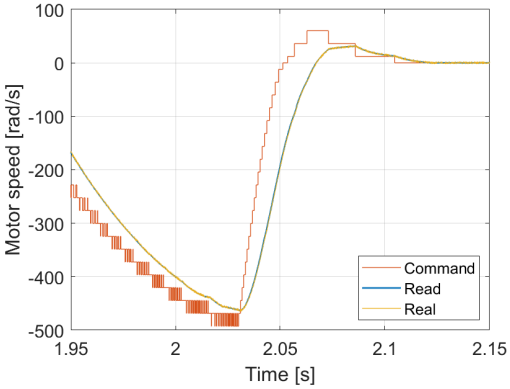

(d) Motor speeds (zoom).

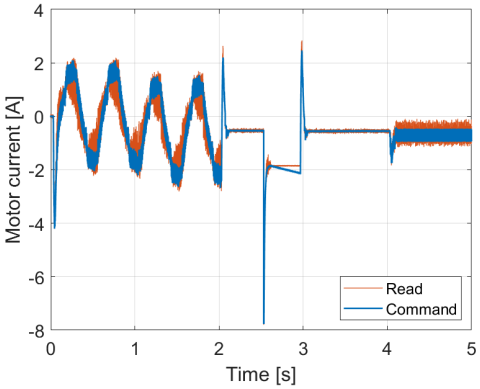

(e) Motor current.

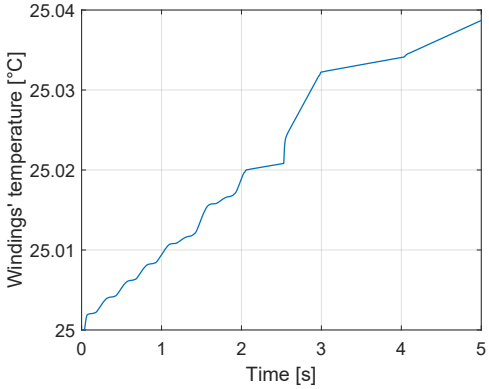

(f) Windings' temperature.

Fig. 9.6 An example of simulation results in nominal conditions.

applied by the cylinder depends on the pressures on the two chambers (Fig. 9.7c), which vary according to the flow rates and the velocity of the piston. Because of the velocity disturbance of the piston and because of the different pressure difference of

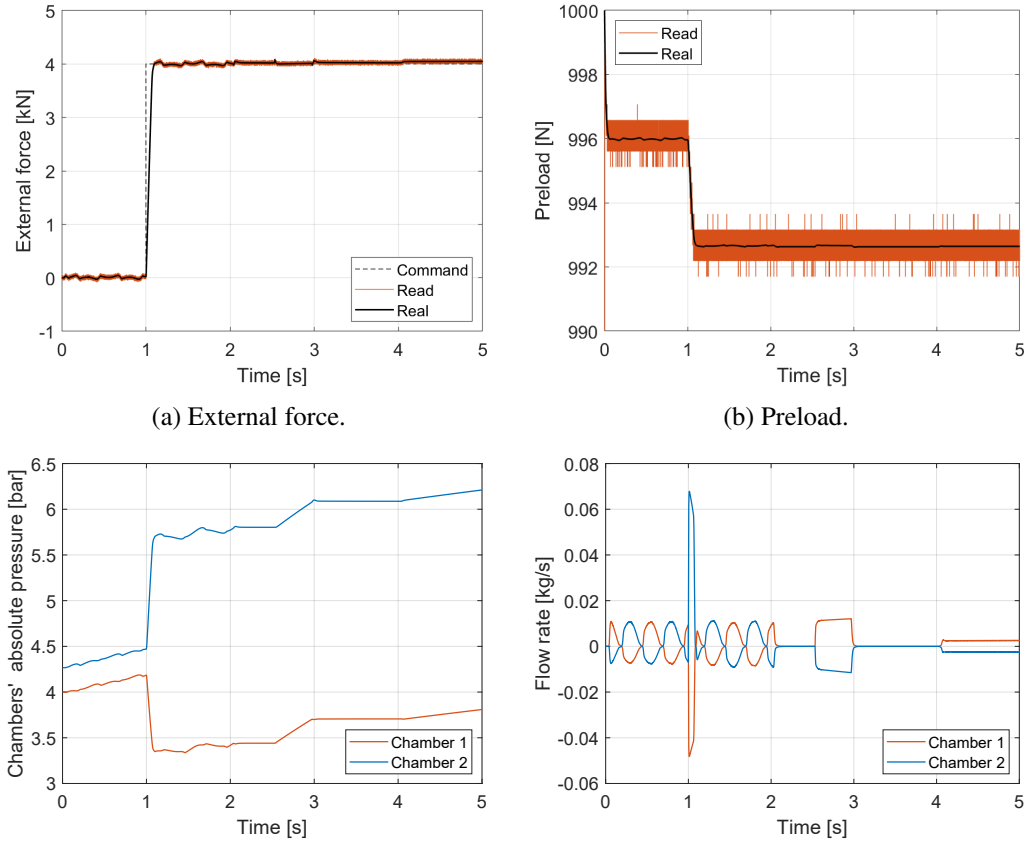

(a) External force.

(b) Preload.

(c) Chambers' pressures.

(d) Flow rates.

Fig. 9.7 An example of simulation results in nominal conditions (continued).

the chambers with the supply and ambient pressure, the input flow rates are always slightly bigger than the output flow rates and, hence, the pressures presents a small increasing trend. In fact the control is performed on the applied force, which means on the Δp between the two chambers, and not on the absolute values of the two pressures.

Since the initial conditions of the simulation consider all the elements unloaded, the presence of the tightened disc springs originates a preload on the two nuts and, thus, initial deformations. Consequently, the initial preload of 1000 [N] decreases a little as the elastic deformations arise (Fig. 9.7b). When, at 1[s], the external force is applied on the master nut, the preload varies again since the load redistributes on the two nuts through the preload springs.

Table 9.4 Data set conditions.

Data set	**Backlash** [μm]	**Preload** [N]	**External force** [N]
1	80	1000	0
2	80	0	0
3	0	0	4000
4	0	0	0
5	0	1000	0

9.4 Monte Carlo analysis

In order to investigate the influence of the uncertainties in the geometrical and sensors' parameters, several simulation have been performed in the frame of a Monte Carlo analysis.

For every simulation, the value of each uncertain parameter has been randomly extracted from its probability distribution. The list of the uncertainty sources is reported in Tab. 9.5, together with the data sheet range and the typology of distribution: Gaussian (G), uniform (U) or constant (C).

Furthermore, the overall sensitivity and offset of each sensor with respect to the temperature has been calculated as a function of the deviation of the room temperature from the nominal one of 25°C. The room temperature and the supply pressure have been considered variable from test to test.

An electrical noise is added to each measured signal in the model to take into account the electromagnetic pollution that can be present in the test environment.

Using the model presented in Sec. 9.3, the observability of the growth of the axial backlash has been investigated. The same command sequence of Fig. 9.6a [252] has been given as position command to the controller for each simulation and five data sets, of 1000 simulations each, have been obtained. Each data set is associated with different operating conditions, listed in Tab. 9.4, representative of the presence or not of the backlash degradation and of the test with or without the preload and external force.

To keep track of the backlash size, a first trial feature has been computed, expressed as the average value of the difference between the equivalent linear positions of the translating nut and the rotating screw:

Table 9.5 Parameters' uncertainties.

Parameter	Range	Dist
Environment		
Temperature	$15 \div 35$ °C	U
Pressure	$-10 \div 0$ %Nom	U
Torque meter		
Sensitivity range 1	± 0.2 %Nom	G
Sensitivity range 2	± 0.2 %Nom	G
Temperature on offset range 1	± 0.01 %FS/K	G
Temperature on offset range 2	± 0.02 %FS/K	G
Temperature on sensitivity range 1	± 0.015 %Nom/K	G
Temperature on sensitivity range 2	± 0.03 %Nom/K	G
Load cell		
Repeatability	± 0.085 %Read	G
Offset	± 0.02 %FS	G
Temperature on offset	± 0.03 % FS/K	G
Sensitivity	± 0.1 %Nom	G
Temperature on sensitivity	± 0.011 %Nom/K	G
Preload load cell		
Accuracy	± 0.2 %Nom	G
Sensitivity range 1	± 0.5 %Nom	G
Sensitivity range 2	± 0.5 %Nom	G
Temperature on offset range 1	± 0.02 %FS/K	G
Temperature on offset range 2	± 0.02 %FS/K	G
Temperature on sensitivity range 1	± 0.02 %Nom/K	G
Temperature on sensitivity range 2	± 0.02 %Nom/K	G
Preload load cell conditioning module		
Temperature on offset	± 0.0015 %FS/K	G
Temperature on sensitivity range 1	± 0.0015 %Nom/K	G
Temperature on sensitivity range 2	± 0.0015 %Nom/K	G
Linear encoder		
Precision	$-5 \div 5$ µm	G
Tolerance between phases	$-45 \div 45$ deg	G
Asymmetry in each phase	$-15 \div 15$ deg	G
Motor resolver		
Offset	± 0.02 %FS	G
Resolution	$0.8'$	C
Accuracy	$\pm 10'$	G
Torque meter encoder		
Tolerance between phases	$-45 \div 45$ deg	G
Asymmetry in each phase	$-15 \div 15$ deg	G
Reducer		
Stiffness	± 5 %Nom	G
Backlash	± 5 %Nom	G
Motor		
Armature resistance	± 10 %Nom	G
Torque constant	± 10 %Nom	G
Speed constant	± 10 %Nom	G
Moment of inertia	± 10 %Nom	G
Electrical noise	± 2.5 %FS	U

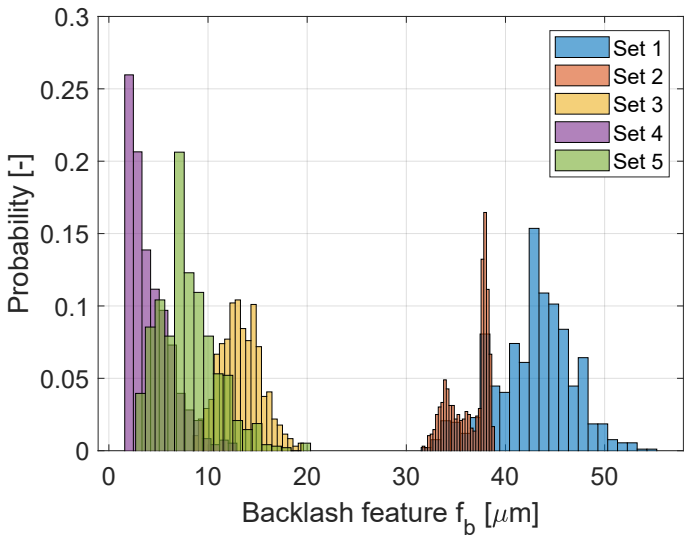

Fig. 9.8 Observed values for the axial backlash.

$$f_b = \frac{1}{N}\sum_{i=1}^{N}\left| x_{n1} - \frac{p\vartheta_s}{2\pi} \right| \tag{9.12}$$

The probability distributions obtained from the analysis of the five data sets are shown in Fig. 9.8. It can be observed that the data sets associated with the presence of backlash achieve a good separation with respect to the data sets in which it is not present. Furthermore, the presence of the preload (data set 5 with respect to data set 4, and data set 1 with respect to data set 2) and of the external force (data set 3 with respect to data set 4) cause the shift of the mean value of the distribution.

This behaviour can be explained considering the elastic deformation of the BS assembly when subjected to a force. The influence of these variable is not negligible but it can be compensated by measuring the external force or the preload with the sensor available in the test rig.

The noise of the obtained data around the mean value of each distribution is given by the uncertainties defined in Tab. 9.5. Since the objective is to determine as accurately as possible the backlash size, it is paramount to find which parameters of Tab. 9.5 are the major responsible for the spread of f_b on a wide range of values.

To do so, the correlation matrix between the observed values of the features and the distribution of each uncertainty source has been evaluated for each data set, in

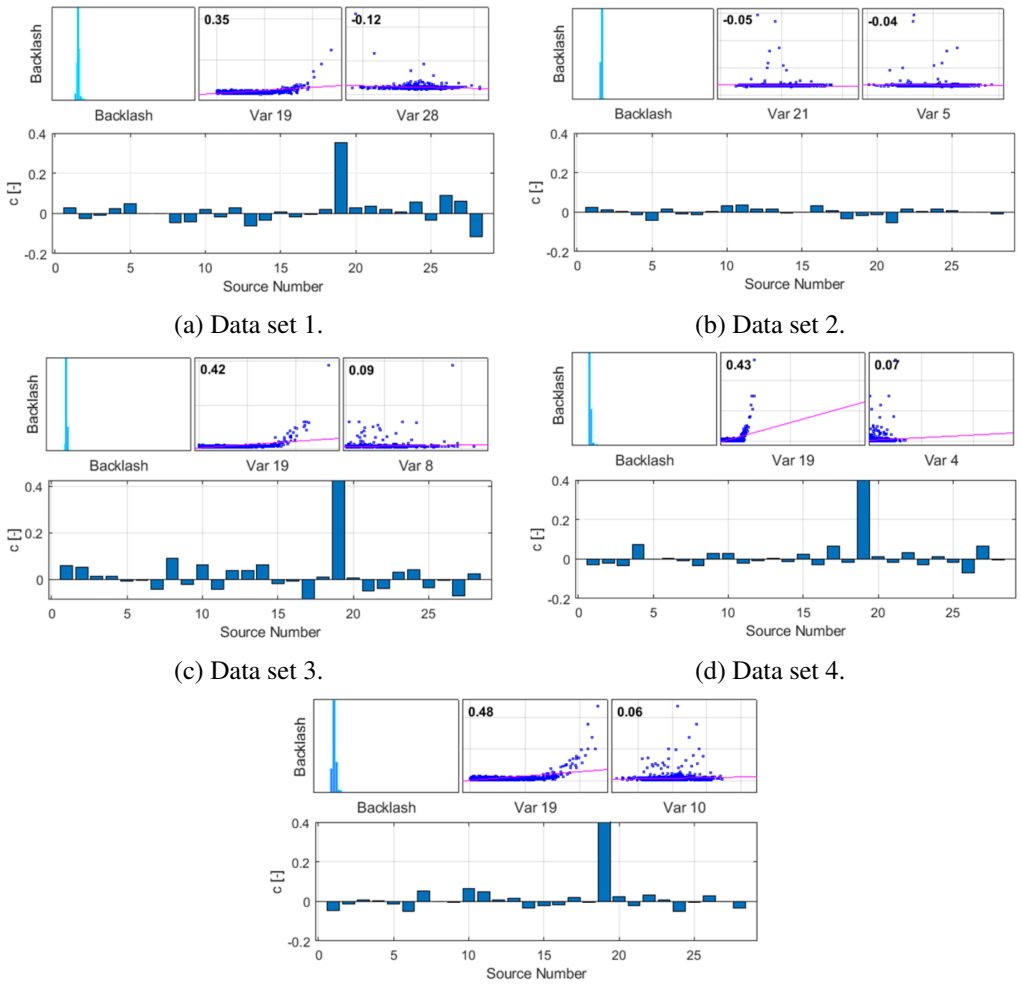

Fig. 9.9 Correlation plot for the various data set.

order to figure out which are the most influencing parameters and which of the five test procedure of Tab. 9.4 is the most suitable to minimise this dependence.

The obtained correlation plots are shown for each data set in Fig. 9.9. It can be observed that, for each data set except the second, there is a strong exponential dependence on the error on the tolerance between the phases of the optical linear encoder (Var 19). In fact, the average of the correlation factors for all the data sets is 0.42 for this uncertainty source, while lower values under 0.1 occur for all the others.

Instead, for the second data set (Fig. 9.9b) the behaviour is completely different: no clear dependences of the backlash feature on any source is evident. This data set has been obtained simulating the test bench under no preload and no force conditions,

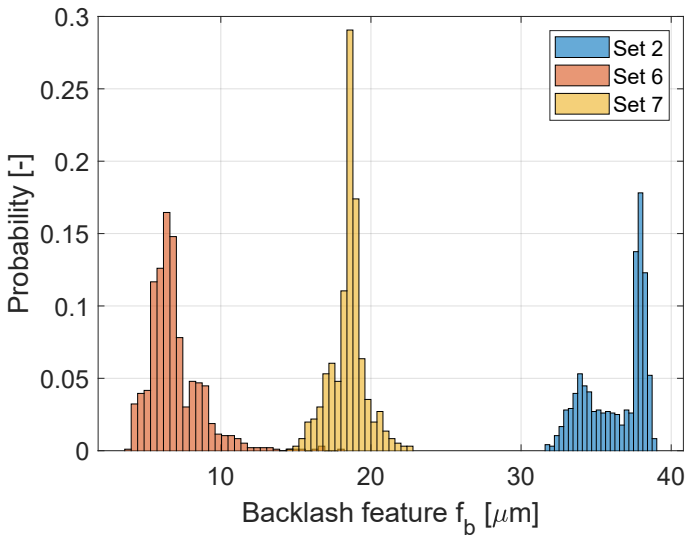

Fig. 9.10 Observed values for the different axial backlash values under test conditions of no preload and external force.

in presence of backlash. Therefore, no mechanical phenomena act to close the backlash gap and, hence, its size is big enough to not be strongly affected by errors in the linear encoder. Furthermore, also the correlation factor associated with the other uncertainty sources is extremely low, most of the time below 0.05.

From these results, it appears that the optimal conditions to accurately evaluate the size of the backlash are to apply neither a preload nor an external force.

Therefore, two additional data sets of 1000 simulations have been created under these optimal test conditions, varying the backlash size to 5 [µm] (data set number 6) and 40 [µm] (data set number 7). The obtained probability distributions are shown in Fig. 9.10. It has been found that, decreasing the size of the backlash gap, the correlation of f_b with the linear encoder errors tends to rise, up to a value of 0.44 for the case with 5 [µm] backlash. However, the three distributions of Fig. 9.10 are sufficiently narrow and allow the backlash size to be tracked during tests.

The difference between the nut position and the equivalent screw axial position is shown in Fig. 9.11 for two randomly selected simulations of the first and second data set.

From the comparison of the two signal, it is clear why the absence of the preload and the external force reduces the influence of the uncertainties on the backlash estimation. In fact, when at least one of two actions is present (Data set 1), the

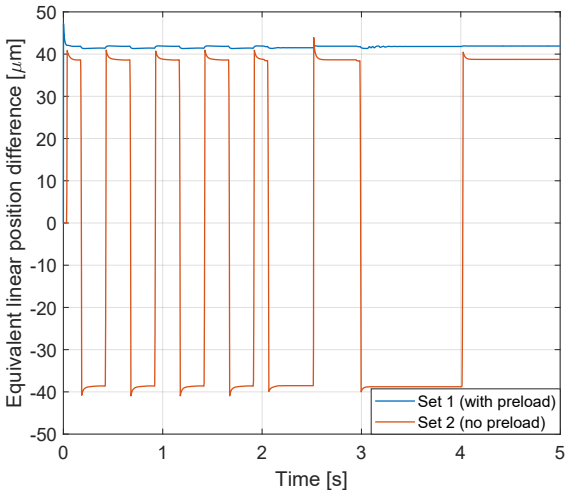

Fig. 9.11 Difference between the axial position of the nut and the equivalent position of the screw shaft for the data set 1 and 2.

backlash gap closes and the oscillations are due only to elastic deformations. On the other hand, in the second data set, the gap opens and closes alternatively in the positive or negative direction depending on the motion direction: in this condition, the effects of the linear encoder phase errors compensates and become less influential.

It is worth to be mentioned that, in Figs. 9.8 and 9.10, the value of f_b is always half the total backlash, because of the absolute value in the feature definition (Eq. 9.12).

An example of signals obtained from one of the simulation of the second data set, under the conditions of no external force and in presence of backlash and preload, is depicted in Fig. 9.12. Observing Fig. 9.12b, it can be seen that the preload oscillates around the imposed value due to the inertial effects which arise in transients, i.e. during the sinusoidal and step parts of the command. This oscillation cannot be read by the load cell since it is very small with respect to the instrument resolution. However, the variation is so small that it is of no importance in the evaluation of the BS performance. The motor current is plotted in Fig. 9.12c: its noisiness is due to the PWM method with which the command is transmitted to the motor and to the electrical random noise. Because of the right hand structure of the BS, when a positive displacement is requested, e.g. during the step command, the current, and hence the torque, is negative. The peaks correspond to the acceleration and deceleration phases.

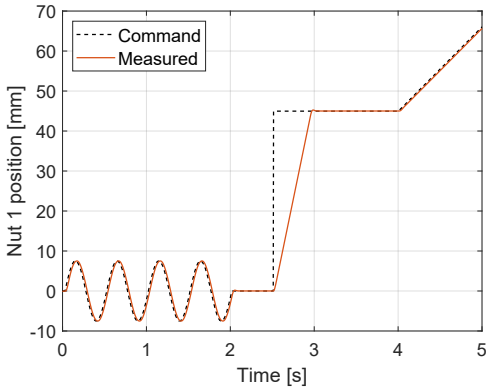

(a) Measured master nut position.

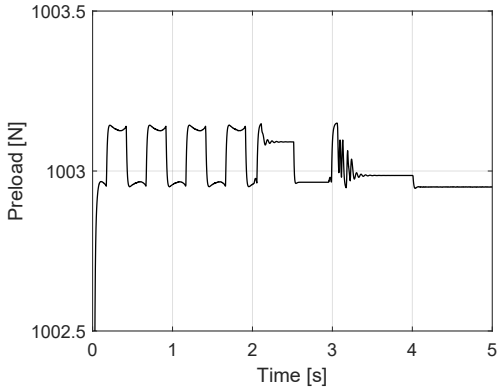

(b) Preload.

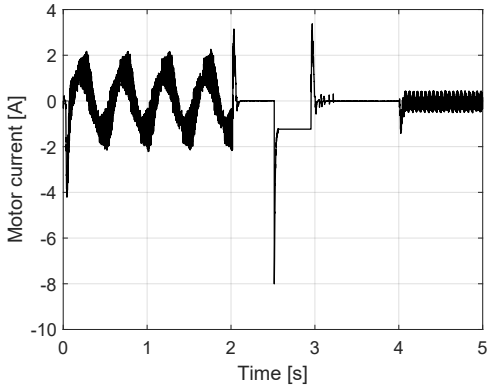

(c) Electric motor current.

Fig. 9.12 An example of simulation results for the simulation condition of data set 1.

9.5 Summary

The architecture of the BS test bench has been presented and described in this chapter. The test rig allows the preload to be varied from test to test and to be dynamically monitored. To verify the insensitivity of the measured signals to the inevitably present variances of the measuring system and geometrical parameters, a dynamic model of the entire test bench has been developed. It has been used to perform a preliminary Monte Carlo analysis to investigate the correlation of the read backlash value and the uncertain parameters' distributions. The results highlighted that the most influencing factor is the presence of phase errors in the linear encoder. Nevertheless, the developed test bench is able to accurately track the evolution of the backlash if optimal test conditions are used, i.e. with no preload and no external force.

Further analyses with the same methodology will be performed to assess the test bench capability to perform PHM studies under different degraded conditions and to define test procedures to highlight the faults effects while reducing the influence of external factors and measuring errors.

Chapter 10

Conclusions

10.1 Brief overview of the current work

In the last decades, a trend towards more electric aircraft has arisen, involving the replacement of EHSAs with EMAs for flight controls. However, this innovation is hindered by the relative increased jamming probability of EMAs. A solution to overcome this issue can be to support the real actuator with a prognostic and health management system, which needs, however, to be accurately trained and tuned. To this purpose, a high–fidelity model can be a cost effective and rapid solution, used as a virtual test bench on which to inject artificial defects to investigate their correlation with measurable signal features. One of the most critical components of EMAs is the BS, thus the current work focused on the study of this mechanism.

First, a review of the state of the art on BS models has been carried out. Then, a first simple dynamic model has been described, capable of taking into account the motion of the spheres within the grooves and the transition between the rolling and sliding conditions in both contact points with the screw and nut grooves. Successively, a more detailed and refined model has been introduced, in which the full dynamics of each component is represented by means of a multibody dynamic approach. A custom three–dimensional contact model has been created for the interaction between the spheres and the helical gothic arch grooves and between adjacent spheres. Two kinds of friction models have been inserted: a fast empirical equivalent friction model and a computational intensive detailed lubrication model. Lubricant

starvation, ageing and grooves wear degradation models have been considered so far. Moreover, the model has been used to simulate the dynamics of a jamming event.

Another multibody model has been developed in parallel in the framework of the commercial software MSC ADAMS to exploit its advanced capability of contact detection between arbitrary shaped bodies. This software has been used to investigate the effect of the recirculation channel on the overall dynamics of the mechanism. Furthermore, the load distribution has been analysed in presence of geometric errors and eccentricity of the external force application point on the nut. Vibration analysis can be performed with this model to investigate the presence of faults on the grooves.

Finally, in order to rely on the model results, an experimental validation process is required. The architecture of the BS test bench currently under construction has been described. The selection of the measuring sensors has been confirmed by the investigation of the faults observability by means of a Monte Carlo analysis. A mathematical model of the entire test bench with uncertain parameters has been used for this goal. The results highlighted the most influential uncertainty sources on the backlash size estimation and the optimal testing conditions to avoid this dependence.

It is worth to be highlighted that the research presented in this thesis has been focused on the aerospace sector, since it has been the research area from which the author's interest in the discussed topic originated, but its applicability is not only limited to this field. In fact, BSs are present in many machines used in several fields. The accurate modelling of the BS dynamics and the application of prognostic techniques on this component can be applied to a variety of situation, such as the feed axis drives of CNC machines in the manufacturing industry.

10.1.1 Models comparison

The comparison between the different models presented in this thesis is described in Tab. 10.1. The check marks refer to the current version of the models; the $\approx$ symbol, instead, signifies that, though not yet present, it is possible to represent the considered characteristic.

Depending on what is the goal of the simulation, different models can be used. In fact, if a tribological investigation or a detailed analysis of the power losses are the main interests, the Simscape model is the most appropriate. Instead, if a kinematic analysis has to be performed, or if the BS model has to be inserted into

Table 10.1 Models comparison.

Characteristic	**Model**		
	Simulink	Simscape	ADAMS
Dynamics of screw, nuts and spheres	✓	✓	✓
Centrifugal force effect	✓	✓	✓
Adherence/sliding independently at each contact point	✓	✓	✓
3D sphere dynamics		✓	✓
Helix torsion effect		✓	✓
Multiple contact points		✓	✓
Variable contact angles		✓	✓
Contact angle dependent contact stiffness		✓	≈
Contact and friction between adjacent spheres		✓	✓
Screw support compliance		≈	✓
Nut support compliance		≈	✓
Recirculation system		≈	✓
Lubricant effect		✓	≈
Wear degradation		✓	
Lubricant ageing degradation		✓	
Lubricant starvation		✓	
Presence of groove faults		≈	≈
Spherical ball shape variation		✓	✓
Ellipsoidal ball shape variation			≈
Vibration analysis		≈	✓

a more general model, only the speed and position are important and, thus, either the Simscape model with the empirical friction model or the ADAMS model can be adopted. Moreover, if the vibration analysis or the groove defects investigation are the aim of the simulation, the ADAMS model is the most suitable.

10.1.2 Contributions to knowledge

Contribution to the literature can be summarised as follows:

1. A fully comprehensive three-dimensional dynamic model of the ball screw mechanism has been developed to obtain insights on the internal behaviour of the spheres and on the mechanism's performance in presence of time variant operating conditions.
2. Dynamic, self–exciting and mutual interactive degradation models have been inserted in the model to investigate the evolution of the faults.

3. A lubrication friction model, although simplified, has been inserted into the multibody dynamic environment, allowing various lubrication regimes to be considered, as well as the load sharing in boundary and mixed lubrication.

4. A multi–sensorised test bench with variable preload adjustment mechanism and closed loop control of the external force has been designed and is being constructed to validate the model results and to perform experimental campaign on different artificially triggered defects.

10.1.3 Critical assessment of approach

Both the developed multibody models can describe the dynamics of all the sub-components of a ball screw but they are computational intensive, specially the one developed in the Simscape environment. Hence, several improvements could be still performed from the point of view of the mathematical implementation to reduce the computational time and to allow a more straightforward investigation of different faulty situations.

10.2 Recommendations and future work

This dissertation suggests the following issues to be considered for further research:

- The model implementation of the Simscape model can be enhanced to reduce the computational time.
- The recirculation channel is going to be inserted into the Simscape model to simulate realistic trajectories of the spheres. In such a way, the ideal constraints can be removed and vibration signal evaluations can be made on this model as well, and the possible link with the lubrication condition can be examined.
- Lubrication forces and wear maps can be calculated off–line and then inserted into the dynamic model in order to take into account realistic and accurate interaction analyses between the grooves while maintaining a reduced simulation time.

- The ADAMS model's contact subroutines can be customised to more accurately describe the variation of the contact stiffness and to insert more detailed formulations for the evaluation of the friction forces.
- More lubricant and mechanical degradations and faults will be studied and introduced in the Simscape model.
- Notch on the grooves can be added in both models to evaluate the vibration signature in the time–frequency domain.
- The developed models can be inserted into a more general model of an EMA to investigate the interaction of faults between the different components.
- The results of both simulation environments can be compared to obtain a first confirmation of the validity of the two approach.
- The model results will be validated with the experimental data coming from the developed test bench.
- A simulation campaign can be carried out inserting uncertain geometrical and lubricant parameters under healthy and degraded conditions to find meaningful health indicators for PHM purposes.

References

[1] T. Ford. More-electric aircraft. *Aircraft Engineering and Aerospace Technology*, 77, 2005.

[2] S. Hesse, G. Konrad, R. Reichel, I. Schäfer, P. Bourlier, and M. Buff. An Electro - Mechanical Actuator for General Aviation Aircraft. In *Aerospace Technology Conference and Exposition*, page 11. SAE, sep 2007.

[3] Jean-Charles Maré and Jian Fu. Review on signal-by-wire and power-by-wire actuation for more electric aircraft. *Chinese Journal of Aeronautics*, 30(3):857–870, 2017.

[4] Jean-Charles Maré. *Aerospace actuators 2 : signal-by-wire and power-by-wire*. John Wiley & Sons, Inc., 2017.

[5] Jean-Charles Maré. *Aerospace Actuators 1: needs, reliability and hydraulic power solutions*. John Wiley & Sons, Inc., 2016.

[6] J.A. Weimer. The role of electric machines and drives in the more electric aircraft. In *IEEE International Electric Machines and Drives Conference, 2003. IEMDC'03.*, volume 1, pages 11–15, Madison, WI, USA, 2003. IEEE.

[7] Alireza R. Behbahani and Kenneth J. Semega. Control Strategy for Electro-Mechanical Actuators Versus Hydraulic Actuation Systems for Aerospace Applications. In *Power System Conference*, page 13. SAE, nov 2010.

[8] Michel Todeschi. Airbus - EMAs for flight actuation systems - perspectives. In *International Conference on Recent Advances in Aerospace Actuation Systems and Components*, pages 1–8, 2010.

[9] Jean-Claude Derrien, Pierre Tieys, David Senegas, and Michel Todeschi. EMA Aileron COVADIS Development. In *Aerospace Technology Conference and Exposition*, page 13. SAE, oct 2011.

[10] Jean-Claude Derrien. Electromechanical Actuator (EMA) Advanced Technologies for Flight Controls. In *28Th International Congress of the Aeronautical Sciences*, pages 1–10, 2012.

[11] Jian Fu, Jean-Charles Maré, Liming Yu, and Yongling Fu. Multi-level virtual prototyping of electromechanical actuation system for more electric aircraft. *Chinese Journal of Aeronautics*, dec 2017.

[12] J. A. Rosero, J. A. Ortega, E. Aldabas, and L. Romeral. Moving towards a more electric aircraft. *IEEE Aerospace and Electronic Systems Magazine*, 22(3):3–9, 2007.

[13] David E. Blanding and Arsuo J. Watanabe. Fault-tolerant electro-mechanical actuator having motor armatures to drive a ram and having an armature release mechanism, 2007.

[14] J.W. Bennett, B.C. Mecrow, D.J. Atkinson, and G.J. Atkinson. Safety-critical design of electromechanical actuation systems in commercial aircraft. *IET Electric Power Applications*, 5(1):37, 2011.

[15] Lowell L. V. Larson and Richard K. Larsen. Fault-tolerant linear electromechanical actuator, 1993.

[16] Delbert Tesar. Fault tolerant linear actuator, 2004.

[17] Duane H. Grimm and Teddy L. Jones. Jam tolerant linear actuator, 1992.

[18] Dan T. Nguyen, Bruce W. Behar, and Ted A. McKay. Jam-tolerant electromechanical actuator, 2014.

[19] Andrew J. Collins. Flight control surface actuation system, 2004.

[20] Davide Ferrara, Giovanni Jacazio, Andrea Mornacchi, and Massimo Sorli. Robust mechatronic actuation system for UAV primary flight controls. In ASME, editor, *IMECE*, pages 1–11, Houston, Texas, USA, 2012. ASME.

[21] Michel Todeschi and Laura Baxerres. Health monitoring for the flight control EMAs. In *IFAC-PapersOnLine*, volume 48, pages 186–193. Elsevier B.V., 2015.

[22] Andrea De Martin, Giovanni Jacazio, and George Vachtsevanos. Anomaly Detection and Prognosis for Primary Flight Control EMAs. In *European Conference of the Prognostic and Health Management Society*, pages 1–9, 2016.

[23] George Vachtsevanos, Frank Lewis, Michael Roemer, Andrew Hess, and Biqing Wu. *Intelligent Fault Diagnosis and Prognosis for Engineering Systems*. John Wiley & Sons, Inc., Hoboken, NJ, USA, 2006.

[24] Oliver Ritter, Gerko Wende, Rocco Gentile, Francesco Marino, Antonio Carlo Bertolino, and Andrea Raviola. Intelligent diagnostics for aircraft hydraulic equipment. In *4th European Conference of the Prognostics and Health Management Society*, Utrecht, The Nederlands, 2018.

[25] David E. Acuña and Marcos E. Orchard. Particle-filtering-based failure prognosis via sigma-points: Application to Lithium-Ion battery State-of-Charge monitoring. *Mechanical Systems and Signal Processing*, 85:827–848, 2017.

[26] William Hardman. Mechanical and propulsion systems prognostics: U.S. navy strategy and demonstration. *Jom*, 56(3):21–27, 2004.

[27] Chee Keong Tan, Phil Irving, and David Mba. A comparative experimental study on the diagnostic and prognostic capabilities of acoustics emission, vibration and spectrometric oil analysis for spur gears. *Mechanical Systems and Signal Processing*, 21(1):208–233, 2007.

[28] Xiaochuan Li, Fang Duan, David Mba, and Ian Bennett. Multidimensional prognostics for rotating machinery: A review. *Advances in Mechanical Engineering*, 9(2):1–20, 2017.

[29] Yaguo Lei, Naipeng Li, Liang Guo, Ningbo Li, Tao Yan, and Jing Lin. Machinery health prognostics: A systematic review from data acquisition to RUL prediction. *Mechanical Systems and Signal Processing*, 104:799–834, 2018.

[30] Adrian Cubillo, Suresh Perinpanayagam, and Manuel Esperon-Miguez. A review of physics-based models in prognostics: Application to gears and bearings of rotating machinery. *Advances in Mechanical Engineering*, 8(8):1–21, 2016.

[31] Neal N. McCollom and Edward R. Brown. PHM on the F-35 fighter. *2011 IEEE International Conference on Prognostics and Health Management, PHM 2011 - Conference Proceedings*, 76101, 2011.

[32] Zhenhua Wen and Yuanpeng Liu. Applications of Prognostics and Health Management in aviation industry. *2011 Prognostics and System Health Management Conference, PHM-Shenzhen 2011*, 2011.

[33] Mohamed A.A. Ismail, Edward Balaban, and Holger Spangenberg. Fault detection and classification for flight control electromechanical actuators. In *IEEE Aerospace Conference Proceedings*, pages 1–10, 2016.

[34] Aitor Isturiz, Javier Vinals, Jose Manuel Abete, and Aitzol Iturrospe. Health monitoring strategy for electromechanical actuator systems and components. Screw backlash and fatigue estimation. In *Recent Advances in Aerospace Actuation Systems and Components*, 2012.

[35] Yameen M Hussain, Stephen Burrow, Leigh Henson, and Patrick Keogh. A Review of Techniques to Mitigate Jamming in Electromechanical Actuators for Safety Critical Applications. *International Journal of Prognostics and Health Management*, pages 2153–2648, 2018.

[36] Andrea Mornacchi, George Vachtsevanos, and Giovanni Jacazio. Prognostics and Health Management of an Electro-Hydraulic Servo Actuator. In *Annual Conference of the Prognostic and Health Management Society*, pages 1–12, 2015.

[37] Andrea De Martin, Giovanni Jacazio, and Massimo Sorli. Enhanced Particle Filter framework for improved prognosis of Electro-Mechanical flight controls Actuators. *3rd European Conference of the Prognostic and Health Management Society*, pages 1–10, 2017.

[38] M. Sanjeev Arulampalam, Simon Maskell, Neil Gordon, and Tim Clapp. A tutorial on particle filters for online nonlinear/nongaussian bayesian tracking. *Bayesian Bounds for Parameter Estimation and Nonlinear Filtering/Tracking*, 50(2):723–737, 2007.

[39] Cheng He, Jiaming Li, and George Vachtsevanos. Prognostics and health management of an automated machining process. *Mathematical Problems in Engineering*, 2015, 2015.

[40] Donald L. Simon, Sanjay Garg, Gary W. Hunter, Ten Huei Guo, and Kenneth J. Semega. Sensor needs for control and health management of intelligent aircraft engines. *Proceedings of the ASME Turbo Expo 2004*, 2(August):873–882, 2004.

[41] Franciscus Leendert Johannes Linden, Nikolaus Dreyer, and André Dorkel. EMA Health Monitoring: An overview. *Recent Advances in Aerospace Actuation Systems and Components*, pages 21–26, 2016.

[42] Edward Balaban, Abhinav Saxena, and Kai Goebel. Experimental data collection and modeling for nominal and fault conditions on electro-mechanical actuators. In *Annual Conference of the Prognostics and Health Management Society*, pages 1–15, 2009.

[43] Edward Balaban, Abhinav Saxena, Prasun Bansal, Kai F. Goebel, Paul Stoelting, and Simon Curran. A diagnostic approach for electro-mechanical actuators in aerospace systems. In *IEEEAC*, page 1345, 2009.

[44] D. Howe. Magnetic actuators. *Sensors and Actuators A: Physical*, 81:268–274, apr 2000.

[45] Osamu Goto. Development of Active Suspension System with Electromechanical Actuators for Railway Vehicles. Technical Report 105, Nippon steel & Sumitomo metal, 2013.

[46] C. Carnevale and P. D. Resta. Vega electromechanical thrust vector control development. In *43rd AIAA/ASME/ASEE Joint Propulsion Conference and Exhibit*, 2007.

[47] M. J. Kittock. High Power TVC actuator. In *AIAA/SAE/ASME/ASEE 26th Joint Propulsion Conference*, 1993.

[48] D. Teske and D. Faulkner. Electromechanical flight control servoactuator. In *Intersociety Energy Conversion Engineering Conference*, pages 1021–1025, Orlando, FL, USA, 1993.

[49] F. N. Collamore and M. J. Lister. A reliable, low-cost electromechanical actuator for the ALS engine control effectors. In *AIAA/SAE/ASME/ASEE 26th Joint Propulsion Conference*, 1990.

[50] C. Fulmer. 40 HP Electro-mechanical actuator. *NASA Contractor Report 198509*, 1996.

[51] J. T. Edge. An electromechanical actuator technology development program. *SAE Technical Paper 780581*, 1978.

[52] J. Hagen, L. Moore, and J. Estes. The X-38 V-201 flap actuator mechanism. In *Proceedings of the 37th Aerospace Mechanisms Symposium, Johnson Space Center*, pages 377–390, 2004.

[53] Guan Qiao, Geng Liu, Zhenghong Shi, Yawen Wang, Shangjun Ma, and Teik C. Lim. A review of electromechanical actuators for More/All Electric aircraft systems. *Proceedings of the Institution of Mechanical Engineers, Part C: Journal of Mechanical Engineering Science*, 232(22):4128–4151, nov 2017.

[54] C. Whitley and J. Ropert. Development, manufacture & flight test of spoiler EMA system. In *International conference on recent advances in aerospace actuation systems and components*, pages 215–220, Tolouse, France, 2007.

[55] J. Bower. A380 Hydraulic Slat Drive Channel. In *Proceedings of the 2nd International Conference on Recent Advances in Aerospace Actuation Systems and Components*, pages 91–96, 2004.

[56] Antonio Carlo Bertolino, Massimo Sorli, Giovanni Jacazio, and Stefano Mauro. Lumped parameters modelling of the EMAs' ball screw drive with special consideration to ball/grooves interactions to support model-based health monitoring. *Mechanism and Machine Theory*, 137:188–210, jul 2019.

[57] Stewart Andrew Vaculik. *A Framework for Electromechanical Actuator Design*. Phd thesis, The University of Texas at Austin, 2008.

[58] Andrea Dellacasa, Giovanni Jacazio, and Alberto Zunino. EMADEF : a fully comprehensive analytical tool for the initial design of electro-mechanical servo-actuators for primary flight controls. In *Recent Advances in Aerospace Actuation Systems and Components*, Tolouse, France, 2018.

[59] Duane Hanselman. *Brushless Permanent Magnet Motor Design*. Magna Physics Publishing, 2nd ed. edition, 2006.

[60] Ned Mohan. *Power electronics: a first course*. John Wiley & Sons, Inc., 2012.

[61] Andrea Mornacchi. *Design and Development of Prognostic and Health Management System for Fly-by-Wire Primary Flight Control Electrohydraulic Servoactuators*. Ph.d. degree in mechanical engineering, Politecnico di Torino, 2016.

[62] John William Bennett. *Fault Tolerant Electromechanical Actuators for Aircraft*. Phd thesis, Newcastle University, 2010.

[63] Nicholas Elliott and Arnaud Didey. Jam-tolerant actuator, 2011.

[64] Ralph P. Elbert and Michael A. Hafner. Fault tolerant actuation system for flight control actuators, 1998.

[65] Alexander Naubert, Markus Christmann, and Peter Janker. Anti-jamming mechanism for electromechanical actuators. In *Proceedings of the 4th International Workshop on Aircraft System Technologies*, pages 139–147, Hamburg, Germany, 2013.

[66] Alexander Naubert, Hansgeorg Binz, Matthias Bachmann, Markus Christmann, Stefano Toro, and Federico Perni. Disconnect Device Design Options for Jam-Tolerant Electromechanical Actuators. In *Recent Advances in Aerospace Actuation Systems and Components*, pages 187–192, Toulouse, France, 2016.

[67] Lijian Wang, Jean-Charles Maré, and Yongling Fu. Investigation in the Dynamic Force Equalization of Dissimilar Redundant Redundant Actuation Systems Operating in Active/Active Mode. In *28Th International Congress of the Aeronautical Sciences*, 2012.

[68] Michel Todeschi. Airbus - EMAs for Flight Controls Actuation System - An Important Step Achieved in 2011. In *SAE International*, oct 2011.

[69] Edward Balaban, Abhinav Saxena, Sriram Narasimhan, Indranil Roychoudhury, Kai F Goebel, and Michael T Koopmans. Airborne electro-mechanical actuator test stand for development of prognostic health management systems. In *Annual Conference of the Prognostics and Health Management Society*, pages 1–13, 2010.

[70] Edward Balaban, Abhinav Saxena, Sriram Narasimhan, Indranil Roychoudhury, Michael Koopmans, Carl Ott, and Kai Goebel. Prognostic Health-Management System Development for Electromechanical Actuators. *Journal of Aerospace Information Systems*, 12(3):329–344, 2015.

[71] Sriram Narasimhan, Indranil Roychoudhury, Edward Balaban, and Abhinav Saxena. Combining Model-Based and Feature-DrivenFeature-Driven Diagnosis Approaches – A Case Study on Electromechanical Actuators. *21st International Workshop on Principles of Diagnosis*, pages 1–9, 2010.

[72] David S. Bodden, N. Scott Clements, Bill Schley, and Gavin Jenney. Seeded failure testing and analysis of an electro-mechanical actuator. In *IEEE Aerospace Conference Proceedings*, 2007.

[73] T.A. Harris and M.H. Mindel. Rolling element bearing dynamics. *Wear*, 23(3):311–337, mar 1973.

[74] T.A. Harris. *Rolling Bearing Analysis*. John Wiley & Sons, Inc., 3rd edition, 1991.

[75] Jafar Takabi and M. M. Khonsari. On the thermally-induced failure of rolling element bearings. *Tribology International*, 94:661–674, 2015.

[76] Yunchuan Jiang, Wentao Huang, Jianing Luo, and Weijie Wang. An improved dynamic model of defective bearings considering the three-dimensional geometric relationship between the rolling element and defect area. *Mechanical Systems and Signal Processing*, 129:694–716, 2019.

[77] SKF. The SKF model for calculating the frictional moment. Technical report, SKF, 2017.

[78] NSK Corporation. Ball screw catalogue.

[79] Y. Altintas, A. Verl, C. Brecher, L. Uriarte, and G. Pritschow. Machine tool feed drives. *CIRP Annals - Manufacturing Technology*, 60(2):779–796, 2011.

[80] Umbra Group. Industrial Ballscrews catalogue.

[81] KSS. Ball screws catalogue.

[82] A. Verl and S. Frey. Correlation between feed velocity and preloading in ball screw drives. *CIRP Annals - Manufacturing Technology*, 59(1):429–432, 2010.

[83] Tung Lam Nguyen, Seung Kook Ro, and Jong Kweon Park. Study of ball screw system preload monitoring during operation based on the motor current and screw-nut vibration. *Mechanical Systems and Signal Processing*, 131:18–32, 2019.

[84] ISO 3408-4:2006. Ball screws - Part 4: Static axial rigidity, 2006.

[85] Paul Eschmann. *Ball and Roller Bearings: Theory, Design and Application*. John Wiley & Sons, Inc., 1985.

[86] Piet M. Lugt. *Grease Lubrication in Rolling Bearings*. John Wiley & Sons, Inc., 2013.

[87] Gwidon W. Stachowiak and Andrew W. Batchelor. *Engineering tribology, 4th ed.* Elsevier, 2014.

[88] G Popovici. *Effects of Lubricant Starvation on Performance of Elasto-Hydrodynamically Lubricated Contacts*. PhD thesis, University of Twente, 2005.

[89] Chin Chung Wei and Ruei Syuan Lai. Kinematical analyses and transmission efficiency of a preloaded ball screw operating at high rotational speeds. *Mechanism and Machine Theory*, 46(7):880–898, 2011.

[90] ISO 3408-1:2006. Ball screws - Part 5: Static and dynamic axial load ratings and operational life, 2006.

[91] Jerzy Z. Sobolewski. Vibration of the ball screw drive. *Engineering Failure Analysis*, 24:1–8, 2012.

[92] Jui Pin Hung, James Shih-Shyn Wu, and Jerry Y. Chiu. Impact failure analysis of re-circulating mechanism in ball screw. *Engineering Failure Analysis*, 11(4):561–573, 2004.

[93] ISO 3408-1:2006. Ball screws - Part 1: Vocabulary and designation, 2006.

[94] Antonio Carlo Bertolino, Giovanni Jacazio, Stefano Mauro, and Massimo Sorli. Developing of a Simscape Multibody Contact Library for Gothic Arc Ball Screws: A Three-Dimensional Model for Internal Sphere/Grooves Interactions. In ASME, editor, *IMECE Volume 4: Dynamics, Vibration, and Control*, Salt Lake City, UT, USA, nov 2019. American Society of Mechanical Engineers.

[95] M. C. Lin, S. A. Velinsky, and B. Ravani. Design of the Ball Screw Mechanism for Optimal Efficiency. *Journal of Mechanical Design*, 116(3):856–861, 1994.

[96] G.A. Levit. Calculations of recirculating ball screw and nut transmission. *Machines and Tooling*, 5(2):9–16, 1963.

[97] M. C. Lin, B. Ravani, and S. A. Velinsky. Kinematics of the Ball Screw Mechanism. *Journal of Mechanical Design*, 116(3):849–855, 1994.

[98] Chin Chung Wei and Jen Fin Lin. Kinematic Analysis of the Ball Screw Mechanism Considering Variable Contact Angles and Elastic Deformations. *Journal of Mechanical Design*, 125(4):717–733, 2003.

[99] J. J. Moré. The Levenberg-Marquardt Algorithm: Implementation and Theory. *Numerical Analysis*, Lecture No:105–116, 1977.

[100] MOOG. Ball screws and planetary roller screws, 2014.

[101] Chun Jen Chen, Wenyuh Jywe, Yu Chun Liu, and Hsin Hong Jwo. The development of using the digital projection method to measure the contact angle of ball screw. *Physics Procedia*, 19:36–42, 2011.

[102] Yoann Barranger, Romuald Bertolaso, Pascal Doumalin, Jean-Christophe Dupré, Arnaud Germaneau, and Mohammed Cheikh. Experimental validation of a numerical simulation on a ballscrew system by 3D photoelasticity. In *EPJ Web of Conference*. EDP Sciences, 2010.

[103] Romuald Bertolaso, Mohammed Cheikh, Yoann Barranger, Jean-Christophe Dupré, Arnaud Germaneau, and Pascal Doumalin. Experimental and numerical study of the load distribution in a ball-screw system. *Journal of Mechanical Science and Technology*, 28(4):1411–1420, 2014.

[104] G.A. Levit. Recirculating ball screw and nut units. *Machines and Tooling*, 34(4):3–8, 1963.

[105] Y.N. Drozdov. Calculating the wear of a screw and nut transmission with sliding friction. *Soviet Engineering Research*, 4(5):1–12, 1984.

[106] T.A. Harris. An Analytical Method to Predict Skidding in Thrust-Loaded, Angular-Contact Ball Bearings. *Journal of Lubrication Technology*, 93(1):17, 1971.

[107] G. Lundberg. Motions in Loaded Rolling Element Bearings. Technical report, SKF, 1954.

[108] Jianzhong Hu, Min Wang, and Tao Zan. The kinematics of ball-screw mechanisms via the slide-roll ratio. *Mechanism and Machine Theory*, 79:158–172, 2014.

[109] R. Gnanamoorthy, N. Govindarajan, and Y. Mutoh. Effect of slid-roll ratio on the contact fatigue behavior of sintered and hardened steels. *Journal of Failure Analysis and Prevention*, 4(2):78–83, apr 2004.

[110] N. Govindarajan and R. Gnanamoorthy. Rolling/sliding contact fatigue life prediction of sintered and hardened steels. *Wear*, 262(1-2):70–78, jan 2007.

[111] Hual-Te T. Huang and B. Ravani. Contact Stress Analysis in Ball Screw Mechanism Using the Tubular Medial Axis Representation of Contacting Surfaces. *Journal of Mechanical Design*, 119(1):8, 1997.

[112] Takafumi Yoshida, Yasuyoshi Tozaki, and Susumu Matsumoto. Study on Load Distribution and Ball Motion of Ball Screw, 2003.

[113] a. B. Jones. A General Theory for Elastically Constrained Ball and Radial Roller Bearings Under Arbitrary Load and Speed Conditions. *Journal of Basic Engineering*, 82(2):309–320, 1960.

[114] Chin Chung Wei, Jen Fin Lin, and Jeng-Haur Horng. Analysis of a ball screw with a preload and lubrication. *Tribology International*, 42(11-12):1816–1831, dec 2009.

[115] Chang Guang Zhou, Yi Ou, Hu Tian Feng, and Zeng Tao Chen. Investigation of the precision loss for ball screw raceway based on the modified Archard theory. *Industrial Lubrication and Tribology*, 69(2):166–173, 2017.

[116] Nannan Xu and Wencheng Tang. Modeling and Analyzing the Slipping of the Ball Screw. *Latin American Journal of Solids and Structures*, 12(3):612–623, mar 2015.

[117] A. Verl, S. Frey, and T. Heinze. Double nut ball screw with improved operating characteristics. *CIRP Annals - Manufacturing Technology*, 63(1):361–364, 2014.

[118] Chang Guang Zhou, Hu Tian Feng, Zeng Tao Chen, and Yi Ou. Correlation between preload and no-load drag torque of ball screws. *International Journal of Machine Tools and Manufacture*, 102:35–40, 2016.

[119] ISO 3408-3:2006. Ball screws - Part 3: Acceptance conditions and acceptance tests, 2006.

[120] J. F. Cuttino and T. A. Dow. Contact Between Elastic Bodies With an Elliptic Contact Interface in Torsion. *Journal of Mechanical Design*, 64(March 1997):144–148, 1997.

[121] Bo Lin, Molong Duan, Chinedum E. Okwudire, and Jason S. Wou. A simplified analytical model of rolling/sliding behavior and friction in four-point-contact ball bearings and screws. In *Proceedings of the ASME 2017 International Mechanical Engineering Congress and Exposition*, Tampa, Florida, USA, 2017.

[122] R.D. Mindlin. Compliance of elastic bodies in contact. *Journal of Applied Mechanics*, 16:259–268, 1949.

[123] J.L. Lubkin. The torsion of elastic spheres in contact. *Journal of Applied Mechanics*, 18(1):183–187, 1951.

[124] J. F. Cuttino, T. A. Dow, and B. F. Knight. Analytical and Experimental Identification of Nonlinearities in a Single-Nut, Preloaded Ball Screw. *Journal of Mechanical Design*, 119(1):15, 1997.

[125] Stefano Mauro, Stefano Pastorelli, and Tharek Mohtar. Sensitivity Analysis of the Transmission Chain of a Horizontal Machining Tool Axis to Design and Control Parameters. *Advances in Mechanical Engineering*, 6:169064, jan 2014.

[126] Stefano Mauro, Stefano Pastorelli, and Edward Johnston. Influence of controller parameters on the life of ball screw feed drives. *Advances in Mechanical Engineering*, 7(8):1–11, aug 2015.

[127] Liang Mi, Guo fu Yin, Ming nan Sun, and Xiao hu Wang. Effects of preloads on joints on dynamic stiffness of a whole machine tool structure. *Journal of Mechanical Science and Technology*, 26(2):495–508, 2012.

[128] J. Otsuka. Nanometer level positioning using three kinds of lead screws. *Nanotechnology*, 3(1):29–36, jan 1992.

[129] Katuhiro Nakashima, Yuuma Tamaru, and Kazuki Takafuji. Ultraprecision Positioning by Preload Change of Lead Screws. *JSME International Journal*, 44(3):808–815, 2001.

[130] Shigeo Fukada, Bin Fang, and Akira Shigeno. Experimental analysis and simulation of nonlinear microscopic behavior of ball screw mechanism for ultra-precision positioning. *Precision Engineering*, 35(4):650–668, 2011.

[131] Kripa K Varanasi and Samir A Nayfeh. The Dynamics of Lead-Screw Drives: Low-Order Modeling and Experiments. *Journal of Dynamic Systems, Measurement, and Control*, 126(2):388–396, 2004.

[132] X. Min and S. Jiang. A thermal model of a ball screw feed drive system for a machine tool. *Proceedings of the Institution of Mechanical Engineers, Part C: Journal of Mechanical Engineering Science*, 225(1):186–193, 2011.

[133] Takehiko Kodera, Kazuhiro Yokoyama, Kazuo Miyaguchi, Yutaka Nagai, Takamasa Suzuki, Masami Masuda, and Takanori Yazawa. Real-time estimation of ball-screw thermal elongation based upon temperature distribution of ball-screw. *JSME International Journal, Series C: Mechanical Systems, Machine Elements and Manufacturing*, 47(4):1175–1181, 2004.

[134] Walther Maier and Uwe Heisel. Experimental investigation of a ball screw for increasing the accuracy of thermal FE simulations. *TMT2012*, pages 423–426, 2012.

[135] J. Y. Ahn and S. C. Chung. Real-time estimation of the temperature distribution and expansion of a ball screw system using an observer. *Proceedings of the Institution of Mechanical Engineers, Part B: Journal of Engineering Manufacture*, 218(12):1667–1681, 2004.

[136] Amin Kamalzadeh, Daniel J. Gordon, and Kaan Erkorkmaz. Robust compensation of elastic deformations in ball screw drives. *International Journal of Machine Tools and Manufacture*, 50(6):559–574, 2010.

[137] Otakar Horejs. Thermo-Mechanical Model of Ball Screw With Non-Steady Heat Sources. In *2007 International Conference on Thermal Issues in Emerging Technologies: Theory and Application*, pages 133–137. IEEE, jan 2007.

[138] Diego A. Vicente, Rogelio L. Hecker, Fernando J. Villegas, and Gustavo M. Flores. Modeling and vibration mode analysis of a ball screw drive. *International Journal of Advanced Manufacturing Technology*, 58(1-4):257–265, 2012.

[139] M.F. Zaeh, Th. Oertli, and J. Milberg. Finite Element Modelling of Ball Screw Feed Drive Systems. *CIRP Annals - Manufacturing Technology*, 53(1):289–292, 2004.

[140] Meng Duan, Hong Lu, Xinbao Zhang, Yongquan Zhang, Zhangjie Li, and Qi Liu. Dynamic Modeling and Experiment Research on Twin Ball Screw Feed System Considering the Joint Stiffness. *Symmetry*, 10(12):686, dec 2018.

[141] Zhe Du, Xiao-lan Zhang, and Tao Tao. Study of the Dynamic Characteristics of Ball Screw with a Load Disturbance. *Mathematical Problems in Engineering*, 2016:1–10, 2016.

[142] Christian Brecher, Bastian Eßer, Jens Falker, Florian Kneer, and Marcel Fey. Modelling of ball screw drives rolling element contact characteristics. In *CIRP Annals - Manufacturing Technology*, pages 4–7. CIRP, 2018.

[143] Yongjiang Chen and Wencheng Tang. Determination of contact stiffness in ball screws considering variable contact angles. *Proceedings of the Institution of Mechanical Engineers, Part C: Journal of Mechanical Engineering Science*, 228(12):2193–2203, 2014.

[144] Xuesong Mei, Masaomi Tsutsumi, Tao Tao, and Nuogang Sun. Study on the load distribution of ball screws with errors. *Mechanism and Machine Theory*, 38(11):1257–1269, 2003.

[145] Ni Zhen and Qi An. Analysis of stress and fatigue life of ball screw with considering the dimension errors of balls. *International Journal of Mechanical Sciences*, 137(December 2017):68–76, 2018.

[146] Sheng Xu, Zhenqiang Yao, Yaofei Sun, and Hong Shen. Load Distribution of Ball Screw With Consideration of Contact Angle Variation and Geometry Errors. In ASME, editor, *IMECE2014 - Volume 2B: Advanced Manufacturing*, Montreal, Quebec, Canada, nov 2014. ASME.

[147] Chinedum E. Okwudire and Yusuf Altintas. Hybrid Modeling of Ball Screw Drives With Coupled Axial, Torsional, and Lateral Dynamics. *Journal of Mechanical Design*, 131(7):071002, 2009.

[148] Chinedum E. Okwudire. Improved Screw–Nut Interface Model for High-Performance Ball Screw Drives. *Journal of Mechanical Design*, 133(4):041009, 2011.

[149] Chinedum E. Okwudire. Reduction of torque-induced bending vibrations in ball screw-driven machines via optimal design of the nut. *Journal of Mechanical Design, Transactions of the ASME*, 134(11):1–9, 2012.

[150] Bo Lin and Chinedum E. Okwudire. Low-Order Contact Load Distribution Model for Ball Nut Assemblies. *SAE International Journal of Passenger Cars - Mechanical Systems*, 9(2):535–540, 2016.

[151] Bo Lin, Chinedum E. Okwudire, and Jason S. Wou. Low Order Static Load Distribution Model for Ball Screw Mechanisms including Effects of Lateral Deformation and Geometric Errors. *Journal of Mechanical Design*, 140(February):1–12, 2018.

[152] A. Oyanguren, P. Zahn, A. H. Alberdi, J. Larrañaga, A. Lechler, and I. Ulacia. Preload variation due to temperature increase in double nut ball screws. *Production Engineering*, 10(4-5):529–537, 2016.

[153] A. Oyanguren, J. Larrañaga, and I. Ulacia. Thermo-mechanical modelling of ball screw preload force variation in different working conditions. *International Journal of Advanced Manufacturing Technology*, 97(1-4):723–739, 2018.

[154] Juan Wen, Hongli Gao, Qi Liu, Xin Hong, and Yi Sun. A new method for identifying the ball screw degradation level based on the multiple classifier system. *Measurement: Journal of the International Measurement Confederation*, 130:118–127, 2018.

[155] A. Garinei and R. Marsili. A new diagnostic technique for ball screw actuators. *Measurement: Journal of the International Measurement Confederation*, 45(5):819–828, 2012.

[156] Chang Fu Han, He Qing He, Chin Chung Wei, Jeng Haur Horng, Yueh Lin Chiu, Yih Chyun Hwang, and Jen Fin Lin. Techniques developed for fault diagnosis of long-range running ball screw drive machine to evaluate lubrication condition. *Measurement: Journal of the International Measurement Confederation*, 126(May):274–288, 2018.

[157] Pin Li, Xiaodong Jia, Jianshe Feng, Hossein Davari, Guan Qiao, Yihchyun Hwang, and Jay Lee. Prognosability study of ball screw degradation using systematic methodology. *Mechanical Systems and Signal Processing*, 109:45–57, 2018.

[158] Yi-Cheng Huang and Yan-Chen Shin. Method of Intelligent Fault Diagnosis of Preload Loss for Single Nut Ball Screws through the Sensed Vibration Signals. *International Journal of Mechanical and Mechatronics Engineering*, 6(5):1247–1254, 2012.

[159] Huang Yai-Cheng and Sun Shi-Lun. Ball Nut Preload Diagnosis of the Hollow Ball Screw through Sensed Current Signals. *International Journal of Automation and Smart Technology*, 4(3):134–142, 2014.

[160] Guo Hua Feng and Yi Lu Pan. Establishing a cost-effective sensing system and signal processing method to diagnose preload levels of ball screws. *Mechanical Systems and Signal Processing*, 28:78–88, 2012.

[161] Guo Hua Feng and Yi Lu Pan. Investigation of ball screw preload variation based on dynamic modeling of a preload adjustable feed-drive system and spectrum analysis of ball-nuts sensed vibration signals. *International Journal of Machine Tools and Manufacture*, 52(1):85–96, 2012.

[162] T.L. Nguyen, S.K. Ro, C.K. Song, and J.K. Park. Study on preload monitoring of ball screw feed drive system using natural frequency detection. *Journal of the Korean Society for Precision Engineering*, 35(2):135–143, 2018.

[163] Jiajia Zhao, Mingxing Lin, Xianchun Song, and Hongkui Jiang. Research on the precision loss of ball screw with short-time overload impact. *Advances in Mechanical Engineering*, 10(12):1–9, 2018.

[164] Christian Brecher, Stephan Witt, and Türker Yagmur. Influences of oil additives on the wear behavior of ball screws. *Production Engineering*, 3(3):323–327, 2009.

[165] Chin Chung Wei, Wei Lun Liou, and Ruei Syuan Lai. Wear analysis of the offset type preloaded ball-screw operating at high speed. *Wear*, 292-293:111–123, 2012.

[166] Jiajia Zhao, Mingxing Lin, Xianchun Song, Hongkui Jiang, and Xiaojian Wu. Investigation on the Precision Loss of Ball Screw Considering the Full Ball Load Distribution. *IOP Conference Series: Materials Science and Engineering*, 422(1), 2018.

[167] Qiang Cheng, Baobao Qi, Zhifeng Liu, Caixia Zhang, and Deyi Xue. An accuracy degradation analysis of ball screw mechanism considering time-varying motion and loading working conditions. *Mechanism and Machine Theory*, 134:1–23, apr 2019.

[168] Jialan Liu, Chi Ma, and Shilong Wang. Precision loss modeling method of ball screw pair. *Mechanical Systems and Signal Processing*, 135:106397, 2020.

[169] Dumitru N. Olaru, G. C. Puiu, L. C. Balan, and Vasile Puiu. A New Model to Estimate Friction Torque in a Ball Screw System, 2005.

[170] Dumitru N. Olaru and Vasile Puiu. Friction Torque and Efficiency in Ball-Screw Systems. *Acta Tribologica*, 17:25–29, 2009.

[171] Nannan Xu, Wencheng Tang, Yongjiang Chen, Dafei Bao, and Yujie Guo. Modeling analysis and experimental study for the friction of a ball screw. *Mechanism and Machine Theory*, 87:57–69, may 2015.

[172] Joost J. Kalker. *Three-Dimensional Elastic Bodies in Rolling Contact*, volume 2. Springer-Science+Business Media, B.V., 1990.

[173] J.J. Kalker. A Fast Algorithm for the Simplified Theory of Rolling-Contact. *Vehicle System Dynamics*, 11(1):pp. 1–13, 1982.

[174] J.J. Kalker. Rolling Contact Phenomena : Linear Elasticity. *CISM Courses and Lectures*, pages 1–84, 2000.

[175] Kwang Je Oh, Lei Cao, and Sung Chong Chung. Explicit modeling and investigation of friction torques in double-nut ball screws for the precision design of ball screw feed drives. *Tribology International*, 141(February 2019):105841, 2020.

[176] Claudio Braccesi and Luca Landi. A general elastic-plastic approach to impact analisys for stress state limit evaluation in ball screw bearings return system. *International Journal of Impact Engineering*, 34(7):1272–1285, 2007.

[177] Hongkui Jiang, Xianchun Song, Xiangrong Xu, Wencheng Tang, Chunling Zhang, and Yuming Han. Multibody dynamics simulation of Balls impact-contact mechanics in Ball Screw Mechanism. In *Proceedings - International Conference on Electrical and Control Engineering, ICECE 2010*, pages 1320–1323, 2010.

[178] Hongkui Jiang, Xianchun Song, Wencheng Tang, Xiangrong Xu, and Chengrui Zhang. Research on the contact-impact between balls and re-circulating mechanism using the multibody dynamics simulation. *3rd International Conference on Advanced Computer Theory and Engineering, Proceedings*, 4(1):10–13, 2010.

[179] De-Shin Liu, Pen-Chen Lin, Jheng-Jie Lin, Chuen-Ren Wang, and Ting-Nung Shiau. Effect of environmental temperature on dynamic behavior of an adjustable preload double-nut ball screw. *The International Journal of Advanced Manufacturing Technology*, dec 2018.

[180] Giorgio Balbo and Roberto Graziosi. *Viti a ricircolazione di sfere: risultato del contratto di ricerca con oggetto: analisi sperimentale di sitemi a ricircolazione di sfere, per mezzo di un apposito banco di misura - Parte prima*. Consiglio nazionale delle ricerche - Programma di ricerca sull'automazione nell'industria meccanica con speciale riguardo alle macchine utensili, Milano, collana di edition, 1970.

[181] Antonio Carlo Bertolino, Giovanni Jacazio, Stefano Mauro, and Massimo Sorli. High Fidelity Model of a Ball Screw Drive for a Flight Control Servoactuator. In ASME, editor, *IMECE Volume 1: Advances in Aerospace Technology*, volume 1, Tampa, Florida, USA, nov 2017. ASME.

[182] Antonio Carlo Bertolino, Giovanni Jacazio, Stefano Mauro, and Massimo Sorli. High fidelity model for efficiency calculation of ball screws for flight control actuators. In Institut national des sciences appliquées Toulouse, editor, *Recent Advances in Aerospace Actuation Systems and Components*, pages 153–163, Tolouse, France, 2018.

[183] Sören Andersson, Anders Söderberg, and Stefan Björklund. Friction models for sliding dry, boundary and mixed lubricated contacts. *Tribology International*, 40(4):580–587, 2007.

[184] Mattias Nordin, Johann Galic', and Per-Olof Gutman. New models for backlash and gear play. *International Journal of Adaptive Control and Signal Processing*, 11(1):49–63, feb 1997.

[185] Jean-Charles Maré. Requirement-based system-level simulation of mechanical transmissions with special consideration of friction, backlash and preload. *Simulation Modelling Practice and Theory*, 63:58–82, 2016.

[186] C. Makkar, W. E. Dixon, W. G. Sawyer, and G. Hu. A New Continuously Differentiable Friction Model for Control Systems Design. In *International Conference on Advanced Intelligent Mechatronics*, pages 600–605, Monterey, California, 2005. IEEE/ASME.

[187] Giovanni Jacazio and B. Piombo. *Meccanica applicata alle macchine - Vol. I*. Levrotto & Bella, Torino, 1991.

[188] P. C. Tsai, C. C. Cheng, and Y. C. Hwang. Ball screw preload loss detection using ball pass frequency. *Mechanical Systems and Signal Processing*, 48(1-2):77–91, 2014.

[189] Yuxin Zhou, Rob Bosman, and Piet M. Lugt. A Model for Shear Degradation of Lithium Soap Grease at Ambient Temperature. *Tribology Transactions*, 61(1):61–70, 2018.

[190] H. A. Barnes, J. F. Hutton, and K. F. R. S. Walters. *An Introduction to Rheology*, volume 3. Elsevier B.V., 1993.

[191] Yuxin Zhou. *On the mechanical aging of lubricating greases, PhD thesis*. PhD thesis, University of Twente, 2018.

[192] Bernard J Hamrock. Fundamentals of Fluid Film Lubrication. *Nasa Publication 1255*, 1991.

[193] Victoria Wikström and Erik Höglund. Investigation of parameters affecting the limiting shear stress-pressure coefficient: A new model incorporating temperature. *Journal of Tribology*, 116(3):612–620, 1994.

[194] Dong Zhu and Q. Jane Wang. Elastohydrodynamic Lubrication: A Gateway to Interfacial Mechanics—Review and Prospect. *Journal of Tribology*, 133(4):041001, 2011.

[195] P. K. Gupta, H. S. Cheng, D. Zhu, N. H. Forster, and J. B. Schrand. Viscoelastic effects in MIL-L-7808-type lubricant, part I: Analytical formulation. *Tribology Transactions*, 35(2):269–274, 1992.

[196] L. Houpert. New Results of Traction Force Calculations in Elastohydrodynamic Contacts. *Journal of Tribology*, 107(2):241, 2009.

[197] Cristiana Delprete and Abbas Razavykia. Piston dynamics, lubrication and tribological performance evaluation: A review. *International Journal of Engine Research*, 21(5):725–741, 2020.

[198] C. H. Venner and A.A. Lubrecht. *Multilevel methods in lubrication, Tribology series 37*. Elsevier B.V., 2000.

[199] Bharat Bhushan. *Introduction to Tribology*. John Wiley & Sons, Inc., 2013.

[200] Xiao Liang Yan, Xiao Li Wang, and Yu Yan Zhang. A numerical study of fatigue life in non-Newtonian thermal EHL rolling-sliding contacts with spinning. *Tribology International*, 80:156–165, 2014.

[201] Enrico Ciulli. Formulas for entraining velocity in lubricated line contacts. *Journal of Tribology*, 124(4):856–858, 2002.

[202] Hugh Spikes. Basics of EHL for practical application. *Lubrication Science*, 27(1):45–67, jan 2015.

[203] Bernard J Hamrock and Duncan Dowson. Elastohydrodynamic lubrication of elliptical contacts for materials of low elastic modulus. *ASME journal of Tribology*, 100:236–245, 1978.

[204] G Nijenbanning, C H Venner, and H Moes. Film thickness in elastohydrodynamically contacts. *Wear*, 176(2):217–229, 1994.

[205] L. E. Murch and W. R. D. Wilson. A Thermal Elastohydrodynamic Inlet Zone Analysis. *Journal of Lubrication Technology*, 97(2):212, 1975.

[206] Dennis Fischer, Helko Mues, Georg Jacobs, and Andreas Stratmann. Effect of Over Rolling Frequency on the Film Formation in Grease Lubricated EHD Contacts under Starved Conditions. *Lubricants*, 7(2):19, 2019.

[207] T. E. Tallian. On competing failure modes in rolling contact. *ASLE Transactions*, 10(4):418–439, 1967.

[208] J. Castro and J. Seabra. Global and local analysis of gear scuffing tests using a mixed film lubrication model. *Tribology International*, 41(4):244–255, 2008.

[209] Dong Zhu and Yuan Zhong Hu. A computer program package for the prediction of ehl and mixed lubrication characteristics, friction, subsurface stresses and flash temperatures based on measured 3-d surface roughness. *Tribology Transactions*, 44(3):383–390, 2001.

[210] J. de Vicente, J. R. Stokes, and H. A. Spikes. Rolling and sliding friction in compliant, lubricated contact. *Proceedings of the Institution of Mechanical Engineers, Part J: Journal of Engineering Tribology*, 220(2):55–63, 2006.

[211] Mihaela Rodica D Balan, Vasile Ciprian Stamate, Luc Houpert, and Dumitru N. Olaru. The influence of the lubricant viscosity on the rolling friction torque. *Tribology International*, 72:1–12, 2014.

[212] Luc Houpert. Ball Bearing and Tapered Roller Bearing Torque: Analytical, Numerical and Experimental Results. *Tribology Transactions*, 45(3):345–353, 2002.

[213] N. Biboulet and L. Houpert. Hydrodynamic force and moment in pure rolling lubricated contacts. Part 2: Point contacts. *Proceedings of the Institution of Mechanical Engineers, Part J: Journal of Engineering Tribology*, 224(8):777–787, aug 2010.

[214] Tiago Cousseau, Beatriz Graca, Armando Campos, and Jorge Seabra. Friction torque in grease lubricated thrust ball bearings. *Tribology International*, 44:523–531, 2011.

[215] L. Houpert. Piezoviscous-Rigid Rolling and Sliding Traction Forces, Application: The Rolling Element–Cage Pocket Contact. *Journal of Tribology*, 109(2):363, 2009.

[216] Mihaela Bălan, Luc Houpert, Ana Tufescu, and Dumitru Olaru. Rolling Friction Torque in Ball-Race Contacts Operating in Mixed Lubrication Conditions. *Lubricants*, 3(2):222–243, 2015.

[217] G. Ianuş, A. C. Dumitraşcu, V. Cârlescu, and D. N. Olaru. Friction torque in thrust ball bearings grease lubricated. *IOP Conference Series: Materials Science and Engineering*, 147(1), aug 2016.

[218] Leonid Gershuni, Mats G. Larson, and Piet M. Lugt. Lubricant replenishment in rolling bearing contacts. *Tribology Transactions*, 51(5):643–651, 2008.

[219] B. Damiens. *Modelisation de la lubrification sous-alimentee dans les contacts elastohydrodynamiques elliptiques*. Phd thesis, INSA de Lyon, 2003.

[220] B. Damiens, C. H. Venner, P. M. E. Cann, and A. A. Lubrecht. Starved Lubrication of Elliptical EHD Contacts. *Journal of Tribology*, 126(1):105, 2004.

[221] F. Chevalier, A. A. Lubrecht, P. M. E. Cann, F. Colin, and G. Dalmaz. Film Thickness in Starved EHL Point Contacts. *Journal of Tribology*, 120(1):126, 1998.

[222] M. T. Van Zoelen, C. H. Venner, and P. M. Lugt. Prediction of film thickness decay in starved elasto-hydrodynamically lubricated contacts using a thin layer flow model. *Proceedings of the Institution of Mechanical Engineers, Part J: Journal of Engineering Tribology*, 223(3):541–552, 2009.

[223] J-S. Mérieux, S. Hurley, A.A. Lubrecht, and P.M. Cann. Shear-degradation of grease and base oil availability in starved EHL lubrication. In *Thinning Films and Tribological Interfaces - Tribology series 38*, pages 581–588. Elsevier Science B.V., 2000.

[224] Ton Lubrecht, Denis Mazuyer, and Philippa Cann. Starved elastohydrodynamic lubrication theory: Application to emulsions and greases. *Comptes Rendus de l'Academie des Sciences - Series IV: Physics, Astrophysics*, 2(5):717–728, 2001.

[225] Dennis Fischer, Georg Jacobs, Andreas Stratmann, and Gero Burghardt. Effect of base oil type in grease composition on the lubricating film formation in EHD contacts. *Lubricants*, 6(2):1–13, 2018.

[226] Balasubramaniam Vengudusamy, Marius Kuhn, Michael Rankl, and Reiner Spallek. Film Forming Behavior of Greases Under Starved and Fully Flooded EHL Conditions. *Tribology Transactions*, 59(1):62–71, 2016.

[227] Giovanni Jacazio, Marco Libraro, Andrea Mornacchi, and Massimo Sorli. Lubricants Health Monitoring. *Phm*, pages 39–48, 2013.

[228] Yuxin Zhou, Rob Bosman, and Piet M. Lugt. A Master-Curve for the Shear Degradation of Rolling Bearing Greases. In *STLE Annual Meeting & Exhibition*, Minneapolis, 2018.

[229] Asghar Rezasoltani and M. M. Khonsari. An engineering model to estimate consistency reduction of lubricating grease subjected to mechanical degradation under shear. *Tribology International*, 103:465–474, 2016.

[230] Tiago Cousseau, Beatriz Graça, Armando Campos, and Jorge Seabra. Grease Aging Effects on Film Formation under Fully-Flooded and Starved Lubrication. *Lubricants*, 3(2):197–221, 2015.

[231] F. Cyriac, P. M. Lugt, R. Bosman, C. J. Padberg, and C. H. Venner. Effect of Thickener Particle Geometry and Concentration on the Grease EHL Film Thickness at Medium Speeds. *Tribology Letters*, 61(2):1–13, 2016.

[232] Yuta Kanazawa, Nicola De Laurentis, and Amir Kadiric. Studies of Friction in Grease-Lubricated Rolling Bearings Using Ball-on-Disc and Full Bearing Tests. *Tribology Transactions*, 63(1):77–89, jan 2020.

[233] J-F. Antoine, C. Visa, C. Sauvey, and G. Abba. Approximate Analytical Model for Hertzian Elliptical Contact Problems. *Journal of Tribology*, 128(3):660, 2006.

[234] Milton Abramowitz and Irene A. Stegun. *Handbook of Mathematical Functions with Formulas, Graphs, and Mathematical Tables*, volume 55. National Bureau of Standards, 1964.

[235] Ew Deeg. New algorithms for calculating Hertzian stresses, deformations, and conatact zone parameters. *AMP Journal of Technology*, 2:14–24, 1992.

[236] K. L. Johnson. *Contact Mechanics*. Cambridge University Press, Cambridge, 1985.

[237] J F Archard. Wear Theory and Mechanisms. In W.O. Winer and M.B. Peterson, editors, *Wear Control Handbook*, pages 35–80. ASME, 1980.

[238] Pascal Guay and Ahmed Frikha. Ball Bearing Stiffness: A New Approach Offering Analytical Expressions. In *16th European Space Mechanisms and Tribology Symposium*, 2015.

[239] S. Gottschalk, M. C. Lin, and D. Manocha. OBBTree: A hierarchical structure for rapid interference detection. *Proceedings of the ACM SIGGRAPH Conference on Computer Graphics*, pages 171–180, 1996.

[240] MSC Software. MSC Adams Solver user guide, 2017.

[241] N. V. Orlandea. A study of the effects of the lower index methods on ADAMS sparse tableau formulation for the computational dynamics of multi-body mechanical systems. *Proceedings of the Institution of Mechanical Engineers*, 213(K), 1999.

[242] K. E. Brenan, S. L. Campbell, and L. R. Petzold. *Numerical Solution of Initial-Values Problems in Differential-Algebraic Equations*. Society for Industrial and Applied Mathematics, Philadelphia, 1996.

[243] Antonio Carlo Bertolino, Andrea De Martin, Giovanni Jacazio, Stefano Mauro, and Massimo Sorli. Robust Design of a Test Bench for PHM Study of Ball Screw Drives. In ASME, editor, *IMECE Volume 1: Advances in Aerospace Technology*, Salt Lake City, UT, USA, nov 2019. American Society of Mechanical Engineers.

[244] Wenjing Jin, Yan Chen, and Jay Lee. Methodology for Ball Screw Component Health Assessment and Failure Analysis. *Volume 2: Systems; Micro and Nano Technologies; Sustainable Manufacturing*, page V002T02A031, 2013.

[245] Iñaki Navarro y de Sosa, André Bucht, Tom Junker, Kenny Pagel, and Welf Guntram Drossel. Novel compensation of axial thermal expansion in ball screw drives. *Production Engineering*, 8(3):397–406, 2014.

[246] Masih Hanifzadegan and Ryozo Nagamune. Tracking and structural vibration control of flexible ball-screw drives with dynamic variations. *IEEE/ASME Transactions on Mechatronics*, 20(1):133–142, 2015.

[247] Edward Balaban, Abhinav Saxena, and Kai Goebel. Experimental data collection and modeling for nominal and fault conditions on electro-mechanical actuators. *Annual Conference of the Prognostics and . . .*, pages 1–15, 2009.

[248] Fuhua Li, Tiemin Li, Yao Jiang, and Fengchun Li. Effects of Velocity on Elastic Deformation in Ball Screw Drives and its Compensation. In ASME, editor, *Proceedings of the ASME 2017 International Mechanical Engineering Congress and Exposition*, Tampa, Florida, USA, 2017. ASME.

[249] Giovanni Jacazio and B. Piombo. *Meccanica applicata alle macchine - Vol. II*. Levrotto & Bella, Torino, 1992.

[250] Ioan Iov Incze, Alin Negrea, Maria Imecs, and Csaba Szabó. Incremental Encoder Based Position and Speed Identification: Modeling and Simulation. *Acta Universitatis Sapientiae Electrical and Mechanical Engineering*, 2:27–39, 2010.

[251] M. Sorli, L. Gastaldi, E. Codina, and S. De Las Heras. Dynamic analysis of pneumatic actuators. *Simulation Practice and Theory*, 1999.

[252] Sylvain Autin, Jérôme Socheleau, Andrea Dellacasa, Andrea De Martin, Giovanni Jacazio, and George Vachtsevanos. Feasibility Study of a PHM System for Electro-hydraulic Servo- actuators for Primary Flight Controls. In *Annual Conference of the Prognostic and Health Management Society*, pages 1–19, 2018.

Appendix A

Over rolling frequencies

A.1 Screw shaft groove

During BS operations, the screw rotates with an angular speed ω and the spheres perform an orbital motion around the screw shaft axis with an angular speed ω_m. The screw angular velocity relative to a ball can be written as [98]:

$$\omega_i = (\omega - \omega_m)\cos(\alpha_e) \tag{A.1}$$

Substituting the expression of ω_m from [98], it can be rewritten in terms of only the screw speed ω:

$$\omega_i = \omega\cos(\alpha_e)\frac{r_m + r_b\cos(\alpha_e)}{2r_m} \tag{A.2}$$

To obtain Eq. A.2 the following simplifications have been assumed:

- Negligible gyroscopic angle, which imply that the spin speed of the spheres lays on the $n-b$ plane;
- The contact angles with the screw and nut grooves are coincident and equal to $\alpha_{sn} = 45^\circ$;
- Contact deformations are ignored;

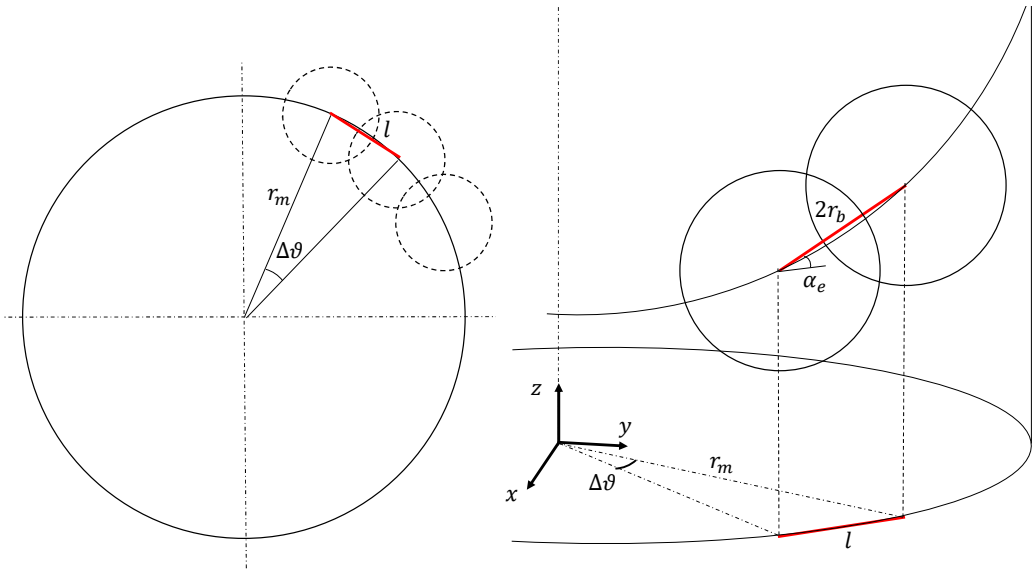

Fig. A.1 Spheres relative position.

The over rolling frequency is defined as the number of spheres which passes on the same point on the screw shaft in 1 [s]. Thus, knowing the angular speed of the screw with respect to the spheres ω_i, this value can be obtained calculating the angle of rotation $\Delta\vartheta$ of the screw relative to the spheres correspondent to the angular distance between two adjacent spheres.

Looking at Fig. A.1, if the spheres, which are tangent on the helix, are projected on the plane normal to the screw axis ($x-y$ plane), there is a little overlaps of the projected circumferences. The distance between the centres of the spheres is $2r_b$. Assuming their ideal positions on the helix, their distance from the screw axis is r_m. The projection of the segment connecting the two spheres' centres on the $x-y$ plane is

$$l = 2r_b \cos(\alpha_e) \tag{A.3}$$

but, applying the rope theorem on the pitch circle diameter, it can also be expressed as

$$l = 2r_m \sin\left(\frac{\Delta\vartheta}{2}\right) \tag{A.4}$$

From Eqns. A.1 and A.2 the interval angle is found:

$$\Delta\vartheta = 2\arcsin\left(\frac{r_b}{r_m}\cos\left(\alpha_e\right)\right) \tag{A.5}$$

Therefore, the over rolling frequency [Hz] on the screw groove can be obtained as follows:

$$f_{screwgroove} = \frac{\omega_i}{\Delta\vartheta} = \frac{|\omega|\cos(\alpha_e)\left(1+\frac{r_b}{r_m}\cos(\alpha_{sn})\right)}{4\arcsin\left(\frac{r_b}{r_m}\cos(\alpha_e)\right)} \tag{A.6}$$

A.2 Nut groove

Under the same hypotheses, the angular velocity of the nut with respect to the spheres can be written as [98]:

$$\omega_o = -\omega\cos\left(\alpha_e\right)\frac{r_m - r_b\cos(\alpha_e)}{2r_m} \tag{A.7}$$

Being the distance between the spheres a constant, the over rolling frequency [Hz] on the nut groove can be written as:

$$f_{nut\ groove} = \frac{\omega_o}{\Delta\vartheta} = \frac{|\omega|\cos(\alpha_e)\left(1-\frac{r_b}{r_m}\cos(\alpha_{sn})\right)}{4\arcsin\left(\frac{r_b}{r_m}\cos(\alpha_e)\right)} \tag{A.8}$$

A.3 Sphere

Having assumed a null gyroscopic angle, the component of the spin speed ω_R of the sphere on the $\widehat{\mathbf{t}}$ axis is equal to zero, while the other are [98]:

$$\begin{aligned}\omega_t &= 0\\ \omega_n &= -\omega_R\cos\left(\beta\right)\\ \omega_b &= -\omega_R\sin\left(\beta\right)\end{aligned} \tag{A.9}$$

where, using the notation in [98], β is the angle between the spin speed ω_R and the $\widehat{\mathbf{b}}$ axis in the case of null gyroscopic angle. If the gyroscopic angle is neglected, it is equal to the contact angle α_{sn}.

The relationship between the spin speed and the revolution velocity is [98]:

$$\omega_R = \frac{-\omega_m \left[1 + \frac{r_b}{r_m}\cos(\alpha_{sn})\right]\cos(\alpha_{sn})}{\frac{r_b}{r_m}\left[\cos(\beta)\cos(\alpha_{sn}) + \sin(\beta)\sin(\alpha_{sn})\right]} = \sqrt{\omega_t^2 + \omega_n^2 + \omega_b^2} \tag{A.10}$$

The revolution velocity ω_m of the spheres can be related to the screw angular velocity as [98]:

$$\omega_m = \frac{\omega}{2}\left[1 - \frac{r_b}{r_m}\cos(\alpha_{sn})\right] \tag{A.11}$$

Inserting Eq. A.11 into Eq. A.10, and recalling that β is equal to α_{sn} under the assumptions made, the spin speed can be written as

$$\omega_R = -\frac{\omega r_m}{2r_b}\left[1 - \left(\frac{r_b}{r_m}\cos(\alpha_{sn})\right)^2\right]\cos(\alpha_e) \tag{A.12}$$

Finally, the over rolling frequency on the sphere surface [86] can be written as follows:

$$f_{sphere} = \frac{\omega_R}{2\pi r_b} = \frac{|\omega|\, r_m \cos(\alpha_e)}{4\pi r_b}\left[1 - \left(\frac{r_b}{r_m}\cos(\alpha_{sn})\right)^2\right] \tag{A.13}$$

Appendix B

Test bench components data

Table B.1 Lenze MCS09F38 electri motor data sheet characteristics.

Characteristic	**Value**
Rated speed [rpm]	3750
Standstill torque [Nm]	4.2
Rated torque [Nm]	3.1
Maximum torque [Nm]	15
Rated power [kW]	1.2
Standstill current [A]	3
Rated current [A]	2.5
Maximum current [A]	15
Thermal time constant [s]	120
Nominal frequency [Hz]	250
Polar pairs	4
Efficiency [%]	91
Moment of inertia (without brake) [kgm^2]	1.5×10^{-4}
Speed constant @ 150 °C [V/rad/s]	0.762
Torque constant @ 150 °C [Nm/A]	1.4
Windings resistance @ 20 °C [Ω]	5.2
Windings resistance @ 150 °C [Ω]	7
Windings inductance [mH]	24.6
Maximum permissible speed [rpm]	7000
Mass [kg]	5.20
Supply voltage [V]	3×400

Table B.2 Lenze g700-P44 reducer data sheet characteristics.

Characteristic	**Value**
Nominal torque [Nm]	44
Continuative torque @ nominal speed [Nm]	38
Maximum torque [Nm]	61
Maximum permissible input speed [rpm]	13000
Reduction ratio	4
Moment of inertia [kgm^2]	6.6×10^{-6}
Nominal efficiency	0.96
Maximum axial force [N]	400
Maximum radial force[N]	500
Backlash [deg]	0.1667
Torsional stiffness [Nm/rad]	7906.8
Output flange diameter [mm]	60

Table B.3 Lenze 9400 High Line motor driver data sheet characteristics.

Characteristic	**Value**
Input AC voltage [V]	$340 \div 528$
DC supply [V]	$460 \div 740$
Analogue input resolution [bits]	11 + sign
Analogue input range [V]	± 10
Output nominal current [A]	4
Nominal switching frequency [kHz]	8
DC-bus nominal current [A]	6.7
Power loss [kW]	0.16
Recovery current [A]	3.8
Overload duration 1 [s]	0.5
Maximum current 1 [A]	16
Recovery time 1 [s]	4.5
Overload duration 2 [s]	60
Maximum current 2 [A]	7.5
Recovery time 2 [s]	120

Table B.4 ELCIS RV1846 linear encoder data sheet characteristics.

Characteristic	**Value**
Code	L–RV1846–320–5–BZ–N–1
Supply voltage [V]	$5 \pm 5\%$
Resolution [µm]	1
Precision [µm]	± 5
Start force [N]	< 3
Maximum frequency [kHZ]	50
Measuring stroke [mm]	320
Total length [mm]	425
Phase tolerance [deg]	± 45
Phase symmetry [deg]	± 15

Table B.5 BURSTER 8661–5050 torque meter data sheet characteristics.

Characteristic	**Value**
Nominal torque I range [Nm]	50
Nominal torque II range [Nm]	5
Maximum torque [Nm]	75
Limit torque [Nm]	150
Encoder increments [pulses/turn]	2000
Supply voltage [V]	$10 \div 30$
Output voltage range [VDC]	± 10
Encoder output	5V TTL
D/A converter bit [V]	16
Temperature effect on zero signal range I [%F.S./K]	± 0.015
Temperature effect on zero signal range II [%F.S./K]	± 0.03
Temperature effect on sensitivity range I [%F.S./K]	± 0.01
Temperature effect on sensitivity range II [%F.S./K]	± 0.02
Relative linearity deviation [%F.S.]	$< \pm 0.1$
Relative reversal error [%F.S.]	$< \pm 0.2$
Relative tolerance on sensitivity [%F.S.]	± 0.2
Stiffness [Nm/rad]	14000
Motor side Moment of inertia [kgm^2]	85.7×10^{-6}
Load side Moment of inertia [kgm^2]	33.3×10^{-6}
Maximum axial load [N]	300
Maximum radial load [N]	125
Torque measure refresh rate [Hz]	1000

Table B.6 RADEX NC 25 DK torque coupling data sheet characteristics.

Characteristic	**Value**
Code	RADEX NC 25 DK
Nominal torque [Nm]	60
Maximum torque [Nm]	120
Maximum speed [rpm]	10000
Maximum radial misalignment [mm]	0.30
Maximum axial misalignment [mm]	1.6
Moment of inertia [kgm^2]	5.08×10^{-4}
Torsional stiffness [Nm/rad]	30000

Table B.7 K-1882 Lorenz Messtechnik GmbH load cell data sheet characteristics.

Characteristic	**Value**
Nominal force [kN]	1/10
Measuring range I [kN]	0 -1
Measuring range II [kN]	1-10
Mass [kg]	3.9
Accuracy [% Nominal force]	0.4
Relative repeatability error [% Nominal force]	0.1
Sensitivity [mV/V]	$1.00 \pm 0.5\%$
Temperature effect on zero signal [% Nominal force/10K]	± 0.2
Temperature effect on sensitivity [% Nominal force/10K]	± 0.2
Limit force [kN]	15
Breaking force [kN]	> 18
Nominal deflection @ Nominal force [mm]	0.4

Table B.8 LCV/U10 Lorenz Messtechnik GmbH conditioner data sheet characteristics.

Characteristic	**Value**
Supply voltage [VDC]	$12 \div 28$
Supply voltage maximum ripple [%]	10
Output voltage range [V]	± 10
Output voltage maximum ripple [mV]	10
Gain drift [%/10K]	< 0.015
Zero point drift [%/10K]	< 0.015
Linearità [%]	< 0.02
Output resistance [Ω]	< 1
Cut-off frequency -3dB [kHz]	10

Table B.9 SKF BSA201C bearing data sheet characteristics.

Characteristic	**Value**
Dynamic load coefficient [kN]	11.8
Static load coefficient [kN]	21.2
Fatigue limit load [kN]	0.8
Limit speed [rpm]	14000
Preload [N]	650
Friction torque [Nm]	0.016
Axial static stiffness [N/µm]	400
Contact angle [deg]	62
Mass [kg]	0.043

Table B.10 Hiwin linear guide data sheet characteristics.

Characteristic	**Value**
Dynamic load rating [kN]	21.3
Static load rating [kN]	46.7
Mass [kg]	0.4
Maximum dynamic roll moment [Nm]	296
Maximum dynamic pitch moment [Nm]	210
Maximum dynamic yaw moment [Nm]	210
Maximum static roll moment [Nm]	647
Maximum static roll moment [Nm]	460
Maximum static roll moment [Nm]	460

Table B.11 Angst+Pfister end stroke damper data sheet characteristics.

Characteristic	**Value**
Code	12.2037.1003
Compression force F_z [N]	4000
Stiffness [N/m]	250000
Deflection s_z [mm]	16
Energy absorption [J]	20

Table B.12 FESTO MPYE proportional flow valve data sheet characteristics.

Dati tecnici generali	Definizione
Valve function	5/3–way, normally closed
Nominal size [mm]	10
Standard nominal flow rate [l/min]	2000
Weight [kg]	0.685
Supply voltage [VDC]	$17 \div 30$
Maximum hysteresis [%]	0.4
Valve mid–position [VDC]	$5\,(\pm 0.1)$
Residual ripple [%]	5
Critical frequency [Hz]	70
Operating pressure [bar]	$0 \div 10$

Table B.13 HBM K–U9C–2020 load cell data sheet characteristics.

Characteristic	**Value**
Code	K–U9C–20K0–03M0–Y–S
Nominal force [kN]	20
Nominal sensitivity [mV/V]	1
Relative zero signal error [mV/V]	± 0.2
Sensitivity error [%]	± 1 tensile, ± 2 compressive
Relative repeatability error [%]	0.2
Relative reproducibility error [%]	0.2
Relative reversibility error [%]	0.2
Non–linearity [%]	0.2
Temperature effect on zero signal [%/10K]	0.2
Temperature effect on sensitivity [%/10K]	0.2
Supply voltage [V]	5
Limit force [% Nominal force]	150
Breaking force [% Nominal force]	400
Deflection with nominal force [mm]	0.018
Fundamental resonance frequenct [kHz]	13.2
Mass [kg]	0.1
Conditioner measuring rate [kHz]	19.2
Conditioner cut-off frequency -3dB [kHz]	3.8